

Alma Mater Studiorum – Università di Bologna

DOTTORATO DI RICERCA IN

CHIMICA

Ciclo XXXIV

**Settore Concorsuale:** 03/B1, 03/A2

**Settore Scientifico Disciplinare:** CHIM/03-CHIMICA GENERALE E INORGANICA  
CHIM/02 - CHIMICA FISICA

GREEN SUPERCAPACITIVE SYSTEMS

**Presentata da:** Federico Poli

**Coordinatore Dottorato**

**Prof.ssa Domenica Tonelli**

**Supervisore**

**Prof.ssa Francesca Soavi**

**Co-supervisor**

**Prof. Carlo Santoro**

**Prof.ssa Clara Santato**

**Prof. Ncholu Manyala**

**Esame finale anno 2022**

# Index:

<i>Abstract</i> .....	3
Chapter 1: Introduction .....	5
1.1 The energetic landscape and the Water energy nexus .....	5
1.2 Electrochemical energy storage devices (EES).....	11
1.3 Electrochemical double-layer supercapacitors.....	15
EDLCs: Main components.....	20
1.3.1 Current collectors.....	21
1.3.2 High surface area carbon electrode.....	22
1.3.3 Conductive carbon additive .....	33
1.3.4 Binder.....	34
1.3.5 Electrolyte .....	36
1.3.6 Separator .....	37
1.4 Microbial fuel cell (MFC).....	38
1.4.1 Anode.....	40
1.4.2 Current collector .....	40
1.4.5 Biofilm .....	41
1.4.6 Air-breathing cathode .....	42
1.5 Supercapacitive microbial fuel cell.....	44
1.6 Aim of the work .....	47
Chapter 1 references: .....	48
Chapter 2: Green supercapacitors .....	53
2.1 Pullulan as water processable polymer for high voltage supercapacitors .....	55
2.2 Novel N-doped carbons .....	80
2.3 Novel electrolytes .....	90
2.3.1 Electrochemical stability of Ti, stainless steel and Cu current collector in water-in-salt based on LiTFSi.....	90
2.3.2 A novel Water in Salt electrolyte based on ammonium acetate.....	103
Chapter 2 references: .....	115
Chapter 3: Supercapacitive system .....	116
3.1 Integration of MFCs with commercial supercapacitors to boost power performances.....	118
3.2 Valorization of lignin waste from biodigester plant in MFC and SC .....	131
3.3 Supercapacitor based on Lignin-derived carbon and calcium alginate binder.....	145

3.3.1 Electrode preparation and EDLC assembly .....	146
3.3.2 LAC2-alginate electrode performance .....	147
3.3.3 All aqueous supercapacitor (AaSC) .....	150
3.3.4 Conclusions.....	157
3.4 Strategies to improve MFC power output.....	158
3.4.1 MFC assembly and MFC-EDLC integration .....	158
3.4.3 External integration of MFC with the green AaSC supercapacitor (MFC//SC) .....	165
3.4.4 Capacitive additional electrode, short-circuited with MFC cathode (AAC-MFC) .....	168
3.4.5 Monolithic Supercapacitive MFC (MSC-MFC) .....	172
3.4.6 Comparison of the different strategies .....	175
3.4.6 Conclusion: .....	177
Conclusion: .....	177
Reference chapter 3: .....	178
Chapter 4: Getting insight into the electrode/electrolyte interface .....	179
4.1 Electrochemical Investigation of the biofilm growth.....	180
4.2 Investigation of the electronic properties of lithium-ion battery materials through ion-gated transistors .....	188
4.2.4 Conclusion .....	201
Chapter 5 Conclusions and perspectives:.....	204
Appendix A (Supercapacitors).....	211
Appendix B: BET surface area measurements .....	220

## *Abstract*

The continuous growth of the global population together with the rising incomes bring about the willingness to spend these incomes on energy-water-intensive goods. These two sectors (energy and water) are deeply interlinked in the so-called water-energy nexus. Common strategies capable of simultaneously addressing sustainable water consumption, limiting the depletion of this precious resource, together with a reduced environmental footprint are needed to tackle the challenges of the nexus. In this context, electrochemical energy storage systems based on bioderived components and sustainable processes, together with novel electrochemical conversion systems such as microbial fuel cells rise as a valuable strategy that aims to produce clean water while providing direct electric energy stored in sustainable devices. The low power output of the MFCs is the main limit to their practical applications. The low cell voltage is an intrinsic characteristic of MFCs and therefore strategies that aim at improving the output current are more likely to be adopted to improve power performances.

For this reason, this Ph.D. thesis addresses the challenging goal of integrating supercapacitive features in MFCs by sustainable materials and processes and valorizing wastes by their processing as key components of supercapacitors and MFCs. Three main research lines have been pursued: i) the development of green supercapacitors by exploiting natural polymers as binders and electrospun separators, ii) the improvement of the power output of MFCs by the external integration of commercial and green supercapacitors, and ii) the development of supercapacitive microbial fuel cells by the monolithic integration of supercapacitive features in MFCs. This Thesis is articulated in the following Sections. Chapter 1 introduce the energy-water nexus, highlights the role played by supercapacitors and MFCs in this context, and describes the main components, and processes in these devices. In Chapter 2, different approaches followed to improve the sustainability of supercapacitor manufacturing are reported. The strategies to both integrate external supercapacitors and monolithic supercapacitive features in MFCs that have been carried out are reported in Chapter 3. Finally, a third more explorative line of research followed on this thesis, that regards the study of electrochemical interfaces and is reported and discussed in Chapter 4. Overall, the activities carried out during my Ph.D. project are extremely challenging and include a wide spectrum of the different electrochemical processes, from capacitive, to bioelectrochemical and electrocatalytic, the optimization of electrode and system manufacturing, with a focus on sustainability, and device characterization and system integration studies. The main novelty of

my work has therefore been the exploitation and merging of different electrochemical systems and their components, by a green approach, to boost MFCs performance up to two orders of magnitude than conventional air-breathing MFCs. The interdisciplinarity of my work was strengthened by the opportunity to collaborate with different research groups of the Department of Chemistry “Giacomo Ciamician” (Polymer science and biomaterials Lab – Prof. ML.Focarete and Prof. C. Gualandi, and the Nanobio interface Lab-Prof. M. Calvareis), with the University of Padova (Electrocatalysis and Applied Electrochemistry Lab -Prof. C. Durante), the University of Firenze (Dept. of Chemistry Ugo Schiff, Prof. M. Innocenti), Prof. C. Santoro (University of Milano-Bicocca), the University of Pretoria (Research Group Carbon Technology and material - Prof. N. Manyala), and the Polytechnique Montreal (Organic electronics labs-Prof. C. Santato and Prof F. Cicoira).

These extremely fruitful collaborations were carried out under different national and international projects, namely ISARP 2018-2020/Italy-South Africa joint Research Programme 2018-2020 (Italian Ministers of Foreign Affairs and the Environment and NRF of South Africa, grant No. 113132), Fondazione CARISBO/Progetto ricerca n° 354, Piano Triennale di Realizzazione 2019-2021/Progetto ricerca n° 354, Subvention de projets de recherche IE/Appel à projets 2020, OAK RIDGE NATIONAL LABORATORY/CENTER FOR NANOPHASE MATERIALS SCIENCESPROJECT.

The outcomes of my Ph.D. work have contributed to 8 papers published in peer-review international scientific Journals and 12 oral presentations at Conferences.

# Chapter 1: Introduction

## 1.1 The energetic landscape and the Water energy nexus

Today, global warming and its disruptive outcome are widely accepted. The scientific community is continuously trying to propose factual solutions to the matter, as well as the majority of the first world population, through media marketing and social activity shows positive support to tackle these issues by adopting a more sustainable living style. The major indicator of global warming is the earth's surface temperature. Its increase has been related to the greenhouse effect, which is related to the huge amount in the atmosphere of greenhouse gasses. Greenhouse gases, due to their ability to absorb/emit infrared radiations, slow down the radiative dispersion of thermal energy, that earth adsorb from the sun. This causes a constant heat accumulation that in turn increases the surface temperature. The two most abundant atmospheric gases that have Infra-Red (IR) activities are CO<sub>2</sub> (four vibrational modes, of which three are active in the IR region) and H<sub>2</sub>O (three vibrational modes all active in the IR). Clouds and water in the atmosphere are the biggest contributors to the greenhouse effect, although H<sub>2</sub>O emits in the infrared region, it is not considered a greenhouse gas. Indeed, the amount of H<sub>2</sub>O in the atmosphere increases monotonically with the increase of the surface temperature, and therefore atmospheric H<sub>2</sub>O in its different physical form is considered as a consequence, with amplification capability (positive feedback effect), rather than a cause of global warming. On the other hand, heat-independent gas like CO<sub>2</sub>, CH<sub>4</sub>, chlorofluorocarbon, nitrous oxide, and carbon aerosols are considered responsible for the greenhouse effect [1,2]. A sudden spike of greenhouse gases emission, driven by the volcanic activity, and its consequent global warming, before the appearance of humankind, are kept under consideration as a possible cause of the sudden warm-up that led to the oceanic anoxia, that today is considered as the main cause of the second largest of the five mass extinctions in Earth history [3]. Nowadays, volcanic activity covers 1% of the global CO<sub>2</sub> emission in the atmosphere, the rest is produced by human activity and by the combustion of fossil fuel as a power source combustible [4]. Indeed, both CO<sub>2</sub> and methane, emissions have started to strongly increase from the industrial revolution, that is when humankind started to massively adopt fossil fuel to substitute manpower.

The wide exploitation of fossil fuel is related to the growing demand for immediate and cheap power. Indeed, Figure 1.1a) reports the world energy consumption per year that increases together with the CO<sub>2</sub> production per country (Figure 1.1b)). Noticeably, the CO<sub>2</sub> production of Europe decreases, while, in the same years, one of China, USA, and Asia, strongly increase. Interestingly, this is intimately related to the fact that the average richness (Gross Domestic Product, GDP per capita) increases with a similar trend, as highlighted by Figure 1.1d). This trend is confirmed by the constant growth of the GDP that, for the developed Countries, after the industrial revolution, has increased by a 104% with respect to the preindustrial period, along with the human footprint.

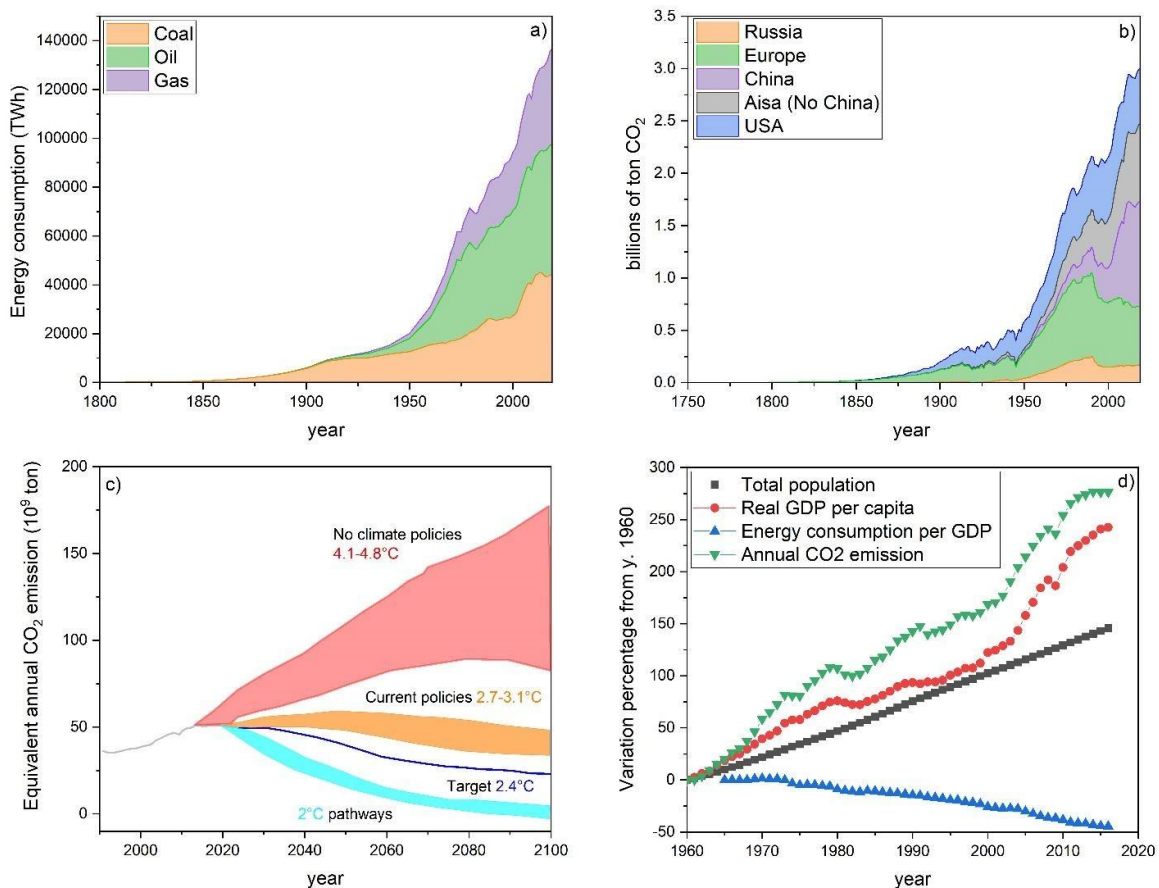


**Figure 1.1:** a) World energy consumption in TWh, b) billions of CO<sub>2</sub> emissions per country c) equivalent billions of CO<sub>2</sub> emissions and possible predicted scenario, d) variation percentage of the total population, Real GDP per capita, energy consumption, and Annual CO<sub>2</sub> emission.

At the global level, the major producer of CO<sub>2</sub> per capita is in the United States. Their energy source is composed of 80% of fossil fuel in particular, natural gas, petroleum, and coal. This energy is consumed mostly for transportation 28.2%, industrial 32.4 %, and commercial 18.1%

activity. It is worth mentioning that this distribution is in line with the main recognized greenhouse gases sources, by transportation, manufacturing, heating, and electricity generation [5]. The international community, driven by the activity of scientific one, has recognized the danger of climate change, and several mitigation actions are being pursued nowadays. Starting from the United Nations Framework Council on Climate Change, 1994, (UNFCCC), in which greenhouse gas concentrations were established to limit the harmful capability of humankind to interfere with the climate system. The treaty called for scientific research, regular meeting, negotiations, and planned future policy to mitigate the climate changes and to adapt to their eventual impact. With the Kyoto protocol in 1997, the UNFCC objectives were subsequently extended with a legally binding agreement. The adhering developed countries were supposed to reduce their greenhouse gases emission in the period 2008-2012. The developed country's responsibilities, the fact that the matter was becoming more urgent, and that quantified actions were needed were highlighted. This has set the base for the Paris agreement in 2016, which, at first, sets the long-term temperature goals below  $2^{\circ}\text{C}$ , and to pursue efforts to limit the temperature increase to  $1.5^{\circ}\text{C}$  above the pre-industrial level. Secondly, the agreement defines the need for climate resilience and low greenhouse emissions, in a manner that doesn't treat food production, and finally defines a financial flow that has to be consistent with a pathway towards low greenhouse emission and climate resilience. The objectives of the Paris agreement are extremely ambitious, and they need urgent actions. The Paris agreement is implemented through national actions that aim to improve energy efficiency, reduce energy intensity, and fossil fuel cut back in favour of sustainable energy sources [6]. The urgency of climate action is highlighted by the possible scenario reported in Figure 1.1 d), according to which, nowadays we are at the turning point and strong policies are needed to invert the trend that the data in Figure 1.1 are reporting. To sustain an extremely energetically consumptive lifestyle, the widespread use of renewable energy sources must be balanced by performances and reduced cost as well as raw materials availability. It is known that renewable energy sources are intermittent by their nature which in turn affect power performances that depend upon the climatic condition, such as the sun and wind availability. In this context, an energy storage system will play a critical role to improve the power output and sustain a power grid that is required to be independent of fossil fuel. Electrochemical energy storage systems like batteries and supercapacitors will play a critical role given their ubiquitous nature, their modularity, and the fact that at the present state of technology these are the only available solution for sustainable mobility. Nowadays, the exploitation of critical raw materials (CRMs) in electrochemical energy storage as well as in sustainable power sources is a major concern for



their adoption, in particular, concerns are related to their price volatility and rise [7]. Indeed, the criticality of a material refers to a broad concept that includes a risk of supply disruption (or supply risk) and the economic relevance of materials (the price impact resulting from a shortage). More precisely, the European Union recognizes as the main source of danger both the geographical localization of raw materials as well as its processing in violation of human rights. The first is related to the danger of escalating trade tension (e.g. China and the US) that could lead to price volatility and shortage with dramatic consequences for the industry. And the second is based on the consideration that it is not acceptable to exploit the violation of human rights in the 21<sup>st</sup> century. Nowadays, critical raw materials, such as transition metal oxides and rare earth elements, play a central role both in electrochemical energy storage systems and renewable power sources. Indeed, wind turbines exploit rare earth elements like neodymium, dysprosium, praseodymium, and terbium for the permanent magnet as well as concrete, steel, plastic, glass, iron, chromium, copper, aluminum, manganese, nickel, zinc, and molybdenum for the structural side. While the materials for the permanent magnet require significant R&D efforts to be substituted, steel and concrete are major players in the greenhouse gases emission, and their substitution is mandatory. In addition, solar panels where rare earth such as germanium, cadmium, tellurium, silicon, selenium, gallium, indium, and silver are exploited together with critical materials such as crystalline silicon [8]. Similar considerations can be drawn for electrochemical energy storage systems (EES). In general, an EES is composed of an anode a cathode, an electrolyte, and a membrane that the two electrodes. Nowadays, the best performing EES on the market in terms of energy density, are lithium-ion batteries (LiBs). The main critical materials of LiBs today are cobalt and lithium, these raw materials are highly concentrated in a few countries. For example, from 2014 through 2016 an average of 53% of global mined cobalt production came from the Democratic Republic of Congo (DRC), while 47 % of the cobalt refinement took place in China. Indeed, in these years, 4.5 billion dollars' worth of cobalt have been extracted from the DRC with about 3.5 billion dollars' worth imported in China in the same period. Additionally, more than 80% of the global lithium production comes from Australia, Chile, and Argentina while more than 60% of manganese is mined in South Africa, China, Australia. Due to the high geographic concentration in production, the markets for most of these materials are generally less transparent than those of conventional materials like aluminum and copper. These materials are also used in other industries, but in recent years given the growing demand mostly pushed by electric vehicles, battery production is becoming an increasingly important source of demand. This analysis suggests that the cobalt supply chain is relatively less secure than the

lithium supply chain. Moreover, cobalt experienced strong price volatility between 2014 and 2016. Cobalt is mainly produced as a by-product of copper and nickel and both these materials have a volatile market. Although Australia holds about 47% of the lithium reserves, China controls 47% of the lithium carbonate refinery mostly because it possesses most of the Australian lithium.

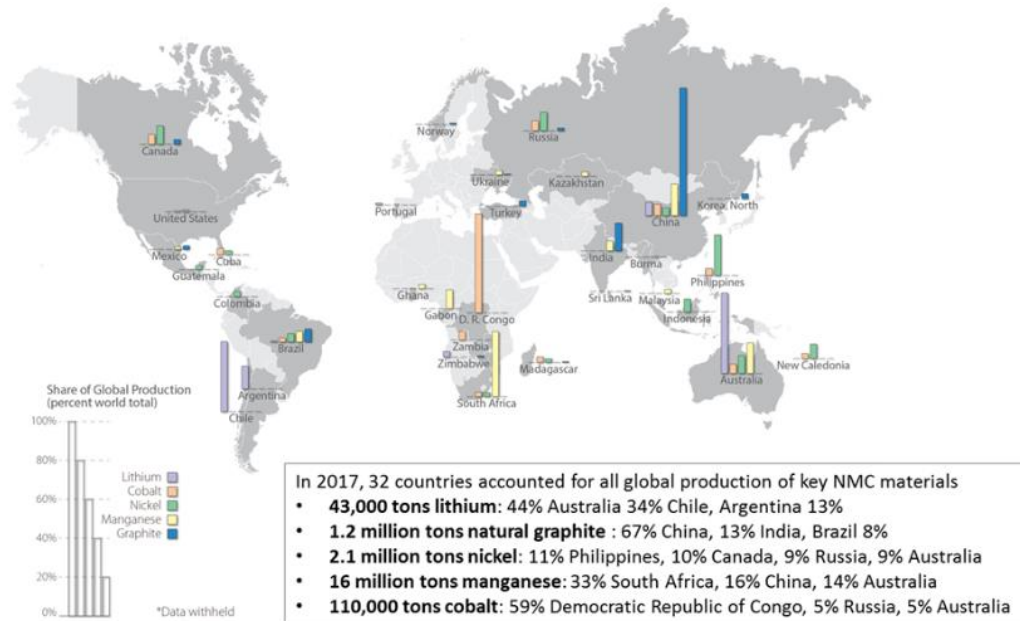


**Figure 1.2:** Critical raw material distribution [9]

The European Union considers extremely critical the exploitation of raw materials that come from the Democratic Republic of Congo and in the report for critical raw materials defines the Country as “one of the world's poorest and most fragile countries. Perhaps unsurprisingly, many of these precious critical raw materials are also associated with pronounced risks of human rights violations, such as child labor and environmental degradation.” To tackle these issues the European Union launched in March 2020 the Critical Raw Materials action plans (CRMs that is focused on four actions i) the development of resilient value chains for EU industrial ecosystems, ii) reduction of dependency upon primary CRMs through circular economy use of resources, sustainable products of raw materials in EU, iii) strengthening the sustainable and responsible domestic sourcing and processing of raw materials in EU, and iv) diversity in supply with sustainable and responsible sourcing.

A further argument that needs to be discussed is the consumption or the utilization of water for energy storage. Indeed, all types of energy generation processes, as well as many industrial

processes, consume water, either for raw material processing or for operation. This link between water consumption and energy production is the so-called water-energy Nexus. The water-energy nexus underlines the inextricable relation between water and energy utilization. Indeed, the production of energy often requires significant quantities of water, and energy is needed for water purification.

### 1.1 The water-energy nexus

The nexus between water and energy is well highlighted in the 2014 US Department of Energy (DOE) report [10]. The report of the DOE highlights the inextricable relation that correlates water consumption and energy production. In addition, the depletion of the hydric sources due to climate change is reported as a matter of national security. These concepts have been further developed into the 2019 water, energy, and food security nexus, stated by the Food and Agriculture Organization (FAO) [11]. Indeed, the international organization underlines that due to the evolution that our society is facing, namely the growth of the population, the migration from rural areas to urban ones, rising incomes, more human beings are willing to spend their incomes on energy-intensive goods. These three sectors (energy, food, and water) are necessary for the sustainable development of human well-being and poverty reduction. The nexus approach aims to highlight potential synergies and to identify critical conflicts to be dealt with, two of them had a central role in this thesis which are

- Water security is defined in the Millennium Development Goals as “the access to safe drinking water and sanitation”, both of which have recently become a human right [12].
- Energy security is defined as “access to clean, reliable, and affordable energy services” in terms of continuity of the service and affordability of the cost [13].

To tackle the challenges addressed by the water-energy nexus, novel electrochemical energy conversion systems like microbial fuel cells (MFCs) will play a critical role in the next future. Indeed, microbial fuel cells exploit microbial colonies to oxidize the organic pollutants that are present in water, while directly producing electric energy. Indeed, MFCs water while producing electric energy and are extremely interesting candidates for water purification [14]. Today, the major limitation of MFCs is their extremely low power output and, therefore, novel strategies are required to improve the power output of these devices [15].

Moreover, to meet the target of the Paris agreement, the energy transition must face a change of paradigm, in which sustainable processes as well non-CRMs such as bioderived

components, that inherently avoid the exploitation of harmful substances, are central to the realization of novel EES capable to provide performances that could sustain the energetic consumption of our lives. In this context, carbon-based electrochemical energy storage arises as a suitable solution both for EES and as the main component of alternative electrochemical energy sources such as MFCs. Indeed, carbon is the sixth most abundant material on Earth and therefore is not a CRMs. Moreover, carbon is the main building block of all organic matter and therefore is ubiquitous. Electrochemical double-layer capacitors (EDLCs) are high-power EES devices that exploit activated carbon as the main component and store electric energy in an electrical double layer at the interface between the electrodes and the current electrolyte [16]. The integration of EDLCs in MFC systems has been demonstrated as a promising approach to boost MFC performance [17].

However, as highlighted in the following sections, which are devoted to the description of EDLC and MFC components, manufacturing, and operation processes, still both MFCs and EDLCs cannot be considered as totally green in terms of materials and manufacturing processes. Specifically, in Sections 1.3 and 1.4, EES, and particularly EDLCs, and MFCs are briefly introduced, and the main features of these systems are discussed. The main formula that has been used in this thesis to evaluate the performances of EDLCs are discussed in detail in Appendix A. Appendix B is devoted to the description of one of the main techniques adopted for the quantitative evaluation of the carbon-specific surface area and pore size distribution, that are key features both for EDLC and MFC electrodes.

## **1.2 Electrochemical energy storage devices (EES)**

Figure 1.3 summarizes the different types of EES available today. In EES devices, electric energy can be stored within two main mechanisms: i) in batteries as potential available chemical energy-requiring simultaneous reduction and oxidation reaction of electrochemically active compound, that spontaneously discharge when connected to an external load, and ii) in capacitors as the potential energy of an electrostatic field to maintain the accumulation of charges at the electrodes. The first mechanism is driven by reversible Faradaic reactions, while the latter exploit non Faradaic processes.

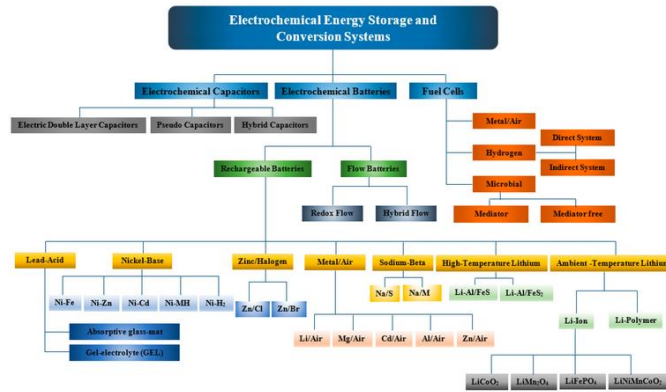
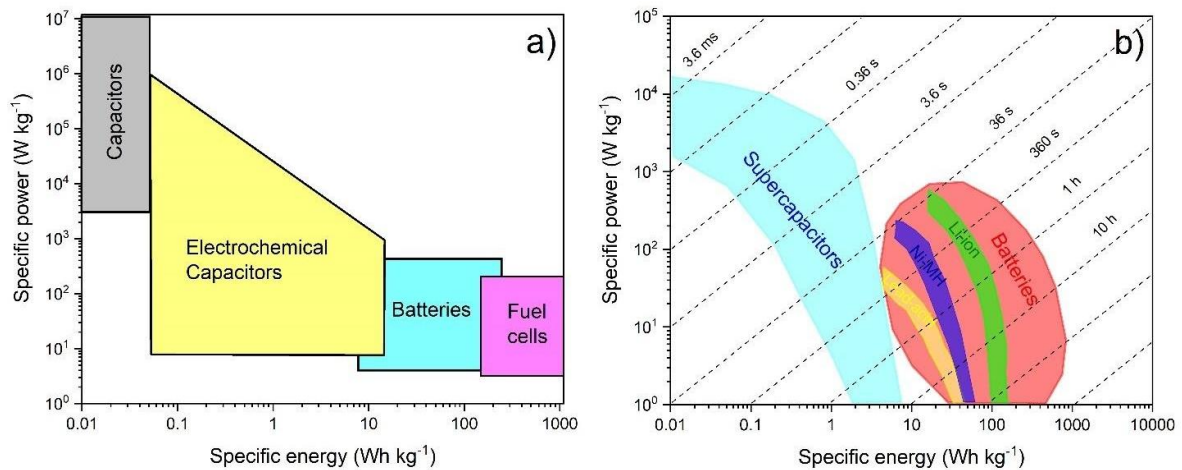


Figure 1. Classification of electrical energy storage and conversion devices.

Figure 1.3.1: Classification of EES systems [18]

Although the overall energy conversion can be conducted in a relatively reversible thermodynamic way, if compared to an internal combustion engine, batteries charge/discharge cycles often involve a certain degree of irreversibility that limits the cycle life of batteries to several thousand discharges and recharge cycles. By contrast, capacitors have almost unlimited cyclability since no chemical and phase changes are involved in charging/discharging. These profound differences, which are related to the physical principle according to which the energy is stored, are highlighted by the position in which energy storage devices are positioned in specific energy and power diagram, referred to as the Ragone plot (Figure 1.4). Indeed, in real-world application constraints like the available volume, the kind of application (high power small time, low power for a longer time) defines which energy storage system better suits the desired application. High specific energy low power devices are exploited when a long discharge time at modest power is required. Typical examples are fuel cells and batteries, in which the real-world application lasts for hours or even days. However, in these systems, the kinetics of the faradaic processes, typically limit power performance. On the contrary, when high power for a short time, and therefore, lower specific energy is required, electrochemical double-layer capacitors or, at higher power levels and smaller times, capacitors are exploited. Therefore, the Ragone plot region in which an electrochemical energy storage device is placed reflects the typical time scale of the processes that drive energy storage.



**Figures 1.3.2:** a) Ragone plot with data digitized from the work of Kotz et al [16], b) Ragone plot from [19]

In Figures 1.3.2 are reported Ragone plots of different families of electrochemical energy storage devices, it is possible to appreciate that electrochemical energy storage systems can be classified into high specific energy, low specific power, high specific power, low specific energy, respectively lower right side and upper left side. According to this classification, fuel cells are high energy density devices with a typical gravimetric specific energy of 800-100  $Wh\ kg^{-1}$  and specific powers of 5-200  $W\ kg^{-1}$ , Batteries are more versatile since they occupy the middle region of the Ragone plot, with a specific energy of 4-250  $Wh\ kg^{-1}$  and specific power of 4-400  $kW\ kg^{-1}$ , Electrochemical capacitors, on the other hand, are low specific energy devices, ranging from 0.01-230  $Wh\ kg^{-1}$  with outstanding specific power ranging from 10- $10^5\ W\ kg^{-1}$ . The family of batteries and electrochemical capacitors contains other subfamilies that usually are classified according to the chemistry of the species involved in the electrochemical energy storage or based on the cell construction (e.g. Electrolytic capacitors vs. Electrical double-layer capacitors). Capacitors can be divided into Electrolytic capacitors and Electrical double-layer capacitors. Electrolytic capacitors feature specific energy in the range of 0.01-0.3  $Wh\ kg^{-1}$ , with impressive specific power, up to  $10^5\ W\ kg^{-1}$  but with modest discharge times ranging from  $10^{-6}$  to  $10^{-3}\ s$  and capacitance from  $1\ \mu F$  to  $50\ mF$ . Electrolytic capacitors are polarized capacitors in which the anode (or the positive plate) is a valve metal (a metal that undergoes spontaneous oxidation, e.g. Al Ta or Zr), this forms an insulating layer that acts as a dielectric. A solid or liquid electrolyte is exploited that serves as the cathode to maximize the available surface area; the energy is stored as charge separation at the interface between the oxide. This mechanism is extremely fast and reversible and requires very high voltage to be

maintained since the dielectric materials are usually insulating ones, therefore the specific energy is extremely low, but the specific power is considerably high since a very high current can stand for a small time. Electrical double-layer supercapacitors (EDLCs) are characterized by greater energy densities, ranging from 5-10 Wh kg<sup>-1</sup>, with smaller specific power from 1-10 kW kg<sup>-1</sup>, and longer discharge times from fraction of seconds to several minutes but impressive specific capacitance from 20 to 50 F g<sup>-1</sup>(of the device), respect to electrolytic capacitors. EDLCs exploit the formation of the double layers at the interface between the electrolyte and a high surface area electrode, usually realized with carbon materials. The charge/discharge mechanism of the electrical double layer doesn't involve chemical reactions and therefore these devices featured extremely high cycle life and high specific power with respect to batteries [16,20,21]. A further family of supercapacitors is the one that exploits fast electrochemical surface reactions, also referred to as pseudocapacitive materials. Pseudocapacitance occurs when the fast electrochemical reaction occurs at the interface of the polarized electrode. The exploitation of this fast Faradaic reaction allows reaching higher specific energy with respect to EDLCs, which can be even higher than 10 Wh kg<sup>-1</sup> at comparable power densities of 1-10 kW kg<sup>-1</sup>. Metal oxides, as well as electroactive polymers, are exploited in these systems and examples are MnO<sub>2</sub>, RuO<sub>2</sub>, and polyaniline or derivatives of the polythiophene. In hybrid supercapacitors, one electrode is the pseudocapacitive one while the other one exploits an electrostatic process to store the electrochemical energy [16,20,21]. This concept can be further pushed by exploiting material adopted also for lithium-ion batteries, as an anode and electrical double layer electrode as a cathode. Anodes that can undergo a rapid intercalation reaction of lithium-ion are exploited such as lithium titanium oxides (LTO), which strongly improves the energy density of these devices. For supercapacitors, the presence of these subfamilies is highlighted by the shape of the Ragone plot in Figure 1.3.2b, where the supercapacitor region has two evident areas: one that bends like in the case of the batteries, at higher specific energy and lowers specific power, and another one that bends with a different slope, at higher specific power and lowers specific energies. These two regions are characterized also by different discharge times. The former has times between 0.36 s and 1 h, and the latter has discharge time in the order of 3.6 ms-3.6 s. This reflects the fact that nowadays supercapacitors also exploit different energy storage mechanisms as previously discussed [22].

Moreover, the evolution of the Ragone plot in these 20 years strongly reflects the evolution of the electrochemical energy storage devices. The expansion of the area of batteries towards

higher specific energies and power values reflects the present capability to widely exploit lithium intercalation/deintercalation reactions in Lithium-ion batteries. In turn, the supercapacitor region is expanding towards high specific energy values by the smart combination and design of capacitive, pseudocapacitive, and battery-like electrodes. h higher specific power. Noteworthy, for both systems, the electrolyte plays a key role, and it has to be designed accordingly to the electrode materials and processes.

In this thesis, the focus has been on EDLCs. The main components of these devices are discussed in the next section while the expected performances, as well as the typical electrochemical response together with the main characterization technique exploited to evaluate the BET surface, are discussed in appendix sections A and B.

### **1.3 Electrochemical double-layer supercapacitors**

Electric double-layer capacitors (EDLCs) are electrochemical energy storage systems that, unlike batteries, do not exploit chemical reactions to store electric energy but electrostatic interactions between the electrolyte and the electrodes. In this thesis work, the focus has been on Electric double-layer capacitors (EDLCs). EDLCs enable high specific power up to 10 kW kg<sup>-1</sup> with more modest specific energy typically lower than 10 Wh kg<sup>-1</sup>. EDLCs are characterized by robust performances due to the absence of a faradaic process, simplicity of design, impressive cycle life, and rapid response times. This unique combination of features enables the use of EDLC in a great number of applications such as stabilization of fluctuating loads both in consumer electronics and at grid level, low-power equipment buffer, voltage stabilizer in photovoltaic and wind system, motor start-up, and special application in electric mobility (kinetic energy recovery system and acceleration boost) [23,24].

Nowadays, it is recognized that capacitive behaviors are associated with two kinds of physical phenomena, the double layer at the electrode interfaces or pseudocapacitive ones. These two phenomena are developed in certain kinds of processes in which the amount of charge (q) that passes is some function of the potential V so that a derivative dq/dV arises that is equivalent to a capacitance. Indeed, capacitance is defined as

$$C = \frac{q}{V} \quad (1.3.1)$$



Where  $q$ , is the charge (Coulomb) and  $V$  is the voltage (Volt) leading to a capacitance  $C$  (Farad). In EDLCs, the large capacitance, and hence the energy storage potential of supercapacitors arises due to the small separation distance  $d$  (c.a. 1 nm), and from the high specific surface area that is exploited in this system (typical values are from 500 to 2000 m<sup>2</sup> g<sup>-1</sup>). The first is related to the thickness of the electrical double layer that is formed at the interface of the electrolyte electrode, during the cell polarization, while the latter is related to the synthetic high specific surface area that is targeted during the synthesis of the main component of the electrodes, typically carbon. The first proposed model was the one of Helmholtz (1879), Figure 1.3.2 [25], the author proposed this model at the first interface of colloidal particles. According to this model, the capacitance  $C$  associated with the formation of the electrical double layer at the interface between the electrode and the electrolyte can be treated as a parallel plate condenser, described by the following equation, in which

$$C = A \frac{\epsilon_r \cdot \epsilon_0}{d_H} \quad (1.3.2)$$

$A$  is the electrode area, with a plate placed at a distance  $d_H$ , that is the average thickness of the double layer structures ( $d_H \sim 1 - 2 \text{ nm}$ , depending on the temperature, concentration, and nature of the electrolyte),  $\epsilon_r$  dielectric of effective dielectric constant  $\epsilon_r$ , that is the local relative permittivity of the double layer, that depends upon the nature of the electrolyte and  $\epsilon_0$  which represents the vacuum permittivity. The potential along  $d_H$  decreases linearly through the bulk of the solution. In this model, the thickness of this layer is not affected by the thermal energy due to the strong electrostatic forces, the positive charges of the ions are balanced by a greater electronic/vacation density at the electrode interface. This latter phenomenon implies the existence of a distribution of charges that decreases through the bulk of the electrode, this distribution follows exactly the mathematical description of a diffused double layer and therefore can be represented as a further capacitor in series with the Helmholtz one. The main limitation of the Helmholtz model is the assumption that the capacitance is constant at the electrode/electrolyte interface and independent from the concentration of the electrolyte or surface potential. The formation and the formal study of the double layer at the electrolyte/electrodes involves several physical quantities both from the solution side and from the electrode side, therefore is a complex phenomenon [20].

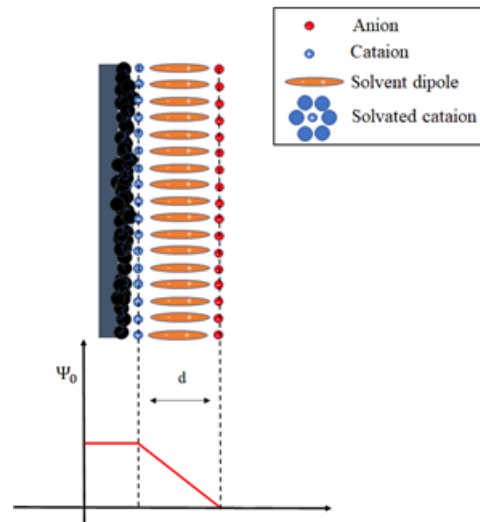


**Figure 1.3.1** Sketch of the *Helmholtz double layer model* [20]

Nevertheless, the model proposed by Helmholtz, equation 1.3.2, is widely adopted in the current scientific literature to give an intuitive representation of the governing phenomena involved in the formation of the electrical double layer in supercapacitors, indeed the relation between  $C$  and  $A$  postulated equation (1.3.2), high specific surface area electrodes will feature greater specific capacitance. Indeed, in EDLCs electrodes, high specific surface area ( $A > 1500 \text{ m}^2 \text{ g}^{-1}$ ), together with extremely small charge separations (Amstrong) lead to high specific capacitance value. Moreover, this equation highlights the dependency of the specific capacitance to the nature of the electrolyte. Indeed, considering two electrodes with the same surface area exploiting different electrolytes, the one that features the solvent with the higher dielectric constant, will show a greater capacitance. This is the case of aqueous electrolytes with respect to organic ones, indeed, the first (e.g.  $\text{K}(\text{OH})$  solutions).

In Figure 1.3.2 is reported a sketch of an EDLC, where the main components are highlighted. The device is composed of two electrodes that are polarized as positive and negative during the charge phase. The polarization is accompanied by the formation of two electrical double layers at the interphases between the electrodes and the electrolyte with opposite polarization, where the energy is stored [17,20,21].

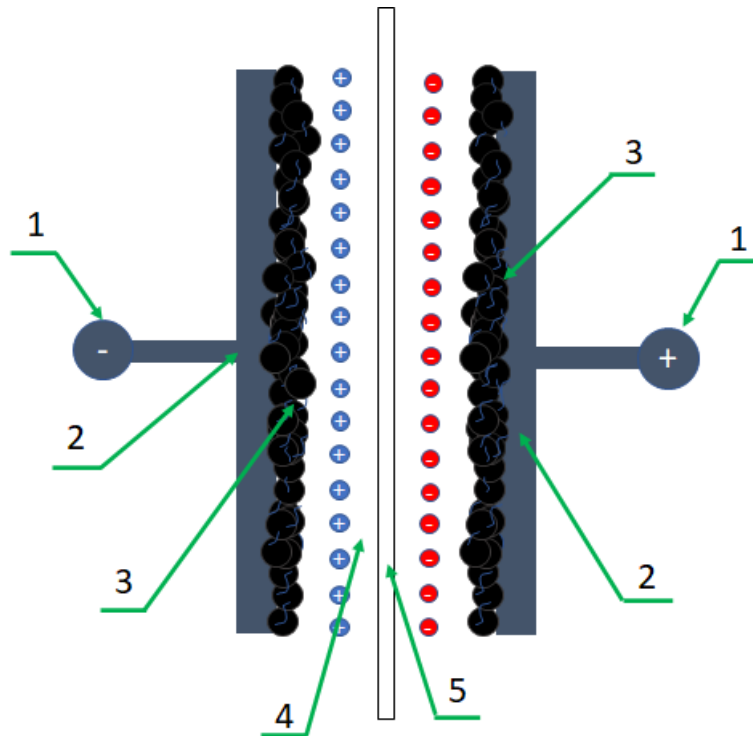


**Figure 1.3.2:** Sketch of an electrical double layer supercapacitor

The main components of an EDLC are

- 1) **Negative and positive terminal:** Physical poles of the device.
- 2) **Current collectors:** In commercial devices are made of aluminum foil. The current collector gives mechanical resistance to the electrode and allows the electric connection between the terminal and the surface of the electrode.
- 3) **Electrodes:** Composite of high surface area powder, polymeric binder to improve the inter-particle contacts as well as the contact of the composite with the current collector, and conductive additive to further improve the electronic percolation between the electrode's particles.
- 4) **Electrolyte:** Solution of ionic salts into an organic or aqueous solvent that contains the ions that are responsible for the formation of the electrical double layer in which the charge is stored
- 5) **Separator:** Usually made of electronic insulating material, its main purpose is to avoid short circuits between the electrode when pressed one against the other.

The electrodes are placed over a metallic current collector from which the electrical contact is taken out from the device. In between, there is the separator that is made of an electronically

insulating material to avoid the short circuits of the two electrodes during the polarization. The first practical exploitation of storing electric energy in the double layer at the interface of high surface area carbonaceous electrodes appears in 1957 with the General Electric patent [26] of a porous carbon electrode exploiting an aqueous electrolyte. The first commercial supercapacitor was commercialized by SOHIO in 1966. The first successful commercial applications were memory backup applications, NEC in 1971 [27]. These early devices had a low voltage and high internal resistance if compared with the modern ones. By 1980 extremely different products were on the market, from the Matsushita (Gold capacitor), Elna (Dynacap), and PRI ultracapacitor, the latter featured relatively expensive metal oxide electrodes, for military applications [16]. Today the trend is of cells from few mF to traction-oriented cells, that feature more than 100kF [23]. The EDLCs market can be therefore divided into large scale and small scale, in Figure 1.6 reports the market forecast for EDLCs up to 2026. Based on this forecast it is evident that the main market driving force in the next years is going to be sustainable mobility. The high cost per *kWh* however requires this technology to improve energy densities to increase its market penetration [24]. The cell production process involves three main steps

- Electrode fabrication
- Cell preparation that is conducted in a dry room
- Formation cycling

Each of these steps is accompanied by a material and production cost, in 2013 it was estimated that the production/materials cost ratio was in the order of 70/30 [28]. The greatest cost for the materials was the electrolyte salt, with the second larger one the NMP required for the manufacturing of the electrodes.

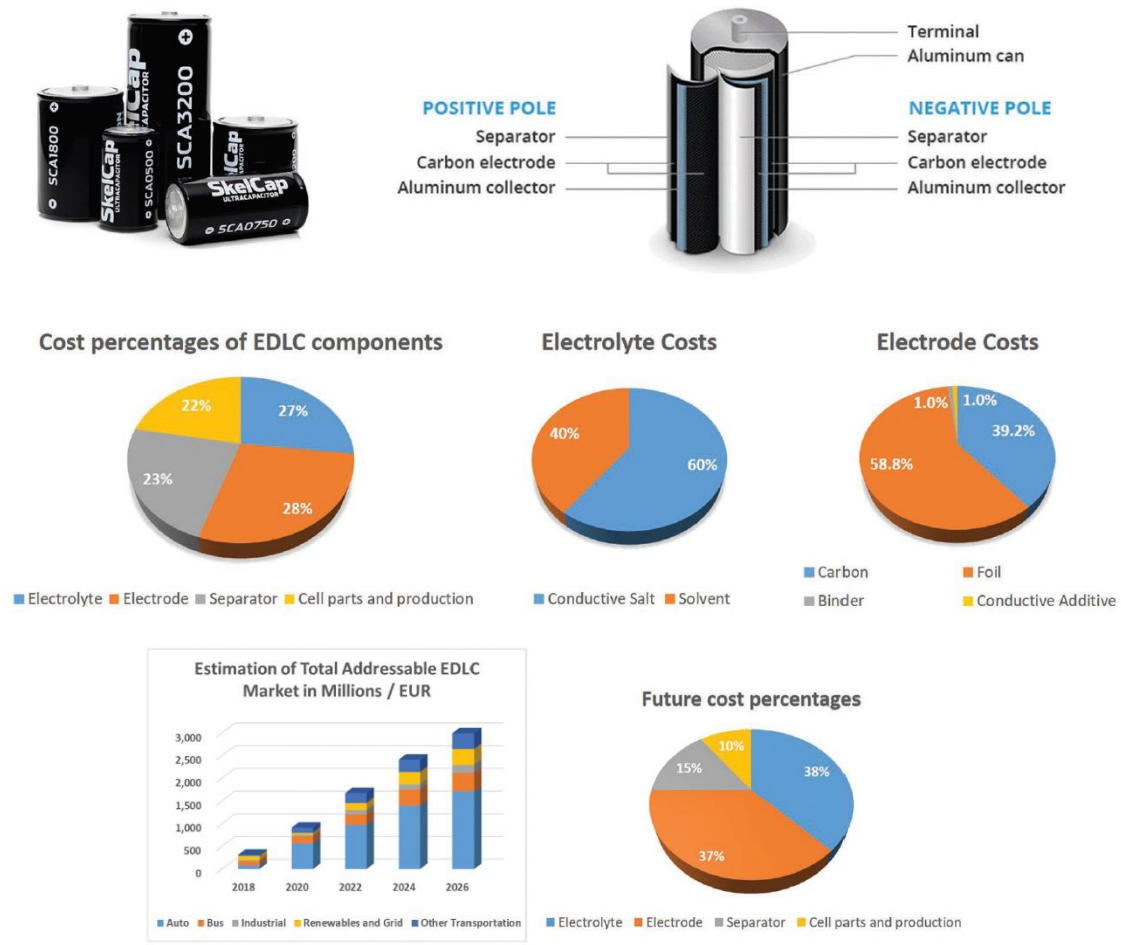


**Figure 1.3.3:** Picture of an actual EDLCs cell with an exploded view and cost distribution of the EDLCs components [24].

A more recent estimation of the component's cost distribution is reported in Figure 1.3.3. The percentage of the material/production is slightly different to those reported by [24], indeed from Figure 1.3.3 it is possible to see that: In 2019, the production/material cost ratio was c.a. 20/80 each cell component almost equally weighed into cell cost. Moreover, the cost of the electrolyte is dominated by the salt, while the electrode by the current collector. The future cost projection is attributed to the wide adoption of thick electrodes that will reduce the current collector fraction in the final device and therefore is important as cost fraction. In applied research, the reduction of production costs is one of the main critical goals.

## EDLCs: Main components

### 1.3.1 Current collectors

Current collectors in electrochemical energy storage devices play a critical role. A current collector must equally distribute the charge/discharge current along the surface of the electrode and therefore it must have an extremely low bulk resistance to electron conduction to minimize the equivalent series resistance (ESR), i.e. the internal resistance, of the device. It must have a good chemical and electrochemical inertia to the electrolyte, to avoid both spontaneous corrosions, which could lead to passivation or loss of electric contact with the electrode, as well as a parasitic reaction during the charge/discharge process, that will reduce the final efficiency of the device. The current collector must be a low mass element since it doesn't participate in the charge/discharge process and therefore all the mass that is not involved in its mechanical stability is considered as pure dead weight. It must be made of a cheap element that exploits scalable and cheap manufacturing processes. Moreover, it must be chemically compatible with the solvent exploited during the electrode's productive process, which, in the case of EDLCs, is often a "roll to roll" coating procedure, capable of meeting fast production time together with high scalability [24].

For these reasons, the most common commercially exploited material is aluminum. Indeed, aluminum current collectors are extremely cheap, light, and allow the possibility to cheaply prepare thin light foil with good mechanical integrity. It must be stressed that in today's commercial EDLCs organic solvents are exploited both for electrodes processing and as main electrolytes components. The major limitation of aluminum is related to the impossibility to exploit it in aqueous electrolytes due to corrosion problems. For what concerns the aqueous processing of electrodes, several strategies to avoid aluminum corrosion have been developed. Indeed, it has been already demonstrated that with some particular attention it is possible to run aqueous electrode processing on aluminum foil both in Li-ion batteries and SCs [29].

In today's scientific literature, other materials than aluminum foil are exploited especially given the use of aqueous electrolytes. Examples are Ni foam, Stainless steel, and carbon-based materials. Among the latter, carbon felt, carbon tissues, carbon paper, and graphite foil have been reported. This is because carbon-based materials offer a unique combination of light, cheapness, and both chemical and electrochemical stability with most of the common electrolytes [30]. It should be highlighted that materials other than aluminum are not suitable for commercial application either because they are too expensive or because they are significantly reducing the energy density of the device, for example, stainless steel [24].

### 1.3.2 High surface area carbon electrode

The most widely exploited material for EDLCs electrodes is carbon, this is due to its unique combination of physical and chemical properties. Indeed, carbonaceous materials feature high conductivity, high surface area range (from c.a  $1 \text{ m}^2\text{g}^{-1}$  to  $2000 \text{ m}^2\text{g}^{-1}$ ), good corrosion resistance, high-temperature stability, controlled pore structure, processability, and compatibility in composite material, and relatively low cost. EDLC's electrodes are composite of high surface area carbonaceous material, that is the main specific component, together with conductive additive, and a polymeric binder. Obtained usually, starting from a suspension with an adequate composition and viscosity that is subsequently used to coat the current collector, the control of the variable that is involved in the electrode's formation process have tremendous consequence over the SC's performance and it is not trivial to distinguish the different contribution to the final performance of both electrodes and device. Carbonaceous material allows, by means of different processes to reach an extremely different value of the specific surface area, conductivity, and pores size distribution, these quantities together with the electrolyte play a critical role in supercapacitors performances. Elemental carbon has four crystalline allotropes, diamond ( $\text{sp}^3$ ), graphite ( $\text{sp}^2$ ), carbyne ( $\text{sp}^1$ ), and fullerene (distorted  $\text{sp}^2$ ). Two of these allotropes are found in nature as mineral, graphite, and diamond, while the other is synthetic. While the term carbon refers to the chemical element, to avoid confusion, carbonaceous materials can be classified as "carbon black", "vitreous carbon", "graphites" or "activated carbon" [16,20,21].

Table 1.1 reports the main kinds of carbons, grouped by the physical phase of the precursor, as well as the most common precursor, the controlling production factor, and the main structural and textural features. These qualifiers univocally identify precise material that features a unique combination of physical properties, most of the carbon that is exploited today has an amorphous structure with disordered microstructures based on graphite.

**Table 1.3.1:** *Common precursors, controlling production factor, and main structural and textural features of different kinds of carbon materials, from [16,21]*

Carbon material (phase during aggregation)	Common precursors	Controlling production factor	Structural/textural feature
<b>Gas phase</b>			
Carbon blacks	Hydrocarbon gas or liquid	Precursor concentration	Colloidal/nanosized
Pyrolytic carbon	Hydrocarbon gas	Deposition on a substrate	Preferred orientation
Vapour-grown carbon fibres	Hydrocarbon gas	Presence of a catalyst	Catalyst particle size/shape
Fullerene	Graphite rod	Condensation of carbon vapour	Nanosize molecule
Nanotubes	Hydrocarbon vapour	Condensation of carbon vapour	Single wall, multi-wall, chiral
<b>Liquid phase</b>			
Cokes	Coals, petroleum pitch	Shear stress	Mesophase formation and growth
Graphite	Petroleum coke	High temperature	Mesophase formation and growth
Carbon fibres (pitch derived)	Coal pitch, petroleum pitch	Spinning	Mesophase formation and growth
<b>Solid phase</b>			
Activated carbons	Biomass, coals, petroleum coke, selected polymers	Carbonization/activation	Nanosize pores
Molecular sieve carbon	Selected biomass, coals, polymers	Selective pore development	Nanosize pore/constrictions
Glass-like carbons	Thermosetting polymers (e.g., polyfurfuryl alcohol)	Slow carbonization	Random crystallites, impervious
Carbon fibres (polymer derived)	Selected polymers (e.g., polyacrylonitrile)	Slow carbonization	Random crystallites, non-porous
Highly oriented graphite	Pyrolytic carbon, poly-imide film	High molecular orientation	Highly oriented crystallites

Mostly, carbonaceous materials are obtained from organic precursors (C, O, N-based chemical compounds) by heat treatment at high temperatures, the carbonization. The combination of physical properties of the obtained material depends upon the carbon precursor, its aggregation states (liquid, solid), and the structural and textural features of the products [21]. During the carbonization process, the carbon precursor goes through a thermal decomposition (pyrolysis), which eliminates the volatile components that include the heteroatoms. Increasing temperatures, condensation reaction starts to occur accompanied by the growth and allineation of a graphitic unit into small graphite-like microcrystals. The carbon precursor and its processing conditions will determine the size of the graphite sheets and the relative orientation of the crystallite, these two properties define the texture of the obtained material and are strongly related to the electrical conductivity [31]. Petroleum, coal, and some polymers pass through a fluid stage (referred to as mesophase) during carbonization, which allows large aromatic molecules to align with each other forming an extensive pre-graphitic structure, that at high temperatures (>2500 °C) is converted into highly ordered graphite [32]. Other carbon precursors retain a solid phase during carbonization and the limited mobility of the crystallite leads to the formation of rigid amorphous structures that consist of randomly oriented graphene layers [33]. These materials cannot be readily converted into graphite by further high-temperature treatment and are referred to as non-graphitizing carbons. Non-graphitizing carbon is obtained from materials such as biomass, non-fusing coals, and many thermosetting polymers. The loss of volatiles and the retention of a rigid and complex molecular structure during the carbonization of many non-graphitizing carbons led to highly porous structures without the need for further activation.



Electrode resistivity plays a critical role in SC (as highlighted by equation A.2.8) therefore the minimization of this quantity is critical to maximizing the power performance of EDLCs. The intrinsic resistivity of carbon material depends upon its chemical and structural morphology, while the electrical resistance of a packed bed of carbon particles depends upon both intra-particle and inter-particle resistance. Graphite crystals show anisotropic resistivity. Indeed, considering a single lattice in the direction of the aromatic ring (a-axis) is  $10^{-5} \Omega \cdot \text{cm}$ , while along the perpendicular plane (c-axis) is c.a.  $10^{-2} \Omega \text{ cm}$ . Similar considerations can be drawn for other  $\text{sp}^2$  allotropes of carbon. In the a-axis, the electrons of the  $\text{sp}^2$  hybridized carbon exploit the delocalized bond as a charge carrier while in the other direction they can't. Since the electrical conductivity of carbon materials is entangled with the carbon structure, the carbonization process temperature plays a critical role; Indeed, increasing the temperature leads to an increased degree of ordered graphitization and electronic conductivity. Nevertheless, it should be underlined that an increased degree of graphitization usually is accompanied by a diminution of the specific surface area. An interesting example of the process that occurs at carbonaceous material under heat treatments at increasing temperatures is given by the work of Chu and Kinoshita reported by Conway in [20]. Here the authors show the effect of the temperature on the modification of surface area and in terms of the oxygen content of the commercial carbon Vulcan XC-72. Figure 1.3.4 reports the trend of the specific surface area versus the temperature of the heat treatment as well as the oxygen content. The heat treatment lasted 2h. There is an interval of temperatures in which there is a maximum of the specific surface area. The increasing temperature at values higher than those of the maximum leads to a continuous decrease of the specific surface area.

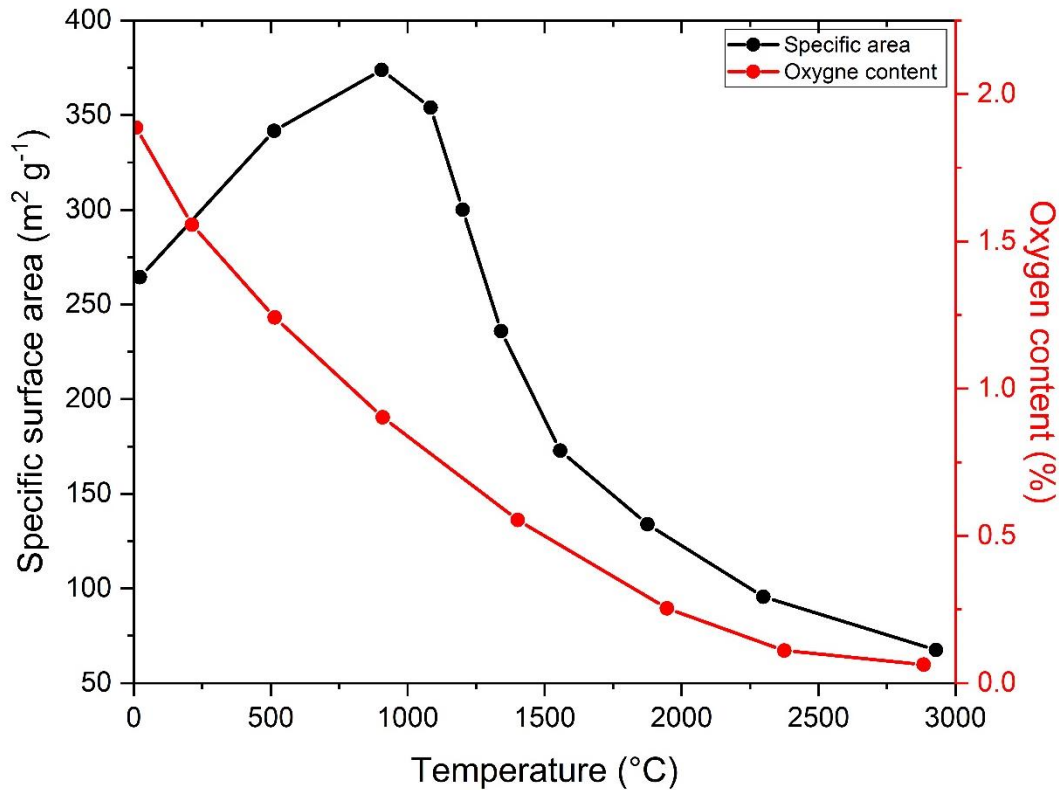


**Figure 1.3.4:** Specific surface area black, oxygen content data digitalized from [20], referring to the work of [35].

The presence of surface oxygen also affects the resistivity of carbon powders, oxygen functionalities, which preferentially form at the edges of the graphite-like microcrystallites, increase the barrier for electron transfer [16,21]. As reported in Figure 1.3.4 the oxygen content during the carbonization process decreases continuously increasing the temperature. This trend has been related to the fact that oxygen present on the surface of the carbon has surface functionalities such as carboxylic acid, phenol, and other organic molecules containing oxygen groups. Increasing the heat treatment temperature leads to the removal of these surface functionalities that are converted to CO<sub>2</sub> or CO. Therefore, a process that increases the surface oxygen content for example by the exposure of carbon to oxygen at elevated temperatures or by prolonged grinding also increases their electrical resistivity [20]. Conversely, carbon heat treatment at 1000°C under an inert atmosphere, decreases the electrical resistivity due to the elimination of oxygen moieties. Oxygen moieties are classified as acidic and basic, respectively. Acidic surface oxides are formed when carbon is exposed to oxygen between 200 and 700 °C or by reaction with oxidizing solutions at room temperature, acidic surface oxides are considered less stable and include functional groups such as carboxylic acids, lactonic and

phenolic functionalities. Basic and neutral surface oxides on the other hand are considered more stable than acidic ones and tend to form after a carbon surface free from all surface compounds encounters oxygen at low temperatures. Functional groups that are electrochemically inert in the potential range of operation of the electrode, could enhance the wettability of the electrode and consequently increase the specific capacitance of the electrode. On the other hand, it has been highlighted that carbon with a high concentration of acidic surface functionalities exhibits high rates of self-discharge. This increase in leakage current suggests that the oxygen functional group may serve as an active site, which can catalyze the electrochemical oxidation or reduction of the carbon or the electrolyte decomposition [35]. Conversely, the removal of oxygen moieties by high-temperature treatment in inert gas has been related to lower leakage currents. The exploitation of surface moieties to improve the charge storage of carbonaceous material has been explored widely but a modest increase in the electrode capacitance, due to the pseudocapacitive faradaic reactions, comes at a price that is the increased leakage current and internal resistance.

The most exploited carbonaceous materials are activated carbon, carbon fibers, carbon felts, and carbon aerogels. As said, these are obtained employing heat treatment under an inert atmosphere (carbonization of the precursor). One of the main advantages of carbonaceous materials is the possibility to engineer them by controlling the process condition, the nature of the precursor that allows the precise modification of the surface in terms of introduction of new functionalities, the opening or changing in the pores structures and increasing in the degree of graphitization. In the next subsection, the main kind of carbonaceous material exploited in EDLCs is briefly discussed, with a particular focus on the ones that exploit bioderived precursors.

### *Carbon aerogel*

Carbon aerogel is a highly porous material prepared by the pyrolysis of organic aerogel. They are usually synthesized by polycondensation of resorcinol and formaldehyde through a sol-gel process that allows strong control over the density, pores size, and shape of the resulting carbonaceous aerogel. Carbon aerogels are more electrically conductive than most activated carbon. Carbon aerogel obtained from the pyrolysis of resorcinol-formaldehyde are preferred as they tend to have a high surface area, (400-1000 m<sup>2</sup> g<sup>-1</sup>), uniform pores size between 2 and 50 nm, and high density. It is possible to also produce monolith, composites, thin-film,

powders, and micro-spheres. Interestingly, in carbon aerogel, the capacitance is more strongly correlated with mesopore surface area rather than with the total BET surface area. Increasing the surface area of carbon aerogels by thermal activation results in a high specific surface area of 650-2500 m<sup>2</sup>g<sup>-1</sup> with a relatively small increase in the electrode capacitance [21].

### *Carbon fiber*

Commercial carbon fibers are produced by thermosetting organic materials such as cellulose or rayon, phenolic resin, polyacrylonitrile. Starting from the polymer, at first, there is the preparation of the fiber by the extrusion, a first thermal treatment referred to as stabilization (200-400°C) and carbonization at (800-1500°C), the raw fibers can be activated in a controlled oxidizing environment at 400-900°C or graphitized (at elevated temperatures). As in other kinds of carbons, the quality of the fibers strongly depends on the precursor and assembly of aromatic constituents and their alignment. Usually, carbon fiber features extremely thin fiber, e.g., 10 μm of diameter and in case of activation, and unlike particular forms of activated carbon, both pore diameter and pore length can be more readily controlled in activated carbon fiber. Carbon fiber is available in many forms, tow (bundles), chopped fiber, math, felt, cloth and thread. ACF cloths with surface area up to 2500 m<sup>2</sup>g<sup>-1</sup> are now commercially available [32]. Compared with electrodes realized with powder, ACF offers the advantage of high surface area, good electrical conductivity, and ease of electrode formation and containment. On the other hand, the cost of ACF is in general higher with respect to the cost of powdered forms of carbon. Moreover, although carbon fiber-based materials are not very resistive, the metal/carbon electrical contact, as well as the carbon/carbon inter-fiber contact, could be a source of increased electrode resistivity. Similarly, to the powdered-based materials, increasing the pressure on a mechanical contact could be a solution as well as metallization of one layer e.g. by plasma spraying [21].

### *Activated carbon (AC)*

High surface area carbonaceous material for EDLCs electrodes must fulfill well-developed specific surface area, high microporosity, chemical and thermal stability, good conductivity, tailorable porosity, low cost, and ease of processability [21]. Nowadays, the lion part is played by the activated carbonaceous electrode. The process employed to increase surface area (and porosity) from a carbonized organic precursor (a “char”) is referred to as activation and the resulting materials are referred to as activated carbons. Chars, usually have relatively low porosity and their structures consist of elementary crystallites with a large number of

interstices, that are usually filled with “disorganized” carbon residues (tar). The activation process opens the pores and can create additional porosity. There are mainly two routes to activate carbonaceous materials, the physical activation, and the chemical activation [16].

Physical or thermal activation consists of carbonization at temperatures between 400 °C and 850 °C and activation of the resulting carbon char by controlled gasification using oxidizing agents such as carbon dioxide, air or steam or a mixture of these gas in a range of temperatures of 700 °C to 1100-1200°C. During the high-temperature phase of the thermal activation, the oxidizing atmosphere generally increases the pore volume and surface area of the material by means of a controlled carbon “burn-off” with the elimination of volatile pyrolysis products. The level of burn-off is extremely important and is controlled by the temperature during the activation; a high degree of activation is achieved by increased burn-off [21].

Chemical activation, on the other hand, is carried out at slightly lower temperatures (400-700 °C). In chemical activation, the precursor material is mixed with activating agents such as K(OH), Na(OH), ZnCl<sub>2</sub>, K<sub>2</sub>CO<sub>3</sub>, KHCO<sub>3</sub>, H<sub>3</sub>PO<sub>4</sub>, and FeCl<sub>3</sub>. According to the activation agents, the carbon precursor, and the process conditions (the maximum temperature, the heating rate comprising of eventual preheating before the pyrolysis, the flow rate of the inert gas, the ratio of activating agent to biomass, but also chemical or physical post-process comprising water or acidic wash), the obtained AC will possess extremely different textural properties, pores size distributions and specific surface area. Exceptionally high specific surface carbons have been obtained exploiting potassium hydroxide (>2500 m<sup>2</sup>g<sup>-1</sup> [36]).

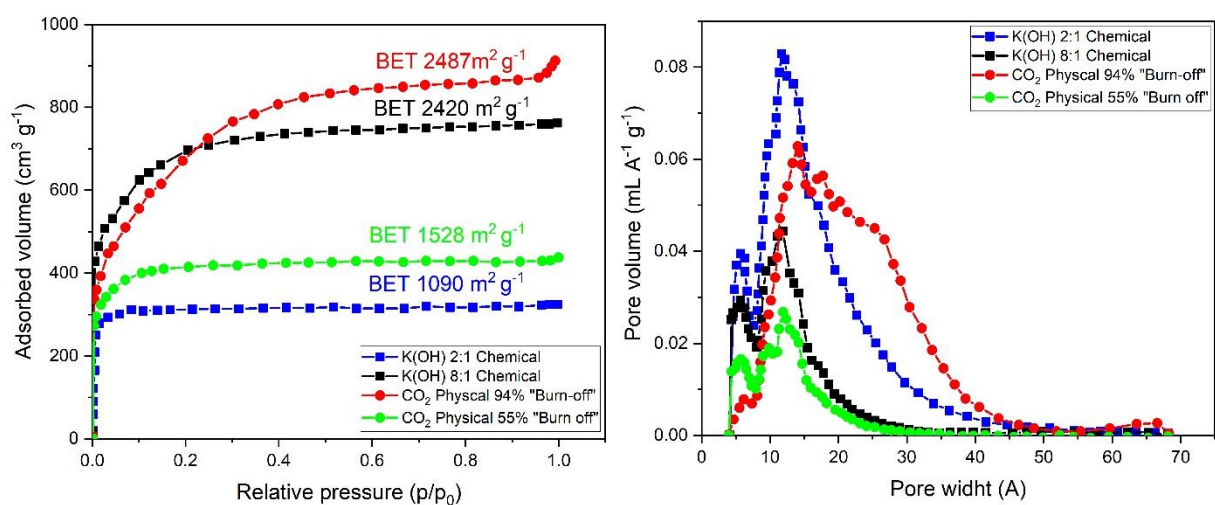
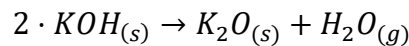
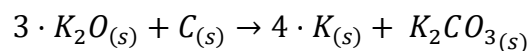


**Figure 1.3.5:** Comparison of the nitrogen adsorption isotherm and pore size distribution of carbon fibers derived from coal tar pitch precursor [32].

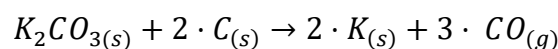
Figure 1.3.5: reports a comparison of the nitrogen adsorption isotherm and pore size distribution of carbon fibers derived from coal tar pitch precursor from [32]. Here the authors report that increasing the burn-off time led to an increase of the BET area with the major drawback of a great consumption of the material and a wider pores size distribution. These two facts lead the authors to the conclusion that for industrial application, the chemical activation process is more interesting, due to the higher yields and more sharp pore size distribution. The mechanism of the activation process is not yet completely elucidated. Models of activation of coke or lignocellulosic material with K(OH) and Na(OH) have been suggested, combining Gibbs free energy of reaction with inline analysis of the gas that is evolved during the pyrolysis. Interestingly, several authors propend through the idea that alkali metals are produced during the high-temperature process following the chemical reaction. At first, between 300-400°C there is the dehydration reaction that is [37].



According to some authors, this reaction is accompanied by an expansion of the carbon/precursor matrix due to the presence of K<sub>2</sub>O, this mechanical action will subsequently lead to a fragmentation of the material [38]. The authors underline that the melting temperature of KOH is around 360-380°C attributing this phenomenon to the tendency of KOH to produce fragmented carbon, with respect to more mild activating agents e.g. K<sub>2</sub>CO<sub>3</sub> that melts at 890°C [39]. It is likely that e melting increases the activity of the dehydration reaction. Increasing the temperature at 500-600°C there is the carbonization reaction of the precursor, in case of organic material and at temperatures greater than 700°C there is the reduction reaction of K<sub>2</sub>O

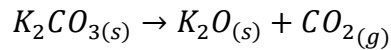


This reaction mechanism has been proposed by [40] by analyzing the is confirmed by the observation of metallic potassium in the furnace after pyrolysis with K(OH) as activating agent. Through TGA studies it has been shown that potassium bicarbonate can react with C at a temperature higher than 700°C leading to a further activation step that brings about the formation of metallic potassium

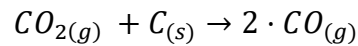


Detection of white stain, attributed to metallic potassium in the cold part of the reactor, as well as the lower porosity, developed when K<sub>2</sub>CO<sub>3</sub> is exploited instead of KOH, together with TGA

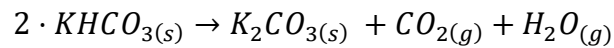
studies, are the main evidence of this reaction path. Finally, at 850°C, there is the decomposition of the potassium carbonate that slowly start to take place as



At these temperatures CO<sub>2</sub> can act as a physical activating agent since it exercises an oxidative action over the C matrix according to the burn-off reaction, that is



Although K(OH) is the most exploited activation agent, its corrosivity poses serious concern and other mild activation agents such as KHCO<sub>3</sub> and K<sub>2</sub>CO<sub>3</sub>. The exploitation of KHCO<sub>3</sub> as an activating agent allows a further activation step which is the decomposition reaction of KHCO<sub>3</sub> that according to TGA studies becomes relevant at 150°C.



Indeed, some authors report that this reaction is also responsible for carbon fragmentation. It should be highlighted that since this reaction leads to the formation of K<sub>2</sub>CO<sub>3</sub>, and becomes important at 150°C, the only difference in the exploitation of K<sub>2</sub>CO<sub>3</sub> with respect to KHCO<sub>3</sub> is this decomposition reaction that occurs at relatively low temperatures. However, the exploitation of both KHCO<sub>3</sub> and K<sub>2</sub>CO<sub>3</sub> offers a more mild and less corrosive activation agent with respect to KOH. Moreover, sodium bicarbonate has been explored as an activating agent with biochar leading to poor textural properties (e.g. BET surface area of 550 m<sup>2</sup>g<sup>-1</sup>), which are in agreement with the general concept that sodium salts are less effective as activating agents than potassium salt [40,41]. In the work of [39], the authors report SEM images of glucose-derived hydro-char (carbonization reaction takes place under high-pressure steam) treated with K(OH), KHCO<sub>3</sub> and K<sub>2</sub>CO<sub>3</sub> reported in Figure 1.3.6. In ref [39], the authors report SEM images of glucose-derived hydro-char (carbonization reaction takes place under high-pressure steam) treated with K(OH), KHCO<sub>3</sub> and K<sub>2</sub>CO<sub>3</sub> reported in Figure 1.3.6. From these SEM images, it is evident that K(OH) destroys the material whereas the spherical morphology of the is well preserved both for KHCO<sub>3</sub> and K<sub>2</sub>CO<sub>3</sub> [39].

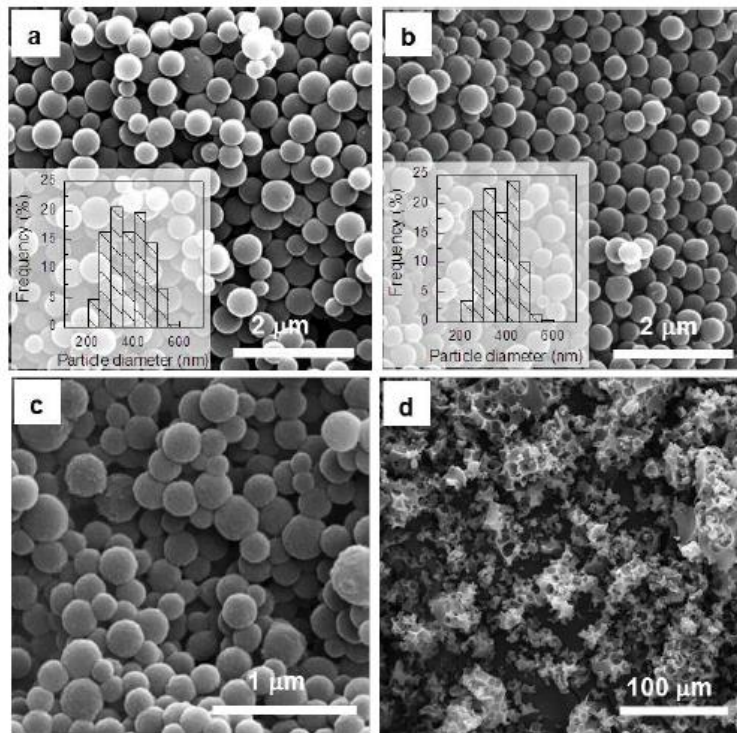


**Figure 1.3.6:** SEM images of glucose-derived hydro-char (carbonization reaction takes place under high-pressure steam) treated with  $K(OH)$ ,  $KHCO_3$ , and  $K_2CO_3$ , from the work of [39]

From these SEM images, it is evident that  $K(OH)$  destroys the material whereas the spherical morphology of the is well preserved both for  $KHCO_3$  and  $K_2CO_3$  [39]. In Figure 1.3.7, nitrogen adsorption isotherms of carbon activated by exploiting  $K(OH)$ ,  $KHCO_3$ , and  $K_2CO_3$  as activating agents, highlight that, the amount of  $N_2$  adsorbed depends substantially on the activating agent. In this case, porosity development follows the trend  $KOH > KHCO_3 \sim K_2CO_3$ . The fact that the nitrogen adsorption isotherm of the carbons activated by  $KHCO_3$  and  $K_2CO_3$  are extremely similar highlights the fact that a similar activation mechanism takes place during the activation reaction. Moreover, the authors comment that this could be attributed to the fact the  $CO_2$  generated during the decomposition of  $KHCO_3$  doesn't have a significant effect. Indeed, since the reaction is quantitative at low temperatures, it is reasonable to assume that the "burn-off" carried out by  $CO_2$ , which usually in physical activation is exploited at temperatures between 400-600°C, doesn't play a significant role.



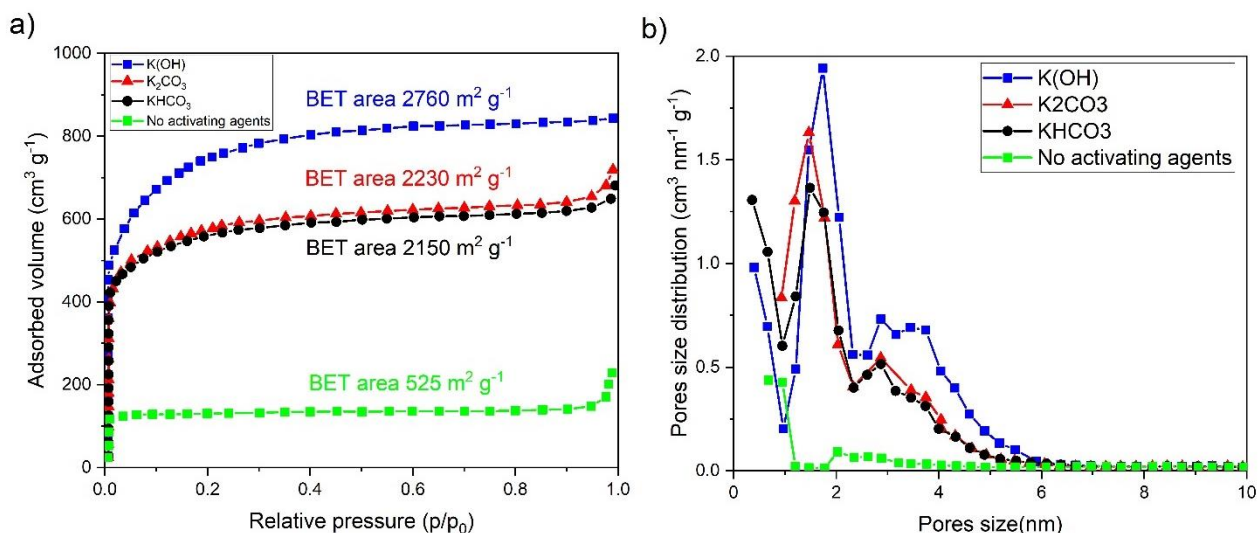


**Figure 1.3.7:** Nitrogen adsorption isotherms of four different carbonaceous materials obtained by carbonization of glucose, with blue  $K(OH)$ , red  $K_2CO_3$ , black  $KHCO_3$  as activating agents, and green without activating agents, from ref [39].

From Figure 1.3.7 it is evident that the exploitation of activating agents leads to a greater BET area: the BET specific area of the carbon obtained without an activating agent is c.a. one-fourth of the others. Moreover,  $K(OH)$  leads to the largest surface area ( $2760 \text{ m}^2 \text{ g}^{-1}$ ) with respect to  $K_2CO_3$  ( $2230 \text{ m}^2 \text{ g}^{-1}$ ), and  $KHCO_3$  ( $2150 \text{ m}^2 \text{ g}^{-1}$ ). The fact that the latter two nitrogen adsorption isotherms are comparable may indicate that similar activation mechanisms are present, for these two activating agents and that the decomposition at low temperature that  $KHCO_3$  experience doesn't play a significant role in developing the AC area. Further confirmation of this fact could be the pores size distribution of carbons activated with  $KHCO_3$  and  $K_2CO_3$  that share extremely similar distributions. Chemically activated carbonaceous materials require to be washed by the residual of the activating agents adsorbed on their surface. Although this post-treatment could seem a simple matter, this step is critical and strongly affects carbon porosity. This post-treatment is called "deashing". Since activated carbon features a high specific surface area, they tend to strongly adsorb chemical compounds on their surface. The micropores, due to their high surface area and less accessible surface, require several water-rinsing to be free from the residual of the activation agent. Acid solutions such as  $HCl$ ,  $HF$ , and  $H_3PO_4$  are exploited to facilitate the dissolution of the residual of the activating agent, as well as mild temperature. The exploitation of oxidizing agents such as  $H_2SO_4$ ,  $HNO_3$ , and high temperature should be avoided because it has been reported that these conditions could lead to pore's wall thinning that lead to micropores collapses into bigger pores with a reduction of the BET surface area and consequently of the capacitance [42].

Commercial activated carbons are produced from fossil fuels (petroleum and coal) which made them not environmentally friendly hence, in recent years a lot of efforts have been focused on biomass precursors, which are cheaper, readily available, structurally porous, and environmentally friendly. The renewable organic materials derived from plants and animals' wastes can serve as a source of carbon for developing activated carbons for EDLCs. Woody biomasses contain in varying proportions hemicellulose, cellulose, and lignin that are referred to as lignocellulose materials, and a small amount of simple sugar and protein and starches and lipids. The constituents of lignocellulose are strongly intermeshed and are chemically bonded by either non-covalent forces or covalent linkage [39], and their composition varies from one plant species to another. As an example, in recent years different biomass precursors have been studied as a precursor of high surface area carbon e.g. coffee beans, lignin coconut shell, cassava peel waste, sunflower seed shell, oil palm empty fruit bunch, camelia oleifera shell, palm kernel shell, olive stone and waste [43]. It should be highlighted that for practical purposes, a biomass source for this application must be abundant and cheap. Indeed, the exploitation of *exotic* biomass may allow high specific surface area as well as high capacitance due to a combination of chemical composition/matrices effect. The impossibility to scale up the process due to the availability of the biomass is a serious constraint that must be always considered when applied research is conducted. In summary, to conclude this section, the exploitation of chemical activation of bio-derived carbons featuring proper textural properties suitable for EDLCs represents a low-cost approach to valorize wastes, mild activating agents such as  $\text{KHCO}_3$  and  $\text{K}_2\text{CO}_3$  allow to reach high surface area and are fewer corrosives with respect to  $\text{KOH}$ , therefore they are of interest in view of the upscaling of the activation process.

### 1.3.3 Conductive carbon additive

The mechanical stability of supercapacitor electrodes is achieved by mechanical binding of carbon particles between each other and with the current collector exploiting a polymeric binder. This in turn reduces both the electronic conductivity across the electrodes and the specific surface area and therefore, to overcome these issues, conductive carbon additives are exploited. Graphite nanoparticles, carbon nanotubes, carbon onions, and carbon black have been investigated. Among these materials, carbon black is one of the most widely exploited conductive carbon additives due to its combination of relatively high specific surface area, low particle size, and high electronic conductivity [44].

### *Carbon black*

Carbon blacks are a group of materials that are characterized by having near-spherical carbon particles, which are produced by the partial combustion or thermal decomposition of hydrocarbon (usually gas, oil, or distillates) in the gas phase. During the production, the spherical carbon particles coalesce into chemically fused aggregates with various morphologies. Their fundamental properties vary with manufacturing conditions and precursors. This carbon is categorized by the method of preparation or intended application. The key properties of carbon blacks are the particle size, structures of the particles, porosity, and surface chemistry. Carbon blacks are used mainly as conductive additives in batteries and supercapacitors electrodes. Highly conductive carbon blacks are characterized by aggregates with high branched open structure, high porosity, small particle size, and oxygen-free surface. The conductivity of carbon black is typically in the range of  $10^{-1}$ - $10^2 \Omega \text{ cm}^{-1}$  and it is influenced by the ability of electrons to jump the gap between aggregates or pass across a graphitic junction of toughing aggregates. The loading of carbon black is of critical importance, because, at low loading, the average inter aggregate gap is too large to permit conduction. As the loading increases, the mean interparticle distance decreases until the percolation threshold is reached whereby the conduction increases up to a limiting value. High porosity or carbon blacks featuring a small particle size have more particles per unit and therefore smaller average distance between aggregates. The BET surface area of carbon black covers a wide range, from  $< 10$  to greater than  $1500 \text{ m}^2\text{g}^{-1}$ . For what concerns the porosity, the surface area of carbon black is more accessible to other kinds of AC, and in some works, specific capacitances of  $250 \text{ F g}^{-1}$  are reported [45,46]. On the other hand, given the fact that this carbon is made of extremely small spherical size, to realize mechanically stable electrodes, a high level of binder is required resulting in electrodes with low capacitance. The fine, highly branched structures of carbon black make them ideally suited to filling interparticle voids created by coarse particles and for this reason, are exploited as conductive carbon additives in electrodes. Moreover, the ability of carbon black to fill the interparticle void can reduce the amount of electrolyte between the particles giving the electrode further capacitance [21,47].

#### 1.3.4 Binder

Supercapacitor performances are influenced by binder types and content in electrodes. Electrodes are usually formed by brushing, casting, or printing electrode paste or slurry on metallic current collectors. Electrode slurries are usually prepared by mechanical stirring or

ultrasonically mixing high surface area carbonaceous materials particles with conductive agents and a polymeric binder. The role of the binder is to provide enough mechanical strength during electrode deformation, since the binder action is carried out by mechanical adhesion between the surface of the connected particles of the high surface area carbon, the amount of binder cannot exceed a certain threshold. Indeed, an excessive amount of polymeric binder results in micropores clogging and therefore reduction of the capacitance, moreover, the polymeric binder, unless electrochemically active polymers are exploited, doesn't participate in the electrical energy storage. Low binder content, lead to the poor mechanical strength of the electrode as well as a poor connection between the current collector and the electrode, increasing the equivalent series resistance. Indeed, mechanical strength capability to flex the electrode has been related to binder content, type, and electrode processing. Indeed, to evaluate this capability binding, that aim to measure the ability of the formed electrode to be rolled are employed [48]. The electrochemical inertia of the binder plays a critical role, the binder must allow drying at high temperature without degrading and being electrochemically inert to not jeopardize the operation of the EDLC.

So far, due to the electrochemical/chemical inertia and good mechanical performances, fluorinated thermoplastics binders, such as polytetrafluoroethylene (PTFE) and polyvinylidene difluoride (PVdF), are the most widely exploited and represent the state-of-the-art binders in EDLCs. Moreover, while PTFE is usually used as aqueous suspensions, PVdF requires the use of cost-expensive (and in some case toxic) organic solvents like N-methyl pyrrolidone (NMP). Indeed, the exploitation of aqueous processable binders represents a critical turning point in the reduction of the environmental footprint of the production process and cost [29,49]. Indeed, in 1998, Sodium-carboxymethyl cellulose (CMC), an aqueous processable biopolymer, has been proposed as a binder for EDLC electrodes [50]. CMC is environmentally more friendly (fluorine-free) and most of all cheaper than the state-of-the-art fluorinated binders. Indeed, nowadays (CMC) is the state-of-the-art aqueous binder for carbon-based supercapacitors. The main drawback of CMC is the inability to realize high mass loading AC electrodes, and high binder content (maximum AC as weight percentage in the electrode 80%) necessary to maintain the mechanical stability. In their systematic study to realize green supercapacitors Dyatkin et al. highlight that naturally derived biopolymer didn't enable sufficient mechanical stability due to poor elasticity, high molecular mass, and a number of bonds capable of binding the AC particles [30].

Other than CMC, mixtures of natural carbohydrates from potato starch and guar gum enable flexible yet high-mass-loading electrodes. Their electrochemical stability and performance are equivalent to CMC [51]. A valuable green solution is constituted by the exploitation of polyisoprene and polyvinyl acetate and crosslinked PVA-based glue. Indeed, this polymer provides comparable malleability to PTFE, resulting in flexible, but free-standing electrodes. Comparison of the polymeric morphology by SEM images highlighted that while the PTFE-based electrodes form a fibrous network, the PVA ones show a lamellar deposit on the carbon surface, and most of all, in terms of electrode capacitance, none of the greener binders could outperform PTFE. One of the main limitations of CMC is the high solubility of this biopolymer in the aqueous electrolyte that therefore inhibits the exploitation of CMC based electrodes in this solution, which are promising in terms of reducing the environmental footprint of the organic ones and enabling the exploitation of fast faradaic reaction to improve the energy density of EDLCs [29,48]. Recently, it has been shown that starch from nonedible potatoes can be used as the main component for binder. Natural starch like sodium alginate is a linear polymer composed of a mixture of amylose and amylopectin, it is cheap and abundant, and it has been shown to be suitable for the production of EDLCs electrodes [52]. The exploitation of protein-based binders, which have been widely used in painting since ancient times, e.g. collagen and white egg have been exploited as the main component of aqueous processable bioderived binder, in particular, casein has been shown to have excellent mechanical stability without jeopardizing the performances of acetonitrile ET4BF4 based EDLCs [52].

### 1.3.5 Electrolyte

The electrolyte is composed of a solvent and salt in the solution. According to the solvent, it is possible to classify the electrolyte into organic and aqueous. The organic electrolyte family can be further divided into two main subfamilies: organic solutions and ionic liquids. In turn, the aqueous electrolyte can be classified as acidic, neutral, and alkaline. A third emerging group is represented by water-in-salt electrolytes that will be discussed in this section [53].

Electrolytes strongly affect cell performances in terms of equivalent series resistance and capacitance [54]. Nowadays, organic electrolytes are widely exploited in commercial EDLCs. The advantage of the exploitation of organic electrolytes is mainly related to the higher maximum energy achievable with these electrolytes. Indeed, according to the definition of maximum specific energy in equation A.2.7, the maximum energy goes with the square of the cell voltage. Typically, organic electrolytes feature cell voltage above 2 V (2.6 to 2.9 V). Liquid

cyclic alkylene carbonates are polar aprotic solvents of great technological importance. Among these solvents, propylene carbonates exhibit physical properties which are extremely suitable for electrochemical energy storage purposes. Indeed, PC shows a liquid phase with a large temperature range, with a melting temperature of about  $-49^{\circ}\text{C}$  and a high boiling point of about  $242^{\circ}\text{C}$ , at ambient pressure, a good capability to dissolve both organic and inorganic compounds together with a moderate biotoxicity and biodegradability. The electrochemical attractiveness of PC results from its high static permittivity and high dipole moment and the fact that these solvents are extremely cheap in large quantities.

Aqueous electrolytes, with respect to organic, have two significant advantages: higher ionic conductivity and the fact that these electrolytes allow a simpler EDLC manufacturing process both at laboratory and at industrial scale. Indeed, the preparation of aqueous electrolytes can be performed in the atmosphere without the need for an anhydrous condition. However, they feature the major drawbacks of both corrosion problems and lower cell voltage if compared with organic electrolytes. Hence, supercapacitors exploiting aqueous electrolytes possess both high conductivity and capacitance, but low energy density with respect to organic ones and leakage problems [47].

Ionic liquids (ILs) represent a relatively new class of electrolytes. ILs are organic salts (molten salts) that have a lower melting point ( $<100^{\circ}\text{C}$ ). Moreover, they are composed of organic cations, such as pyridinium (PY) imidazolium (Im), and inorganic anion ( $\text{PF}_6^-$ ,  $\text{BF}_4^-$ , TFSI $^-$ ) [55]. Room temperature ionic liquids (RTILs) have been acknowledged with noteworthy attention due to their excellent miscellaneous properties, such as thermal and chemical stability, tunable structure over the wide range of operating temperature, a broad electrochemical stability window, high ionic conductivity in the range of  $10^{-3}$ – $10^{-2}$   $\text{S cm}^{-1}$  at room temperature, and non-flammability as a potential candidate for electric double-layer SCs [56,57].

### 1.3.6 Separator

The separator cost represents c.a. 23% of the cost of the complete cell [24], it avoids the short circuit between the positive and the negative electrodes, allowing them to store the charge. Therefore, the separator must be electronically insulating and capable to minimizing as much as possible to resistance to be crossed by ions. It must feature a mechanical resistance capable of overcoming the volume variation of the cell during cell operation. The separators include materials such as glass paper, ceramic, and polymers such as polypropylene, polypropylene-carbonate, polyvinylidene difluoride, polyethylene, and polyamide. An important quantity to

quantify the performances of a separator is the porosity percentage, defined by following equation

$$P = \frac{(W - W_0)}{\rho_e \cdot V} \cdot 100$$

Where  $P$  is the porosity,  $W$  is the weight of the separator after immersing in the electrolyte,  $W_0$  is the weight of the separator before immersing in the electrolyte and,  $\rho_e$  is the density of the electrolyte, and  $V$  is the volume of the separator. The separator must feature sufficient porosity to provide an optimal amount of the electrolyte to the supercapacitor. Indeed, an excessive amount of electrolyte will act as a dead weight, taking down the specific cell performances, at the same time, poorly wetted electrodes, will feature poor rate-capability response and high equivalent series resistance [58,59].

## 1.4 Microbial fuel cell (MFC)

Fuel cells are primary electrochemical cells that convert chemical energy to electricity through the oxidation process at the anode and reduction process at the cathode. Microbial fuel cells (MFCs) are promising devices that use microorganisms as biocatalysts to convert the chemical energy stored in organic matter to electricity [60]. The first scientific evidence of the “*disgregation of organic compound accompanied by the liberation of electric energy*”, was reported by Potter in 1911. Here the author, exploiting a platinum electrode, was able to measure cell voltage from 300 to 500 mV under different conditions of temperature, the concentration of the nutrient, and the number of active organisms present. These observations brought to the conclusion that “*the measured effects were only found within the limits of temperature suitable to micro-organism and under conditions which are favorable to protoplasmic activity*”. The original work of Potter in 1991 has been a milestone in the exploitation of biological systems for electrochemical energy conversion. Indeed, with his work, it has been shown for the first time that simple living organisms can produce electricity because of their metabolic activity [61].

Since the first decade of the past century, several advancements have been made in the field of MCs. Indeed, today MFCs represent one of the most sustainable approaches for generating bioelectricity from biomass. In an MFC, microorganisms degrade organic matter, producing electrons that travel through a series of respiratory enzymes to form valuable biomolecules such as ATP and NADH. The electrons are then released to a terminal electron acceptor (TEA)

which, accepting electrons, becomes reduced. Examples of TEA are oxygen, nitrates, sulfate, and other molecules that accept electrons to form products that diffuse out of the cell. However, it is known that some bacteria can transfer electrons exogenously, that is to a TEA outside from the cell, these bacteria are called *exoelectrongens* Figure 1.4.1 is the kind of MFC that has been exploited in this Thesis, i.e a single chamber, air-breathing MFC. In single-chamber MFC no separation membrane is adopted. The TEA that has been exploited is molecular oxygen through an air-breathing cathode based on activated carbon as the main component [63].

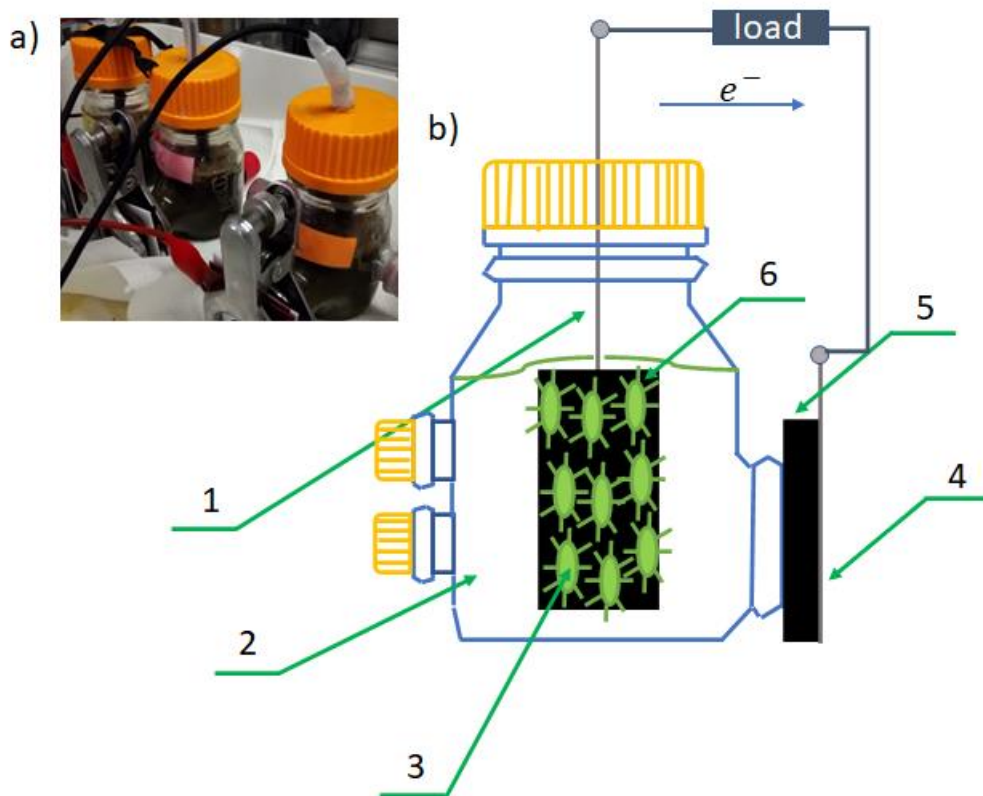


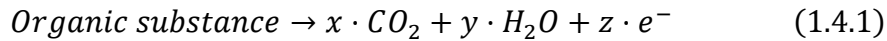
**Figure 1.4.1:** a) Picture of the single chamber microbial fuel cell used in this Thesis work, b) sketch with the main components of the microbial fuel cell exploited in this work.

In Figure are reported the main components of the single chamber microbial fuel cell that has been used in this Thesis

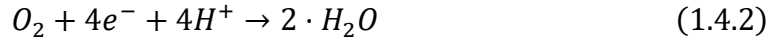
- 1) Anode contact in Titanium wire
- 2) Electrolyte composed of activated sludge and Phosphate buffer saline solution
- 3) Anaerobic colony
- 4) Titanium grid for the cathode contact
- 5) Air-breathing cathode
- 6) Carbon brush

In the anode chamber, the oxidation of the organic substances that are present in the electrolyte and that constitutes the fuel of the cell, equation 1.4.1 reports as an example the complete oxidation reaction of the organic substance.





At the cathode side, there is the reduction of the oxygen to water, reported as an example in acidic condition, equation 1.4.2, and discussed in deepest detail in the following paragraph.



The MFC open circuit cell voltage ( $\Delta V_{OCV}$ ) corresponds to the difference between the anode and the cathode potentials (equation 1.4.3).

$$\Delta V = V_{cat} - V_{anode} \quad (1.4.3)$$

The practical voltage of an MFC is far more complicated to be predicted than that of inorganic fuel cells. Indeed, MFCs are a real and complex environment, and it results difficult to point out a precise anodic redox couple. The same issue occurs with the cathode since it has been demonstrated that biofilms are capable also to act as an electron acceptor with a non-trivial reaction mechanism [62].

#### 1.4.1 Anode

For sake of clarity, it should be highlighted that the anode of an MFC is composed of mainly two parts: the current collector and the biofilm that grows on the current collector. Given the complex environment, the current collector material must have several features like high conductivity, biocompatibility, chemical stability, resistance to corrosion, mechanical strength, and reduced cost. Carbon materials are therefore predominantly applied as main current collector anodic materials, including graphite rod, carbon brush, reticulated vitreous carbon, carbon cloth, and carbon felt. On the other hand, the biofilm that grows on the current collector is composed of a complex ecosystem of microorganisms capable of carrying out extracellular electron transfer. The direct electron transfer from the biofilm to the electrode is fundamental but today it is still an open issue since it involves an extremely complex environment with a plethora of chemical compounds and biomolecules [63].

#### 1.4.2 Current collector

Carbon papers current collectors have the main advantage to be very thin, easy to connect, compact, and with a light structure that positively impacts the system's volumetric energy density. The major drawback of carbon papers is the relatively smooth surface, low specific area high cost, and brittleness. Logan et al reported in 2006 a power density of 600 mW m<sup>-2</sup> (0.98 W m<sup>3</sup>) on a cell volume of 320 mL with a cathode of wet proof carbon cloth with Pt-based catalyst [64]. Carbon cloth-based current collectors, on the other hand, are more flexible and thinner with respect to carbon paper, with higher porosity but also higher cost e. Logan et.

al. in [65] reported a power density of  $1070 \text{ mW cm}^{-2}$ , with a cell volume of 26 mL, and a cathode of wet proof carbon cloth decorated with Pt-based catalyst. An alternative to the two previously reported current collectors is graphite plates. These offer compact structures with a relatively smooth surface, a low specific area with the major drawback of high cost. Dewan et al. in [66] reported a maximum specific power, normalized by the area of anodic graphite plate of  $3290 \text{ mW cm}^{-2}$ . Further electrode carbonaceous materials are reticulated vitreous carbon (RVC), available with different pores sizes, highly conductive but rigid and brittle, and carbon brush. Carbon brush is the ideal electrode material, with high surface area and high porosity. Logan et al in [60] report that using a carbon brush anodes, power density in the order of  $2400 \text{ mW m}^{-2}$  is achievable. Hence, carbon brushes have been used in this Thesis work as the anode current collector material.

#### 1.4.5 Biofilm

A microbial biofilm is a complex three-dimensional structure in which microorganisms grow embedded in a polymeric matrix of extracellular substances. Several studies have highlighted the ability of biofilms to achieve direct electron transfer to the electrode [66-69]. Indeed, in MFCs, the series of oxidative metabolic reactions of the microorganism that are present in the biofilm has been related to the electricity production of MFCs, *referred to as exoelectrogenous activity*. The *exoelectrogenous* activity is carried out mainly by three reported mechanisms, i) bacterial nanowire, ii) redox mediators in the electrolyte, and iii) through shared metabolic intermediates. *Shewanella*, is a genus of Gram-negative facultatively anaerobic bacteria colonies. Its colonies grow *filus* type nanowires connecting the cells. Gorby et al. reported in 2006 demonstrated by conductive scanning tunnelling microscopy (STM) that these nanoscopic filaments are electronic conductors and the possible role of this nanowire in interspecies electron transport between fermentative bacteria to methanogen to regenerate intracellular NADH [67,68]. That is if the metabolism of the fermentative bacteria is inhibited by feedback on the coproduct that brings to the NADH e.g  $H_2$ , the fermentative bacteria could transfer electrons to the methanogen one, avoiding the feedback on the  $H_2$  while producing NADH. This cooperative behavior is known as the *synergic effect*.

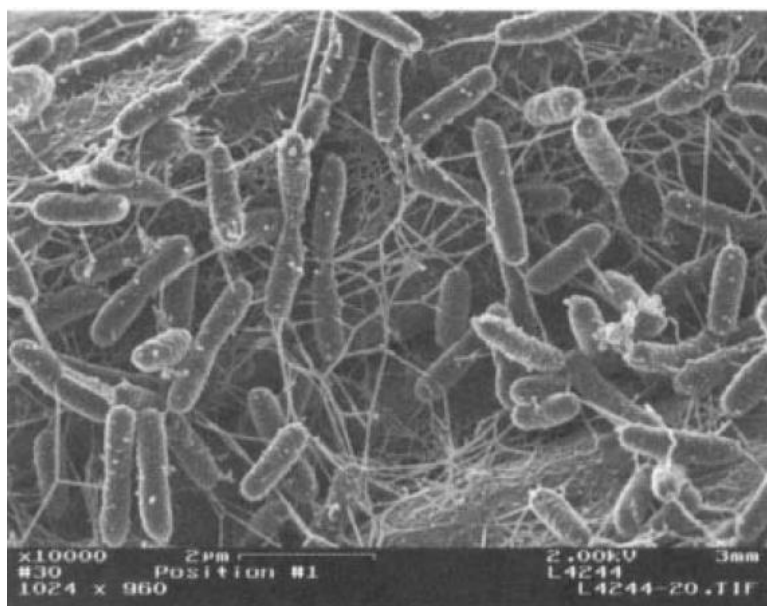
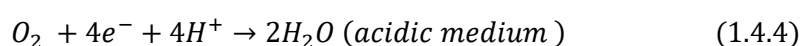


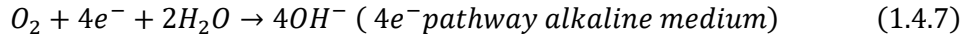
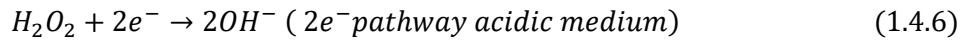
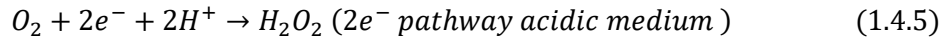
**Figure 1.4.2:** Nanowires produced by *Shewanella oneidensis* MR-1 growing on an electrode in an MF [67].

The second mechanism for electron transfer is the exploitation of redox mediators, this has been the first discovered mechanism. These exogenous mediators include, for example, neutral red [69], anthraquinone-2,6-disulfonate (AQDS), thionin, potassium ferrocyanide, methylviologen, and others. It is not clear if these compounds are produced primarily as a mechanism for exogenous electron transfer or other reasons. Some of these compounds are also known for their antibiotic activity. Thus, one of the main reasons for excretion may be respiratory inhibitors or toxins to inactivate competitors [70]. Electron transfer can also occur through interspecies hydrogen transfer or the production of intermediates metabolites such as formate and acetate and other chemicals. Thus, for all the reasons explained above mixed culture seems to have a better capability to produce energy. [62].

#### 1.4.6 Air-breathing cathode

Oxygen is an ideal choice as TEA for MFCs because of its high standard potential and ubiquitous existence. Air-breathing cathodes are electrodes exposed to the atmosphere that exploit the oxygen as reacting species. At the air-breathing cathode, the Oxygen Reduction Reaction (ORR) occurs. The pathway of ORR depends upon the pH as well as on the electrode material. Two main pathways are known, the direct  $4e^-$  mechanism and the sequential  $2 \times 2e^-$  ones that are reported in the following chemical equations (1.4.4-1.4.5).





Air-breathing cathodes have the main advantages of being extremely simple in construction and passive (no need for agitation or oxygen insufflation). On the other hand, since the oxygen freely diffuses to the cathode, these electrodes suffer from mass transport limitation at high specific currents. To improve air-breathing cathode performances, in particular the ORR kinetics, catalysts are exploited. Historically, at first Pt group metal catalysts were exploited due to their superior performances. The high cost and the poisoning that could occur due to the complex chemical environment of MFCs [71], has driven the Pt group metal catalysts substitution with more economical ones, such as Pt-group metal-free catalysts but also carbonaceous ones. Indeed, carbonaceous catalysts are extremely attractive as the main components of air breathing cathodes in MFCs. This is due to their contained cost if compared with transition metal-based catalyst and their chemical stability in complex chemical environments such as those of MFCs. Numerous researchers have reported on the use of carbon nanotubes, carbon nanofibers, and graphene [72] as ORR catalysts. Activated carbons are excellent candidates for ORR electrocatalytic activity. This is due to their tunable surface areas, environmental friendliness, and sustainability. Indeed, activated carbon, as mentioned in Section 1.3.2 can be obtained from sustainable sources like biomass pyrolysis and activation with mild agents [73]. During pyrolysis in presence of an activating agent, a porous carbon matrix is created depending on the type and amount of activating agent, reaction time as well as temperature [39,40]. Thus, the surface area, as well as the pore volume of biomass-derived carbons, can be tuned by selecting optimum reaction conditions large surface areas and hierarchical porous structure enable faster ORR kinetics, more positive ORR onset potentials, and high-power output in MFCs. Typically, activated carbons bring about a 2x2 ORR mechanism [74]. In an air-breathing cathode, two different segments are present, one facing the electrolyte and another one facing the atmosphere. To avoid water leaking and evaporation the surface exposed to air should be hydrophobic, while the surface facing the sludge should be hydrophilic to allow protons to reach the reaction sites. This architecture generates a hydrophobic/hydrophilic gradient and creates the so-called triple-phase interface, which is an interface in which gas/solid/liquid is present. High surface area carbon electrodes with hydrophobic binder allow this kind of interface.

In this thesis, activated carbon-based air-breathing cathodes have been exploited. Indeed, this approach offers the possibility to have a sustainable air-breathing cathode that has both an ORR catalytic activity and the possibility to exploit the supercapacitive response of the high surface area air-breathing cathode at high current densities. Indeed, as has been discussed in Section 1.5, AC-based electrodes are a valuable strategy to realize green supercapacitive systems.

To conclude, MFCs are very low energy sources, it has been widely shown that MFCs are capable to degrade a plethora of simple organics and complex civil and industrial wastewaters [14,62]. Microbial fuel cells have a great potential for many applications like electricity generation [75], wastewater treatment [76], biosensors [77], and bioremediation. However, their low power outputs limit real-world application. Indeed, the power density of MFCs is affected by several factors such as the electron transfer from microbe, ohmic loss, microbial inoculum, substrate, ORR at the cathode as well as the cost of the components and the cell design [64,78]. Cell design, electrode materials as well as the inoculum much affect MFC performance [66].

Typically, MFCs operate in a (circum) neutral pH at room temperature to support the activity of the bacteria and its survival. At a neutral pH of 7, the concentration of active reactants such as  $H^+$  ( $10^{-7}$  M) and  $OH^-$  ( $10^{-7}$  M) is 7 orders of magnitude lower compared to extreme pH (acid and alkaline) which consequently influence the oxygen reduction reaction [79-80]. Therefore, given the low reactant concentration, the oxygen reduction reaction is extremely sluggish. The microbial colony at the anode is responsible for the oxidation of the organic substances present in the electrolyte. In this Thesis it has been added regularly a solution of sodium acetate as an oxidable substrate.

## **1.5 Supercapacitive microbial fuel cell**

Dewan and co-worker in [66] showed that a common procedure is to report the specific power of microbial fuel cells as a function of the area of the limiting electrode. In particular, the authors highlight that it is quite common to obtain a lab cell scale impressive values of specific power that decrease when the volume of the cell increases. This fact urges to find alternative strategies that allow improved power performance for MFCs. The exploitation of catalysts to improve the sluggish cathode kinetics, as well as the introduction of supercapacitive features, as system integration and at the cell level, are approaches that have been reported to improve the power performance of MFCs [71]. MFCs are usually coupled with an energy storage system

such as supercapacitors or batteries, that accumulate the energy produced by the cell during the conversion and deliver it when needed. A successful example of this strategy is the combination of MFCs with batteries and supercapacitors that comes from the field of robotics with Gastrobot and EcoBot [81,82]. Other practical applications through a combination of MFCs and supercapacitors have also been reported [83-85], and different combinations of MFCs with power management systems are described in the literature [87]. A further strategy that has been explored is the exploitation of the MFCs electrodes as the electrodes of an internal supercapacitor, described as supercapacitive mode. In particular, the supercapacitive operational mode of MFCs is an effective strategy to boost power [77]. The supercapacitive mode on MFCs exploits the formation of the electrical double layer related to the natural polarization that occurs at the electrodes, during the anodic colonization. That is, the first stage of the anode is colonization by electroactive bacteria that act as biocatalysts for the oxidation reaction. Oxygen is consumed, and anaerobic biotic conditions are established. Therefore, the electrode is negatively polarized with respect to the initial conditions, where the bare anode was in contact with an aqueous electrolyte with a certain content of  $O_2$  [81]. In parallel, the cathode is exposed to air, and oxygen is used for the oxygen reduction reaction. The cathode electrode is positively polarized, and the potential moves toward positive values [74]. Because of these two different established bioelectrochemical environments, the electrodes are polarized (Figure 1.4.3 a). Electrochemical double layers are therefore set at each electrode/electrolyte interface (Figure 1.4.3 a). At the cathode surface, the excess of positive charges is balanced by electrolyte anions. In parallel, on the anode surface, the excess of negative charges is counterbalanced by the electrolyte cations (Figure 1.4.3 a). Opposite charges move from the electrolyte to the charged electrodes, forming an electrochemical double layer at each electrode/electrolyte interface. In such conditions, the cell can be described as a charged EDLC. The anode and cathode of MFCs are behaving similarly to the negative and positive electrodes of an internal supercapacitor. Once left in rest conditions and a stable cell voltage is reached, the electrodes can be discharged electrostatically, the electrode charges are neutralized, and the counterions are released in the electrolyte (Figure 1.4.3 b). The energy stored electrostatically on the electrodes can then be released to an external load (Figure 1.4.3 b). Once the discharge is completed, the electrodes are self-recharged at their initial potential value, self-polarized, and an electrochemical double layer is formed at each electrode. The internal EDLC is, therefore self-recharged thanks to the different anaerobic and aerobic environments and the specific bioelectrochemical environment [82]. The discharge process during the operation of the supercapacitive MFC, in pulsed mode, is reported in Figure 1.4.3.

The pulsed mode of an MFC consists in discharging the cell galvanostatic until a certain cell voltage is reached, followed by an open circuit condition to recover the initial voltage. A further approach that has been demonstrated to significantly boost MFC power is the use of an Additional Electrode (AdE), which are described in Figure 1.4.3. The additional electrode is short-circuited with the cathode, therefore is positively polarized. Given the cell geometry, this strategy allows a strong reduction of the cell internal resistance enabling higher current, with respect to supercapacitive MFCs without the AdE. Moreover, the increase of the cathode surface area achieved by the short-circuited AdE, also increases the capacitive response of the system.

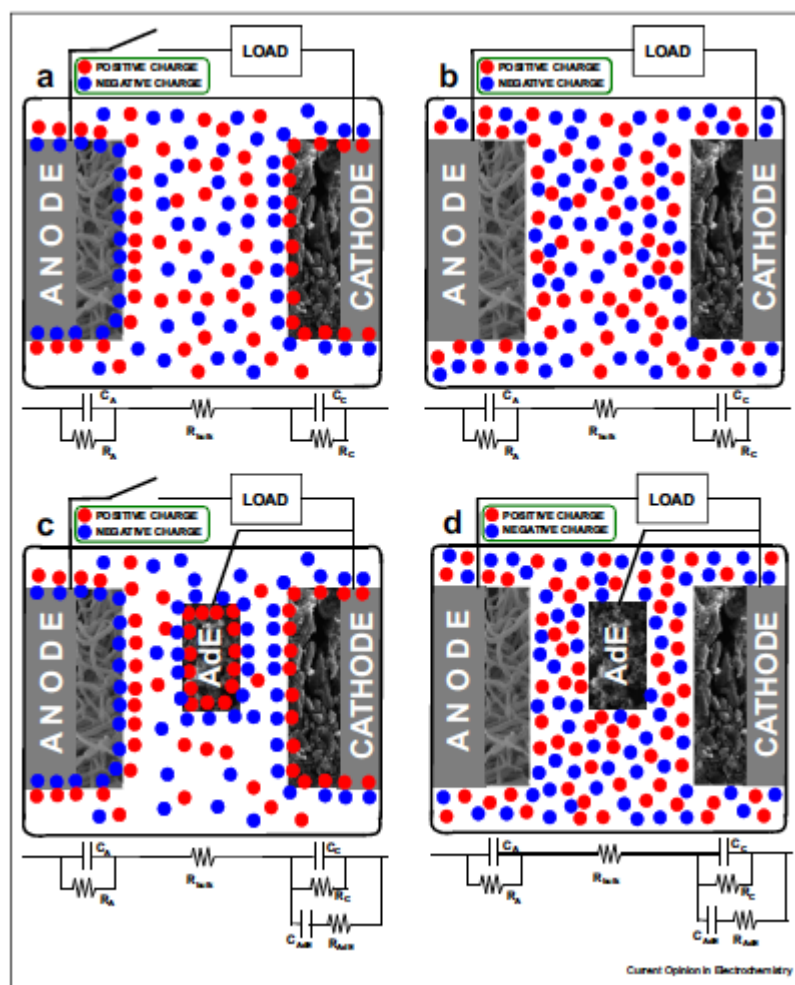


**Figure 1.4.3:** a) Supercapacitive microbial fuel cell in open circuit, b) closed circuit, c) Supercapacitive microbial fuel cell with an additional electrode in open circuit d). Supercapacitive microbial fuel cell with an additional electrode under load conditions [83].

However, it has to be underlined that in these supercapacitive MFCs, during discharge, different processes overlap: the irreversible faradic reactions driving the MFC operation and

the reversible discharge of the electrical double layers that occur simultaneously. This makes it more appropriate to identify the capacitance as ‘*apparent capacitance*’ [82]. Faradaic and electrostatic processes feature diverse rates and kinetics with the first one slower than the latter. Apparent capacitance depends on current and pulse time: (i) at lowest currents and short times, the electrostatic process drives the cell response; (ii) at low currents and long times, the faradic contribution becomes predominant. The first supercapacitive MFC in which both anode and cathode were considered as internal electrodes of a supercapacitor and where an AdE was exploited, was patented in 2016 by scientists from the University of Bologna (Italy) and the University of New Mexico (USA). In that study, the cell was galvanostatically discharged at different currents (up to 4.5 mA) with a peak of maximum power ( $P_{max}$ ) achieved was of c.a. 0.67 mW ( $2.98 \text{ Wm}^{-2}$ ) [37].

## **1.6 Aim of the work**

The challenging aim of this Ph.D. work is to exploit and merge of different electrochemical systems and their components, like supercapacitors and MFCs, by a green approach, to design a monolithically integrated system that boosts MFCs power well beyond State-of art air-breathing MFCs. In parallel, sustainability and waste valorization are central themes in this thesis. Indeed, the planned work targeted the exploitation of the main solid waste of the biogas plant from which the MFCs inoculum was taken, to produce carbon electrodes to be implemented in the supercapacitive MFC systems. This approach fully addresses the water-waste-energy nexus, by a circular economy. Three main strategic research lines have been followed: i) the development of green supercapacitors, ii) the external integration of green supercapacitors with MFCs and, iii) the development of supercapacitive microbial fuel cells by the monolithic integration of supercapacitive features in MFC electrodes. In addition to getting further insight into the electrode/electrolyte interface of electrochemical energy storage/conversion technique, a novel approach, that is consolidated in the field of organic electronics, like ion-gate transistor setup has been here exploited.

Chapter 1 introduces the energy-water nexus, highlights the role played by supercapacitors and MFCs in this scenario, and describes the main components and processes in these devices. In Chapter 2, different approaches followed to improve the sustainability of supercapacitor manufacturing are reported. The strategies to both integrate external supercapacitors and



integrate monolithic supercapacitive features in MCs have been carried out and are reported in Chapter 3. The third more explorative line of research followed on this thesis regards the study of electrochemical interfaces and is discussed in Chapter 4.

## Chapter 1 references:

- [1] Schmidt, G. A., Ruedy, R. A., Miller, R. L., and, Lacis, A. A., "Attribution of the present-day total greenhouse effect", *J. Geophys. Res.*, 115, (2010), D20106
- [2] Kiehl, J. T., and Trenberth, K.E., "Earth's annual global mean energy budget." *Bulletin of the American meteorological society*, 78.2 (1997), 197-208.
- [3] Bond, D. PG, and Grasby, S.E., "Late Ordovician mass extinction caused by volcanism, warming, and anoxia, not cooling and glaciation.", *Geology*, 48.8, (2020), 777-781.
- [4] Fischer, T. P., and Aiuppa, A., "AGU Centennial Grand Challenge: Volcanoes and deep carbon global CO<sub>2</sub> emissions from subaerial volcanism—Recent progress and future challenges.", *Geochemistry, Geophysics, Geosystems* 21.3, (2020), e2019GC008690.
- [5] Gołasa, P., et al., "Sources of greenhouse gas emissions in agriculture, with particular emphasis on emissions from energy used.", *Energies*, 14.13, (2021), 3784.
- [6] Agreement, Paris. "Paris agreement.," *Report of the Conference of the Parties to the United Nations Framework Convention on Climate Change*, (21st Session, 2015: Paris), Retrieved December, Vol. 4,(2015).
- [7] Bardt, H., "Raw materials in the field of electrochemical energy storage—A risk analysis." *AIP Conference Proceedings*, Vol. 1765, No. 1, AIP Publishing LLC, (2016).
- [8] ENTR, DG., "Report on critical raw materials for the EU.", *European Commission*, (2014).
- [9] Darlene, S., Mayyas, A., and Mann, M., "Economics and challenges of Li-ion battery recycling from end-of-life vehicles.," *Procedia Manufacturing*, 33, (2019), 272-279.
- [10] Bauer, D., et al., "The water-energy nexus: Challenges and opportunities." *US Department of Energy*, (2014).
- [11] "Water-Energy-Food-Nexus", *Food and Agriculture Organization of the United Nations*, Archived from the original on 2019-03-11, Retrieved 2019-09-15.
- [12] UNDP: Millennium Development Goals, Goal 7: Ensure environmental sustainability
- [13] UN Secretary General's Advisory Group on Energy and Climate Change (AGECC), Summary Report and Recommendations, (28 April 2010), p. 13

- [14] Cao, T. N.-D., et al. "A promising bioelectrochemical reactor integrating membrane distillation and microbial fuel cell for dual advantages of power generation and water recovery," *Environmental Science: Water Research & Technology*, 6.10,(2020), 2776-2788.
- [16] Kötz, R., and Carlen, M. J. E. A., "Principles and applications of electrochemical capacitors." *Electrochimica acta* 45.15-16 ,(2000), 2483-2498.
- [17] Soavi, F., and Santoro, C., "Supercapacitive operational mode in microbial fuel cell." *Current Opinion in Electrochemistry*, 22,(2020), 1-8.
- [18] Abbas, Q., et al., "Current State and Future Prospects for Electrochemical Energy Storage and Conversion Systems." *Energies*, 13.21,(2020), 5847.
- [19] Mathis, T.S., et al., "Energy storage data reporting in perspective—guidelines for interpreting the performance of electrochemical energy storage systems." *Advanced Energy Materials*, 9.39,(2019), 1902007.
- [20] Conway, B., E., *Electrochemical supercapacitors: scientific fundamentals and technological applications*. Springer Science & Business Media, (2013).
- [21] Pandolfo, A. G., and Hollenkamp, A. F., "Carbon properties and their role in supercapacitors." *Journal of power sources*, 157.1,(2006), 11-27.
- [22] Vlad, A., et al., "Hybrid supercapacitor-battery materials for fast electrochemical charge storage." *Scientific reports*, 4.1,(2014), 1-7.
- [23] Miller, J. R., and Burke. A., "Electrochemical capacitors: challenges and opportunities for real-world applications." *The electrochemical society interface* 17.1,(2008), 53.
- [24] Schütter, C., Pohlmann, S., and Balducci, A., "Industrial requirements of materials for electrical double layer capacitors: impact on current and future applications." *Advanced Energy Materials*, 9.25,(2019), 1900334.
- [25] Helmholtz, H. von. "Ueber einige Gesetze der Vertheilung elektrischer Ströme in körperlichen Leitern, mit Anwendung auf die thierisch-elektrischen Versuche (Schluss.)." *Annalen der Physik*, 165.7,(1853), 353-377.
- [26] H.I. Becker, Low voltage electrolytic capacitor, United States Patent 2,800,616,(1957).
- [27] Edwards, I. AS., Marsh, H., and Menendez, R., *Introduction to carbon science.*, Butterworth-Heinemann, (2013).
- [28] Dura, H., et al., "Cost analysis of supercapacitor cell production." *2013 international conference on clean electrical power, (ICCEP)*. IEEE, (2013).
- [29] Bresser, D, et al., "Alternative binders for sustainable electrochemical energy storage—the transition to aqueous electrode processing and bio-derived polymers." *Energy & Environmental Science*, 11.11,(2018), 3096-3127.
- [30] Dyatkin, B., et al., "Development of a green supercapacitor composed entirely of environmentally friendly materials." *ChemSusChem*, 6.12,(2013), 2269-2280.
- [31] M.,Inagaki, Radovic, L.R., *Carbon*, 40,(2002), 2263.

- [32] X., Bourrat, Marsh, H., Rodriguez-Reinoso, F., (Eds.), *Science of Carbon Materials*, Universidad de Alicante, (2000), p. 1.
- [33] H., Marsh, *Introduction to Carbon Science*, Butterworths, (1989).
- [34] Radeke, K. H., Backhaus, K. O., and Swiatkowski, A., "Electrical conductivity of activated carbons.", *Carbon*, 29.1,(1991), 122-123.
- [35] Akihiko, Y., Tanahashi, I. and, Nishino, A., "Effect of concentration of surface acidic functional groups on electric double-layer properties of activated carbon fibers.", *Carbon* 28.5,(1990), 611-615.
- [36] Maciá-Agulló, J. A., et al., "Activation of coal tar pitch carbon fibres: Physical activation vs. chemical activation.", *Carbon*, 42.7,(2004), 1367-1370.
- [37] Deng, H., et al., "Preparation of activated carbons from cotton stalk by microwave assisted KOH and K<sub>2</sub>CO<sub>3</sub> activation.", *Chemical Engineering Journal*, 163.3,(2010), 373-381.
- [38] Hu, Z., and Vansant., E. F., "Chemical activation of elutrilite producing carbon-aluminosilicate composite adsorbent.", *Carbon*, 33.9,(1995), 1293-1300.
- [39] Sevilla, M., and Fuertes, A. B., "A green approach to high-performance supercapacitor electrodes: the chemical activation of hydrochar with potassium bicarbonate.", *ChemSusChem*, 9.14,(2016), 1880-1888.
- [40] Lillo-Ródenas, M. A., Cazorla-Amorós, D. and, Linares-Solano., A., "Understanding chemical reactions between carbons and NaOH and KOH: an insight into the chemical activation mechanism.", *Carbon*, 41.2,(2003), 267-275.
- [41] Raymundo-Pinero, E., et al., "KOH and NaOH activation mechanisms of multiwalled carbon nanotubes with different structural organisation." *Carbon* 43.4,(2005), 786-795.
- [42] Basta, A. H., et al., "Effect of deashing rice straws on their derived activated carbons produced by phosphoric acid activation." *Biomass and Bioenergy* 35.5,(2011), 1954-1959.
- [43] Abioye, A. M., and Ani., F. N., "Recent development in the production of activated carbon electrodes from agricultural waste biomass for supercapacitors: a review.", *Renewable and sustainable energy reviews*, 52,(2015), 1282-1293.
- [44] Jäckel, N., et al. "Performance evaluation of conductive additives for activated carbon supercapacitors in organic electrolyte." *Electrochimica Acta* 191 (2016), 284-298.
- [45] Beck, F., et al., "Electrochemical supercapacitors based on industrial carbon blacks in aqueous H<sub>2</sub>SO<sub>4</sub>.", *Journal of applied electrochemistry* 31.8, (2001), 845-853.
- [46] Richner, R, Müller, S., and Wokaun., A., "Grafted and crosslinked carbon black as an electrode material for double layer capacitors.", *Carbon*, 40.3,(2002), 307-314.
- [47] Hess, W.M., Herd, C.R., Donet, J.B., Bansal R.C., Wang, M.J. (Eds.), *Carbon Black*, 2nd ed., Marcel Dekker, New York, 1993, p. 89.
- [48] Ruschhaupt, P., Varzi, A. and Stefano Passerini., "Natural Polymers as Green Binders for High-Loading Supercapacitor Electrodes.", *ChemSusChem*, 13.4,(2020), 763.

- [49] Böckenfeld, N., et al., "Natural, cheap and environmentally friendly binder for supercapacitors.", *Journal of power sources*, 221,(2013), 14-20.
- [50] Bonnefoi, L., et al., "Electrode compositions for carbon power supercapacitors.", *Journal of power sources*, 80.1-2,(1999), 149-155.
- [51] Varzi, A., and Passerini, S., "Enabling high areal capacitance in electrochemical double layer capacitors by means of the environmentally friendly starch binder." *Journal of Power Sources* 300,(2015), 216-222.
- [52] Varzi, A., et al., "Probing the characteristics of casein as green binder for non-aqueous electrochemical double layer capacitors' electrodes.", *Journal of Power Sources*, 326 ,(2016), 672-679.
- [53] Pal, B., et al., "Electrolyte selection for supercapacitive devices: A critical review.", *Nanoscale Advances*, 1.10,(2019), 3807-3835.
- [54] Arulepp, M., et al., "Influence of the solvent properties on the characteristics of a double layer capacitor.", *Journal of Power Sources*, 133.2,(2004), 320-328.
- [55] Karuppasamy, K., et al., "Ionic liquid-based electrolytes for energy storage devices: A brief review on their limits and applications.", *Polymers*, 12.4,(2020), 918.
- [56] Liew, C.-W., Ramesh, S., and Arof., A. K., "Investigation of ionic liquid-doped ion conducting polymer electrolytes for carbon-based electric double layer capacitors (EDLCs).", *Materials & Design*, 92, (2016), 829-835.
- [57] Wang, A., et al., "Polymeric ionic liquid enhanced all-solid-state electrolyte membrane for high-performance lithium-ion batteries.", *Electrochimica Acta*, 276,(2018), 184-193.
- [58] Muzaffar, A., et al., "A review on recent advances in hybrid supercapacitors: Design, fabrication and applications.", *Renewable and sustainable energy reviews*, 101,(2019), 123-145.
- [59] Verma K.D., Sinha P., Banerjee S., Kar K.K., Ghorai M.K. (2020) *Characteristics of Separator Materials for Supercapacitors*. In: Kar K. (eds) *Handbook of Nanocomposite Supercapacitor Materials I*. Springer Series in Materials Science, vol 300. Springer, Cham. [https://doi.org/10.1007/978-3-030-43009-2\\_11](https://doi.org/10.1007/978-3-030-43009-2_11)
- [60] Logan, B.E., Exoelectrogenic bacteria that power microbial fuel cells., *Nature Rev Microb*,(2009), 7:375-381.
- [61] Potter, M. C., "Electrical effects accompanying the decomposition of organic compounds.", *Proceedings of the royal society of London. Series b, containing papers of a biological character*, 84.571 ,(1911), 260-276.
- [62] Logan, B.E., *Microbial fuel cells*., John Wiley & Sons, (2008).
- [63] Kim, B. H., et al., "Enrichment of microbial community generating electricity using a fuel-cell-type electrochemical cell.", *Applied microbiology and biotechnology*, 63.6,(2004), 672-681.
- [64] Logan, B. E., and John M. Regan. "Electricity-producing bacterial communities in microbial fuel cells.", *TRENDS in Microbiology*, 14.12,(2006), 512-518.

- [65] Cheng, Shaoan, H. L., and Bruce E. L., "Increased performance of single-chamber microbial fuel cells using an improved cathode structure.", *Electrochemistry communications*, 8.3,(2006), 489-494.
- [66] Dewan, A., Beyenal, H., and Lewandowski, Z. "Scaling up microbial fuel cells.", *Environmental science & technology*, 42.20 ,(2008), 7643-7648.
- [67] Gorby, Y. A., et al., "Electrically conductive bacterial nanowires produced by *Shewanella oneidensis* strain MR-1 and other microorganisms.", *Proceedings of the National Academy of Sciences*, 103.30,(2006), 11358-11363.
- [68] Reguera, G, et al., "Extracellular electron transfer via microbial nanowires." ,*Nature*, 435.7045 ,(2005), 1098-1101.
- [69] Gandasasmita, S., "Electropolymerized neutral red as redox mediator for yeast fuel cell." ,*Int. J. Electrochem. Sci*, 10 ,(2015), 8886-8898.
- [70] Voggu, L., et al., "Microevolution of cytochrome bd oxidase in staphylococci and its implication in resistance to respiratory toxins released by *Pseudomonas*.", *Journal of bacteriology*, 188.23 ,(2006), 8079-8086
- [71] Santoro, C., et al., "Platinum group metal-free oxygen reduction electrocatalysts used in neutral electrolytes for bioelectrochemical reactor applications.", *Current Opinion in Electrochemistry* 23 ,(2020), 106-113.
- [72] Stacy, J., et al., "The recent progress and future of oxygen reduction reaction catalysis: A review." *Renewable and Sustainable Energy Reviews* 69 ,(2017), 401-414.
- [73] Mutuma, B. K., et al., "Valorization of biodigester plant waste in electrodes for supercapacitors and microbial fuel cells.," *Electrochimica Acta* 391 ,(2021), 138960.
- [74] Kinoshita, K., *Electrochemical oxygen technology.*, Vol. 30., John Wiley & Sons, 1992.
- [75] Liu, H., and Logan, B.E., "Electricity generation using an air-cathode single chamber microbial fuel cell in the presence and absence of a proton exchange membrane.", *Environmental science & technology*, 38.14,(2004), 4040-4046.
- [76] Hao, X., et al., "Energy recovery from wastewater: Heat over organics.", *Water research*, 161 ,(2019), 74-77.
- [77] Santoro, C., et al., "Self-powered supercapacitive microbial fuel cell: the ultimate way of boosting and harvesting power.," *Biosensors and Bioelectronics* 78 ,(2016), 229-235.
- [78] Call, D. F., Wagner, R.C., and Logan, B.E., "Hydrogen production by *Geobacter* species and a mixed consortium in a microbial electrolysis cell.", *Applied and environmental microbiology*, 75.24,(2009), 7579-7587.
- [79] Rojas-Carbonell, S. et al., "Transition metal-nitrogen-carbon catalysts for oxygen reduction reaction in neutral electrolyte.," *Electrochemistry Communications*, 75 ,(2017), 38-42.
- [80] Malko, D., Kucernak A., and Lopes T., "In situ electrochemical quantification of active sites in Fe–N/C non-precious metal catalysts.", *Nature communications*, 7.1 ,(2016), 1-7.

- [81] Papaharalabos, G., et al., "Dynamic electrical reconfiguration for improved capacitor charging in microbial fuel cell stacks.," *Journal of Power Sources* 272 ,(2014), 34-38.
- [82] Melhuish, C., et al., "Energetically autonomous robots: Food for thought.," *Autonomous Robots*, 21.3,(2006), 187-198.
- [83] Caizán-Juanarena, L., et al., "Combination of bioelectrochemical systems and electrochemical capacitors: principles, analysis and opportunities.," *Biotechnology advances* 39 ,(2020), 107456.
- [84] Arias-Thode, Y. Meriah, et al., "Demonstration of the SeptiStrand benthic microbial fuel cell powering a magnetometer for ship detection.," *Journal of Power Sources*, 356 ,(2017), 419-429.
- [85] Donovan, C., et al., "Sediment microbial fuel cell powering a submersible ultrasonic receiver: New approach to remote monitoring.," *Journal of Power Sources*, 233 ,(2013), 79-85.
- [86] Wang, H., Park,J-D. and Ren, Z.J., "Practical energy harvesting for microbial fuel cells: a review.," *Environmental science & technology*, 49.6 ,(2015), 3267-3277.
- [87] Grattieri, M., et al., "Enzymatic oxygen microsensor based on bilirubin oxidase applied to microbial fuel cells analysis.," *Electroanalysis* 27.2 ,(2015), 327-335.

## Chapter 2: Green supercapacitors

This chapter is devoted to the description of the main achievements in the design and realization of green supercapacitors, specifically, different challenges that have been addressed and are here reported

The main part of my Ph.D. activity on this topic was focused on the exploitation of novel bio-derived aqueous processable polymers, such as pullulan as main components, namely separator, and binder, for high voltage green supercapacitors under the collaborative ISARP project with the University of Pretoria (SA), the PTR 2019-2021 MISE-ENEA Project. The main results and experimental approaches are summarized in section 2.1.1 and have been published in the attached papers [1,2].

Moreover, I contributed to exploring different electrode and electrolyte components to improve both the sustainability and the energy density of modern supercapacitors, working under a collaborative project with groups from partner Universities, namely:

- i) Together with the group “Gruppo di Elettrocatalisi ed Electrochimica Applicata” of Professor Christian Durante of UNIVERSITÀ DEGLI STUDI DI PADOVA, the utilization of N-doped carbon as strategy to improve the energy density of ionic liquid based EDLC has been investigated. The main results and experimental approaches are summarized in Section 2.2 and have been published in the attached paper [3].
- ii) With the group of Professor Massimo Innocenti, from the Department of Chemistry “Ugo Schiff” of the UNIVERSITÀ DEGLI STUDI DI FIRENZE a detailed electrochemical study on the corrosion of current collectors in a novel class of electrolytes, namely water in salt has been investigated. The main results and experimental approaches are summarized in Subsection 2.3.1 and have been published in the attached paper [4].
- iii) With the group of NanoBio Interface Lab of Professor Calvaresi, University of Bologna, in collaboration with Mohammad Said El Halimi, a Ph.D. student in Cotelutele between the University of Bologna and the University of Tangeri, I have worked in developing novel water in a salt electrolyte (WiSE) based on ammonium acetate for EDLCs. The main results and experimental approaches are summarized in Subsection 2.3.2 and have been published in the attached paper [5].

## 2.1 Pullulan as water processable polymer for high voltage supercapacitors

Pullulan, a water processable bioderived polymer has been exploited as the main component of novel binder and electrospun separator for green high voltage supercapacitors. The separator has been obtained by means of electrospinning starting from an aqueous solution, therefore overcoming issues related to conventional organic molecules-based separators that require processing by organic solvents. To meet proper mechanical properties needed for EDLCs separator, and the binder, pullulan has been used in a blend with glycerol.

At first, the work has been focused on the electrochemical response and thermal stability of electrospun separators based on natural polymers, provided by the group of Professor Focarete, POLYMER SCIENCE AND BIOMATERIALS of the University of Bologna. In particular, pullulan (PU) and cellulose triacetate (CTA) electrospun separators have been studied in different electrolytes, namely 1-ethyl-3-methyl-Imidazolium bis-(trifluoromethylsulfonyl) imide (EmimTFSi), 0.5 m solution of lithium bis-(trifluoromethylsulfonyl)imide (LiTFSI) in Tetraethylene glycol dimethyl ether (TEGDME), and 1-Butyl-1-methylpyrrolidinium bis-(trifluoromethylsulfonyl)-imide (PYR<sub>14</sub>TFSI). The contribution to ionic resistance of the electrospun separator soaked with the different electrolytes has been investigated by Electrochemical Impedance Spectroscopy (EIS) at different temperatures. Pullulan/EmimTFSI was the combination that showed the minimum resistance at each tested temperature, and therefore, this combination of separator and electrolyte has been selected has to assemble two different EDLCs with electrodes based on a commercial activated carbon (BP10, PICAactif):

- HBLME: low electrode mass loading and high binder content (HBLME)
- LBHME high mass loading and low binder content (LBHME).

The EDLCs have been tested by cyclic voltammetry, EIS, and galvanostatic charge/discharge cycles. The highest specific capacitance was featured at the lowest scan rate of 5 mV s<sup>-1</sup> for both devices and was 18 F g<sup>-1</sup> and 14 F g<sup>-1</sup> for HBLME-EDLC and LBHME-EDLC, respectively. Both supercapacitors featured good capacitance retention with the increase of the scan rate, which however was higher for HBLME-EDLC (22%) than LBHME-EDLC (50%). Galvanostatic cycling with high coulombic efficiency (higher than 98%) was demonstrated for both devices at the high cell voltage of 3.2 V. Noticeably, the EDLC featured a very good cycling behavior demonstrated over more than 2000 cycles even at low binder content,



confirming the stability of the Pu-polymer in EmimTFSI. The high cell voltage and good specific capacitance provided specific energy of  $19.6 \text{ Wh kg}^{-1}$  and  $7.2 \text{ Wh kg}^{-1}$  at  $0.5 \text{ A g}^{-1}$  that well compared with those of EDLCs featuring the same electrolyte and active carbon but employing a fluorinated binder and fiberglass separators. The highest specific power was  $4.6 \text{ kW kg}^{-1}$  and  $3.7 \text{ kW kg}^{-1}$  at  $4\text{--}5 \text{ A g}^{-1}$  respectively for HBLME-EDLC and for the LBHME-EDLC. The gravimetric performance of the HBLME-EDLC is superior to that of the LBHME-EDLC. The experimental methods and the results of this study are reported in [1]. Following such interesting results, pullulan was used as the electrospun separator and binder in EDLCs featuring electrodes based on a bioderived carbon obtained from pepper-seeds waste (PP-AC). IL EmimTFSi has been selected as the electrolyte. This IL is known for its good electrochemical properties in terms of chemical and electrochemical stability, conductivity ionic. However, here an additional advantage in the use of this IL was demonstrated. Indeed, the exploitation of pullulan, an aqueous processable biopolymer in combination with hydrophobic ionic liquid, brings about a smart combination of material that enables an easy to dispose of strategy. That is, by soaking in water the device at its end of life, the aqueous processable binder quickly dissolves and the immiscible ionic liquid separates enabling the direct recovery of the EDLCs main components.

The pullulan-based supercapacitor delivered a maximum specific power of up to  $5 \text{ kW kg}^{-1}$ , and maximum specific energy of  $27.8 \text{ Wh kg}^{-1}$  specific energy at  $3.2 \text{ V}$ , these values well compare with conventional electrical double-layer capacitor performance with the added value of being eco-friendly and cheap with cell capacitance of  $20 \text{ F g}^{-1}$ . The Pullulan-based EDLCs showed good cycling stability up to 5000 cycles.

Notably, a comparison of the findings achieved in [1] and [2] demonstrate that the biochar EDLC, with pepper seeds-derived carbon, outperforms the EDLC based on a commercial carbon.

The experimental methods and the results of this study are reported in [1,2], which are here attached as complete publications



## Pullulan-ionic liquid-based supercapacitor: A novel, smart combination of components for an easy-to-dispose device

Federico Poli <sup>a,1</sup>, Damilola Momodu <sup>b,1</sup>, Giovanni Emanuele Spina <sup>a</sup>, Antonio Terella <sup>a</sup>, Bridget. K. Mutuma <sup>b</sup>, Maria Letizia Focarete <sup>a</sup>, Ncholu Manyala <sup>b,\*\*</sup>, Francesca Soavi <sup>a,\*</sup>

<sup>a</sup> Department of Chemistry "Giacomo Ciamician", Alma Mater Studiorum – Università di Bologna, Italy

<sup>b</sup> Department of Physics, Institute of Applied Materials, SARCHI in Carbon Technology and Materials, University of Pretoria, Pretoria, South Africa



### ARTICLE INFO

#### Article history:

Received 2 October 2019

Received in revised form

4 February 2020

Accepted 6 February 2020

Available online 7 February 2020

#### Keywords:

Green supercapacitor

Pullulan

Electrospinning

Ionic liquid

Bio-char carbon

### ABSTRACT

Strategies that simultaneously target energy/power performance, sustainable manufacturing processes, valorization of green raw materials, and easy recycling of supercapacitors are urgently needed. Today, efforts have to be devoted not only to improve system performance but also to address the sustainability of materials and devices manufacturing and recyclability. Specifically, pullulan is herein proposed as a novel bio-degradable binder and separator for green supercapacitors. It is processed by electrospinning from aqueous solutions, therefore overcoming issues related to conventional membrane processing by organic solvents. Furthermore, combining the water-soluble, biodegradable pullulan with a hydrophobic ionic liquid electrolyte brings about a novel approach for end-of-life management of devices. The use of pullulan is demonstrated in a supercapacitor with carbon electrodes obtained from pepper-seeds waste and 1-Ethyl-3-methylimidazoliumbis(trifluoromethylsulfonyl)imide as the electrolyte. The supercapacitor delivers up to 5 kW kg<sup>-1</sup> specific power and 27.8 Wh kg<sup>-1</sup> specific energy at 3.2 V, that well compare with conventional electrical double-layer capacitor performance with the added value of being eco-friendly and cheap.

© 2020 Elsevier Ltd. All rights reserved.

### 1. Introduction

The skyrocketing demand for electricity and backup power for advanced transportation and most portable electronic devices has necessitated a great investment in energy research [1].

To fully exploit renewable energy sources, adequate storage systems capable of dealing with the inconsistent generation associated with most renewable energy sources are needed. Supercapacitors, on the other hand, are potential storage systems that have been recently employed to complement battery systems and adopted as stand-alone backup units in more complex systems. With the numerous advancements being made by researchers to solve the drawback of the low energy density, supercapacitors can play a role for advanced applications requiring high-power, long cycle life and low maintenance costs [2–4].

A key application is the storage of energy from intermittent

renewable sources, like the sun and wind. Better exploitation of renewable sources will render electrical energy more available, even in developing countries.

Today supercapacitors make use of organic electrolytes, mostly based on acetonitrile, a flammable and toxic solvent, and fluorinated salts (e.g. tetraethylammonium tetrafluoroborate). Expensive fluorinated polymers such as polytetrafluoroethylene and polyvinylidene difluoride that even require solubilization in the toxic N-Methyl-2-pyrrolidone solvent [5] are also used as electrode binders and separators. Notably, such F-containing components impact on cell manufacturing and waste managing cost. Indeed, toxic and volatile fluorocarbons might be generated during the traditional incineration of end-of-life systems. Thus, it can be harmful to the environment, considering the increasing demand and market of supercapacitors.

In this scenario, lowering the price and minimizing the environmental and economic impact of disassembly and recycling of end-of-life supercapacitors is mandatory [6,7]. The valorization of organic wastes and natural sources by their transformation into valuable components of supercapacitors within a circular economy approach is also to be pursued.

Recently, the use of activated carbon from biological waste

\* Corresponding author.

\*\* Corresponding author.

E-mail address: [francesca.soavi@unibo.it](mailto:francesca.soavi@unibo.it) (F. Soavi).

<sup>1</sup> These authors equally contributed.

(biochar) as a means of obtaining abundant, low-cost supercapacitor electrode materials was extensively investigated and reported [8–14].

Other studies have focused on developing suitable conductive electrolytes which permit the electrode material to operate at the largest achievable potential ranges [15–19]. Aqueous electrolytes are limited to operation at a threshold voltage of 1.2 V due to the water present in them, but in some specific cases, values as high as 2.2 V can be achieved. Moreover, conventional organic and aqueous electrolytes cannot be used in high-temperature applications due to the flammability and low boiling point temperatures, respectively. Ionic liquids (ILs) provide the solution to the problems associated with organic and aqueous electrolytes but are saddled with low ionic conductivities and high costs. Thus, a trade-in on the cost of other less crucial components (such as separator, binders, current collectors) as compared to specific key elements could compensate for the overall cost.

Water-processable binders (e.g. carboxymethyl cellulose, alginate) are relatively cheaper options for use and improve the environmental compatibility of the electrode preparation process that can be done in ambient conditions. They represent an emerging viable alternative in place of much more expensive fluorinated polymers.

The present study demonstrates for the first time the design and assembly of a pullulan-based electrical double layer capacitor (EDLCs). Pullulan is a biodegradable polysaccharide-based biopolymer that is obtained from starch by the fungal species *Aureobasidium pullulan* [20]. Pullulan films exhibit high solubility in water. Their transparency, flexibility and low permeability to oxygen make them ideal packaging materials for food, pharmaceutical, and biomedical applications [21,22]. Specifically, here pullulan is adopted as both a water-processable binder and an electrospun separator. Electrospinning is an emerging technology for the preparation of controlled diameter fibers ranging from tens of nanometers to few micrometers. In recent years it has been considered as a promising process for the preparation of free-standing fiber mats to be used as electrode materials and separators in supercapacitors [23].

The pullulan-based EDLC featured 1-Ethyl-3-methylimidazolium-bis(trifluoromethylsulfonyl)imide (EMIMTFSI) ionic liquid (IL) as the electrolyte. While its low volatility and flammability make it safer than the state-of-art electrolytes of supercapacitors, it cannot be considered as a totally green alternative. For this reason, it is of great interest to design strategies to recover it [24].

The choice of this IL is driven by its good ionic conductivity matched with wide electrochemical stability that enables EDLCs to operate at voltages even higher than 3 V [2,3,7,25]. More importantly, EMIMTFSI is a hydrophobic electrolyte, and this peculiar characteristic permits the design of a smart process to manage pullulan-based EDLC waste disposal. Fig. 1 shows that at the end-of-life, the pullulan-IL-based EDLC can be readily separated into each of its components by immersion in water. The pullulan binder and separator are dissolved in water. Simultaneously, a physical separation of the carbon powder, the hydrophobic IL, the current collector and the aqueous solution containing the biodegradable biopolymer takes place. The carbon powder and current collector can be recovered from the IL by filtration. The pullulan aqueous solution is biodegradable and can be disposed off without any negative impact on the environment.

## 2. Experimental

### 2.1. Preparation of the electrospun pullulan separator

An electrospinning technique was used to prepare the pullulan

separator. The home-made electrospinning apparatus consisted of a high-voltage power supply (Spellman SL 50 P 10/CE/230), a syringe pump (KD Scientific 200 series), a glass syringe containing the polymer solution and connected to a stainless-steel blunt-ended needle (inner diameter = 0.51 mm) through a polytetrafluoroethylene (PTFE) tube. The pullulan membrane was electrospun using a 23% w/v solution of pullulan in Milli-Q water. The solution was spun at 18 kV at 20 cm from the collector with a flow rate of 0.9 mL/h. Electrospinning was performed at room temperature (RT) and relative humidity of 40–50%.

### 2.2. Synthesis of pepper seed-derived porous carbon

The synthesis of the porous carbon derived from pepper seeds (PP-AC) is as described in our earlier work [25]. Briefly, the seeds were obtained as waste from cheap Bell peppers and thoroughly mixed with potassium hydrogen carbonate ( $\text{KHCO}_3$ ) serving as the activating agent to obtain a homogenous mixture (mass ratio of raw material to  $\text{KHCO}_3$  was 1:1). Compactification of the final mixture into a rectangular mold was done by adding little deionized water to the powder in an agate mortar before drying in an oven at 80 °C for 6 h to remove the water. The dried mold was placed in a furnace purged with a regulated flow of argon gas (250 sccm) at a 5 °C min<sup>-1</sup> ramp rate for 2.8 h to an 850 °C final temperature. The carbonization process was run for a period of 2 h with subsequent cooling to 25 °C. The final product was sonicated for 0.5 h, washed with 3 M HCl and rigorously rinsed with deionized water to attain a neutral pH [14,26,27].

### 2.3. Preparation of the electrodes

Electrode composition was 70% PP-AC, 10% Carbon black, 20% pullulan-glycerol (1:1 wt). To be specific, a slurry containing 24.0 mg of PP-AC, 3.4 mg of carbon black (as conducting additive), 3.4 mg of pullulan (P0978, TCI) and 3.4 mg of Glycerol (Sigma Aldrich), in 0.9 g of MilliQ water was casted on pre-cut Nickel foams (Alantum, Munich, Germany, diameter 0.9 cm) and labelled as PP-AC-EDLC. The electrodes were then dried in an oven (under vacuum) overnight at room temperature (Büchi glass oven B-585). The composite electrode loading (excluding the Nickel foam mass) was in the range of 4–7.5 mg cm<sup>-2</sup> [28].

### 2.4. Supercapacitor assembly

Supercapacitors were assembled from two carbon composite electrodes alienated by a circular sheet of electrospun pullulan separator, with 1-Ethyl-3-methylimidazolium bis(trifluoromethylsulfonyl)imide IL (EMIMTFSI, Solvionic) as the electrolyte. A T Swagelok-type cell assembly (BOLA Cell made from Teflon) with a silver quasi-reference electrode disk was used. Cells were assembled in a dry box (MBraun Labmaster 130, H<sub>2</sub>O, and O<sub>2</sub> < 0.1 ppm). The separator and electrodes were soaked under vacuum with the IL before the assembly. The positive to negative electrode composite loading ratio was >1 to achieve cell voltages higher than 3 V.

### 2.5. Materials characterization

Scanning electron microscopy (SEM) images of the membrane were collected using a ZEISS EVO 50 apparatus. Tensile stress-strain measurements of the electrospun membrane were performed by using a Dynamic Mechanical Thermal Analyzer (DMTA, TA Instruments Q800 series) equipped with tension-film clamps. The analyses were performed on rectangular strips cut from the electrospun mat (width 5 mm; gauge length about

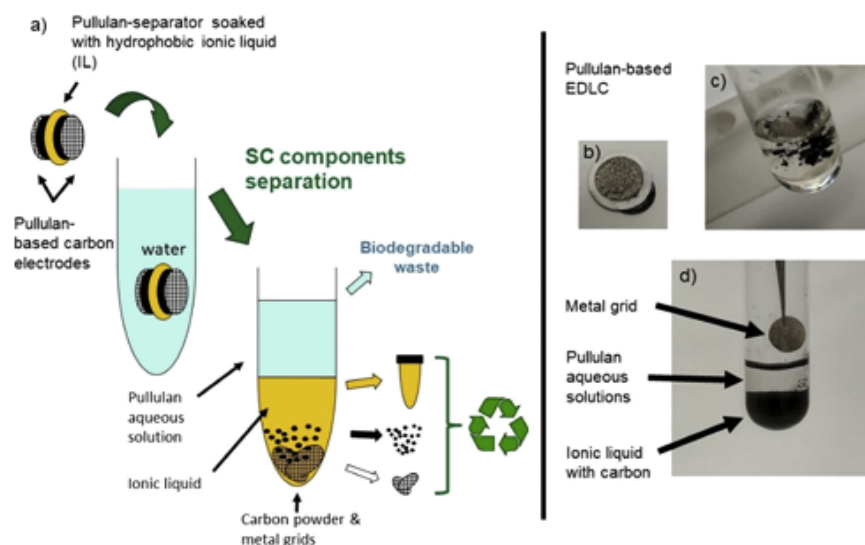


**Fig. 1.** a) Concept of pullulan-IL-based EDLC waste management, b) pullulan-IL-based EDLC, and c) first moments after its immersion in water and d) its components separation.

10 mm). Stress-strain measurements were carried out at RT by applying a preload force of 0.01 N and using a cross-head speed of 5 mm/min. Six rectangular specimens were analyzed for each sample. The specimen thickness (about 0.05 mm), measured with a digital micro-meter, was used to obtain stress-strain curves from raw load-displacement data. Stress and strain at yield ( $\sigma_y$  and  $\epsilon_y$ ), stress and strain at break ( $\sigma_b$  and  $\epsilon_b$ ) as well as the tensile modulus (E) were determined as the average value  $\pm$  standard deviation. Details on the electrode preparation and measurements are provided in the supplementary section.

Nitrogen adsorption porosimetry measurements for the PP-AC carbons were carried out at 77 K with an ASAP 2020 system (Micromeritics) after a drying step for 24 h at 180 °C. The  $N_2$  adsorption isotherms were analyzed by density functional theory (DFT) to obtain the pores size distribution (PSD). The complete chemical and physical characterization of the PP-AC carbon is reported in the earlier work [25]. The electrochemical tests were performed in a thermostatic oven at 30 °C using a BioLogic VSP multichannel potentiostat/galvanostat/FRA. Cyclic voltammograms were analyzed to evaluate the capacitance. Specifically, the capacitance values were obtained by the slope of the discharge voltametric current integrated over time vs. electrode potential (or cell voltage for the 2-electrode case) plots. Values are normalized to the composite electrode mass. Electrochemical impedance spectroscopy (EIS) was performed with a 100 kHz–100 mHz frequency range and 5 mV AC perturbation, acquiring 10 points per decade. For three electrode measurements, the working and counter electrodes were the positive and negative electrodes of the EDLC respectively. The silver disk was the reference electrode. For two electrode measurements, the silver disk was disconnected, the EDLC positive electrode was the working, and the EDLC negative electrode was connected to the counter and reference instrument plugs. The electronic resistivity of the PP-AC composite was evaluated with a Jandel multi-height four point probe apparatus connected to an Amel 2053 galvanostat/potentiostat and a Hewlett Packard 3478A multimeter. The test was carried out on composite material deposited on a non-conductive substrate (Mylar film).

### 3. Results and discussion

Pullulan is a highly water-soluble polymer that makes it of interest as the binder for water-processable electrodes. However, the brittleness of pullulan films requires blending with plasticizers to improve the mechanical properties. In Refs. [21,22], it is reported that glycerol is a suitable plasticizer. Indeed, pullulan-glycerol films casted from aqueous solution with a glycerol concentration of 20–30% w/w featured physical-mechanical properties acceptable for pharmaceutical and food packaging applications. This can be visually appreciated in Fig. 2a that shows a stretchable self-standing transparent film that is easily peeled-off from the Petri plate.

We, therefore, used a blend of pullulan and glycerol as a binder of supercapacitor carbon electrodes. In our study, the best adhesion of the carbon layer to the current collector was achieved by mixing pullulan and glycerol with a 1:1 wt Ratio. Fig. 2b shows the image of a carbon electrode obtained by casting a layer based on 70% high surface carbon – 10% conductive carbon – 20% pullulan-glycerol (1:1 wt) on nickel foam.

Pullulan was then processed from aqueous solutions as a non-woven mat to yield the bio-polymer separator used to assemble the green supercapacitor. Fig. 3a and b report the images of the electrospun pullulan membrane. It features interconnected defect-free fibers. The mat thickness was 55  $\mu$ m and the mean fiber diameter was around 0.3  $\mu$ m. Fig. 3c displays the tensile stress-strain curve of the pullulan electrospun fiber mat. The mat showed an elastic modulus  $E = 85 \pm 27$  MPa, stress at break  $\sigma_b = 3.4 \pm 0.4$  MPa and a strain at break  $\epsilon_b = 32 \pm 9\%$ . It is known that fiber arrangement in the mat usually changes in the course of a stress-strain analysis, fibers tend to align in the direction of the applied force before getting thinner and finally breaking [29]. The complex phenomena of fiber rearrangement that occurs during scaffold deformation might explain the high variability of mechanical data that is often found when analyzing electrospun mats.

Fig. 3d reports the Nyquist plots of symmetric cells with stainless steel blocking electrodes separated by the pullulan membrane

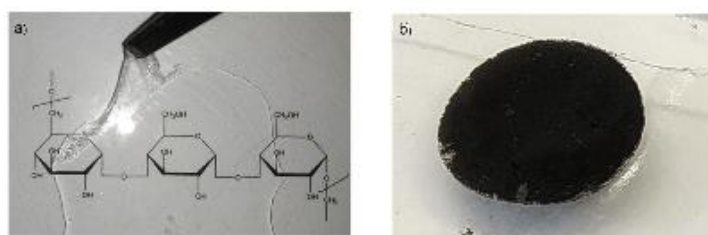


Fig. 2. a) Pullulan glycerol film obtained by drying at 60 °C a casted layer of 100 mg pullulan – 30 mg glycerol in ca. 15 g of water, and b) carbon electrode prepared by casting an aqueous ink with carbon powder, pullulan and glycerol on nickel foam.

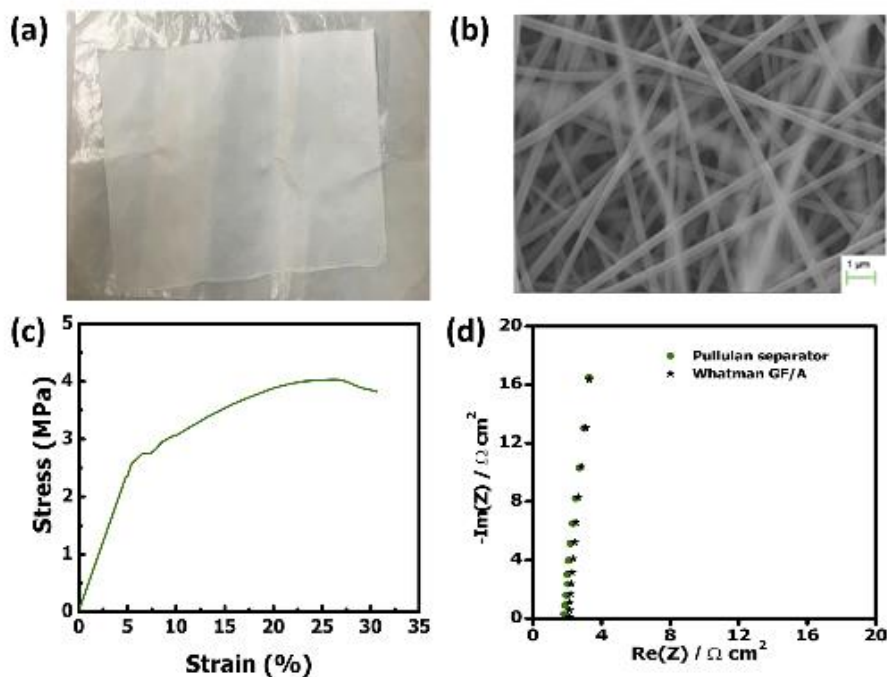


Fig. 3. a) Picture and b) SEM image of the electrospun pullulan separator, c) stress-strain curve of the pullulan electrospun mat from which the EDLC separator has been cut and (d) Nyquist plot of symmetric cells with stainless steel blocking electrodes separated by the pullulan membrane used in this work or a commercial membrane (Whatman GF/A, fiberglass) soaked in EMIMTFSI (frequency range from 150 kHz to 18 kHz).

(used in this work) or a commercial membrane (Whatman GF/A, fiberglass) soaked in EMIMTFSI. The intercept on the real axis of the Nyquist plot at the highest frequency (ca. 150 kHz) is representative of the ionic resistance through the membrane. For the pullulan membrane, the resistance was  $1.8 \Omega \text{ cm}^2$  and well compared with that of the commercial separator that featured  $2.1 \Omega \text{ cm}^2$ .

As it concerns the carbon electrode material, biomass-derived activated carbon prepared from a facile and environmentally safe technique with a mild activating agent, was used. Specifically, pepper seed waste was the carbon precursor, and potassium hydrogen carbonate served as the activating agent [8–12,16,25,27,30,31].

Table 1 summarizes the main porosity features of the pepper

seed-derived activated carbon (PP-AC) along with the Raman  $I_D/I_G$  ratio of the D-band and G-band intensities. The  $I_D/I_G$  ratio of 0.96 indicates a moderate degree of graphitization. PP-AC featured a BET surface area of  $1990 \text{ m}^2 \text{ g}^{-1}$  and a bi-modal pore size distribution centered at 0.8 nm and 2.5 nm (see Supplementary Information and Fig. S1). This pore size distribution fits with the requirement for use in IL-based supercapacitors [32,33].

Indeed, to avoid electrolyte starving effects that cause limitations in charge storage capability, carbon pores should be wider than the IL-ion size. For EMIMTFSI, the optimal size that enables the full exploitation of the carbon surface for the double-layer capacitance is ca. 0.8 nm [25,33–36]. The cumulative volume for pores larger than 0.4 nm is  $0.94 \text{ cm}^3 \text{ g}^{-1}$ .

**Table 1**  
 PP-AC carbon characteristics: BET surface area ( $S_{BET}$ ), DFT specific pore volume from pores with size > 0.4 nm ( $V_{>0.4 \text{ nm}}$ ) specific capacitance ( $C_{Carbon}$ ) from CVs at  $40 \text{ mV s}^{-1}$  in EMITFSA.  $I_D/I_G$  is the ratio of the Raman D-band and G-band intensities.

Carbon	Code	$S_{BET} \text{ m}^2 \text{ g}^{-1}$	$V_{>0.4 \text{ nm}} \text{ cm}^3 \text{ g}^{-1}$	$C_{Carbon} \text{ Fg}^{-1}$	$I_D/I_G$
Pepper-derived	PP-AC	1990	0.94	115	0.96

<sup>a</sup> From Ref. [25].

The pullulan-based PP-AC electrodes and the electrospun separator were used to assemble supercapacitor cells with EMITFSA as the electrolyte. The cells were electrochemically tested in both three- and two-electrodes setup. Fig. 4a reports the cyclic voltammograms of the single electrode carried out in a 3-electrode set up. The Figure demonstrates that the positive and the negative electrodes can be polarized within the potential range of +1.4 V and -1.4 V vs Ag without evidence of additional signatures eventually related to side reactions that can be ascribed to pullulan. The

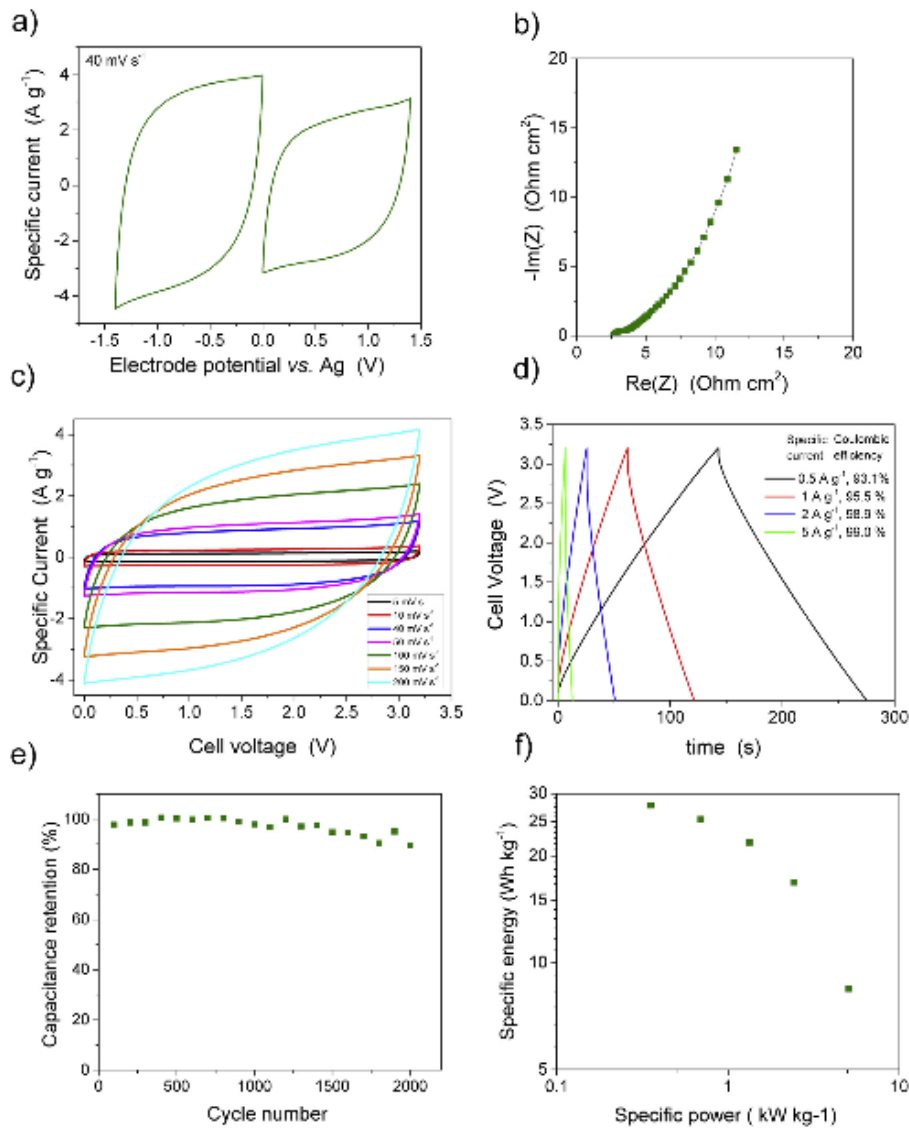


**Fig. 4.** a) Cyclic voltammograms of single PP-AC electrode at  $40 \text{ mV s}^{-1}$  carried out in a 3-electrode set up, and b) Nyquist plot (frequency range: 100 kHz to 10 mHz), c) cyclic voltammograms at different scan rates, d) cell voltage profiles under galvanostatic charge/discharge between 0 V and 3.2 V at different specific currents ( $I$ ) of the PP-AC based EDLC carried out in a 2-electrode setup and, e) trend of the percentage of the capacitance normalized to the higher value  $C_0/C_0\%$  at  $1 \text{ A g}^{-1}$ , and f) Ragone plot of PP-AC EDLC.

**Table 2**

Comparison of the specific energy and power at  $1 \text{ A g}^{-1}$  of PP-AC EDLC and of other EMITFSI-based EDLCs reported in literature [25,31,37,38] and assembled with conventional binders, separators and different carbons. The BET surface area of the carbons and electrode mass loadings are also reported.

Carbon source	BET Surface area [ $\text{m}^2/\text{g}$ ]	Binder and Separator <sup>a</sup>	E [Wh/kg]	P [kW/kg]	Mass loading $\text{mg}/\text{cm}^2$	Ref.
Bamboo char	1732	PVDF	40	1.4	1.0	[37]
Paper pulp sludge waste	2980	Polypropylene PVDF	44	0.72	2.5	[38]
Resorcinol-formaldehyde	600 <sup>b</sup>	Porous polymer PTFE	31 <sup>c</sup>	9.5 <sup>c</sup>	6–13	[31]
Pepper seed	2201	Fiber glass PVDF	26	1.1	7.5–8	[25]
Pepper seed	1990	Filter paper Pullulan	21.8	1.33	4–7.5	This work

<sup>a</sup> PVDF: polyvinylidene fluoride; PTFE: polytetrafluoroethylene.

<sup>b</sup> From pores larger than 1.5 nm.

<sup>c</sup> At  $0.2 \text{ A/g}$ .

specific capacitance averaged on the positive and negative domains and normalized only to the mass of the PP-AC carbon (excluding carbon black and binder) is  $115 \text{ F g}^{-1}$  (Table 1). This value well compares to that featured by electrodes produced with the same carbon, the same electrolyte but with a polyvinylidene fluoride (PVDF) binder (20%). These electrodes featured a specific capacitance of  $116 \text{ F g}^{-1}$  at  $1 \text{ A g}^{-1}$  [25].

Fig. 4a reports the 2-electrode voltammograms of the PP-AC based EDLCs (PP-AC-EDLC) at different scan rates up to a cell voltage as high as  $3.2 \text{ V}$ .

Notably, the voltammograms maintain a symmetric, box-like shape even at a high scan rate up to  $200 \text{ mV s}^{-1}$ . At this scan rate, the specific currents (evaluated considering the total composite mass loading of the two electrodes,  $m_{\text{EDLC}}$ ) approach a high value of  $\sim 4 \text{ A g}^{-1}$ . The analysis of the CVs at  $5 \text{ mV s}^{-1}$  provided a specific capacitance of the PP-AC-EDLC of  $27 \text{ F g}^{-1}$ . This value decreased by 33% at  $200 \text{ mV s}^{-1}$  (see Figure 4).

The cycling performance of the PP-AC-EDLC was evaluated by galvanostatic charge-discharge cycles at different specific currents. Fig. 4b reports the cell voltage as a function of the time at different specific currents and between  $0 \text{ V}$  and  $3.2 \text{ V}$ . The charge/discharge profiles are symmetric, triangular shaped with linear voltage vs. time profile. The coulombic efficiencies of the charge/discharge cycles of the EDLC, reported in Fig. 4b approach 100% at the highest currents of  $4\text{--}5 \text{ A g}^{-1}$ . These high specific currents can be achieved thanks to the low equivalent series resistance (ESR) of  $2.7 \Omega \text{ cm}^2$ . The ESR of the 2-electrode system was evaluated from the high frequency intercept of the Nyquist plot on the real axis (Fig. S4). The ESR was much lower than that featured by an EDLC assembled with the same EMITFSI electrolyte, nickel foam current collectors, and PP-AC carbon, but using PVDF binder, that was  $20 \Omega \text{ cm}^2$  [25].

The contribution to ESR of the electrical resistance of the electrode was evaluated by four-point probe resistivity measurements that provided a sheet resistance of the PP-AC composite of  $4.09 \pm 0.01 \text{ Ohm cm}$ .

Fig. 4c shows the trend of the capacitance of PP-AC-EDLC normalized by the value featured at in the first cycle under cycling at  $1 \text{ A g}^{-1}$ . Though preliminary, these results suggest that pullulan can also be effective in keeping a good cyclability of the EDLCs.

The discharge profiles reported in Fig. 4b were analysed to build the Ragone plot reported in Fig. 4d in terms of specific energy (E, in  $\text{Wh kg}^{-1}$ ) and power (P, in  $\text{kW kg}^{-1}$ ) which were calculated using Eqs. (1) and (2):

$$E = I \int V \frac{dt}{3600} \quad (1)$$

$$P = 3600 \frac{E}{\Delta t} \quad (2)$$

where  $I$  is the specific current (in  $\text{A g}^{-1}$ ) and  $\Delta t$  is the discharge time (in s). The specific current is normalized to the total amount of composite material of the two electrodes.

The Ragone plot shows that at the highest current ( $5 \text{ A g}^{-1}$ ) the PP-AC displayed  $5 \text{ kW kg}^{-1}$  specific power. The highest specific energy was delivered at the lowest current ( $0.25 \text{ A g}^{-1}$ ) and was  $27.8 \text{ Wh kg}^{-1}$ .

A comparative summary in Table 2 shows that the use of pullulan both as a binder and separator results in specific power and energy values that are of the same order of magnitude than those featured by lab-scale cells already reported in literature that share the same EMITFSI electrolyte, but that are assembled with conventional binders and separator [25,31,37,38].

#### 4. Conclusions

For the first time, we demonstrated that pullulan can be used to design major components (binder and separator) of green supercapacitors by sustainable, water-based manufacturing procedures (electrospinning). The electrode and membrane processes that we propose represent environmentally improved and safer routes that can substitute the conventional manufacturing of fluorinated polymers based on the use of the toxic solvent N-Methyl-pyrrolidone. Combining the binding properties of pullulan-glycerol blends with the adequate mechanical properties of the electrospun fibers of pullulan mats and the electrochemical performance of the PP-AC carbon electrodes brings about EDLCs featuring up to  $20 \text{ F g}^{-1}$ ,  $5 \text{ kW kg}^{-1}$  and  $27.8 \text{ Wh kg}^{-1}$  at  $3.2 \text{ V}$ . The IL is herein used not only for its good electrochemical properties in terms of stability and conductivity but also because of its hydrophobicity, which enables the development of a novel concept of an end-of-life management of the EDLC. Indeed, it can be easily separated from the water soluble, bio-degradable polymer, from the carbons and current collectors by simple immersion of the cell in water. Starting from this concept, further work will be carried out to optimize the recycling of the carbon and the ionic liquid.

Our study demonstrates that supercapacitors can be manufactured in compliance with the following green chemistry principles [39]:

- (i), (N\*1) Prevention: in PP-AC-EDLC, fluorinated polymers and toxic organic solvents (NMP and acetonitrile) are avoided
- (ii), (N\*6) Design for energy efficiency: PP-AC-EDLC electrodes are manufactured at ambient conditions by exploiting natural and bio-inspired components.

- (iii). (N°7) Use of renewable feedstocks. PP-AC-EDLC carbon is derived from agriculture waste.
- (iv). (N° 10) Design for degradation: in PP-AC-EDLC, electrode binder and separator are bio-degradable. Carbon, electrolyte and metal grids can be easily recovered by physical means.

Furthermore, our approach can be applied to develop new supercapacitors making use of advanced electrode materials and ionic liquids to further improve energy and power performance, by a green approach.

#### CRedit authorship contribution statement

**Federico Poli:** Data curation, Investigation, Writing - original draft, Writing - review & editing. **Damilola Momodu:** Data curation, Investigation, Writing - original draft, Writing - review & editing. **Giovanni Emanuele Spina:** Data curation, Investigation, Writing - original draft, Writing - review & editing. **Antonio Terella:** Investigation, Writing - original draft, Writing - review & editing. **Bridget. K. Mutuma:** Data curation, Investigation, Writing - original draft, Writing - review & editing. **Maria Letizia Focarete:** Investigation, Writing - original draft, Writing - review & editing. **Ncholu Manyala:** Funding acquisition. **Francesca Soavi:** Conceptualization, Funding acquisition.

#### Acknowledgments

The present research reports the results obtained under the Italy-South Africa joint Research Programme 2018–2020 (Italian Ministers of Foreign Affairs and of the Environment and NRF of South Africa, grant No. 113132), that target the integration of high-power energy storage systems for sustainable water and renewable sources management (<https://site.unibo.it/isarp/en>.) The projects target the design of sustainable electrode materials and electrolytes which are environmentally benign (green), relatively low cost, recyclable and easily degradable. Fondazione CARISBO (Progetto Bando Ricerca n 354) and “Piano Triennale di Realizzazione 2019–2021, Accordo di Programma Ministero dello Sviluppo Economico” – ENEA Projects are also acknowledged.

#### Appendix A. Supplementary data

Supplementary data to this article can be found online at <https://doi.org/10.1016/j.electacta.2020.135872>.


#### References

- [1] J.F. Peters, M. Baumann, B. Zimmermann, J. Braun, M. Weil, *Renew. Sustain. Energy Rev.* 67 (2017) 491–506.
- [2] A. González, E. Goikolea, J.A. Barrera, R. Mysyk, *Renew. Sustain. Energy Rev.* 58 (2016) 1189–1206.
- [3] Z. Lin, P.L. Taberna, P. Simon, *Curr. Opin. Electrochem.* 6 (2017) 115–119.
- [4] Z. Lin, E. Goikolea, A. Balducci, K. Naoi, P.L. Taberna, M. Salanne, G. Yushin, P. Simon, *Mater. Today* 21 (2018) 419–436.
- [5] D. Bresser, D. Buchholz, A. Moretti, A. Varzi, S. Passerini, *Energy Environ. Sci.* 11 (2018) 3096–3127.
- [6] B. Dyatkin, V. Presser, M. Heon, M.R. Lukatskaya, M. Beldaghi, Y. Gogotsi, *ChemSusChem* 6 (2013) 2269–2280.
- [7] C. Schütler, T. Husch, V. Viswanathan, S. Passerini, A. Balducci, M. Korth, *J. Power Sources* 326 (2016) 541–548.
- [8] A. Jain, C. Xu, S. Jayaraman, R. Balasubramanian, J.Y. Lee, M.P. Srinivasan, *Microporous Mesoporous Mater.* 218 (2015) 55–61.
- [9] M. Sevilla, A.B. Fuertes, *ChemSusChem* 9 (2016) 1880–1888.
- [10] W. Zhao, - L. Luo, - X. Wu, - T. Chen, - Z. Li, - Z. Zhang, - J. Rao, - M. Fan, *Wood Sci. Technol.* 53 (2019) 227–248.
- [11] K.S. Sulaiman, A. Mat, *Ionics* 22 (2016) 911–918.
- [12] S. Koutcheiko, V. Vorontsov, *J. Biobased Mater. Bioenergy* 7 (2013) 733–740.
- [13] F. Ochai-Ejeh, *Synthesis and characterization of activated carbon and manganese-based oxide/layered double hydroxide materials for supercapacitor application*, <https://repository.up.ac.za/handle/2263/53524>, 2016.
- [14] E. Raymundo-Piñero, M. Cadek, F. Béguin, *Adv. Funct. Mater.* 19 (2009) 1032–1039.
- [15] K. Fic, M. Meller, J. Menzel, E. Frackowiak, *Electrochim. Acta* 206 (2016) 496–503.
- [16] R. Thangavel, A.G. Kannan, R. Ponraj, V. Thangavel, D.W. Kim, Y.S. Lee, *J. Power Sources* 383 (2018) 102–109.
- [17] A. Bello, D.Y. Momodu, M.J. Madito, K. Makgopa, K.M. Rambau, J.K. Dangbegnon, N.M. Mutsyoka, N. Manyala, *Mater. Chem. Phys.* 209 (2018) 262–270.
- [18] Q. Abbas, P. Ratajczak, P. Babuchowska, A. le Comte, D. Bèlanger, T. Brousse, F. Béguin, *J. Electrochem. Soc.* 162 (2015) A5148–A5157.
- [19] L. Demarconay, E. Raymundo-Piñero, F. Béguin, *Electrochem. Commun.* 12 (2010) 1275–1278.
- [20] K.C. Cheng, A. Demirci, J.M. Catchmark, *Appl. Microbiol. Biotechnol.* 92 (2011) 29–44.
- [21] P.R. Vuddanda, M. Montenegro-Nicolini, J.O. Morales, S. Velaga, *Eur. J. Pharmacol.* 96 (2017) 290–298.
- [22] Q. Tong, Q. Xian, L.T. Lim, *Food Res. Int.* 41 (2008) 1007–1014.
- [23] S. Chen, S. He, H. Hou, *Curr. Org. Chem.* 17 (2013) 1402–1410.
- [24] T.P. Thuy Pham, C.W. Cho, Y.S. Yun, *Water Res.* 44 (2010) 352–372.
- [25] D. Momodu, N.F. Sylla, B. Mutuma, A. Bello, T. Masikhwa, S. Lindberg, A. Matic, N. Manyala, *J. Electroanal. Chem.* 838 (2019) 119–128.
- [26] C. Shi, L. Hu, K. Guo, H. Li, T. Zhai, Highly porous carbon with graphene nanoplatelet microstructure derived from biomass waste for high-performance supercapacitors in universal electrolyte, *Adv. Sustain. Syst.* 1 (1–2) (2017) 1600011–1600021.
- [27] B. Hu, L.-B. Kong, L. Kang, K. Yan, T. Zhang, K. Li, Y.-C. Luo, *RCS Adv.* 7 (2017) 14516–14528.
- [28] Mariachiara Lazzari, Catia Arbizzani, F. Soavi, M. Mastragostino, EDLCs based on solvent-free ionic liquids, in: E. by F B, E.F. Şackowiak (Eds.), *Supercapacitors*, 2013, p. 539.
- [29] J.-W. Lu, Z.-P. Zhang, X.-Z. Ren, Y.-Z. Chen, J. Yu, Z.-X. Guo, *Macromolecules* 41 (2008) 3762–3764.
- [30] M. Serebrych, M. Kosciński, M. Sliwinska Bartkowiak, T.J. Bandosz, *J. Power Sources* 220 (2012) 243–252.
- [31] M. Lazzari, F. Soavi, M. Mastragostino, *J. Power Sources* 178 (2008) 490–496.
- [32] J.C. Groen, L.A.A. Peffer, J. Pérez-Ramírez, *Microporous Mesoporous Mater.* 60 (2003) 1–17.
- [33] S. Kondrat, C.R. Pérez, V. Presser, Y. Gogotsi, A.A. Kornyshev, *Energy Environ. Sci.* 5 (2012) 6474–6479.
- [34] C. Largeot, C. Portet, J. Chmiola, P.L. Taberna, Y. Gogotsi, P. Simon, *J. Am. Chem. Soc.* 130 (2008) 2730–2731.
- [35] M. Lazzari, F. Soavi, M. Mastragostino, *Fuel Cell* 10 (2010) 840–847.
- [36] M. Lazzari, M. Mastragostino, A.G. Pandolfo, V. Ruiz, F. Soavi, *J. Electrochem. Soc.* 158 (1) (2011) A22–A25.
- [37] Y. Gong, D. Li, C. Luo, Q. Fu, C. Pan, *Green Chem.* 19 (2017) 4132–4140.
- [38] H. Wang, Z. Li, J.K. Tak, C.M.B. Holt, X. Tan, Z. Xu, B.S. Amirkhiz, D. Harfield, A. Anyia, T. Stephenson, D. Mitlin, *Carbon* 57 (2013) 317–328.
- [39] <https://www.acs.org/content/acs/en/greenchemistry/>.



Article

# Natural Polymers for Green Supercapacitors

Giovanni Emanuele Spina <sup>†</sup>, Federico Poli <sup>†</sup>, Alessandro Brilloni, Daniele Marchese and Francesca Soavi <sup>\*†</sup> 

Department of Chemistry “Giacomo Ciamician”, Alma Mater Studiorum Università di Bologna, Via Selmi 2, 40126 Bologna, Italy; giovanni.spina3@unibo.it (G.E.S.); federico.poli8@unibo.it (F.P.); alessandro.brilloni2@unibo.it (A.B.); daniele.marchese@studio.unibo.it (D.M.)

<sup>\*</sup> Correspondence: francesca.soavi@unibo.it

<sup>†</sup> These authors contributed equally.

Received: 11 May 2020; Accepted: 10 June 2020; Published: 16 June 2020



**Abstract:** Water-processable natural polymers represent a valuable alternative for the sustainable manufacturing of electrical double layer capacitors (EDLCs). Here, we demonstrate for the first time the feasibility of the use of pullulan to produce high mass loading electrodes ( $>10 \text{ mg cm}^{-2}$ ) at low binder content (10%) for ionic-liquid based EDLCs. Pullulan has also been processed as a porous separator by electrospinning. Its ionic resistance and thermal stability have been evaluated in different electrolytes and were found to be superior compared to those of a cellulose triacetate electrospun separator. Pullulan-ionic liquid EDLCs were, thus, assembled and charged up to 3.2 V. The EDLCs delivered specific energy and power of  $7.2 \text{ Wh kg}^{-1}$  and  $3.7 \text{ kW kg}^{-1}$  and featured good cycling stability over 5000 cycles.

**Keywords:** green supercapacitor; water processable polymer; pullulan; ionic liquid; electrospinning

## 1. Introduction

Today one of the biggest challenges our society is facing is how to replace the use of fossil energy sources (coal, oil, gas) with renewable ones (solar and wind). The inherent intermittence of the latter sources requires the development of efficient energy storage systems. Among all the possibilities, electrochemical energy storage by secondary batteries and electrical double layer capacitors (EDLCs) is one of the most efficient approach [1–4]. EDLCs are receiving great attention for their unique characteristics of outstanding power and cycle life, that are related to their electrostatic operating mechanism. However specific energies of EDLCs are one order of magnitude lower than that of batteries.

Commercial EDLCs feature activated carbon (AC) electrodes, a porous polymer separator, and an organic electrolyte, typically a solution of alkylammonium salts in acetonitrile or propylene carbonate. The use of the organic electrolyte enables cell voltages as high as 2.5 V [5].

The energy density of EDLCs can be improved by increasing: (i) the operating voltage window, (ii) electrodes specific capacitance, and (iii) the mass loading of the electrodes.

High operating voltage can be achieved by using an electrolyte with a wide electrochemical stability window, like ionic liquids (ILs) or highly concentrated aqueous electrolytes [6–9]. Electrode specific capacitance can be improved by tailoring carbon porosity to the electrolyte, in order to enhance ion access to the carbon surface. An alternative strategy is represented by the use of redox (pseudocapacitive) electrode materials, like metal oxides or electronically conductive polymers, in asymmetric or hybrid supercapacitors. Regarding the third approach, literature provides a very limited number of publications. Achieving mass loading higher than  $5\text{--}10 \text{ mg cm}^{-2}$  is considered a great challenge. Indeed, thick electrodes might delaminate from the current collector that is detrimental

for cycling stability. Furthermore, high mass loading may lead to worse ionic and electronic connection between the carbon particles, leading to higher internal resistance [10–12].

Ionic liquids, thanks to their low flammability, represent an even safer alternative to the more volatile acetonitrile solutions. In addition, ILs are known for their high thermal stability, good conductivity and wide electrochemical stability window ( $>3$  V). Despite these interesting properties, they cannot be considered as totally green and strategies to recover them after use are needed. The most investigated ILs for EDLCs are based on the bis(trifluoromethanesulfonyl)imide (TFSI) anion [13–15]. ILs feature bulky ions, therefore in order to promote a high and efficient exploitation of the electron carbon surface of the double layer, the porosity of the carbon has to be properly designed [16,17]. Furthermore, it has been demonstrated that the chemistry of ILs affects the double layer thickness and permittivity, and hence, the electrode capacitance. Indeed, in Ref. [1,2], the capacitive response of different carbon electrodes in *N*-butyl-*N*-methylpyrrolidinium bis(trifluoromethane-sulfonyl)imide (PYR<sub>14</sub>TFSI), 1-ethyl-3-methylimidazolium bis(trifluoromethanesulfonyl)imide (EmimTFSI) and PYR<sub>(20)</sub>TFSI was compared. In EmimTFSI, all the tested electrodes featured a specific capacitance that was double than that exhibited in the other ILs.

In EDLCs the biggest share of the cost is related to electrodes (28%) and electrolytes (27%). Electrodes are processed by casting slurries made of AC, conductive carbon, binder, and suitable solvents on metal current collectors. The binder material itself does not contribute significantly to the overall cost. However, its chemistry drives the selection of the solvent used for electrode processing, that has a great economic and environmental impact on EDLCs manufacturing [18]. Indeed, nowadays, commercial AC electrodes are mostly fabricated with F-based polymers as binders, such as poly(vinylidene difluoride) (PVDF) which needs *N*-methyl-2-pyrrolidone (NMP) as solvent/dispersant, both very toxic for humans and environment. This process requires expensive atmosphere-controlled environments [19].

In light of that and to meet the requirements of sustainable and cheaper production processes, much effort is being devoted to the substitution of F-based components with alternative ones. Transition to aqueous electrode preparation by non-toxic binders is expected to provide a great step forward towards an ideally sustainable and environmentally friendly technology for energy storage systems [20,21].

Carboxymethyl cellulose (CMC) represents the state of the art of water-soluble binders [10,21–24]. One of the first attempts of substituting F-based compounds with CMC, was reported by Bonnefoi et al. in 1999 [25]. Two of the major drawbacks in the use of CMC, are: (i) the relatively low achievable electrode mass loading, and (ii) the brittleness shown after the drying step. Winter et al. [23], first proposed Natural Cellulose (NC). While NC is cheaper (0.5–1.5 EUR kg<sup>-1</sup> vs. 1–2 EUR kg<sup>-1</sup>) and more abundant than CMC, it cannot be dissolved in water nor in almost all organic solvents while being soluble in certain ionic liquids [26–29]. Varzi et al. dissolved NC in 1-ethyl-3-methylimidazolium acetate (EmimAc) and demonstrated that NC has enhanced stability at high voltages. An EDLC assembled with electrodes featuring 10% NC binder and a mass loading of ca. 3 mg cm<sup>-2</sup> and PYR<sub>14</sub>TFSI ionic liquid electrolyte, exhibited a specific capacitance of ca. 13 F g<sup>-1</sup> at 10 mA cm<sup>-2</sup>, and a capacitance retention of 52%, after cycling for 750 h at 3.7 V [30]. Pursuing the research of even more eco-friendly binders, potato starch, a highly abundant polysaccharide that can be extracted from non-edible potatoes, was also proposed. By the use of this polysaccharide, the production of thick electrodes (240 μm, 9.3 mg cm<sup>-2</sup>) was demonstrated [18]. These electrodes were used to assemble a 2.5 V-EDLC with 1 M Et<sub>4</sub>NBF<sub>4</sub> in propylene carbonate (PC) electrolyte, that delivered 0.36 F cm<sup>-2</sup> at 10 mA cm<sup>-2</sup>.

Recently, we demonstrated the use of the biodegradable biopolymer pullulan (Pu) as a water processable separator and binder for EDLCs. Specifically, the separator was obtained by electrospinning and the EDLCs featured EmimTFSI electrolyte and pepper seed derived biochar carbon. The EDLC was able to operate at 3.2 V and delivered up to 5 kW kg<sup>-1</sup> specific power and 27.8 Wh kg<sup>-1</sup> specific energy. Its performances were compared with that of conventional electrical double-layer capacitor, with the added value of being eco-friendly and cheap.

Furthermore, the smart combination of the water-soluble, biodegradable Pu with the hydrophobic ionic liquid EmimTFSI, enabled a novel and easy approach for the recovery of EDLC components at the end-of-life. Indeed, the IL and carbon easily separate when immersed in water. The expensive IL can therefore be recollected for a second use [31].

Following these preliminary results, here we report the challenging study that aims to demonstrate the feasibility of the use of Pu to process electrodes at low binder content (10%) and high mass loading ( $>10 \text{ mg cm}^{-2}$ ). In the first part of our work we compare the electrochemical response and thermal stability of Pu and cellulose triacetate (CTA) in different electrolytes, namely EmimTFSI, 0.5 M LiTFSI TEGDME, PYR<sub>14</sub>TFSI. The two natural polymers have been processed by electrospinning and their contribution to ionic resistance of the electrolyte has been investigated by Electrochemical Impedance Spectroscopy (EIS) at different temperatures. On the basis of this investigation, Pu and EmimTFSI were selected to assemble two different EDLCs, one with low electrode mass loading and high binder content (HBLME) and a second one with high mass loading and low binder content (LBHME). The EDLCs have been tested by cyclic voltammetry, EIS and galvanostatic charge/discharge cycles. A deep analysis of the EDLCs performance is reported and discussed to demonstrate that natural polymers and, specifically Pu, may pave the way towards a new approach for a green manufacturing of EDLCs.

## 2. Materials and Methods

### 2.1. Materials

*N*-butyl-*N*-methylpyrrolidinium bis(trifluoromethanesulfonyl)imide (PYR<sub>14</sub>TFSI, purity >99.9%) was purchased from Solvionic (Toulouse, France). 1-Ethyl-3-methylimidazolium bis(trifluoromethanesulfonyl) imide (EmimTFSI, purity >99%) was purchased from Solvent Innovation (Köln, Germany). Lithium bis(trifluoromethanesulfonyl)imide and tetraethylene glycol dimethyl ether (TEGDME) (purity >99%) were both purchased from Sigma-Aldrich (St. Louis, MO, USA). Activated carbon PICACTIF was purchased from PICA (Basiano, Italy). Conductive carbon additive (SUPER C45) was purchased from TIMCAL (Bodio, Switzerland). Pullulan (P0978,  $\eta = 15.0 \div 180.0 \text{ mPa s}$ , 10% in H<sub>2</sub>O at 30 °C) was purchased from TCI Europe (Zwijndrecht, Belgium). Cellulose triacetate (CTA, Mw = 74,000 g/mol, DS 3.0) was purchased from Honeywell Fluka (Charlotte, NC, USA). Glycerol (purity >99%) was purchased from Sigma-Aldrich. Nickel foam was purchased from Alantum (Munich, Germany).

### 2.2. Preparation of the Electrospun Separator

Electrospinning was used to prepare the non-woven separator. In particular an home-made electrospinning apparatus has been used, this consisted of a high-voltage power supply (SI 50 P 10/CE/230, Spellman, West Sussex, UK), a syringe pump (200 series, KD Scientific, Holliston, MA, USA), a glass syringe containing the polymer solution and connected to a stainless-steel blunt-ended needle (inner diameter = 0.51 mm) through a polytetrafluoroethylene (PTFE) tube. The Pu membrane was electrospun starting from a 23% *w/v* solution of pullulan in Milli-Q water. The solution was spun at 18 kV at 20 cm from the collector with a flow rate of  $1 \text{ mL h}^{-1}$ . The cellulose triacetate (CTA) separator has been electrospun starting from a 6% *w/v*. solution in DCM/EtOH 80/20 solution. The solution was spun at 15 kV and at a 15 cm distance from the collector with a flowrate of 2 mL/h, at room temperature (RT) with a relative humidity of 40–50%. After electrospinning the mat has been soaked into a 0.1 M solution of sodium hydroxide in a mixture of Ethanol and water 4:1 *v/v* for 24 h. In the end the electrospun separator was washed in MilliQ water twice for fifteen minutes each.

### 2.3. Membrane Characterization

Electrospun membranes have been characterized at first by scanning electron microscopy (SEM) using an EVO 50 apparatus (Zeiss, Oberkochen, Germany). The feasibility of the use of the electrospun mats as separators was evaluated by EIS. Swagelok-type cells with two stainless steel blocking electrodes (0.9 cm diameter), separated by the membranes (dried overnight before use at RT) soaked in

the different investigated electrolytes, were used. The EIS spectra were collected by a VSP multichannel potentiostat/galvanostat/FRA (BioLogic, Seyssinet-Pariset, France) within 500 kHz–100 mHz frequency range and 5 mV AC perturbation, acquiring 10 points per decade. The cells were thermostated at 30, 40 and 60 °C by a thermostatic oven. The bulk conductivity of the electrolytes without membranes were measured by a CDM 210 Conductivity Meter (MeterLab, Milano, Italy) with an Amel standard cell (platinum electrodes). The temperature was controlled by a DC50 K40 thermocryostat (Haake, Thermo Fisher Scientific, Karlsruhe, Germany) with an accuracy of 0.1 °C. Samples were thermostated for 1 h before every measurement.

#### 2.4. Preparation of the Electrodes

Electrodes were prepared using the mesoporous carbon PICA TIF from PICA (BP10) as reported in [8] and described in Figure S1a. BP10 featured a Brunauer, Emmett and Teller (BET) specific surface >2000 m<sup>2</sup> g<sup>-1</sup> and a pores size distribution centered at 2.7 nm [8]. Two water processable formulations have been studied. A first one with 70% BP10, 10% Carbon black, 20% pullulan-glycerol (1:1 wt) and low mass loading (3.6–4.6 mg cm<sup>-2</sup>) is referred in the following text as high binder low mass electrode (HBLME). A second one with 85% BP10, 5% Carbon black, 10% pullulan-glycerol and higher mass loading is labelled as low binder high mass electrode (LBHME). Electrodes have been obtained by casting on pre-cut nickel foams (diameter 0.9 cm) a slurry containing 23.5 mg of BP10, 3.5 mg of carbon black (as conducting additive), 6.7 mg of pullulan (P0978, TCI) and glycerol in 0.8 g of MilliQ water for HBLME. For LBHME the ink was composed of 40.2 mg of BP10, 2.3 mg of carbon black (as conducting additive), 4.7 mg of pullulan and glycerol in 0.57 g of MilliQ water. The electrodes were then dried in an oven (under vacuum) overnight at room temperature (Büchi glass oven B-585). The composite electrode loadings (excluding the nickel foam mass) are reported in Table 1.

**Table 1.** Composition and mass loading of High Binder Low Mass Electrode (HBLME) and Low Binder High Mass Electrode (LBHME).

Name	Composition	Mass Loading Range *
HBLME	70% BP10/10% CB/20% binder	3.6–4.6 mg cm <sup>-2</sup>
LBHME	85% BP10/5% CB/10% binder	6.3–7.5 mg cm <sup>-2</sup>

\* single electrodes mass loading.

#### 2.5. Supercapacitor Assembly

A T Swagelok-type cell assembly (BOLA Cell made from Teflon, BOLA GmbH, Grünsfeld, Germany) with a silver quasi-reference electrode disk and stainless-steel current collectors was used. Cells were assembled in a dry box (Labmaster 130, H<sub>2</sub>O, and O<sub>2</sub> <0.1 ppm MBraun, Garching, Germany). The separator (12 mm diameter) and the electrodes (9 mm diameter) were soaked under vacuum together with the IL before the assembly. The ratio of the positive to negative electrode composite loading was >1 to achieve cell voltages higher than 3 V [32]. EDLCs were assembled with two carbon based composite electrodes alienated by a circular sheet of electrospun pullulan separator, with 1-ethyl-3-methylimidazolium bis(trifluoro-methylsulfonyl) imide IL (EmimTFSI) as the electrolyte, as described in Figure S1b.

#### 2.6. Supercapacitor Characterization

The electrochemical tests consisted in EIS, cyclic voltammetry (CV) and galvanostatic (GCPL) tests and were performed in a thermostatic oven at 30 °C using a BioLogic VSP multichannel potentiostat/galvanostat/FRA. EIS was performed with a 100 kHz–100 mHz frequency range and 5 mV AC perturbation, acquiring 10 points per decade. To evaluate the impedance of each of the EDLC electrodes, three electrode measurements, have been done. A silver disk has been used as pseudo reference. Here, the working electrode was the tested one and counter the other. To evaluate the

complete cell impedance, two electrode measurement have been done. For two electrode measurements, the silver disk was disconnected, the EDLC positive electrode was the working, and the EDLC negative electrode was connected to the counter and reference instrument plugs.

CV discharge curves were analyzed to get a first evaluation of the EDLC specific capacitance ( $C_{EDLC}$ ). Specifically,  $C_{EDLC}$  was calculated from the slope of the voltammetric plots of the discharge capacity vs. cell voltage. The capacity was calculated by the integral of the CV current over time. The slope values were divided by the total composite mass of the two electrodes ( $m_{tot}$ ).

The GCPL curves were analyzed to quantify the equivalent series resistance (ESR) and the  $C_{EDLC}$ , the specific energy and power of the devices at different discharge currents. ESR was calculated according to Equation (1), where  $\Delta V_{ohmic}$  is the ohmic voltage drop at the beginning of discharge, and  $i$  is the current density ( $A\ cm^{-2}$ ):

$$ESR = \Delta V_{ohmic} / (2 \times i) \quad (1)$$

$C_{EDLC}$  was calculated from the reciprocal of the slope of the GCPL voltage profile during the discharge ( $dt/dV$ ) by Equation (2):

$$C_{EDLC} = i \times dt/dV / m_{tot} \quad (2)$$

The single electrode specific capacitance ( $C_{electrode}$ ) was therefore calculated from the EDLC's one by Equation (3)

$$C_{electrode} = 4 \times C_{EDLC} \quad (3)$$

The EDLCs specific energy (E) and power (P) were calculated from the GCPL discharge curves through Equations (4) and (5):

$$E = i \int V \times dt / (3600 \times m_{tot}) \quad (4)$$

$$P = 3600 \times E / \Delta t \quad (5)$$

where  $\Delta t$  is the discharge time in seconds.

### 3. Results

#### 3.1. Electrospun Separator and Electrolyte Selection

Figure 1a,b report the SEM images of the electrospun Pu and CTA membranes, respectively. They feature interconnected fibers, randomly deposited, with a low number of defects. The Pu mat thickness was 55  $\mu m$  and the mean fiber diameter was around 0.3  $\mu m$ . The CTA mat thickness was 22  $\mu m$  and the mean fiber diameter was around 0.6  $\mu m$ . The fiber thickness of the two mats is in line with the value already reported for electrospun separators obtained with different polymers [33]. Furthermore, the PU and CTA mat thicknesses were adequate for an easy handling and assembly of the EDLCs. In addition to the difference in fiber diameter, the two polymers differ in terms of fiber diameter distribution, the CTA fibers being less homogeneous with a broader distribution.

Before the evaluation of the ionic conductivity response of the membranes, at first bulk conductivity of the electrolytes was measured. The values at different temperatures are reported in Table 2. The ionic conductivity of all the tested electrolytes grows with temperature. Among the considered electrolytes, the most conductive one is the EmimTFSI. Specifically, at 30 °C EmimTFSI features 12.6  $mS\ cm^{-1}$ , which is 5-fold higher than the conductivity of 0.5 m LiTFSI in TEGDME (2.05  $mS\ cm^{-1}$ ) and PYR<sub>14</sub>TFSI (3.01  $mS\ cm^{-1}$ ).

The separators of the EDLCs should be designed in order to achieve low ESR. This can be obtained by minimizing their hindrance to the ion flow during the charge/discharge, while guaranteeing the electronic separation of the two electrodes.

In order to evaluate the contribution of the investigated separators and electrolytes to ESR, EIS measurements were performed. The tests were carried out using cells with stainless steel blocking electrodes separated by the separator soaked with the electrolyte. EIS was carried out at constant

interval of time (24 h) and at different temperature (30 °C, 40 °C and 60 °C) to check the chemical and electrochemical stability of the different membranes in the tested electrolytes.

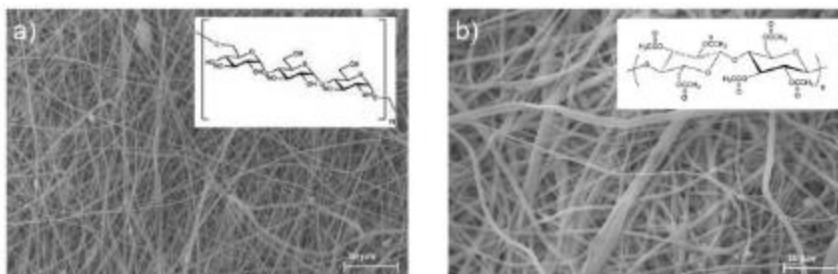


Figure 1. SEM images of electrospun membrane of (a) pullulan and (b) cellulose triacetate with their molecular structures.

Table 2. Ionic conductivity of the tested electrolytes at different temperatures.

Conductivity ( $\text{mS cm}^{-1}$ )	$\sigma$ (30°)	$\sigma$ (40°)	$\sigma$ (60°)
EmimTFSI	12.60	15.10	25.70
0.5 m LiTFSI in TEGDME	2.05	2.63	4.82
PYR <sub>14</sub> TFSI	3.01	3.90	6.30

As an example, Figure 2 reports the Nyquist plots of the electrospun pullulan separator in EmimTFSI over time at the different tested temperatures. The Nyquist plots for all the combination of Pu and CTA membranes with the different electrolytes are reported in Figure S2.

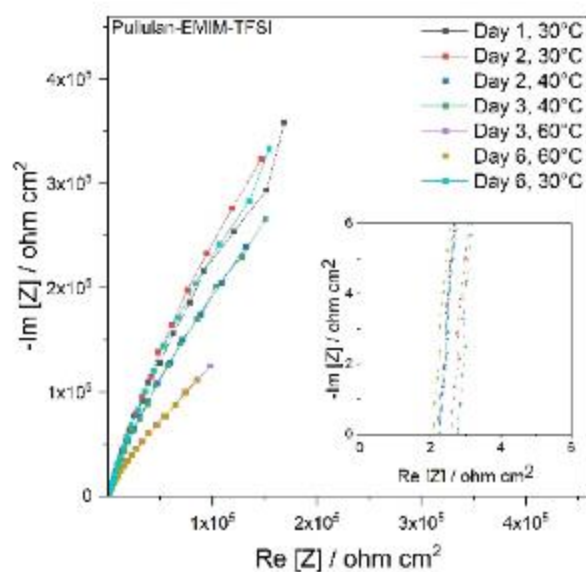


Figure 2. Nyquist plot of Pullulan electrospun membrane in EmimTFSI electrolyte.

In Figure 2, the impedance spectra of the Pullulan membrane resemble a straight line. This response can be modelled with a resistance (R) in series with a constant phase element (Q), therefore the resulting impedance is given by the following equation:

$$Z = R - 1/(j \omega Q)^n \quad (6)$$

In Equation (6), R is the equivalent resistance of the separator soaked in the electrolyte and can be evaluated from the intercept with the real axis in the 150–300 kHz frequencies region. It includes the electronic resistance of the current collectors and the ionic resistance of the cell which reasonably dominates the response. When  $n = 1$ , the plot is a line parallel to the imaginary axis and Q represents the capacitive response of the cell. When  $n = 0.5$ , the plot is a line with a slope of  $45^\circ$  and Q corresponds to the Warburg element that is representative of diffusion-controlled processes.

Figure 2 shows that the temperature increase leads to the decrease of the resistance of the cell that is related to the increase of the electrolyte conductivity (cf. Table 2). In parallel, it is noticeable that the slope of the Nyquist plot decreases, unveiling that ion diffusion through the membrane becomes more sluggish.

This behaviour could be explained with the swelling of the membrane at the highest temperature that, in turn, brings about thickening of the fibres and narrowing of the inter-fibre voids. This might result in a more tortuous path for ion conduction.

Tables S1 and S2 and Figure 3a,b report the values of resistance of Pu and CTA membrane respectively, at different temperatures over time, in the different electrolytes. The values are in the same order of magnitude and span between ca. 2 and 5 ohm  $\text{cm}^2$ . The first day at 30 °C, Pu features 2, 3 and 3.5 Ohm  $\text{cm}^2$  when soaked with EmimTFSI, 0.5 m LiTFSI TEGDME and PYR<sub>14</sub>TFSI, respectively. CTA exhibits 2, 3 and 3.5 Ohm  $\text{cm}^2$  with EmimTFSI, 0.5 m LiTFSI TEGDME and PYR<sub>14</sub>TFSI. Therefore, resistance values are similar for both membranes in the same electrolytes, with EmimTFSI accounting for the smallest values. A more straightforward comparison must consider the mat thickness of both separators and can be carried out referring to the effective resistivity ( $\rho_{\text{eff}}$ ) of the membrane-electrolyte system. The value of  $\rho_{\text{eff}}$  can be obtained by Equation (7):

$$\rho_{\text{eff}} = S \times R/L \quad (7)$$

where R is the resistance (in Ohm), L is the membrane thickness (cm), and S is the current collector area ( $\text{cm}^2$ ).

As commented above, Pu separator features a thickness of 55  $\mu\text{m}$  that is almost 2.5 times larger than the CTA's that is 22  $\mu\text{m}$ . Therefore,  $\rho_{\text{eff}}$  of Pu at 30 °C in EmimTFSI results 450 Ohm cm and is almost half than CTA's (over 1000 Ohm cm). This can be related to the thinner fibres of the former membrane (0.3  $\mu\text{m}$ ) vs. the latter (0.6  $\mu\text{m}$ ). Thinner fibres provide a greater surface area and a greater density of free volume that can be exploited by ions to achieve higher conductivity. Noticeably, the resistance values of Pu at the different temperatures keep almost constant during time. At the contrary, those of CTA membrane gradually increase achieving 5 Ohm  $\text{cm}^2$  at 60 °C, after 5 days, a value that doubles the Pu ones. Furthermore, after six day, the temperature was lowered to 30 °C. The resistance of Pu-EmimTFSI went back to its initial value while the CTA-EmimTFSI ones doubled (4 Ohm  $\text{cm}^2$ ). This indicates that the swelling process promoted by the increase of temperature is reversible for Pu but not for CTA. Overall, the data of Figure 2 suggest that Pu membrane is more stable than CTA.

In order to get further insight into the contribution of the separator to the ESR, the Mac Mullin number ( $N_M$ ) has been calculated for all the tested systems. Indeed,  $N_M$  quantifies the increase of resistivity of the separator soaked in the electrolyte ( $\rho_{\text{eff}}$ ) with respect to the bulk resistivity of the electrolyte solution ( $\rho_0$ ), and it is calculated after Equation (8):

$$N_M = \rho_{\text{eff}}/\rho_0 \quad (8)$$

where  $\rho_{\text{eff}}$  has been evaluated by Equation (6) using the resistance values listed in Tables S3 and S4. In turn,  $\rho_0$  is the reciprocal of the electrolyte conductivity ( $\sigma_0$ ) and is calculated by Equation (9):

$$\rho_0 = 1/\sigma_0 \quad (9)$$

The  $N_M$  values for the different separator/electrolyte combinations at the different temperatures are reported in Tables S5 and S6 and in Figure 3c,d as comparative histograms.

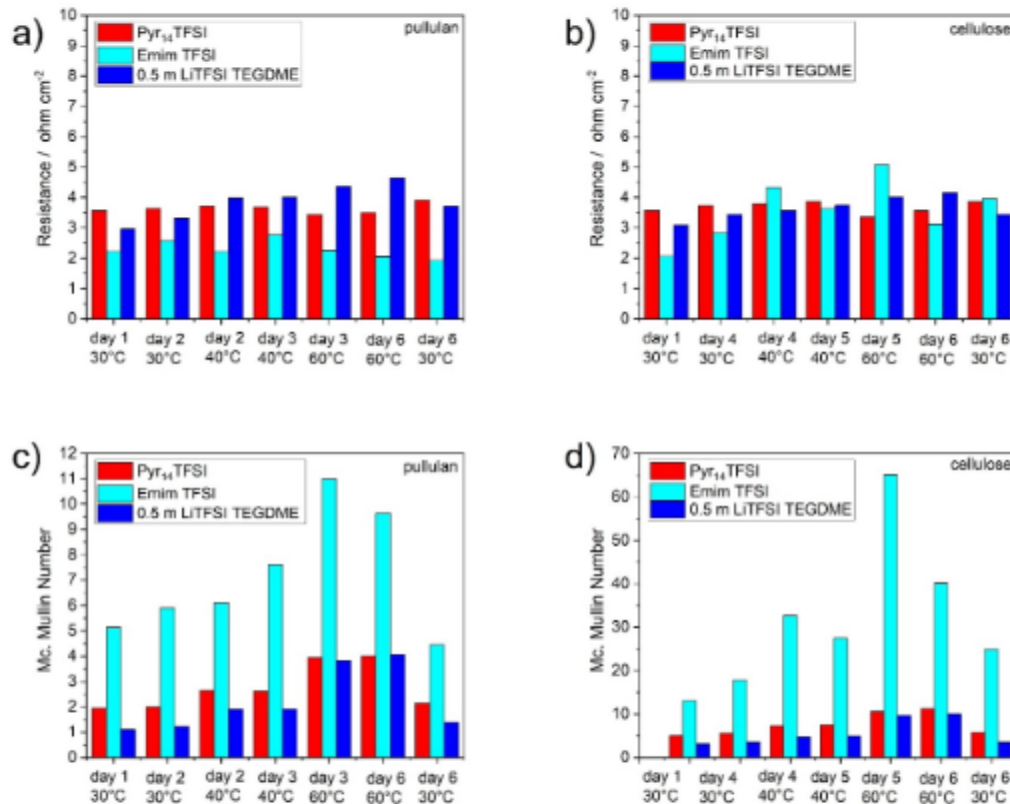


**Figure 3.** Resistance normalized by the plain area and MacMullin number of (a,c) Pullulan and (b,d) Cellulose triacetate electrospun separators in different tested electrolytes.

The values of the Pu are always smaller than those of the CTA in all the tested condition. For both membranes, in all the tested conditions, EmimTFSI holds the greater values of  $N_M$ , while the smaller ones are exhibited by 0.5 m LiTFSI in TEGDME. The first day at 30 °C, Pu features  $N_M$  of 5, 1 and 2 when soaked with EmimTFSI, 0.5 m LiTFSI TEGDME and Pyr<sub>14</sub>TFSI, respectively. For CTA,  $N_M$  is 13, 3 and 5 with EmimTFSI, 0.5 m LiTFSI and PYR<sub>14</sub>TFSI. These trends indicate that EmimTFSI is the electrolyte that has a conductivity that is more affected by the presence of the membranes. In turn, this can be explained taking into account the protic behaviour of EmimTFSI. Indeed, unlike the other electrolytes, EmimTFSI features an acidic proton in alpha position in the imidazolium ring, that contributes to its bulk ionic conductivity. When EmimTFSI is in contact with the membranes this proton drives specific acid-base interactions that decrease its activity. Specifically, it can be claimed that hydrogen bond with the carboxyl functionalities of the membranes are formed (Figure 1).

For both separators soaked with EmimTFSI,  $N_M$  increases with temperature. In case of Pu, it reaches a maximum of 11 on the day 3 at 60 °C. For CTA  $N_M$  is 65 during the day 5 at the same



temperature. Once cooled at 30 °C (day 6), Pu-EmimTFSI's  $N_M$  reversibly reduces to 4 that is even smaller than its initial value, in agreement with the resistance trend (Figure 3a). At the contrary CTA-EmimTFSI's  $N_M$  does not recover its initial value and doubles (25).

To conclude this section, EmimTFSI-Pu featured a resistance considerably smaller than the one obtained with the other electrolytes. Pu exhibited a lower McMullin number than CTA along with a better thermal behaviour. Therefore, the pullulan based electrospun membrane and EmimTFSI were selected to assemble and test EDLCs as described in the next section below.

### 3.2. Supercapacitor Testing

The EDLCs featured the commercial high surface area carbon BP10 and the conductive additive Super C45. We already demonstrated the good binding properties of the pullulan: glycerol mixtures, that was therefore selected for the aqueous processing of the carbon composite electrodes [31].

The following sections report the electrochemical characterization of EDLCs assembled with 20% binder and low composite electrode mass loading (3.6–4.6 mg cm<sup>-2</sup>), referred as high binder low mass electrode (HBLME, Section 3.2.1), and with 10% binder and higher mass loading, labelled as low binder high mass electrode (LBHME, Section 3.2.2). The first composition was meant to verify the feasibility of the use of Pu binder and Pu membrane in the tested electrolyte while the second is meant to reach a formulation closer to that exploited commercial EDLCs. Section 3.2.3 compares the performances of HBLME and LBHME based EDLCs.

The electrochemical tests at first included EIS measurements of both the individual electrodes and of the full cell. These tests enable the evaluation of the EDLCs ESR that accounts for the contributions of (i) the contact resistance between composite material and current collector and (ii) the ionic resistance of the separator/electrolyte. Two electrodes cyclic voltammetry (CV) experiments have been carried out between 0 V and 3.2 V to evaluate the electrochemical stability and the capacitance of the EDLC as function of the scan rate. Galvanostatic (GCPL) charge/discharge measurements between 0 and 3.2 V (GLV) at different specific currents were subsequently performed to evaluate the specific energy and power. Finally, GCPL cycling has carried out at 1 A g<sup>-1</sup> in order to evaluate the stability of the proposed EDLCs.

#### 3.2.1. High Binder Low Mass Loading Electrodes (HBLME)

In this section, the results of the electrochemical characterization of the HBLME-EDLCs are reported. Figure 4a shows the Nyquist plots of the HBLME-EDLC single electrodes and the full cell. The three Nyquist plots share all the same shape. They can be divided into three components: (i) a high frequencies semicircle, (ii) a middle frequencies line with a slope of ca. 45°, and (iii) a low frequency line that approaches a slope of 90°. The intercepts at the highest frequencies of the semicircles represents the ohmic resistances (electronic and ionic) of the electrodes and electrolyte-separator system. Values of 1.4, 1.5 and 3.3 Ohm cm<sup>2</sup> have been measured, respectively for the negative, the positive electrode and the full cell. The small semicircle has been attributed to (i) the ion transport at the electrolyte-carbon interface and (ii) the contact between the electrode and the current collector [34]. For the full cell the semicircle diameter is 0.3 Ohm cm<sup>2</sup>. The middle frequency line with 45° slope is representative of diffusion limited phenomenon. Specifically, it refers to diffusion of ions required to charge inner pores of the carbon electrodes. The low frequency line represents the capacitive behavior of the electrodes and the EDLC. For an ideal EDLC, a vertical line is expected. In Figure 4a the lines deviate from this ideal behavior because of the presence of different class of pores [35]. The real axis intercept of the linear fit of the cell low frequency line gives the ESR that was quantified in 6.4 ohm cm<sup>2</sup>.

Figure 4b reports the CVs of the full HBLME-EDLC cell at different scan rate, between 0 and 3.2 V. The voltammogram are symmetric and box shaped, which indicates the absence of faradic secondary process and an electrical double layer driven process. The maximum current of 3 A g<sup>-1</sup> (25 mA cm<sup>-2</sup>) is reached with a scan rate of 200 mV s<sup>-1</sup>, this value is comparable with the ILs based EDLC already reported in literature [8]. Figure 4c reports the trend of  $C_{EDLC}$  versus the scan rate. The highest specific

capacitance of HBLME-EDLC is  $18 \text{ F g}^{-1}$  at  $5 \text{ mV s}^{-1}$  and decreases to  $14 \text{ F g}^{-1}$  at  $200 \text{ mV s}^{-1}$ . This trend has been widely discussed in literature and is attributed to the ionic diffusion limitation upon the double layer formation in the smallest pores at fast scan rates [36]. Indeed, micropores with an internal area less exposed to the electrolytes need more time for the creation of the electrical double layer than bigger pores. At low scan rate, the polarization is slow and ions have enough time to access the internal area of micro-pores. Increasing the scan rate, only the external surface of the pores becomes easily accessible. This process also explains the  $45^\circ$  Warburg line of the Nyquist plot of Figure 4a.

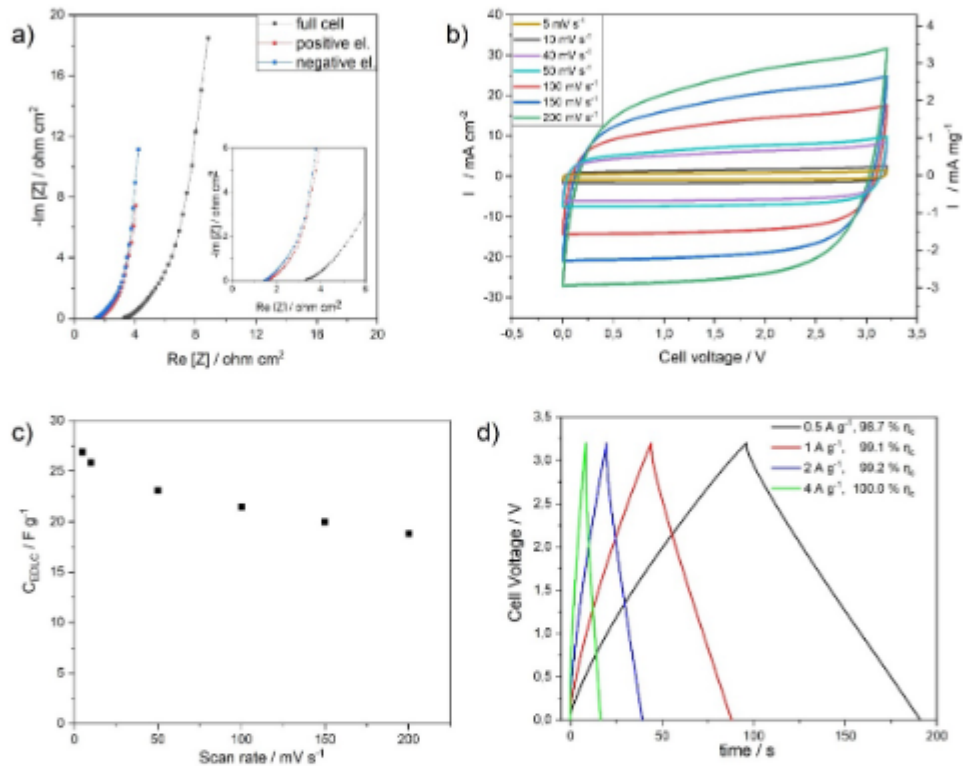


**Figure 4.** Electrochemical characterization of HBLME-EDLC (a) Nyquist plots of the (black) full cell, (red) positive and (blue) negative electrodes (500 kHz and 100 mHz), (b) 2-electrode CVs at different scan rate from  $5 \text{ mV s}^{-1}$  to  $200 \text{ mV s}^{-1}$ , between 0 V and 3.2 V, (c) Capacitance of the EDLC evaluated by CV reported as function of the scan rate; and (d) selected galvanostatic charge/discharge cycles between 0 V and 3.2 V at different current densities from  $0.5 \text{ A g}^{-1}$  to  $4 \text{ A g}^{-1}$ .

Figure 4d reports selected voltage profiles of the HBLME-EDLC under galvanostatic charge/discharge cycles at different current density, between 0 and 3.2 V. The voltage profile of the cell has a symmetric, triangular shape which is characteristic of electrical double layer driven process. Increasing the current from  $0.5$  to  $4 \text{ A g}^{-1}$  leads, as expected, to the decrease of the charge/discharge time. Coulombic efficiency ( $\eta_c$ ), i.e., the ratio between the charge released during discharge and the charge stored during charge, is reported as inset in Figure 3d. This quantity is always greater than 98% and reaches the highest value of 100% at  $4 \text{ A g}^{-1}$ . The GCPL ohmic drops were analyzed to quantify ESR of the device and resulted in  $5.9 \text{ Ohm cm}^2$ , that well compares with the value obtained by EIS. EDLC. Specific capacitance  $C_{\text{EDLC}}$  has been calculated from the slope of the GCPL discharge profile and for HBLME-EDLC resulted in  $15.9$ ,  $15.4$ ,  $14.6$  and  $13.7 \text{ F g}^{-1}$  at  $0.5$ ,  $1$ ,  $2$  and  $4 \text{ A g}^{-1}$ , respectively. The corresponding single electrode specific capacitances ( $C_{\text{electrode}}$ ) are  $63$ ,  $61$ ,  $58$  and  $54.8 \text{ F g}^{-1}$ . These values well compare with those of electrodes featuring the same electrolyte and carbon but employing

a fluorinated binder [8]. Table 3 reports the ESR and  $C_{EDLC}$  at  $0.5 \text{ A g}^{-1}$  of the HBLME-EDLC along with the EDLC areal capacitance.

**Table 3.** Gravimetric and surface quantities of HBLME-EDLC and LBHME-EDLC.

Electrode Label	HBLME-EDLC	LBHME-EDLC
Mass loading ( $\text{mg cm}^{-2}$ )	9.3	13.8
ESR (ohm)	5.9	7.9
Capacitance* ( $\text{F g}^{-1}$ )	15.9	6.2
Areal capacitance ( $\text{mF cm}^{-2}$ )	148.0	85.5
Specific energy** ( $\text{Wh kg}^{-1}$ )	19.6	7.2
Specific power*** ( $\text{kW kg}^{-1}$ )	4.6	3.7
Areal energy density ( $\mu\text{Wh cm}^{-2}$ )	182.3	99.4
Areal power density ( $\text{mW cm}^{-2}$ )	42.8	51.1

\* Capacitance has been calculated from the CV at  $50 \text{ mV s}^{-1}$ , \*\* Specific energy has been calculated from GCPL at minimum current ( $0.5 \text{ A g}^{-1}$ ), \*\*\* Specific power has been calculated at maximum current (4 and  $5 \text{ A g}^{-1}$ ).

### 3.2.2. Lower Binder High Mass Loading Electrodes (LBHME)

In this section, the results of the electrochemical characterization of the LBHME-EDLCs are reported. Figure 5a shows the Nyquist plots of the LBHME-EDLC single electrodes and full cell.

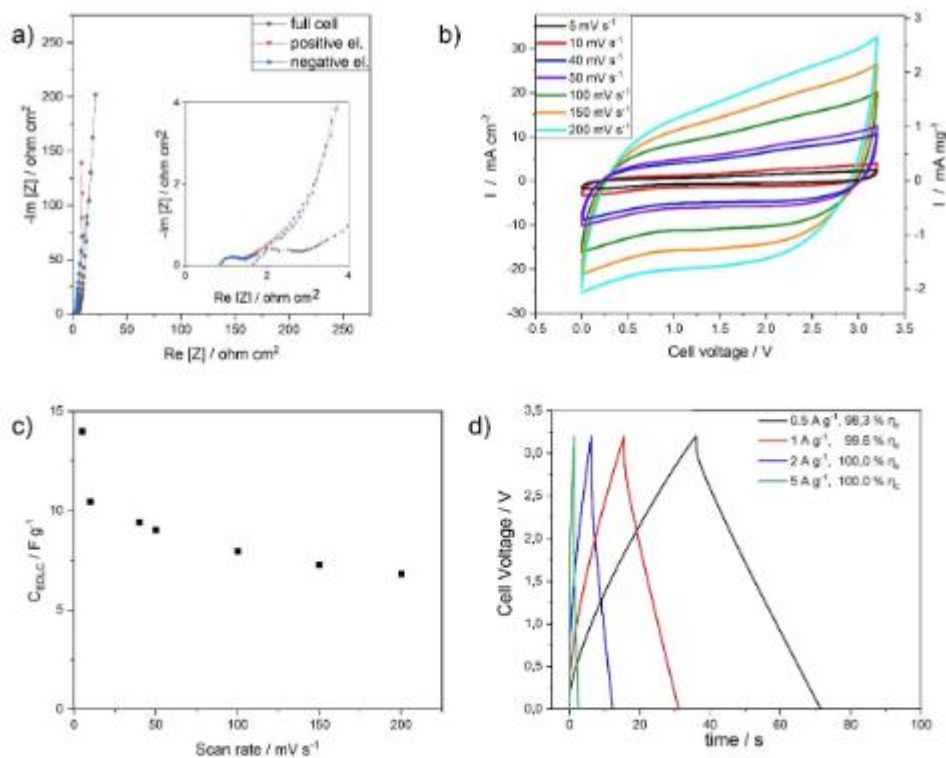


**Figure 5.** Electrochemical characterization of LBHME-EDLC (a) Nyquist plots of the (black) full cell, (red) positive and (blue) negative electrodes ( $500 \text{ kHz}$  and  $100 \text{ mHz}$ ), (b) 2-electrode CVs at different scan rate from  $5 \text{ mV s}^{-1}$  to  $200 \text{ mV s}^{-1}$ , between  $0 \text{ V}$  and  $3.2 \text{ V}$ , (c) Capacitance of the EDLC evaluated by CV reported as function of the scan rate; and (d) selected galvanostatic charge/discharge cycles between  $0 \text{ V}$  and  $3.2 \text{ V}$  at different current densities from  $0.5 \text{ A g}^{-1}$  to  $5 \text{ A g}^{-1}$ .

Like for HBLME, the three Nyquist plots share all the same shape. For the physical interpretation of the Nyquist plots, the considerations that have been drawn in the previous section are still valid. The high frequency intercepts with the real axis of the semicircles are 0.8, 0.9 and 1.7  $\text{Ohm cm}^2$  for the positive and negative electrodes and full cell, respectively. Noticeably these values are halved with respect to those of the HBLME electrodes and EDLC (cf. Figure 4a). In LBHME formulation, the quantity of binder and conductive carbon are halved compared to the HBLME one. Therefore, the decrease of the high frequency impedance achieved by LBHME can be explained with the decrease of the insulating component of the electrode, i.e., the binder. Comparing the high frequency semicircles in Figures 4a and 5a, it is possible to notice that the LBHME's is wider than HBLME's. Indeed, the LBHME-EDLC semicircle diameter is 1.3  $\text{Ohm cm}^2$  while the HBLME's is 0.3  $\text{Ohm cm}^2$ . This difference is due to the high mass loading of LBHME with respect to HBLME (1.5-fold), that brings about a worse ionic and electronic connection between the carbon particles [10]. The LBHME-EDLC middle frequency line ( $45^\circ$  slope) span across the same range of resistance with respect to the HBLME-EDLC. The ESR of the LBHME-EDLC was evaluated from the real axis intercept of the low frequency line and resulted in 7.6  $\text{Ohm cm}^2$ .

Figure 5b reports the CVs of the full LBHME-EDLC cell at different scan rate, between 0 and 3.2 V. From these measurements, voltammetric specific capacitance values have been calculated and are reported as function of the scan rate in Figure 5c. The highest specific capacitance is 14  $\text{F g}^{-1}$  at 5  $\text{mV s}^{-1}$  and decreases to 7  $\text{F g}^{-1}$  at 200  $\text{mV s}^{-1}$ . Therefore, from 5  $\text{mV s}^{-1}$  to 200  $\text{mV s}^{-1}$  there is a 50% specific capacitance reduction, that is higher than what observed for HBLME-EDLC (22%). This can be related to a not optimized electronic and ionic connection of the electrodes carbon particles that has been highlighted by the Nyquist plot analysis reported above (Figure 5a).

The LBHME-EDLC galvanostatic charge/discharge profiles at different current are reported in Figure 5d. The coulombic efficiency was 98.3%, 99.6%, 100%, 100% at 0.5, 1, 2, 5  $\text{A g}^{-1}$ , respectively. These values are slightly higher than those that have been observed for the HBLME. The ESR was 7.9  $\text{Ohm cm}^2$  in agreement with the EIS value. The  $C_{\text{EDLC}}$  was 6.2, 5.8, 5.3 and 4.2  $\text{F g}^{-1}$  at 0.5, 1, 2 and 5  $\text{A g}^{-1}$ . These values are lower than those featured by HBLME-EDLC and this can be explained with the not optimized ionic and electronic connection highlighted by Table 3 that reports the ESR and  $C_{\text{EDLC}}$  at 0.5  $\text{A g}^{-1}$  of LBHME-EDLC. The EDLC areal capacitance is also reported in the Table 3.

### 3.2.3. Cycling Stability, Energy and Power of HBLME- and LBHME-EDLCs

Figure 6a reports the trends of the specific capacitance of the two EDLCs over cycling at 1  $\text{A g}^{-1}$ . The values are normalized by the value of the specific capacitance of the first cycle. Both devices show a good stability with capacitance retention of 90% at the 2000th cycle. This result demonstrates the feasibility of the use of pullulan as alternative separator and binder for green supercapacitors.

Note that the cycling stability of LBHME-EDLC at low binder content was further evaluated even over 5000 cycles (Figure S3). The test indicated that also over prolonged cycling, a capacitance retention of 77% can be obtained.

The specific energy and power values of the two EDLCs, calculated through Equations (4) and (5) are compared in the Ragone plot reported in Figure 6b. Both devices deliver the maximum specific energy at the lowest current, and the maximum power is delivered at the highest current.

Indeed, at 0.5  $\text{A g}^{-1}$ , the specific energy is 19.6  $\text{Wh kg}^{-1}$  and 7.2  $\text{Wh kg}^{-1}$  for HBLME-EDLC and LBHME-EDLC, respectively. At 4  $\text{A g}^{-1}$ , the specific power is 4.7  $\text{kW kg}^{-1}$  for the HBLME EDLC and 3.8  $\text{kW kg}^{-1}$  for the LBHME-EDLC. These values are reported in Table 3. If energy and power are normalized by the electrode area, they become 182  $\mu\text{Wh cm}^{-2}$  and 42.8  $\text{mW cm}^{-2}$  for the HBLME-EDLC, and 99.4  $\mu\text{Wh cm}^{-2}$  and 51  $\text{mW cm}^{-2}$  for the LBHME-EDLC (Table 3). These results clearly demonstrate that increasing electrode thickness is detrimental for energy and power performance. Indeed, specific energy of LBHME-EDLC is lower than HBLME-EDLC and this is mainly related to an inefficient exploitation of the electrode carbon surface. This is highlighted by the comparison of the area capacitance of HBLME-EDLC (148  $\text{mF cm}^{-2}$ ) and LBHME-EDLC (85.5  $\text{mF cm}^{-2}$ ).

Therefore, in LBHME-EDLC, the increase of the electrode mass is not enough to offset such specific energy decrease, and the areal energy density keeps lower than that of HBLME-EDLC. However, power performance of the two EDLCs are comparable, suggesting that the decrease of the binder content has a positive effect.

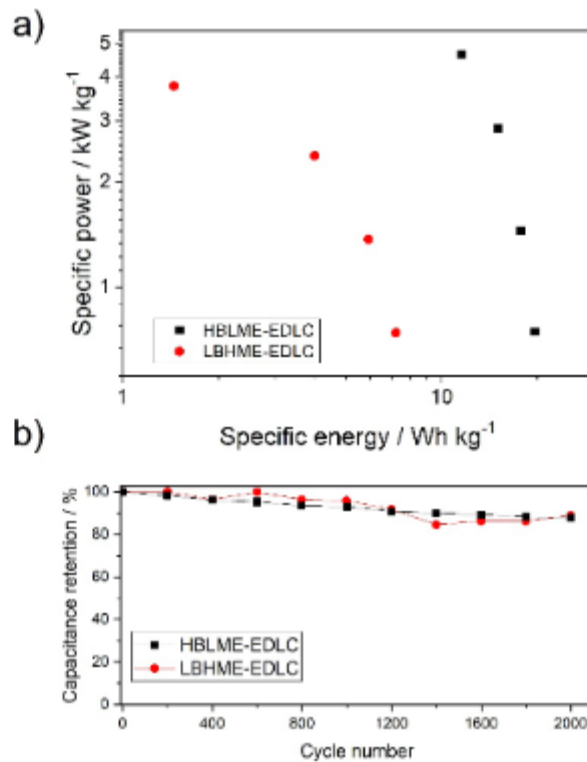


**Figure 6.** EDLC comparison by galvanostatic tests. (a) Trend of the capacitance percentage normalized by the value at first cycle the as function of the cycle number (at  $1 \text{ A g}^{-1}$ , cell voltage cut-off:  $0 \text{ V}$ – $3.2 \text{ V}$ ) and (b) Ragone plots of HBLME-EDLC and LBHME-EDLC.

#### 4. Discussion

Today many efforts are being devoted to increasing the specific energy of supercapacitors by different strategies. Among them promises are held by the use of ionic liquids, thick electrodes and pseudocapacitive active materials [2,6,12]. Ionic liquids enable high practical voltage ( $>3 \text{ V}$ ) and therefore energy density, but their major drawbacks are the greater ESR respect to commercial electrolytes and high cost. The use of thick electrodes ( $>10 \text{ mg cm}^{-2}$ ) may seem the simpler solution, but the achieving high performance with thick electrodes is still an unsolved problem [10,11]. Indeed, thick electrodes suffer of poor electronic and ionic connection between the particles, and only the external portion of the electrodes take part in the charge/discharge processes.

The increasing market for supercapacitors requires that sustainable manufacturing processes and materials are exploited to manufacture green supercapacitors. Aqueous processable bio-derived polymers represent a valuable alternative to today's fluorinated separators and binders. Furthermore, we have already demonstrated that the smart combination of a water processable binder and separator (like pullulan) and a hydrophobic ionic liquid electrolyte (EmimTFSI) enables an easy recovery of the expensive ionic liquid [31]. Indeed, the pullulan-IL-based EDLC can be readily separated into each of its components by immersion in water. After these very interesting but preliminary results, in this

paper we have carried out a study to get further insight into the impact of the use of natural polymer in supercapacitors performance. We have investigated the use of cellulose, which is the most widely studied bio-based polymer for green supercapacitors, and pullulan, that we have proposed for the first time in [31]. CTA and Pu separators were processed as self-standing mats by electrospinning. Their permeability to different electrolytes (EmimTFSI, 0.5 m LiTFSI TEGDME, PYR<sub>14</sub>TFSI), which is critical in the formation of the electrical double layer, has been evaluated by EIS and quantified referring to the Mac Mullin number. This characterization has been done at different temperatures over one week, in order to get insight on the thermal and chemical stability of the tested bio-polymer in the selected electrolytes. Both membranes at 30 °C featured the lower resistance (Pu 2 Ohm cm<sup>2</sup> CTA 2 Ohm cm<sup>2</sup>) when soaked with EmimTFSI. However, given that the thickness of Pu (55 µm) was higher than that of CTA (22 µm), the resistivity of the Pu-EmimTFSI system was considerably smaller (0.407 kOhm cm vs. 1.041 kOhm cm). Furthermore, Pu-EmimTFSI exhibited a better thermal stability respect to the CTA-EmimTFSI. Notably, the  $N_M$  for the Pu is always smaller than that of CTA, in particular, in EmimTFSI values of 5 and 12 were found, respectively. Overall, this study highlighted the presence of different and specific interactions between the tested electrolytes and the membranes that affect the ionic permeability and stability. It also indicated Pu-EmimTFSI as the best system. Indeed, Pu-EmimTFSI was the combination capable to minimize the ESR and avoid performance degradation due to temperature changes.

On the basis of these results, Pu was selected as separator and binder for EmimTFSI-based EDLCs. The big challenge we faced in this study was to reach high electrode mass loading at low binder content.

Two EDLCs have been assembled featuring two different formulations, one with lower mass loading and high binder content (HBLME) and a second one with higher mass loading and lower binder content (LBHME). These have been characterized electrochemically to evaluate how binder decrease and mass loading increase affect performance. In particular, these devices have been characterized at first by EIS. Analysis of the Nyquist plots highlighted an increase of the ESR moving from the HBLME-EDLC to the LBHME-EDLC, (5.9 Ohm cm<sup>2</sup> vs. 7.6 Ohm cm<sup>2</sup>). This trend was mainly related to the increase of the ionic and electronic contact resistances between carbon particles with the increase of electrode mass loading (1.5-fold from HBLME-EDLC to LBHME-EDLC).

For both devices' CVs have shown the absence of faradaic parasitic reactions within the cell voltage range 0 to 3.2 V. This wide range is feasible thanks to the good electrochemical stability of Pu-EmimTFSI. Specific capacitances have been calculated for both EDLCs. The highest specific capacitance was featured at the lowest scan rate of 5 mV s<sup>-1</sup> for both devices and was 18 F g<sup>-1</sup> and 14 F g<sup>-1</sup> for HBLME-EDLC and LBHME-EDLC, respectively. Both supercapacitors featured a good capacitance retention with the increase of the scan rate that however was higher for HBLME-EDLC (22%) than LBHME-EDLC (50%).

GLV cycling with high coulombic efficiency (higher than 98%) was demonstrated for both devices at the high cell voltage of 3.2 V. Noticeably, the EDLC featured a very good cycling behaviour demonstrated over more than 2000 cycles even at low binder content, confirming the stability of the Pu-polymer in EmimTFSI.

The high cell voltage and good specific capacitance provided specific energy of 19.6 Wh kg<sup>-1</sup> and 7.2 Wh kg<sup>-1</sup> at 0.5 A g<sup>-1</sup> that well compare with those of EDLCs featuring the same electrolyte and active carbon but employing a fluorinated binder and fiber glass separators [16]. The highest specific power was 4.6 kW kg<sup>-1</sup> and 3.7 kW kg<sup>-1</sup> at 4–5 A g<sup>-1</sup> respectively for HBLME-EDLC and for the LBHME-EDLC

The gravimetric performance of the HBLME-EDLC is superior respect to that of the LBHME-EDLC. This is due to the lower specific capacitance of the latter vs. the former. In turn, this is due to an inefficient ionic electronic contact between electrode carbon particles that leads to a partial exploitation of the electrodes surface.

## 5. Conclusions

This work demonstrates that aqueous processable biodegradable polymers such as pullulan can be effectively exploited for the development of the major components (separator and binder) of ionic-liquid-based green EDLCs. After studying different combinations of biopolymer and organic electrolyte, pullulan-EmimTFSI was found to be the best system in terms of resistivity and thermal behavior. Therefore, we assembled Pu-based EDLCs with EmimTFSI as electrolyte. Our study demonstrates for the first time the feasibility of the use of pullulan to produce high mass loading electrodes at low binder content for high voltage EDLCs. We prepared electrodes with mass loadings up to  $13.84 \text{ mg cm}^{-2}$  with 10% binder content. Pullulan-EmimTFSI EDLCs were charged up to 3.2 V with good cycling stability over 5000 cycles. Pullulan-EmimTFSI EDLCs featured specific energy and power comparable with those of supercapacitors based on the same activated carbon and ionic liquid, but with fluorinated binder and fiberglass separator.

Further work is in progress to improve the specific capacitance of these thick electrodes by using high surface area carbons with tailored porosity, different conductive carbon additives, and by exploring different electrolytes.

**Supplementary Materials:** The following are available online at <http://www.mdpi.com/1996-1073/13/12/3115/s1>, Figure S1. Schemes of the casting preparation of the pullulan-based electrodes and of the supercapacitor assembly, Figure S2. Nyquist plot of Pullulan electrospun membrane soaked with (a)  $\text{PYR}_{14}\text{TFSI}$ , (c) EmimTFSI, (e) 0.5 m LiTFSI TEGDME and Cellulose triacetate electrospun membrane soaked with (b)  $\text{PYR}_{14}\text{TFSI}$ , (d) EmimTFSI, (f) 0.5 m LiTFSI TEGDME, Figure S3. Trend of the capacitance percentage normalized by the value at first cycle the as function of the cycle number (at  $1 \text{ A g}^{-1}$ , cell voltage cut-off: 0 V–3.2 V), Table S1. Resistance normalized by the plain area of Pullulan electrospun separator in different tested electrolytes, Table S2. Resistance normalized by the plain area of Cellulose triacetate electrospun separator in different tested electrolytes, Table S3. Resistivity of Pullulan electrospun separator in different tested electrolytes, Table S4. Resistivity of Cellulose triacetate electrospun separator in different tested electrolytes, Table S5. Mac Mullin number of Pullulan electrospun separator in different tested electrolytes, Table S6. Mac Mullin number of Cellulose triacetate electrospun separator in different tested electrolytes.

**Author Contributions:** Conceptualization: F.S. Data curation: G.E.S., F.P. Formal analysis: G.E.S., F.P., Funding acquisition: F.S. Investigation: G.E.S., F.P. Project administration: F.S. Supervision: F.S., Writing—original draft: G.E.S., F.P., A.B., D.M., F.S. Writing—review & editing: G.E.S., F.P., A.B., D.M., F.S. All authors have read and agreed to the published version of the manuscript.

**Funding:** This research was funded by the Italy-South Africa joint Research Programme 2018–2020 (Italian Ministers of Foreign Affairs and of the Environments) and “Piano Triennale di Realizzazione 2019–2021, Accordo di Programma Ministero dello Sviluppo Economico”—ENEA.

**Acknowledgments:** Maria Letizia Focarete (University of Bologna) and her research group are acknowledged for their precious contribution and support on electrospinning of natural polymers.

**Conflicts of Interest:** All The authors declare no conflict of interest for this manuscript.

## References

- Dunn, B.; Kamath, H.; Tarascon, J.M. Electrical energy storage for the grid: A battery of choices. *Science* **2011**, *334*, 928–935. [[CrossRef](#)] [[PubMed](#)]
- Yang, Z.; Zhang, J.; Kintner-Meyer, M.C.W.; Lu, X.; Choi, D.; Lemmon, J.P.; Liu, J. Electrochemical energy storage for green grid. *Chem. Rev.* **2011**, *111*, 3577–3613. [[CrossRef](#)] [[PubMed](#)]
- Chen, G.Z. Supercapacitor and supercapattery as emerging electrochemical energy stores. *Int. Mater. Rev.* **2017**, *62*, 173–202. [[CrossRef](#)]
- Siwach, P.; Sharma, K.; Arora, A.; Tripathi, S.K. Review of supercapacitors: Materials and devices. *J. Energy Storage* **2019**, *21*, 801–825. [[CrossRef](#)]
- Schütter, C.; Pohlmann, S.; Balducci, A. Industrial Requirements of Materials for Electrical Double Layer Capacitors: Impact on Current and Future Applications. *Adv. Energy Mater.* **2019**, *9*, 1900334. [[CrossRef](#)]
- DeVos, N.; Maton, C.; Stevens, C.v. Electrochemical Stability of Ionic Liquids: General Influences and Degradation Mechanisms. *ChemElectroChem* **2014**, *1*, 1258–1270. [[CrossRef](#)]
- González, A.; Goikolea, E.; Barrera, J.A.; Mysyk, R. Review on supercapacitors: Technologies and materials. *Renew. Sustain. Energy Rev.* **2016**, *58*, 1189–1206. [[CrossRef](#)]

8. Lazzari, M.; Mastragostino, M.; Soavi, F. Capacitance response of carbons in solvent-free ionic liquid electrolytes. *Electrochem. Commun.* **2007**, *9*, 1567–1572. [[CrossRef](#)]
9. Mauger, A.; Julien, C.M.; Paoella, A.; Armand, M.; Zaghbi, M. A comprehensive review of lithium salts and beyond for rechargeable batteries: Progress and perspectives. *Mater. Sci. Eng. R Rep.* **2018**, *134*, 1–2110. [[CrossRef](#)]
10. Ruschhaupt, P.; Varzi, A.; Passerini, S. Natural Polymers as Green Binders for High-Loading Supercapacitor Electrodes. *ChemSusChem* **2020**, *13*, 763–770. [[CrossRef](#)]
11. Arbizzani, C.; Yu, Y.; Li, J.; Xiao, J.; Xia, Y.; Yang, Y.; Santato, C.; Raccichini, R.; Passerini, S. Good practice guide for papers on supercapacitors and related hybrid capacitors for the Journal of Power Sources. *J. Power Sources* **2020**, *450*, 227636. [[CrossRef](#)]
12. Stojanovska, E.; Kilic, A. Carbon nanofibers as thick electrodes for aqueous supercapacitors. *J. Energy Storage* **2019**, *26*, 100981. [[CrossRef](#)]
13. Krause, A.; Balducci, A. High voltage electrochemical double layer capacitor containing mixtures of ionic liquids and organic carbonate as electrolytes. *Electrochem. Commun.* **2011**, *13*, 814–817. [[CrossRef](#)]
14. Krummacker, J.; Balducci, A. Al(TFSI)<sub>3</sub> as a Conducting Salt for High-Voltage Electrochemical Double-Layer Capacitors. *Chem. Mater.* **2018**, *30*, 4857–4863. [[CrossRef](#)]
15. Krummacker, J.; Hess, L.H.; Balducci, A. Al(TFSI)<sub>3</sub> in Acetonitrile as Electrolytes for Electrochemical Double Layer Capacitors. *J. Electrochem. Soc.* **2019**, *166*, A1763–A1768. [[CrossRef](#)]
16. Lazzari, M.; Soavi, F.; Mastragostino, M. Mesoporous carbon design for ionic liquid-based, double-layer supercapacitors. *Fuel Cells* **2010**, *10*, 840–847. [[CrossRef](#)]
17. Chmiola, J.; Largeot, C.; Taberna, P.L.; Simon, P.; Gogotsi, Y. Desolvation of ions in subnanometer pores and its effect on capacitance and double-layer theory. *Angew. Chem. Int. Ed.* **2008**, *47*, 3392–3395. [[CrossRef](#)]
18. Varzi, A.; Passerini, S. Enabling high areal capacitance in electrochemical double layer capacitors by means of the environmentally friendly starch binder. *J. Power Sources* **2015**, *300*, 216–222. [[CrossRef](#)]
19. Ahmed, S.; Nelson, P.A.; Gallagher, K.G.; Dees, D.W. Energy impact of cathode drying and solvent recovery during lithium-ion battery manufacturing. *J. Power Sources* **2016**, *322*, 169–178. [[CrossRef](#)]
20. Mauger, A.; Julien, C.; Paoella, A.; Armand, M.; Zaghbi, K. Recent Progress on Organic Electrodes Materials for Rechargeable Batteries and Supercapacitors. *Materials* **2019**, *12*, 1770. [[CrossRef](#)] [[PubMed](#)]
21. Bresser, D.; Buchholz, D.; Moretti, A.; Varzi, A.; Passerini, S. Alternative binders for sustainable electrochemical energy storage—the transition to aqueous electrode processing and bio-derived polymers. *Energy Environ. Sci.* **2018**, *11*, 3096–3127. [[CrossRef](#)]
22. Yamagata, M.; Ikebe, S.; Soeda, K.; Ishikawa, M. Ultrahigh-performance nonaqueous electric double-layer capacitors using an activated carbon composite electrode with alginate. *RSC Adv.* **2013**, *3*, 1037–1040. [[CrossRef](#)]
23. Böckenfeld, N.; Jeong, S.S.; Winter, M.; Passerini, S.; Balducci, A. Natural, cheap and environmentally friendly binder for supercapacitors. *J. Power Sources* **2013**, *221*, 14–20. [[CrossRef](#)]
24. Dühnen, S.; Betz, J.; Kolek, M.; Schmuck, R.; Winter, M.; Placket, T. Toward Green Battery Cells: Perspective on Materials and Technologies. *Small Methods* **2020**, 2000039. [[CrossRef](#)]
25. Bonnefoi, L.; Simon, P.; Fauvarque, J.F.; Sarrazin, C.; Sarrau, J.F.; Dugast, A. Electrode compositions for carbon power supercapacitors. *J. Power Sources* **1999**, *80*, 149–155. [[CrossRef](#)]
26. Phillips, D.M.; Drummy, L.F.; Conrady, D.G.; Fox, D.M.; Naik, R.R.; Stone, M.O.; Trulove, P.C.; de Long, H.C.; Mantz, R.A. Dissolution and regeneration of Bombyx mori silk fibroin using ionic liquids. *J. Am. Chem. Soc.* **2004**, *126*, 14350–14351. [[CrossRef](#)]
27. Swatloski, R.P.; Spear, S.K.; Holbrey, J.D.; Rogers, R.D. Dissolution of Cellulose with Ionic Liquids. *J. Am. Chem. Soc.* **2002**, *124*, 4974–4975. [[CrossRef](#)]
28. Recham, N.; Armand, M.; Tarascon, J.M. Novel low temperature approaches for the eco-efficient synthesis of electrode materials for secondary Li-ion batteries. *Comptes Rendus Chim.* **2010**, *13*, 106–116. [[CrossRef](#)]
29. Heinze, T.; Dorn, S.; Schöbitz, M.; Liebert, T.; Köhler, S.; Meister, F. Interactions of Ionic Liquids with Polysaccharides—2: Cellulose. *Macromol. Symp.* **2008**, *262*, 8–22. [[CrossRef](#)]
30. Varzi, A.; Balducci, A.; Passerini, S. Natural Cellulose: A Green Alternative Binder for High Voltage Electrochemical Double Layer Capacitors Containing Ionic Liquid-Based Electrolytes. *J. Electrochem. Soc.* **2014**, *161*, A368–A375. [[CrossRef](#)]



31. Poli, F.; Momodu, D.; Spina, G.E.; Terella, A.; Mutuma, B.K.; Focarete, M.L.; Manyala, N.; Soavi, F. Pullulan-ionic liquid-based supercapacitor: A novel, smart combination of components for an easy-to-dispose device. *Electrochim. Acta* **2020**, *338*, 135872. [[CrossRef](#)]
32. Arbizzani, C.; Lazzari, M.; Soavi, F.; Mastragostino, M.; Conte, M. ILHYPOS Ionic Liquid-Based Supercapacitors. *ECS Trans.* **2010**, *25*, 25–30.
33. Li, Y.; Li, Q.; Tan, Z. A review of electrospun nanofiber-based separators for rechargeable lithium-ion batteries. *J. Power Sources* **2019**, *443*, 227262. [[CrossRef](#)]
34. Yoo, H.D.; Jang, J.H.; Ryu, J.H.; Park, Y.; Oh, S.M. Impedance analysis of porous carbon electrodes to predict rate capability of electric double-layer capacitors. *J. Power Sources* **2014**, *267*, 411–420. [[CrossRef](#)]
35. Conway, B.E. *Electrochemical Supercapacitors: Scientific Fundamentals and Technological*; Springer Science & Business Media: Berlin, Germany, 2013.
36. Kötz, R.; Carlen, M. Principles and applications of electrochemical capacitors. *Electrochim. Acta* **2000**, *45*, 2483–2498. [[CrossRef](#)]



© 2020 by the authors. Licensee MDPI, Basel, Switzerland. This article is an open access article distributed under the terms and conditions of the Creative Commons Attribution (CC BY) license (<http://creativecommons.org/licenses/by/4.0/>).

## 2.2 Novel N-doped carbons

This section reports the main finding about the exploitation of Nitrogen-doped mesoporous carbon, prepared by the group of Prof. C. Durante (University of Padua). My contribution was the testing of these carbons as electrode components for high voltage ionic liquid-based supercapacitors. Nitrogen-doped mesoporous carbonaceous materials featuring high surface area were synthesized by the University of Padua according to an innovative hard template method. The carbon precursor was sucrose and four different materials have been prepared and tested. The carbonization procedure was common to all the four tested samples and consisted of a preheated at 100°C for 1 h followed by a ramp 5°C min<sup>-1</sup> up to 950°C and isotherm treatment at that temperature for 2h, under Ar flux in a quartz tubular oven. The samples were subsequently let cool down at room temperature. The obtained mesoporous carbonaceous material was:

- MC-P200: mesoporous silica (P200) has been added to the sucrose as the templating agent before the carbonization.
- nMC-PA: mesoporous silica functionalized with propylamine (PA) has been added to the sucrose as the templating agent, before the carbonization.
- NMC-P200: mesoporous silica (P200) has been added to the sucrose as the templating agent together with 1,10-phenanthroline, before the carbonization.
- NMC-PA: mesoporous silica functionalized with propylamine (PA) has been added to the sucrose as the templating agent with 1,10-phenanthroline, before the carbonization.

The materials have been characterized with X-ray photoemission spectroscopy, elemental analysis, EDX to investigate the doping action of the adopted strategies. The morphology of the obtained material has been investigated by means of TEM and for all the tested samples, nitrogen adsorption isotherms have been run to investigate the specific surface area. The nitrogen content decreases as NMC-P200>NMC-PA>nMC-PA. Nitrogen adsorption isotherm measurements have been run to determine the BET area, and 1071 m<sup>2</sup>g<sup>-1</sup> (NMC-PA), 1003 m<sup>2</sup>g<sup>-1</sup> (nMC-PA), 1148 m<sup>2</sup>g<sup>-1</sup> (NMC-P200), and 763 m<sup>2</sup>g<sup>-1</sup> (MC-P200) have been measured. The obtained materials have been tested as the main component of electrodes for EDLCs featuring ionic liquid Pyr<sub>1,201</sub> TFSI as electrolytes. Cyclic voltammeteries have been run on all the assembled EDLCs to investigate the presence of reversible faradaic. The cyclic voltammograms were box shaped and symmetrical and only nMC-PA showed reversible broad peaks. The measured electrodes specific capacitance was 65 F g<sup>-1</sup> for NMC-P200, 43 F g<sup>-1</sup> for MC-P200, 35 F g<sup>-1</sup> for NMC-PA and 24 F g<sup>-1</sup> for nMC-PA. The EDLCs have been cycled under galvanostatic charge/discharge conditions between 0 and 3 V of cell voltage and no evident degradation of the carbon electrode performance could be observed over 5k charge/discharge cycles. Highlighting the high stability of the surface chemistry of the mesoporous carbonaceous samples. However, the specific capacitance of the tested carbons was lower than what was achieved with the biochar carbon reported in section 2.1, therefore these materials, though interesting for surface chemistry and porous architecture, were not further investigated for EDLCs. The experimental methods and the results of this study are reported in [3] that is here attached as the complete publication.

Special  
Collection

# Nitrogen-Doped Mesoporous Carbon Electrodes Prepared from Templating Propylamine-Functionalized Silica

Riccardo Brandiele,<sup>[a]</sup> Federico Poli,<sup>[b]</sup> Luca Picelli,<sup>[a]</sup> Roberto Pilot,<sup>[a, c]</sup> Gian Andrea Rizzi,<sup>[a]</sup> Francesca Soavi,<sup>[b]</sup> and Christian Durante<sup>\*[a]</sup>

In this paper, nitrogen doped carbon materials with mesopores 4–8 nm-wide and a high surface area of  $ca. 1100 \text{ m}^2 \text{ g}^{-1}$  were synthesized according to an innovative hard template method. Sucrose was used as carbon source and propylamine functionalized silica acted as both nitrogen source and templating agent. The novel doped carbons were compared with mesoporous carbons featuring similar texture properties (pore size and surface area) but obtained by the pyrolysis of sucrose or 1,10-phenanthroline and employing non-functionalized silica as a templating agent. The interest of this investigation is to

understand how doping occurs when a functionalized silica is employed, and whether the nitrogen doping remains a surface property or it is extended also to the bulk of the material, influencing the morphological and the electrical properties of the resulting carbon. X-ray photoemission spectroscopy, elemental analysis, and EDX confirmed the doping action of the functionalized silica and the electrochemical characterization allowed to compare the different performances as supercapacitor materials.

## 1. Introduction

Mesoporous Carbons (MCs) are materials with pore size distribution in the range 2–50 nm. They are ubiquitously employed in catalysis,<sup>[1]</sup> in separation technology<sup>[2]</sup> and because of their good conductivity, combined with mechanical, chemical and electro-chemical stability, they are widely used in electrocatalysis<sup>[3–5]</sup> as well as in energy storage systems, like supercapacitors.<sup>[6–11]</sup>

The synthesis of porous carbon materials with well controlled pore sizes, high surface area and large pore volume is accomplished using various methods, including (i) pyrolysis of a carbon precursor employing an inorganic template (hard template approach),<sup>[12–15]</sup> (ii) pyrolysis of polymer blends composed of a sacrificial polymer and a pyrolyzable polymer (soft template approach),<sup>[16–18]</sup> (iii) hydro-thermal synthesis from organic precursors,<sup>[19,20]</sup> and others.<sup>[21]</sup> The hard template synthesis is of particular interest because it is robust and reproducible and consists in the employment of an inorganic template such as silica or alumina or Fe, Co and Mn oxide nanoparticles. The template is embedded in the carbon precursor or the carbon precursor is allowed to permeate into

the pores of the template. After carbonization, the removal of the template generates porous carbon materials with isolated or interconnected pores (Figure 1).

MCs are hydrophobic and inert in nature; however, their surface modification with heteroatoms such as nitrogen, sulfur, boron, phosphorus can promote both the electrochemical activity and the electrolyte wettability needed for the implementation of an electrode in an electrochemical device. Nitrogen doped mesoporous carbons are without any doubts the most investigated materials since they can induce a beneficial change on both the electronic and structural properties of the carbon supports, in particular N-doped carbons are by themselves active versus the oxygen reduction reaction,<sup>[17,22]</sup> they can trigger metal nanoparticle catalytic activity by metal support interaction<sup>[4,23,24]</sup> or possess enhanced specific capacitance.<sup>[6–11]</sup>

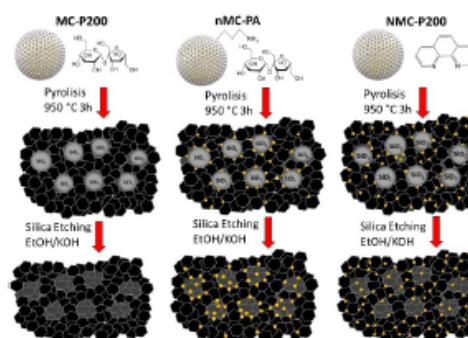


Figure 1. Sketch of the procedure employed for the synthesis of doped mesoporous carbons.

[a] Dr. R. Brandiele, L. Picelli, Dr. R. Pilot, Prof. G. A. Rizzi, Prof. Dr. C. Durante  
Department of Chemical Sciences  
University of Padova  
Via Marzolo, 1 – 36026, Padova, Italy  
E-mail: christian.durante@unipd.it

[b] F. Poli, Prof. Dr. F. Soavi  
Department of Chemistry  
Alma Mater Studiorum University of Bologna  
Via Selmi 2, 40126 Bologna, Italy

[c] Dr. R. Pilot  
Consorzio INSTM, via G. Giusti 9, 50121 Firenze, Italy

Supporting information for this article is available on the WWW under  
<https://doi.org/10.1002/celec.202000098>

An invited contribution to a Special Collection dedicated to *Giornale dell'Elettrochimica Italiana 2019 (GEI2019)*

Nitrogen functional groups are commonly pinned onto the carbon surface according to post functionalization procedure (ion implantation,<sup>[25]</sup> radical reaction,<sup>[26]</sup> grafting<sup>[27]</sup> etc.) or by employing a suitable carbon-nitrogen precursor during the pyrolysis process.<sup>[17,28]</sup> Organic precursors are nitrogen containing molecules or polymers such as 1,10-phenanthroline or polyaniline, but a plethora of examples including biomasses can be found in literature.<sup>[29]</sup>

In this paper we present a novel approach for the hard template synthesis of nitrogen doped carbons by employing a propylamine silica template (PA). PA is a mesoporous silica functionalized with propylamine groups (Figure 1). The degradation of the propylamine group during the pyrolysis process would, in principle, provide nitrogen molecular fragments able at doping the resulting carbon with nitrogen groups. Therefore, the type of synthesis is in between the hard template and soft template synthesis, where the employment of the sacrificial propylamine group grafted on the silica particle surface should provide a more selective nitrogen functionalization in the resulting carbon material without the employment of massive nitrogen containing carbon precursor as 1,10-phenanthroline of polypyrrole polymers. Therefore, the novel concept of this synthesis is that the silica itself acts as both nitrogen source and templating agent, while the carbon source can be a cheap and highly disposable material such as sucrose. Indeed, the propylamine group is a sacrificial part of the template, while the silica skeleton behaves and is managed exactly as a hard template. It is worth noting that the PA is a commercially available reagent and the functionalization of silica is a well consolidated procedure employed for a plethora applications in separation a recognition techniques.<sup>[30]</sup> Therefore, the scope of the paper is to present the development of an innovative synthesis for the preparation of a nitrogen doped carbon (NMC), the NMC chemical and electrochemical characterization and its employment as supercapacitor electrode material. The chemical, morphological and electrochemical properties of novel carbons are also compared with the properties of carbon material prepared with non-functionalized silica.

## 2. Results and Discussion

Mesoporous silica (P200) and propylamine modified mesoporous silica (PA), both commercially available, were used as inorganic templates. The two templating agents have the same morphology in terms of particle dimension (200 nm) and pore size (4 nm), but they slightly differ for the surface area: 543 m<sup>2</sup>g<sup>-1</sup> for the pristine silica and 489 m<sup>2</sup>g<sup>-1</sup> for propylamine silica. Each template was properly mixed with the carbon precursor: sucrose or 1,10-phenanthroline and pyrolyzed at 950 °C (Figure 1). The resulting crude product was then treated with an etching solution (EtOH/NaOH) to remove the SiO<sub>2</sub> NPs, leaving the porous carbon structure (detailed information is given in the experimental part). This synthetic approach aims at understanding whether the employment of PA allows the formation of a nitrogen-doped carbon and whether the nitrogen doping remains localized where it is strictly necessary i.e.

on the accessible carbon surface and not on the bulk carbon material. Therefore, four different carbons were prepared combining the two templates and the two carbon precursors: MC-P200 (P200 + sucrose), nMC-PA (PA + sucrose), NMC-P200 (P200 + 1,10-phenanthroline) and NMC-PA (PA + 1,10-phenanthroline).

Elemental analysis was performed on the differently synthesized samples and the results are summarized in Table 1. EA confirmed the doping action of the propylamine functionalized silica, since the nitrogen content found in nMC-PA was 1.2%<sub>w</sub> (1.96%<sub>w</sub> N/C). If 1,10-phenanthroline is used as carbon precursor, such as in NMC-PA, the nitrogen content increases to 3.6%<sub>w</sub> (5.64%<sub>w</sub> N/C). The nitrogen content is even higher (5.7%<sub>w</sub>, 8.32%<sub>w</sub> N/C) when undoped silica is employed as in NMC-P200, but 1,10-phenanthroline plays both as carbon and nitrogen precursor. Finally, MC-P200 obtained with sucrose and silica P200, did not show, as expected, the presence of nitrogen. It is worth noting that the small quantity of sulfur (< 0.8%) present in all the samples is due to the sulfuric acid used for catalyzing the oligomerization process.

TEM images in Figure 2 show the formation of spherical carbon structures with diameters in the range 150–200 nm for all the prepared carbons, further images are reported in Figure S1. MC-P200 and NMC-P200 are characterized by highly ordered pores of cylindrical form, as expected from the meso-structured silica used for the synthesis. Conversely, the ordered structure is absent when propylamine silica is used as an inorganic template. In fact, it is reasonable to assert that the presence of propylamine influence the way sucrose or 1,10-phenanthroline arrange inside the template pores and over the silica surface. The formation of spherical particles is confirmed also by SEM-EDX analysis, which clearly show the presence of

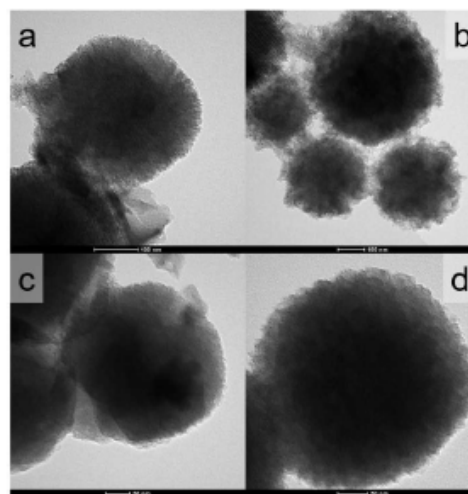


Figure 2. TEM images of a) MC-P200 b) NMC-P200 c) nMC-PA and d) NMC-PA



showed a decomposition temperature ( $T_{\text{deg}}$ ) between 490 and 520 °C. MC-P200 and nMC-PA showed similar thermogravimetric behavior and a degradation temperature almost 30 °C higher than the samples prepared with 1,10-phenanthroline. The different thermal stability of the material prepared from sucrose and 1,10-phenanthroline could be explained by the increase of nitrogen groups in the carbon matrix. This, in turn, decreases the graphitization degree and, as a consequence, the thermal stability. The burn off in  $N_2$  atmosphere is almost complete at 620 °C for all the samples except for nMC-PA, that degrades completely at slightly higher temperature.

MCS showed similar XRD diffraction patterns as reported in Figure 3d. A main diffraction peak at  $2\theta = 24.9$  is present in all the spectra, corresponding to 002 diffraction plane of hexagonal carbon material (JCPDS, Card No. 75-1621). This diffraction peak shows a down-ward shift with respect to a perfect crystallized graphite, that reflects an expansion of the interlayer distance and small crystallite size, as confirmed by the increase of the full width at half maximum (FWHM) along with the decrease of the diffraction angles.

Figure S3 reports Raman spectra of the prepared mesoporous carbons. The two intense bands observed at  $\sim 1600 \text{ cm}^{-1}$  and at  $\sim 1350 \text{ cm}^{-1}$  are the G (graphitic,  $E_{2g}$ ) and the D1 band (defect,  $A_{1g}$ ).

All the spectra were normalized to the maximum of the G band. The presence of defects, the quantification of the amorphous carbon and the dimension of the crystallite domains can be determined by the deconvolution and by the elaboration of the experimental spectra.<sup>[5,12,16,22,31]</sup> All the spectra were deconvoluted with four components D1, D3, D4 and G at  $\sim 1340 \text{ cm}^{-1}$ ,  $\sim 1500 \text{ cm}^{-1}$ ,  $\sim 1200 \text{ cm}^{-1}$  and  $\sim 1600 \text{ cm}^{-1}$ , respectively. In literature, the D3 band is assigned to amorphous carbon and the D4 one is assigned to the presence of polyenes or ionic impurities. All band shapes were chosen Gaussian and FWHMs let free. The Raman spectra were deconvoluted constraining the frequency of the two bands D1 and G between  $1325\text{--}1375 \text{ cm}^{-1}$  and between  $1560\text{--}1620 \text{ cm}^{-1}$ , respectively. The frequency of the other two bands could vary in the range  $1475\text{--}1515 \text{ cm}^{-1}$  (D3 band) and  $1170\text{--}1220 \text{ cm}^{-1}$  (D4 band). The three-stage model proposed by Ferrari envisages a different degree of graphitization of the system on the base on the ratio between the intensity of the D1 and G band ( $I_D/I_G$ ) and the position of the G band in the interval  $1581 \text{ cm}^{-1}$  and  $\sim 1600 \text{ cm}^{-1}$ .<sup>[32]</sup> The peak positions and the  $I_D/I_G$  ratios are close to the values expected for nanocrystalline graphite and are compatible with the second stage of the graphitization trajectory where a transition from nanocrystalline graphite to amorphous carbon occurs. The samples could therefore be envisaged as graphitic nanocrystals embedded in an amorphous carbon matrix. In the second stage the relationship between  $I_D/I_G$  is described by a modified Tuinstra-Koenig equation [Eq. (1)], which binds the intensity ratio in a quadratic dependence with the size of the nanocrystals ( $L_D$ ).

$$\frac{I_D}{I_G} = C(\lambda) L_D^2 \quad (1)$$

It is worth noting that the amorphous carbon components are higher in the carbon prepared from 1,10-phenanthroline than in those synthesized from sucrose, which is in accordance with the TGA findings i.e. the presence of nitrogen groups is detrimental for the thermal stability.

In order to define the exact surface chemical modifications induced by the templating agents, we carried out XPS measurements for all the samples. XPS spectra are reported in Figure 4 and in Figure S4 and S5. The carbon 1s region shows a peak, which was fitted with three components relative to  $C \text{ sp}^2$  284.4 eV,  $C \text{ sp}^3$  284.9 and to  $C \text{ (sp}^3\text{)-O}$  at 286.5 eV (Figure S4).<sup>[23]</sup> The most intense component is associated to graphitic carbon  $\text{sp}^2$ . The oxygen peak was deconvoluted in two components for all the tested carbons (Figure S5): the peak at 533.7 eV is relative to carboxylic group, while the component at 531.8 eV corresponds to the oxygen in ester group.

XPS confirms the doping action of the propylamine silica, in fact, the surface nitrogen content in nMC-PA is 1.1%<sub>at</sub> (1.45%<sub>w</sub> N/C), which is perfectly in line with the values determined by both EDX and elemental analysis. In the samples NMC-P200 and NMC-PA, the heteroatoms content is 2.1%<sub>at</sub> (3.15%<sub>w</sub> N/C) and 2.4%<sub>at</sub> (3.69%<sub>w</sub> N/C), respectively (Table 1). It is worth noting

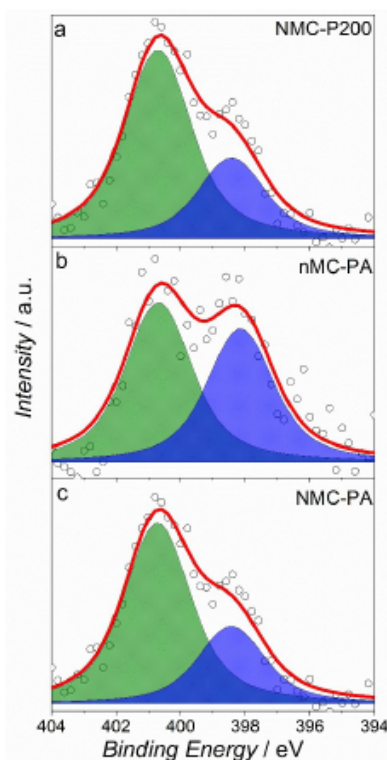


Figure 4. N 1s XPS region and spectra deconvolution of a) NMC-P200, b) nMC-PA, c) NMC-PA.

that the increase of nitrogen doping degree in NMC-P200 and NMC-PA results in a broadening of the C 1s lines and in a shift of the main peak to higher binding energies.

In Figure 4 nitrogen XPS patterns were deconvoluted with two components, one at 400.7 eV relative to the graphitic nitrogen and another one at 398.4 eV identify as pyridinic nitrogen. The graphitic peak is particular intense in NMC-PA and NMC-P200 (figure 4c), i.e. the samples synthesized with 1,10-phenanthroline. Conversely, the graphitic and pyridinic components in nMC-PA have comparable intensity (Figure 4b). Table 1 reports the weight percentages of pyridinic, and graphitic components determined by XPS with respect to the mass of the samples (weight percentages were determined from XPS atomic percentages considering the atomic mass of each elements). It is interesting to observe that the pyridinic percentage (0.4–0.5%) is almost the same in all the samples, while the graphitic nitrogen percentage specifically increases when 1,10-phenanthroline is the main dopant agent. According to literature, pyridinic functional groups are believed to exert the most pronounced influence on the capacitance due to their pseudocapacitive contributions.<sup>[33,34]</sup>

The comparison of the nitrogen content determined by EA, EDX and XPS allows to define whether nitrogen functional groups specifically decorate the carbon surface or the entire material. In fact, EA and EDX are techniques that evaluate the bulk nitrogen content, while XPS determines the nitrogen content in the first few nanometers of the material close to the surface. Table S1 reports and compares the nitrogen contents determined by the three different techniques. EA and EDX data are in good agreement for all the nitrogen doped samples. It is worth noting that EA, EDX and XPS techniques afford similar nitrogen value in nMC-PA. This finding establishes that the nitrogen content is homogeneous from the surface to the bulk of the material. On the contrary EA and EDX data, for both NMC-PA and NMC-P200, indicate that the mean nitrogen content in the sample is higher than the superficial value determined by XPS analysis, so that the most part of the nitrogen is not available on the surface. To evaluate whether the different nitrogen distribution in the synthesized samples is significant in affecting the capacitive performances of these materials, electrochemical characterization was carried out.

Cyclic voltammetry (CV) tests were run in ionic liquid 1-Methyl-1-(2-methoxyethyl)pyrrolidinium bis(trifluoromethanesulfonyl)imide (Pyr<sub>1,201</sub> TFSI) which was selected as the electrolyte for its known, wide electrochemical stability that allows excluding any side electrolyte decomposition reaction. Indeed, it features an electrochemical stability window as wide as 4 V that is also matched with high ionic conductivity of  $2.43 \times 10^{-3} \text{ S cm}^{-1}$  at 20 °C. Very thick electrodes with mass loading of 16–25 mg cm<sup>-2</sup> each were investigated to better highlight eventual faradic processes related to carbon surface moieties. Cyclic voltammetry was run at 5 mVs<sup>-1</sup> between 0 and 3 V using a 2-electrode cell setup. The voltammograms are reported in Figure 5a. The CV response of NMC-P200, MC-P200, NMC-PA and nMC-PA approaches the shape expected for an ideal electrical double layer capacitor. Only the carbon nMC-PA shows reversible broad peaks at 1.7 V and 2.0 V. Therefore, CVs

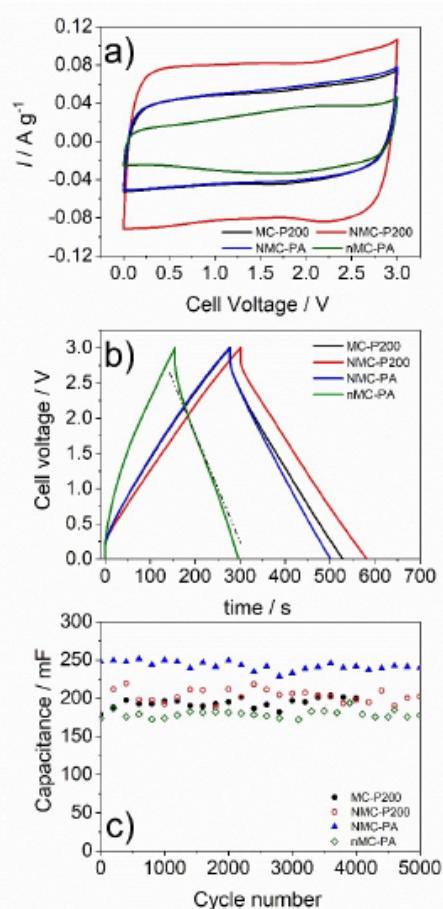


**Figure 5.** a) Voltammograms at 5 mVs<sup>-1</sup> collected by a two electrode cell configuration of the four different tested carbons. b) Cell voltage profile under galvanostatic charge/discharge at 5 mA cm<sup>-2</sup> between 0 and 3 V of the cells featuring the different carbons. c) Capacitance trends of the EDLC featuring the different carbons over repeated galvanostatic charge/discharge at 50 mA cm<sup>-2</sup>.

suggest that, except for nMC-PA, no evident signal that can be related to surface redox processes are present. The voltammetric capacitance values were obtained by the slope of the plots of the discharge current integrated over time vs. the cell voltage. The electrode specific capacitance of NMC-P200 was 65 F g<sup>-1</sup>, for MC-P200 was 43 F g<sup>-1</sup>, for NMC-PA was 35 F g<sup>-1</sup> and for nMC-PA was 24 F g<sup>-1</sup>. These values are normalized to the carbon mass. They are lower than what expected for carbons featuring specific BET surface area higher than 700 m<sup>2</sup> g<sup>-1</sup>. This must be related to the noticeable thickness of the electrodes (Table S2). Indeed, Figure S6 shows that the specific capacitance

doubles when the electrode mass loading is more than halved and reduced to  $10 \text{ mg cm}^{-2}$ . The reason is that in very thick electrodes the available carbon surface in the bulk of the material is not fully exploited and electronic connection among particles is not efficient. Consequently, the specific capacitance typically decreases with the increase of the mass loading.<sup>[35–38]</sup>

The electrochemical stability of the prepared carbons was evaluated by galvanostatic charge-discharge cycles at a specific current of  $3.2 \text{ mA}$  ( $5 \text{ mA cm}^{-2}$ ) between  $0$  and  $3 \text{ V}$ . The corresponding cycles are reported in Figure 5b. In agreement with the voltammetry study, all the carbons, except nMC-PA feature a discharge profile typical for electrical double-layer capacitors. Indeed, the cell voltage linearly decreases with discharge time. In the case of nMC-PA, the redox processes that were observed by CV at  $2 \text{ V}$  and  $1.7 \text{ V}$  (Figure 5a) give rise to a different discharge profile. It can be observed a change in the voltage slope over time in the cell voltage range  $1\text{--}2 \text{ V}$ . Linearity is kept in this range, therefore it is possible to claim about a pseudocapacitive behavior for carbon nMC-PA.

The analysis of the galvanostatic charge/discharge curves provided the coulombic efficiency, the capacitance, the energy and the power of the cells reported in Table 2

The capacitance ( $C$ ) has been calculated by Eq. (2).

$$C = i \cdot \frac{dt}{dV} \quad (2)$$

where,  $i$  is the current density, and  $dt/dV$  is the reciprocal of the slope of the cell voltage as function of time during discharge. The values are normalized to the electrode area.

The equality sign stands for fully capacitive device, therefore is not completely correct for the carbon nMC-PA, for which, the capacitance has been evaluated within the pseudocapacitive voltage range ( $2\text{--}1 \text{ V}$ ). Electrode specific capacitance is evaluated by  $C_{\text{electrode}} = 2 C_{\text{cell}}/m_{\text{electrode}}$ , where  $m_{\text{electrode}}$  is the single electrode mass loading. Specific energy ( $E$ , in Wh/kg) and specific power ( $P$ , in W/kg) were calculated using Eqs. (3) and (4):

$$E = i \int V \cdot \frac{dt}{3600 \cdot 2 \cdot m_{\text{electrode}}} \quad (3)$$

$$P = 3600 \cdot \frac{E}{\Delta t} \quad (4)$$

**Table 2.** Selected quantities obtained from the galvanostatic charge/discharge of the devices featuring the different prepared carbons.

	NMC-P200	MC-P200	NMC-PA	nMC-PA
Capacitance [F/cm <sup>2</sup> ]	0.525	0.470	0.410	0.315
Electrode specific capacitance [F/g]	65	43	35	24
Specific energy [Wh/kg]	16	10	8	5
Specific power [W/kg]	185	185	136	134

where  $\Delta t$  is the discharge time.<sup>[28]</sup>

Finally, the devices featuring the different carbons have been tested for stability under galvanostatic charge/discharge between  $0$  and  $3 \text{ V}$  at  $50 \text{ mA cm}^{-2}$ . The capacitance is reported as function of the cycle number in Figure 5c. The Figure shows that after 5k cycles the devices had very good retention of the value of the capacitance, higher than 95%. This further confirms the absence of side reactions and demonstrates the electrochemical stability of the MCs surface chemistry even in a wide range like the one here investigated ( $3 \text{ V}$ ).

### 3. Conclusions

In this paper a novel procedure for the synthesis of doped mesoporous carbon was introduced, in which the dopant agents are the propylamine groups grafted on the surface of a mesoporous silica particle and the carbon source is sucrose. Different techniques including EA, EDX and XPS were employed for confirming the successful formation of nitrogen functional groups in the carbon material. The percentage of nitrogen in nMC-PA sample was 1.2% in the form of graphitic N and pyridinic nitrogen almost in the same percentage. This material was compared with nitrogen doped carbon obtained by employing a non-functionalized silica and 1,10-phenantroline as both carbon and nitrogen source (NMC-P200). The two materials show similar carbon particle dimension, but the employment of PA affords a lower surface area and a higher content of micropores with respect to mesopores. NMC-P200 showed a similar surface nitrogen content (2.3%) than in nMC-PA (1.2%) but a lower thermal stability due to a higher amount of amorphous carbon.

The two materials were also compared as electrodes for supercapacitors. NMC-P200 showed higher specific capacitance, specific energy and specific power than nMC-PA, that can be rationalized in term of a higher accessible surface area and nitrogen surface functionalization in NMC-P200 with respect to nMC-PA. It is reasonable to assert that the propylamine groups prompt the occlusion of the mesopore so that the intimate contact between the carbon surface and the electrolyte resulted hindered by the slow mass transport inside micropores.

The capacitive performances of the carbon electrodes are low compared with the SoA, but this can be related to the exceptionally high electrode mass loadings here investigated ( $16\text{--}25 \text{ mg cm}^{-2}$ ). This approach was adopted to highlight any side reaction that could be related to and promoted by the different doping strategies. Notably, no evident degradation of the carbon electrode performance could be observed over 5k charge/discharge cycles performed under a wide voltage range of  $3 \text{ V}$ . Such interesting result was achieved by the use of an inert electrolyte, like the ionic liquid Pyr<sub>1,201</sub> TFSI, and, mainly, thanks to the high stability of the surface chemistry of the MC samples. In conclusion, this study demonstrates a novel strategy to synthesize robust, N-doped, mesoporous carbons and might pave the way to their use in different electrochemical devices.



## Experimental Section

### Chemicals

Mesoporous Silica (200 nm particle size, 4 nm pore size), Propylamine functionalized silica (200 nm particle size, 4 nm pore size), 1,10-phenanthroline (>99.5%), sucrose (>98%), were purchased from Sigma Aldrich and used as received. Ethanol (Fluka HPLC, >99.8%), Nafion (Sigma Aldrich, 5 wt% in a mixture of lower aliphatic alcohols and water), Acetone (Sigma Aldrich, >99.5%), H<sub>2</sub>SO<sub>4</sub> (Fluka, 95%, TraceSELECT), NaOH (VWR, >99%), 1-Butyl-1-methylpyrrolidinium bis(trifluoromethylsulfonyl) imide (Sigma Aldrich, >98.5% for electrochemistry), Carbon Super C45 (Imerys Graphite & Carbon).

### Mesoporous Carbon Synthesis

Silica P200 and propylamine silica P200 (PA) were both used as inorganic templates. The two templating agents have the same morphology in terms of particle size and pore size (particle size 200 nm and pore size 4 nm), but the surface slightly differs (543 m<sup>2</sup>g<sup>-1</sup> in P200 and 489 m<sup>2</sup>g<sup>-1</sup> in PA). 1,10-phenanthroline and sucrose were adopted as carbon precursors. The carbon was synthesized by mixing 1 g of carbon precursor and 0.5 g of silica in acetone or ethanol (20 mL) depending on the salt solubility. After 2 h, 250 μL of H<sub>2</sub>SO<sub>4</sub> was added during the impregnation process for accelerated the carbon precursor oligomerization. The solution was dried in oven overnight at 70 °C or until completely solvent evaporation. The substrate was thermally treated in a quartz tube in an argon-controlled atmosphere; for desorbing all residues as oxygen or water the substrate was heated at 100 °C for 1 h and thence pyrolyzed with a ramp of 5 °C until 950 °C for 2 h. The system is then allowed to cool down to room temperature. The silica in the crude product was totally removed by chemical etching in a 20 mL solution of sodium ethanoate (EtOH/NaOH) for 3 days at room temperature. The etching process was supported by sonication and the complete removal of silica was confirmed by XPS and TGA analysis (Figure S7). The resulting carbon is then separated by vacuum filtration on a nylon nanometric filter (GVS, nylon 0.2 mm, 47 mm membrane diameter). Four samples were synthesized with the same procedure but varying the carbon precursor and the silica template: MC-P200 from sucrose+silica P200; NMC-P200 from 1,10 phenanthroline+silica P200, NMC-PA from 1,10-phenanthroline+silica PA and nMC-PA from sucrose+silica PA.

### Physico-Chemical Characterization

BET analysis, Isotherm and Pore distribution were performed with Nitrogen Adsorption-Desorption at 77 K using Micromeritics ASAP2020. The surface area was determinate by the desorption curve in a multipoint BET (Brunauer-Emmett-Teller) analysis, pore distribution was analysed with a DFT model, specific for the matrix structure obtained. Thermogravimetric analyses (TGA) were performed using Q500IRTGA, the analyses were obtaining with a ramped temperature of 5 °Cmin<sup>-1</sup> between 50 °C until 700 °C in a controlled nitrogen atmosphere. Elemental analysis (EA) was carried out using a Thermo Scientific Flash 2000. Transmission electron microscopy (TEM) images were obtained by using a FEI Tecnai G2 transmission electron microscope operating at 100 kV. X-ray photoemission spectroscopy (XPS) measurements were performed in an UHV chamber (base pressure < 5 × 10<sup>-9</sup> mbar), equipped with a double anode X-ray source (omicron DAR-400), a hemispherical electron analyzer (omicron EIS-125) at r.t., using non-monochromatized Mg-Kα radiation (hν = 1253.6 eV) and a pass energy of 50 eV

and 20 eV for the survey and the single spectral windows, respectively. The calibration of the Binding Energy (BE) scale. To perform XPS measurements, 2.5 mg of the MC powders were dispersed in 1 mL of ethanol and then sonicated for 10 min in order to obtain a disperse powders; the solutions were then drop-casted onto polycrystalline copper (with a diameter of 6 mm). Raman scattering experiments were conducted with a homebuilt Macro-Raman setup. The excitation wavelength was 514 nm. The size of the laser spot at the sample was about 3 mm by 80 μm and the power at the sample about 12 mW (Intensity = 5 W cm<sup>2</sup>). Cyclohexane was used as a frequency standard for the calibration of the Raman shift. Every spectrum was acquired as the average of a minimum number of 10 spectra with a minimum of 10 s integration time. A minimum of three points on the sample was recorded and all spectra turned out to be identical. Scanning Electron Microscopy images were obtained using a Zeiss Supra 35VP Gemini scanning electron microscope operating at 5 kV. X-ray Diffraction (XRD) patterns were recorded in the diffraction angular range 5 – 55° 2θ by a Philips X'Pert PRO diffractometer, working in the reflection geometry and equipped with a graphite monochromator on the diffracted beam (Cu-Kα radiation).

### Electrochemical Characterization

The electrochemical response of the carbons described in the previous section has been investigated by a two-electrode symmetric cell, (referred as BOLA) composed by a Teflon case with stainless steel current collectors. The electrochemical tests were performed in a thermostatic oven at 30 °C using a BioLogic VSP multichannel potentiostat/galvanostat/FRA. A fiber glass filter Whatmann GF/F was chosen as separator and the ionic liquid Pyr<sub>1,201</sub> TFSI (Solvionic, 99.5%) as the electrolyte, the selected binder was Teflon. The electrodes were prepared starting from a dispersion of the active carbon, the conductive Super P 45 together with the Teflon suspension (60% Dupont), in 10 mL of Ethanol under vigorous stirring for 2 h. The temperature has been increased at 60 °C to obtain a carbon paste that it has been used to prepare the electrodes. The resulting carbonaceous composite has been pressed and cut on an 0.9 cm of diameter carbon-coated aluminium grid that has been used as current collector. After, the electrode-grid system has been pressed using a pressure of 2000 psi for 1 minute. The mass loading of each tested carbon is reported in Table S2. The electrodes have been dried at 120 °C for 16 h under dynamic vacuum to eliminate the presence of water.

### Acknowledgements

The research leading to these results has received funding from the University of Padova (Attrezzature scientifiche finalizzate alla ricerca – 2015). F.P. and F.S. acknowledge the Italy-South Africa joint Research Programme 2018–2020 (Italian Ministers of Foreign Affairs and of the Environment) and Fondazione CARISBO (Progetto Bando Ricerca n°354)

### Conflict of Interest

The authors declare no conflict of interest.

**Keywords:** carbon · electrochemistry · ionic liquid · nitrogen doped · supercapacitor

- [1] D. S. Su, S. Perathoner, G. Centi, *Chem. Rev.* **2013**, *113*, 5782–5816.
- [2] K. S. Lathi, D.-H. Park, K. Al-Bahily, W. Cha, B. Viswanathan, J.-H. Choy, A. Vinu, *Chem. Soc. Rev.* **2017**, *46*, 72–101.
- [3] R. Brandiele, M. Zerbetto, M. C. Dalconi, G. A. Rizzi, A. A. Isse, C. Durante, A. Gennaro, *ChemSusChem* **2019**, *12*, 4229–4239.
- [4] V. Perazzolo, R. Brandiele, C. Durante, M. Zerbetto, V. Causin, G. A. Rizzi, I. Cerri, G. Granozzi, A. Gennaro, *ACS Catal.* **2018**, *8*, 1122–1137.
- [5] G. Daniel, E. Foltran, R. Brandiele, L. Nodari, R. Pilot, E. Menna, G. A. Rizzi, A. A. Isse, C. Durante, A. Gennaro, *J. Power Sources* **2018**, *402*, 434–446.
- [6] Q. Abbas, R. Raza, I. Shabbir, A. G. Olabi, *J. Sci. Adv. Mater. Devices* **2019**, *4*, 341–352.
- [7] D. Zhang, J. Wang, C. He, Y. Wang, T. Guan, J. Zhao, J. Qiao, K. Li, *ACS Appl. Mater. Interfaces* **2019**, *11*, 13214–13224.
- [8] Y. Zhang, B. Yu, J. Zhang, X. Ding, J. Zeng, M. Chen, C. Wang, *ChemElectroChem* **2018**, *5*, 2142–2149.
- [9] X. Chen, J. Gao, B. Hu, K. Li, L. Kong, *ChemElectroChem* **2019**, *6*, 2648–2658.
- [10] N. Deka, J. Barman, J. Deka, K. Raidongia, G. K. Dutta, *ChemElectroChem* **2019**, *6*, 3327–3336.
- [11] Z. Zhai, B. Ren, Y. Zheng, Y. Xu, S. Wang, L. Zhang, Z. Liu, *ChemElectroChem* **2019**, *6*, 5993–6001.
- [12] V. Perazzolo, C. Durante, R. Pilot, A. Paduano, J. Zheng, G. A. Rizzi, A. Martucci, G. Granozzi, A. Gennaro, *Carbon* **2015**, *95*, 949–963.
- [13] Y. Zhai, Y. Dou, D. Zhao, P. F. Fulvio, R. T. Mayes, S. Dai, *Adv. Mater.* **2011**, *23*, 4828–4850.
- [14] C. Liang, Z. Li, S. Dai, *Angew. Chem. Int. Ed.* **2008**, *47*, 3696–3717.
- [15] X. Sheng, N. Daems, B. Geboes, M. Kurttepelj, S. Bals, T. Breugelmans, A. Hubin, I. F. J. Vankelecom, P. P. Pescarmona, *Appl. Catal. B* **2015**, *176*, 212–224.
- [16] E. Trevisanello, F. De Bon, G. Daniel, F. Lorandi, C. Durante, A. A. Isse, A. Gennaro, *Electrochim. Acta* **2018**, *285*, 344–354.
- [17] A. Stein, S. G. Rudisill, N. D. Petkovich, *Chem. Mater.* **2014**, *26*, 259–276.
- [18] M. Inagaki, M. Toyoda, Y. Soneda, S. Tsujimura, T. Morishita, *Carbon* **2016**, *107*, 448–473.
- [19] Y. Fang, D. Gu, Y. Zou, Z. Wu, F. Li, R. Che, Y. Deng, B. Tu, D. Zhao, *Angew. Chem. Int. Ed.* **2010**, *49*, 7987–7991.
- [20] Y. Huang, H. Cai, D. Feng, D. Gu, Y. Deng, B. Tu, H. Wang, P. A. Webley, D. Zhao, *Chem. Commun.* **2008**, 2641.
- [21] U. B. Nasini, V. Gopal Bairi, S. Kumar Ramasahayam, S. E. Bourdo, T. Viswanathan, A. U. Shaikh, *ChemElectroChem* **2014**, *1*, 573–579.
- [22] V. Perazzolo, C. Durante, A. Gennaro, *J. Electroanal. Chem.* **2016**, *782*, 264–269.
- [23] L. Perini, C. Durante, M. Favaro, V. Perazzolo, S. Agnoli, O. Schneider, G. Granozzi, A. Gennaro, *ACS Appl. Mater. Interfaces* **2015**, *7*, 1170–1179.
- [24] R. Brandiele, C. Durante, M. Zerbetto, N. Vicentini, T. Kosmala, D. Badocco, P. Pastore, G. A. Rizzi, A. A. Isse, A. Gennaro, *Electrochim. Acta* **2018**, *277*, 287–300.
- [25] M. Favaro, L. Perini, S. Agnoli, C. Durante, G. Granozzi, A. Gennaro, *Electrochim. Acta* **2013**, *88*, 477–487.
- [26] M. Favaro, F. Carraro, M. Cattelan, L. Colazzo, C. Durante, M. Sambì, A. Gennaro, S. Agnoli, G. Granozzi, *J. Mater. Chem. A* **2015**, *3*, 14334–14347.
- [27] G. Tuci, C. Zaffaroni, A. Rossin, A. Milella, L. Luconi, M. Innocenti, L. Truong Phuoc, C. Duong-Viet, C. Pham-Huu, G. Giambastiani, *Chem. Mater.* **2014**, *26*, 3460–3470.
- [28] J. Wu, H. Yang, *Acc. Chem. Res.* **2013**, *46*, 1848–1857.
- [29] Z. Bi, Q. Kong, Y. Cao, G. Sun, F. Su, X. Wei, X. Li, A. Ahmad, L. Xie, C.-M. Chen, *J. Mater. Chem. A* **2019**, *7*, 16028–16045.
- [30] B. Sun, G. Zhou, H. Zhang, *Prog. Solid State Chem.* **2016**, *44*, 1–19.
- [31] V. Perazzolo, E. Grądzka, C. Durante, R. Pilot, N. Vicentini, G. A. Rizzi, G. Granozzi, A. Gennaro, *Electrochim. Acta* **2016**, *197*, 251–262.
- [32] A. C. Ferrari, J. Robertson, *Phys. Rev. B* **2000**, *61*, 14095–14107.
- [33] X. Wei, X. Jiang, J. Wei, S. Gao, *Chem. Mater.* **2016**, *28*, 445–458.
- [34] H. Liu, H. Song, X. Chen, S. Zhang, J. Zhou, Z. Ma, *J. Power Sources* **2015**, *285*, 303–309.
- [35] C. Arbizzani, M. Biso, D. Cericola, M. Lazzari, F. Soavi, M. Mastragostino, *J. Power Sources* **2008**, *185*, 1575–1579.
- [36] M. Lazzari, F. Soavi, M. Mastragostino, *J. Electrochem. Soc.* **2009**, *156*, A661.
- [37] M. Lazzari, F. Soavi, M. Mastragostino, *Fuel Cells* **2010**, *10*, 840–847.
- [38] B. E. Conway, *Electrochemical Supercapacitors: Scientific Fundamentals and Technological Applications*, Springer Science & Business Media, **2013**.

Manuscript received: January 17, 2020

Revised manuscript received: March 12, 2020

Accepted manuscript online: April 6, 2020

## 2.3 Novel electrolytes

In the latter part of this chapter, the investigation of a novel class of aqueous electrolytes, i.e., the Water In Salt Electrolyte (WISE), is reported. At first, aqueous solutions based on lithium bis-(trifluoromethane)sulfonimide (LiTFSI), which are the most investigated WISEs, have been studied with a focus on the stability of the current collectors. In subsection 2.3.1 a detailed electrochemical study on the corrosion of different current collectors (Ti, stainless steel, and Cu) in aqueous LiTFSi solutions from low concentration (0.5 m) up to WISE concentration (20 m) are reported. This activity has been carried out in collaboration with the group of Prof. M. Innocenti from the University of Florence and brought about the publication [4].

LiTFSI is an expensive salt, hence novel and cheap WISE formulations are required for practical exploitation of these electrolytes in EDLCs. Ammonium acetate (AmAc) -based WISE represents a valuable option. Therefore, I contributed to the study of the chemical-physical and electrochemical properties of AmAc WiSes, in collaboration with Mohammad Said El Halimi, a Ph.D. student at the University of Bologna, and the group of Prof. Calvaresi (University of Bologna). The experimental approaches and main results of this study have been published in [5].

### 2.3.1 Electrochemical stability of Ti, stainless steel and Cu current collector in water-in-salt based on LiTFSi

Steel, copper, and titanium current collectors' electrochemical behavior in aqueous solutions of lithium bis(trifluoromethanesulfonyl)imide (LiTFSI) at various concentrations, from 0.5 up to 20 m have been investigated by means of electrochemical characterization. In particular linear sweep voltammetries (LSV) and cyclic voltammetries at  $20 \text{ mVs}^{-1}$  were carried out to determine both the cathodic and the anodic stability limits of the different tested metals. The voltammetric anodic and cathodic limits were used to define the experimental conditions of chronoamperometry that consisted in applying different potentials over 30 mins. Microscopic analysis with SEM and compositional analysis with XPS were carried out by the group of Prof. Innocenti, to evaluate the surface modifications related to the electrochemical stress.

The Electrochemical stability window, evaluated from LSV of the stainless steel-based current collector, increases with the salt concentration. Values of 2.05 V for the 0.5 m, 2.16 V for the 5 m, 2.37 V for the 10 m, and 2.5 V for the 20 m LiTFSi aqueous solution were measured. Copper-based current collectors had undergone strong corrosion at each tested LiTFSi

concentration and for this reason, it wasn't possible to study its behavior in the cathodic region. The CV study of the copper-based current collector in the anodic region didn't show a clear trend with the salt concentration each featuring a higher value of the specific reduction current with respect to the stainless-steel current collectors.

Finally, a titanium-based current collector has been investigated. LSVs at increased salt concentration showed a higher potential window than those of the potential window of Titanium-based current collector increases with the salt concentration. Indeed, 2.66 V at 0.5 m, 2.67 V at 5 m, 2.81 V at 10 m, and 2.77 V at 20 m of LiTFSi solution in water have been found. Comparing the CVs of the stainless steel and the titanium at 20 mVs<sup>-1</sup> with 20 m of salt concentration, it was evident that the titanium-based current collector featured a higher electrochemical stability window, with a pronounced tendency of decreasing current during cycling in the cathodic region. Investigating the CVs study, it was evident the appearance of a plateau above 2.75 V has been related to the formation of a passivation layer.

The results of the electrochemical studies were confirmed by the SEM microscopic analysis that highlighted the corrosion in the copper-based current collector and the formation of a passivating layer for the titanium one. Overall, Titanium and stainless steel showed interesting behavior that allows them to be considered as good candidate current collectors for water in salt electrolyte-based electrochemical energy storage devices, while the evident corrosion of copper makes it a less desirable choice.

The experimental methods and the results of this study are reported in [4], here attached as the complete publication.



## Electrochemical stability of steel, Ti, and Cu current collectors in water-in-salt electrolyte for green batteries and supercapacitors

Walter Giurlani<sup>1</sup> · Luca Sergi<sup>1</sup> · Eugenio Crestini<sup>1</sup> · Nicola Calisi<sup>1</sup> · Federico Poli<sup>2</sup> · Francesca Soavi<sup>2</sup> · Massimo Innocenti<sup>1</sup>

Received: 8 September 2020 / Revised: 21 October 2020 / Accepted: 24 October 2020  
© The Author(s) 2020

### Abstract

The electrochemical behaviour of steel, copper, and titanium current collectors was studied in aqueous solutions of lithium bis(trifluoromethanesulfonyl)imide (LiTFSI) at various concentrations, from 0.5 up to 20 m. As the concentration of the electrolyte increases, the electrochemical window of water stability widens according to the “water-in-salt” concept. The metal grids have been studied electrochemically, both under anodic and cathodic conditions, by means of cyclic voltammetry and chronoamperometry. Subsequently, a microscopic analysis with SEM and compositional analysis with XPS was carried out to evaluate the surface modifications following electrochemical stress. We found that copper is not very suitable for this kind of application, while titanium and steel showed interesting behaviour and large electrochemical window.

**Keywords** Water-in-salt · Current collector · Electrochemical stability · Battery · Supercapacitor

### Introduction

Lithium-ion batteries (LIB) are nowadays one of the most important energy storage devices and are currently dominating the consumer electronic market. They have been indicated as the most promising option for the next generation of hybrid and electric vehicles but their possible application for this purpose is still uncertain today mainly because of concerns raised over their safety, cost, and environmental impact [1]. The electrolytes presently used in commercial LIBs are based

on mixtures of organic solvents and contain lithium hexafluorophosphate (LiPF<sub>6</sub>) as lithium salts [2]. The use of these electrolytes allows high performance in terms of energy and cycle life. However, since these electrolytes are flammable and volatile, their use poses serious safety risks and strongly reduces the temperature range of use. Furthermore, it has also been observed that they are particularly aggressive in terms of corrosion towards the working electrodes, under certain operating conditions, consequently reducing the cell performance. Therefore, substantial costs of these systems are incurred not only directly by these electrolytic components but also to a greater extent by the safety management required for the dangerous combination of flammable electrolytes and energy-intensive electrodes that are long-lasting and resistant to corrosion [3, 4]. The main reason for using classical organic electrolytes (acetonitrile or carbonates) was that it permits to design devices with a cell voltage of 2.7–2.8 V.

These organic electrolytes display favourable properties on the negative electrode side, including the formation of a lithium conducting passivation layer on the surface of the electrode, the so-called solid electrolyte interphase (SEI). The presence of this layer extends the electrochemical stability window of the electrolyte at the negative electrode, even with very reducing anode materials, such as metallic Li and lithiated graphite. However, on the positive electrode side, the stability window of these systems limits the number of

---

In memory of Prof. Roberto Marassi, a great scientist and innovator in electrochemistry for energetics and beyond

---

**Supplementary Information** The online version contains supplementary material available at <https://doi.org/10.1007/s10008-020-04853-2>.

---

✉ Walter Giurlani  
walter.giurlani@unifi.it

✉ Francesca Soavi  
francesca.soavi@unibo.it

<sup>1</sup> Department of Chemistry “Ugo Schiff”, Università degli Studi di Firenze, via della Lastruccia 3, 50019 Sesto Fiorentino, FI, Italy

<sup>2</sup> Dipartimento di Chimica “Giacomo Ciamician”, Alma Mater Studiorum Università di Bologna, Via Selmi 2, 40126 Bologna, Italy

applicable active materials, especially due to the limited stability of most of these compounds at potentials exceeding 5 V [5].

As a possible solution to these problems, researchers have proposed in recent years the use of aqueous electrolytes inside the cells of lithium batteries. However, pure water as a solvent shows a window of thermodynamic stability too narrow of only 1.23 V, as defined by the decomposition reaction of water [6], which imposes a restriction on the choice of electrochemical couples and consequently the practical energy output of aqueous battery chemistries and cell voltage [7].

On the other hand, the aqueous solutions display important advantages, e.g. higher conductivity, non-flammability of the electrolyte, and low cost, both regarding the electrolyte itself and the separator material. The higher ion conductivity increases the high-power capability of electrochemical cells based on aqueous electrolyte, recently demonstrated with LiCoO<sub>2</sub> by Cui et al. and with LiMn<sub>2</sub>O<sub>4</sub> and hybrid systems by Wu et al. [8, 9].

In general, the aim of the studies in recent years has been to be able to design a system with aqueous electrolytic solutions that have the same performance as cells with organic solvents, and therefore a comparable electrochemical stability window, but which are above all safer, longer lasting, and with less environmental impact.

Recently, relatively large stability windows of up to 3 V have been reported for highly concentrated, “water-in-salt”, aqueous solutions of lithium bis(trifluoromethylsulfonyl)imide (LiTFSI) providing an opportunity for the development of high-voltage aqueous batteries [10, 11].

LiTFSI (lithium bis(trifluoromethylsulfonyl)imide) was chosen as the salt because of its high solubility in water (> 20 m at 25 °C) and high stability against hydrolysis. The “water-in-salt” definition applies when the LiTFSI concentration is above 5 m, since the salt exceeds the solvent by weight and volume. In this binary system, the average number of water molecules available to solvate each ion is much lower than the “solvation numbers” which are well established in conventional electrolytes (~ 1.0 m) [12, 13]. The solvation shell is completely different from classical aqueous electrolytes: Li<sup>+</sup> ions are not only surrounded by water molecules but rather by TFSI<sup>-</sup> anions together with a limited number of water molecules, depending on the salt concentration. Interionic attractions become more pronounced than solvent-ion interactions causing unusual physicochemical properties. Particularly important is the interphase chemistry on the electrode surfaces which could be modified as a direct consequence of the different cation solvation shell structure. The overall stability window expands as the LiTFSI concentration increases, with both oxygen and hydrogen evolution potentials pushed well beyond the thermodynamic stability limits of water, suppressing water splitting in an extended potential window of 3 V [14].

The first lab-scale batteries utilizing highly concentrated LiTFSI salt in water as the electrolyte were fabricated with stainless-steel current collectors. However, aluminium (Al) is the preferred current collector material on the cathode side of non-aqueous lithium-ion batteries due to its much lower density, higher electronic conductivity, low cost, and the ability to be processed into thin foils by rolling [15–19].

The Pourbaix diagram of Al indicates thermodynamic stability, i.e. the range where passivation due to the air-formed aluminium oxide layer is avoided, only in a small pH range [20]. This small stability window has prevented the use of Al as the current collector in traditional aqueous batteries [21].

In this work, the limits of electrochemical stability of LiTFSI solutions at increasing concentration were evaluated with different metals (steel, copper, and titanium) in order to evaluate their possible use as an anode or as a cathode current collector in aqueous lithium-ion cell. The tests consisted in cyclic voltammetry (CV) and potential step (chronoamperometry) experiments complemented with scanning electron microscopy (SEM) and X-ray photoelectron spectroscopy (XPS) analyses. CVs provided the potential used to define the experimental conditions of chronoamperometry that was used to accelerate current collector ageing and side reactions involving the electrolyte. The corrosion resistance of the metal samples was monitored by observing the trend of the recorded current, at a given potential, as a function of time, and the evolution of the metal surfaces after the ageing tests. The study demonstrates that, despite the recognized wide electrochemical stability of superconcentrated LiTFSI solutions, for practical applications it is important to evaluate the right combination between current collector and salt concentration.

## Experimental

### Materials

Three commercial meshes made of different metals were chosen as samples: steel (3SS5-050 ANF, Dexmet), titanium (5Ti-7-077, Dexmet), and copper (Grid-CTD-Cu-140mm, Lamart). Meshes of different materials had different thickness and holes; the effective contact area of each sample is reported in Table 1.

Lithium bis(trifluoromethanesulfonyl)imide (LiTFSI) salt, used as electrolyte, was purchased from Sigma-Aldrich and

**Table 1** Effective contact area per 1 cm<sup>2</sup> of sample

Sample	Contact area (cm <sup>2</sup> )
Copper	0.715
Steel	1399
Titanium	1369

used without further purifications. Solutions of 0.5, 5, 10, and 20 m (mol/kg) of LiTFSI in Milli-Q water were used.

All electrochemical tests were carried out in a glass cell with a three-electrode configuration (Fig. S1). Before each electrochemical measurement, the solution was deaerated with nitrogen for 30 min directly in the cell. Then, the bubbling was interrupted maintaining a nitrogen flow over the solution. Metal meshes with a  $1 \times 1 \text{ cm}^2$  section were used as working electrode (WE). Before each analysis, the samples were washed with acetone in ultrasonic bath, rinsed in ethanol, and left to dry.

Carbon paper (2050A-1050, Spectracarb) was used as counter electrode (CE). To increase the active area of the CE, a suspension of activated carbon was drop-casted on the carbon paper following this procedure: (i) 10 mg/mL of activated carbon (CV-XC72R, Fuel Cell Earth) was dispersed in 1-methyl-2-pyrrolidinone (Sigma-Aldrich), containing 1 mg/mL polyvinylidene difluoride (PVDF, Sigma-Aldrich) as a binder to keep the powder bound to the substrate; (ii) 0.5 mL of suspension, equivalent to 5 mg of activated carbon, was drop-casted on the carbon paper; (iii) the solvent was evaporated at 130 °C by placing the electrode on a heating plate; (iv) during the measurements, the counter electrode was wrapped in a glass microfiber filter (Whatman grade GF/A) to prevent any detachment. The high surface area capacitive counter electrode can balance the charge stored by the working electrode during the polarization of the latter and this avoids undesired side reaction at the counter electrode.

Silver wire was used as pseudo-reference electrode (RE), and all potentials were converted to the Li/Li<sup>+</sup> electrode scale. In text, we referred to positive and negative potential with respect to the equilibrium potential represented from the open-circuit potential, recorded before each electrochemical measurement.

The electrochemical tests were performed by a multi-channel potentiostat (Metrohm  $\mu$ -autolab, model Fra-2 Type 3). Cyclic voltammetric scans (CV) were carried out in order to evaluate the anodic and cathodic stability limits of the different metals in LiTFSI aqueous solutions at increased salt concentration and at a scan rate of 20 mV/s. Before CV, the relative OCP (open-circuit potential) value was calculated for each metal, which is characteristic of each material. Then, two measurements were then carried out towards only negative potentials or only positive potentials with respect to the previously recorded OCP value. The potential of the voltammetric cycles was increased until very intense anode or cathode currents were observed. The voltammetric anodic and cathodic limits were used to define the experimental conditions of chronoamperometry that consisted in applying different potentials over 30 min. The current density was calculated considering the effective area of the metals (Table 1).

## Microscopic and spectroscopic characterization

Scanning electron microscopy (SEM) analyses were performed with a Hitachi S-2300 equipped with a Thermo Scientific Noran System 7 detector and analysed with Pathfinder software.

X-ray photoelectron spectroscopy (XPS) was used to evaluate the superficial composition of the samples before and after the chronoamperometric stress. The instrument is equipped with a non-monochromatic X-ray source (VSW Scientific Instrument Limited model TA10, Al K $\alpha$  radiation, 1487.7 eV) set to work at 120 W (12 kV and 10 mA) and a hemispherical analyser (VSW Scientific Instrument Limited model HA100, Manchester, UK). The analyser was equipped with a 16-channel detector and a dedicated differential pumping system maintaining the pressure in the chamber to the  $10^{-8}$  mbar range. The pass energy was set to 22 eV. The measured spectra were analysed using CasaXPS software (version 2.3.19, Casa Software Ltd., Teignmouth, UK). The inelastic background was subtracted using Shirley's method [22], and mixed Gaussian and Lorentzian contributions were used for each component. Calibration of the spectra was obtained by shifting to 284.8 eV, the lowest component relative to the 1s transition of carbon for adventitious carbon [23].

Before SEM and XPS measurements, the metals were rinsed with water and dried.

## Results and discussion

### Electrochemical measurements

#### Steel

Figure 1a reports the linear sweep voltammetries carried out at 20 mV/s with steel in LiTFSI solutions at different salt concentrations. Increasing the electrolyte concentration from 0.5 up to 20 m the stability increases in both the anodic and in the cathodic branch of the voltammogram. The anodic onset does not differ much between the three solutions with lower concentration ( $\approx 4.25$  V) but it increases by 10 mV in the case of the 20 m solution. On the other hand, the cathodic onset shows a greater shift with the increase of the electrolyte concentration, reaching 1.84 V for 20 m solution, for an overall window of 2.50 V.

Figure 1b reports the CV run in the lowest potential range after the first linear sweep experiments. The presence of anodic and cathodic peaks suggests that during the first cathodic scan, redox couples are formed on the metal surface as the result of the decomposition of the salt. Increasing the salt concentration, the peak current decreases significantly as well as the potential related to H<sub>2</sub> evolution shifts to more negative values. This is in agreement with the parallel decrease of H<sub>2</sub>O concentration.

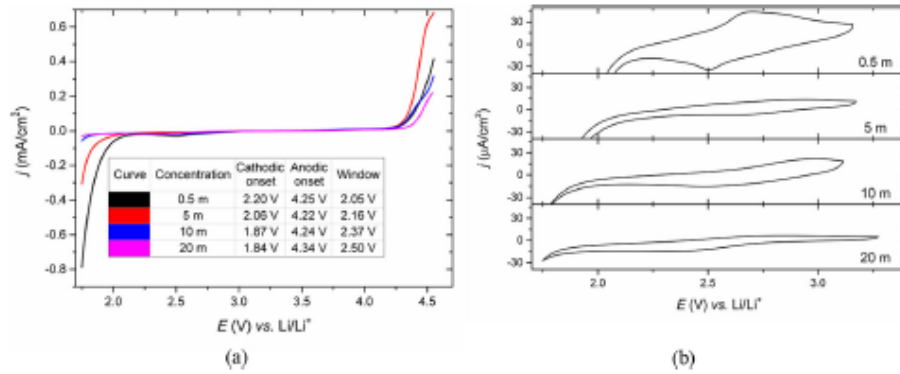


Fig. 1 (a) Linear sweep voltammograms and (b) CVs in the lowest potential range of steel in aqueous LiTFSI solutions at different salt concentrations

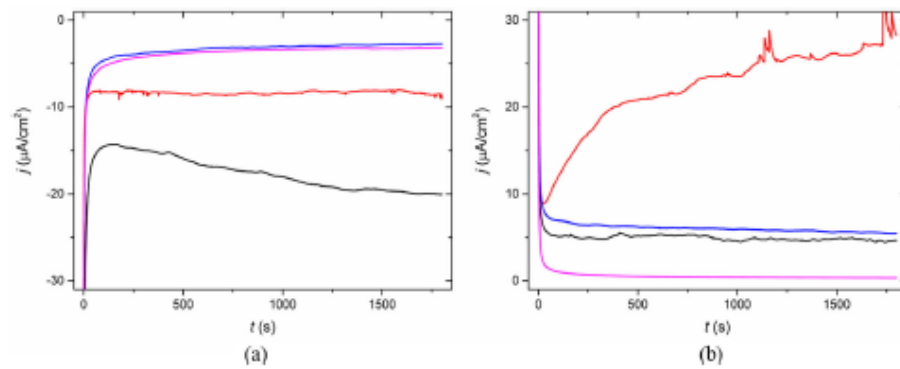


Fig. 2 Chronoamperometric measurements performed at constant potential of (a) 2.25 V (cathodic) and (b) 4.25 V (anodic). Black, 0.5 m; red, 5 m; blue, 10 m; pink, 20 m

We investigate the evolution of the degradation process occurring on the surface of steel by keeping the electrode at different potentials over 30 min and recording the current. The same potential was used for each

solution to compare the different behaviours. The cathodic ageing was carried out at 2.25 V, while the anodic one was performed at 4.25 V. The cathodic tests (Fig. 2a) showed that the current decreased and was

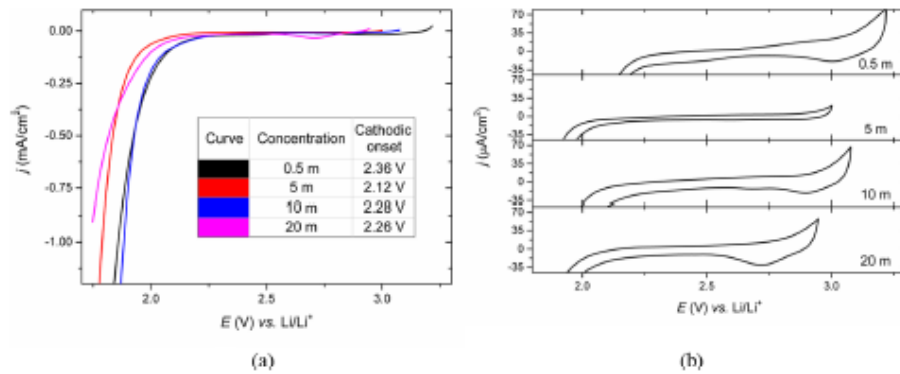
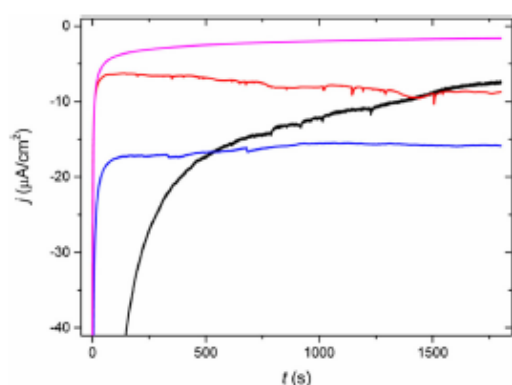


Fig. 3 (a) Linear sweep voltammograms and (b) CVs in the lowest potential range of copper in aqueous LiTFSI solutions at different salt concentrations





**Fig. 4** Chronoamperometric measurements performed at constant potential of 2.25 V (cathodic). Black, 0.5 m; red, 5 m; blue, 10 m; pink, 20 m

more stable for the electrolytic solutions with the highest concentration. The curves recorded with 10 m and 20 m solutions almost overlapped. As it concerns the anodic test (Fig. 2b), the lowest current that was negligible after 30 min was obtained by far using the solution with 20 m concentration. During the anodic stresses, the trend did not completely follow that of concentrations. In fact, unexpectedly, in the 5 m solution, the current did not reach a stationary value but increased during the tests, therefore suggesting that the steel was going against corrosion much more quickly than in the 0.5 m solution.

**Copper**

Unlike the other metals, copper undergoes through strong corrosion for every concentration of the salt if the applied potential is more positive than the OCP. For this reason, we recorded the behaviour of copper only in the cathodic potential

range. The onset of the reduction of hydrogen started at potentials more positive than those observed in the case of steel. Moreover, the onset potentials trend did not follow that of the salt concentration (Fig. 3a). Indeed, in the 0.5 m and 10 m solutions, copper featured a similar behaviour with an anodic limit more positive than that achieved with the 5 m and 20 m solutions. The CV (Fig. 3b) currents are higher with copper than with steel even for high salt concentration. This indicates that the decomposition of the electrolyte is more pronounced in the case of copper with respect to steel. Also, the presence of CV peaks indicates that the passivation layer eventually formed on the metal is not stable. Indeed, a stable passivating layer would insulate the electrode from the solution and, therefore, give rise to very low voltammetric currents.

The chronoamperometric measurement (Fig. 4) was carried out applying a fixed potential of 2.25 V. Also, in this case, as for the onset potentials, there is no direct correlation between the chronoamperometric behaviour and the concentration of the solution. Despite this, solutions with a lower concentration seem to be slower to reach a constant current, suggesting the presence of corrosion reactions at the interphase. The 10 m solution reaches a steady current quickly but maintaining a considerably high value. Only in the case of the 20 m solution does it appear that a stable passivation layer has formed, showing a steady trend and low current values.

**Titanium**

The behaviour of titanium was investigated by linear sweep voltammetry starting from the OCP towards 1.75 V and 5.15 V (Fig. 5). The overpotential for hydrogen evolution is greater on titanium with respect to the other investigated metals. In fact, at low electrolyte concentration, the cathodic current onset is below 2 V. Notably, the onset of reduction reactions is the same for all the solutions and is measured as  $2.04 \pm 0.04$  V. On the other hand, the anodic current onset shifts to more positive potentials with the increase of the salt

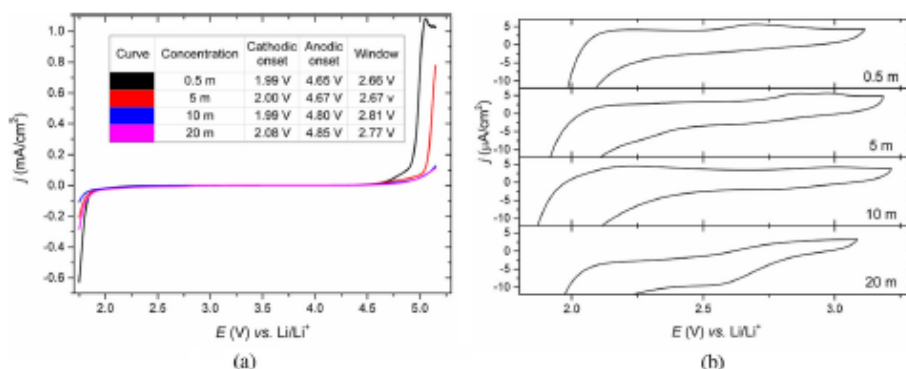


**Fig. 5** (a) Linear sweep voltammeteries and (b) CVs in the lowest potential range of titanium in aqueous LiTFSI solutions at different salt concentrations

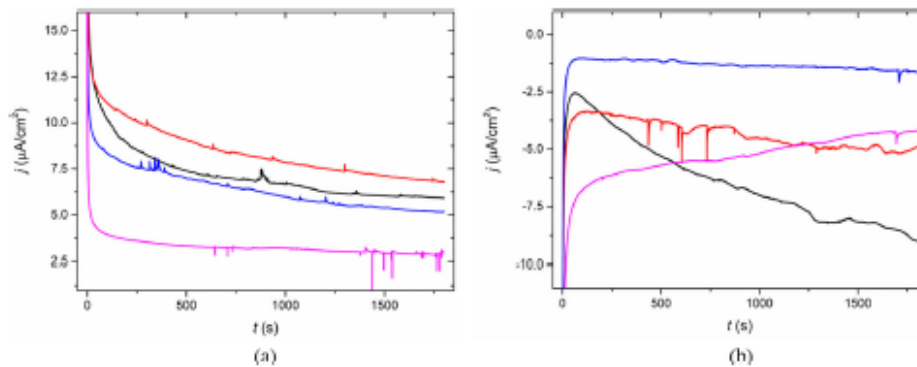


**Fig. 6** Chronoamperometric measurements performed at constant potential of (a) 2.15 V (cathodic) and (b) 4.75 V (anodic). Black, 0.5 m; red, 5 m; blue, 10 m; pink, 20 m

concentration (Fig. 5a). Observing the CVs recorded between the OCP and the cathodic limit (Fig. 5b), in the 20 m solution, there is an initial onset at 2.75 V followed by a plateau suggesting the formation of a passivating layer on the metal surface [10].

The cathodic and anodic chronoamperometric measurements were carried out at potentials of 2.15 V and 4.75 V respectively. Under the cathodic stress (Fig. 6a), the decomposition of salt is evident for the 0.5 m and 5 m solution as it is indicated by the increase of current over time. The same trend, although less evident, can also be noticed in the case of the 10 m solution. On the other hand, the 20 m solution, compatibly with what emerged from the CV, initially shows higher currents, but then they decrease as the passivation layer develops. During the anodic stress (Fig. 6b), the current tends to decrease over time regardless salt concentration. A stable condition is achieved with the solutions with higher concentrations, and mainly with the 20 m solution.

Figure 7 compares two consecutive CVs carried out between the OCP and the anodic limit with titanium and steel in 20 m solution. The figure highlights the higher anodic stability of titanium with respect to steel. Furthermore, during the second cycle, the current decreases considerably in the case of titanium, while it remains almost unchanged in the case of the steel collector.

The different anodic behaviour of titanium and steel can be explained by considering their different inherent reactivity towards the formation of surface passivating layers. It is known that with titanium it is possible going to very positive potentials, in some applications even tens of volts are used [24]. This is due to the formation of a compact titanium oxide layer which protects the metal surface. Titania is not an insulator, and in fact it is used as a support in solar and fuel cells; however, the higher the potential applied, the greater the thickness of oxide that is formed, which has a considerably lower conductivity than metals [25], limiting the current flow. It can be argued that titania is formed on the titanium grid even

during the anodic scan in LiTFSI aqueous solution so that the 2nd cycle CV currents are lower than those of the first CV.

At the contrary, at positive potentials, steel forms porous and partially soluble iron oxides and hydroxides that do not insulate the metal surface. Hence, steel maintains high conductivity and a good connection with the electrolyte, which explains the overlapping voltammograms of the first and second CV cycle. Furthermore, the oxidation of the steel is, at least in part, reversible. This is suggested by the reduction peak that is present at potentials lower than 3.5 V and that is not present in the case of titanium. Indeed, the formation of titanium oxide is irreversible.

#### Microscopic characterization

The SEM analysis of the samples performed after the chronoamperometric stress did not report any significant sign of corrosion with respect to the fresh samples that were not subjected to any stress. This observation confirms the

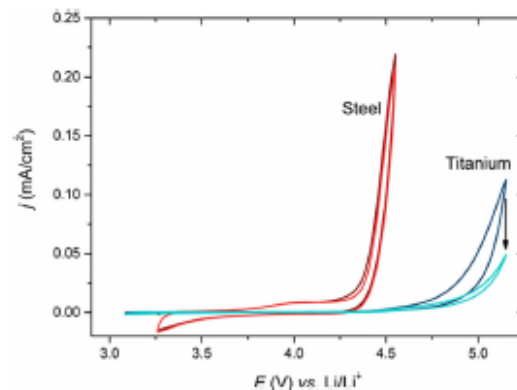


**Fig. 7** Consecutive CVs on Ti and steel collector in 20 m aqueous solution of LiTFSI in the high potential range dark red, 1st cycle steel; light red, 2nd steel; dark blue, 1st cycle Ti; light blue, 2nd cycle Ti

formation of a thin passivation layer on the collectors. In Fig. 8, we reported the SEM analysis performed on the untreated collectors meshes (a, steel; d, copper; g, titanium) and the collector after the chronoamperometric, stress, anodic as well as cathodic in the 0.5 m solution. The remaining SEM analysis can be found in the [supplementary materials](#).

Only the copper mesh subjected to anodic potential looks visibly eroded (Fig. 8e). The untreated steel sample (Fig. 8a) presents some dark areas on the surface; the same stains are steel present also in some steel samples after the cathodic stress, while we did not find them in the samples subjected to anodic stress. On the

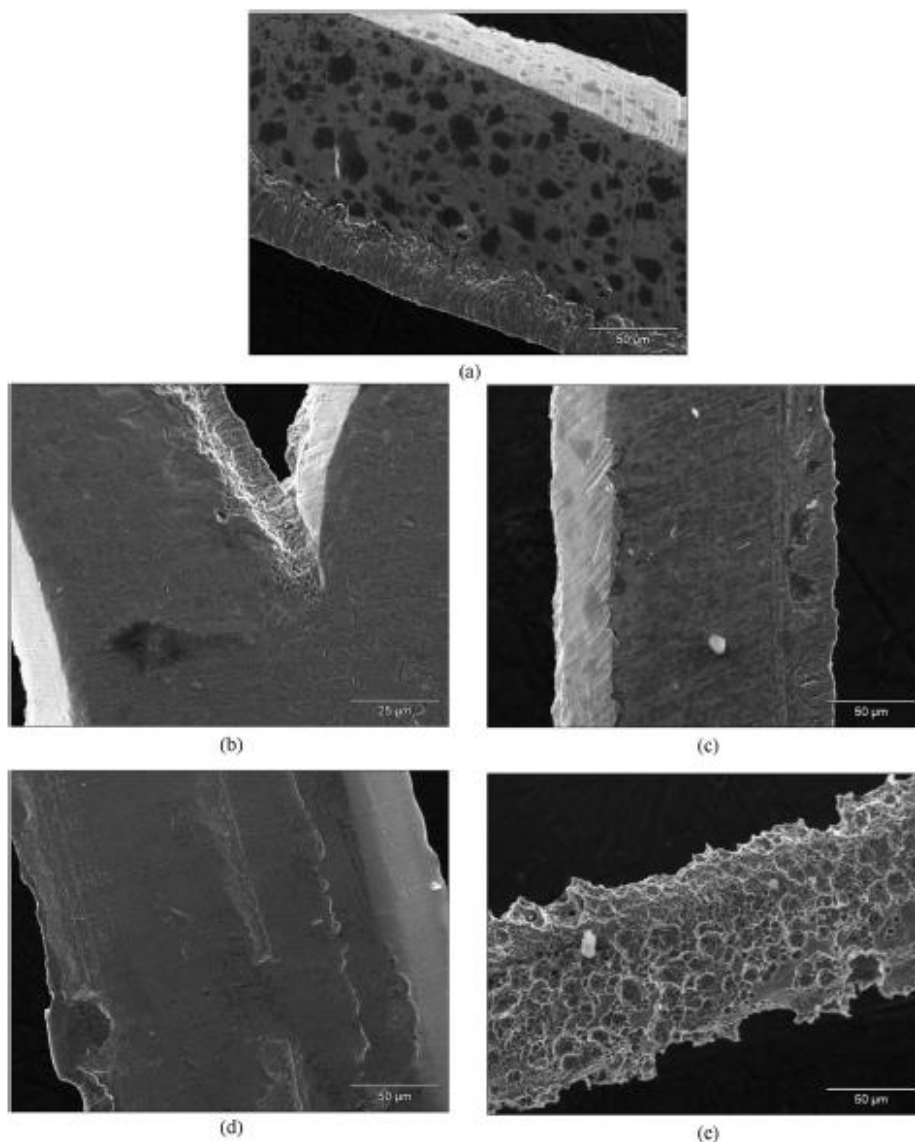


**Fig. 8** SEM analysis of the untreated collectors and the cathodic and anodic stressed collectors in 0.5 m solution, the remaining analyses are reported in the [supplementary material](#). (a) Untreated steel; (b) cathodically stressed steel; (c) anodically stressed steel; (d) untreated copper; (e)

cathodically stressed copper; (f) anodically stressed copper; (g) untreated titanium; (h) cathodically stressed titanium; (i) anodically stressed titanium

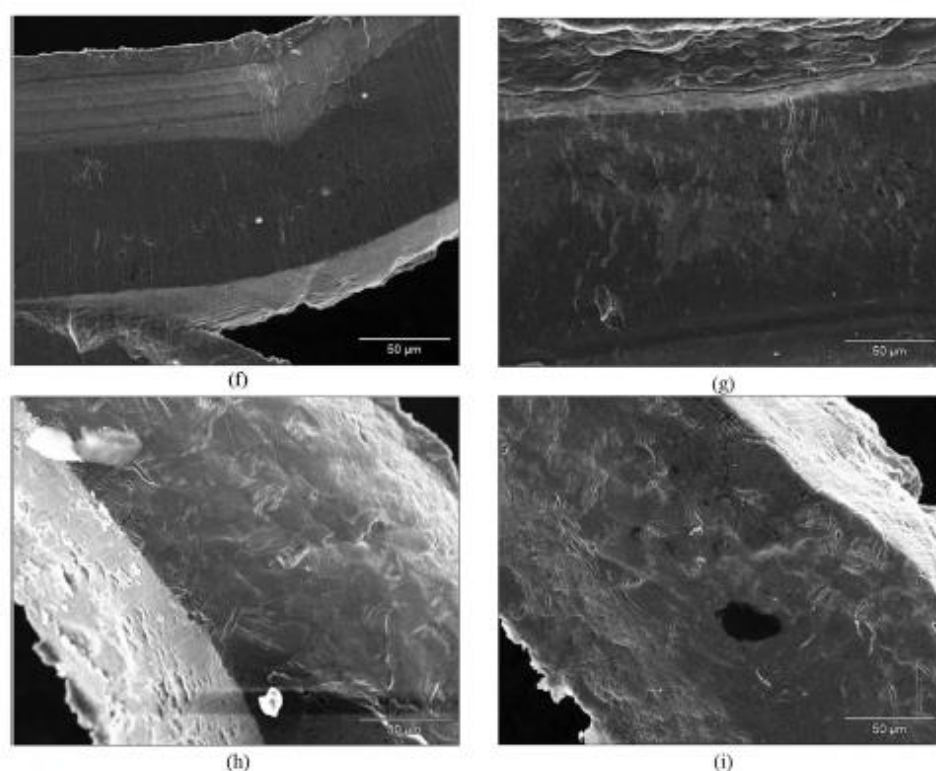


Fig. 8 (continued)

surface of the electrode, we did not find many electrolyte residues.

#### Spectroscopic characterization

XPS analyses were used to characterize the surface of titanium and steel samples, which exhibited better electrochemical stability with respect to copper. The spectroscopic characterization was performed on fresh meshes of the two materials, used as references, and on the samples tested by anodic and cathodic chronoamperometric ageing in 0.5 m and 20 m solutions, representing the extreme of the investigation.

The analysis of steel samples in the region of Fe (Fig. 9a) showed three components in zone 2p of iron at 706.5 eV, 710 eV, and 712 eV corresponding to metallic iron and iron oxide/hydroxide. Due to the very superficial nature of the technique, the metal iron signal is not very intense. The iron oxide signal is present in all the samples, even in the reference because of the natural passivation layer present on the collector surface. The amount of Fe(II) is substantially unchanged between the reference and the sample subjected to 2.15 eV (cathodic stress) in the 20 m solution; in all other cases, the signal is more intense with respect to the reference. However,

by comparing this quantity for the anodic stresses conducted at 4.25 eV, it is observed that the sample analysed in the 20 m solution is less oxidized.

About the steel sample, greater attention was paid to the signals coming from the presence of iron and oxygen, as the former is the element constituting the steel in greater quantities and the oxygen is directly involved in the determination of the degree of collector corrosion.

The presence of oxygen in the surface layer has been confirmed in the transition region 1s (Fig. 9b). In this case, we found the convolutions of 4 signal to the overall peak; the contribution at lower energies around the value of 530 eV is compatible with an iron oxide  $\text{FeO}/\text{Fe}_2\text{O}_3$  structure confirming the trend discussed for the Fe(II) signal.

The measurements carried out on the titanium collectors revealed a similar trend to what was observed on the steel specimens. In the 2p transition region of Ti (Fig. 10), we found two contributions: one at 454 eV, corresponding to metallic titanium, and one at 458 eV, for the Ti(IV) specie. The amount of Ti(IV) is similar between the reference and the sample subjected to cathodic stress in the 20 m solution and increase a little in the case of 0.5 m solution. On the other hand, we found a large amount of titanium oxide in the

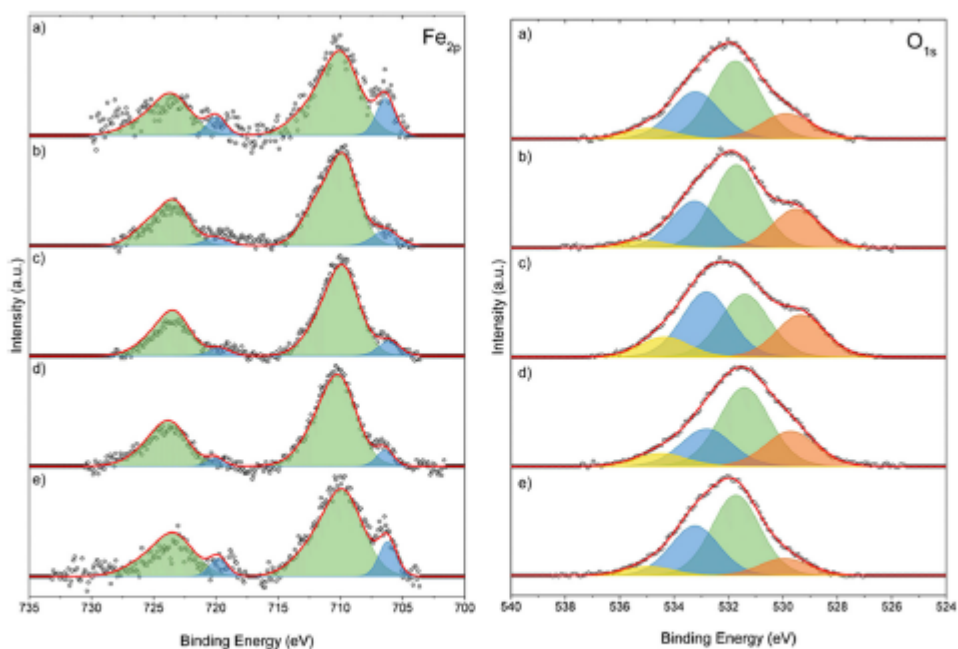


**Fig. 9** XPS measurement of steel samples in the Fe 2p region (left) and O 1s region (right): (a) untreated sample; (b) anodically treated sample in 0.5 m solution; (c) anodically treated sample in 20 m solution; (d) cathodically treated sample in 0.5 m solution; (e) cathodically treated sample in 20 m solution

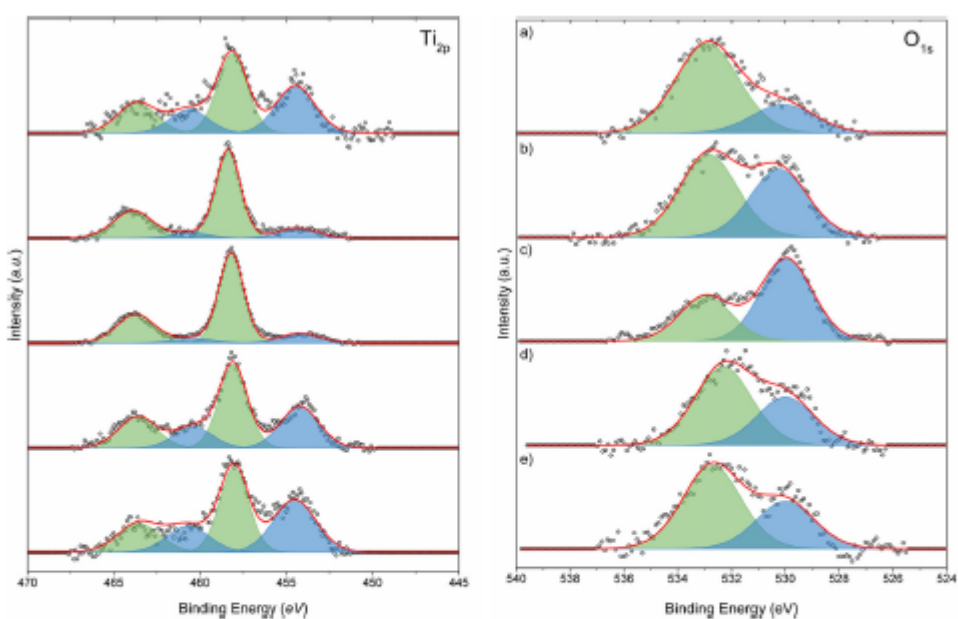


**Fig. 10** XPS measurement of titanium samples in the Ti 2p region (left) and O 1s region (right): (a) untreated sample; (b) anodically treated sample in 0.5 m solution; (c) anodically treated sample in 20 m solution; (d) cathodically treated sample in 0.5 m solution; (e) cathodically treated sample in 20 m solution

collectors subjected to anodic stress. Through the tabulated values of the various binding energy related to oxygen, the signal that appears at 530 eV is compatible with the TiO<sub>2</sub> species and follows the same trend of Ti(IV) signal.

## Conclusions

In this work, we studied the behaviour of different metal meshes for the application as current collectors in “water-in-salt” cells. In this type of electrolyte, the activity of the water is greatly reduced allowing to extend the electrochemical window. Nonetheless, the copper samples went through a rapid anodic corrosion and did not perform well even in the cathodic potential range. Steel and titanium on the other hand showed an electrochemical window much higher than 1.23 V, and of 2.50 V and 2.80 V respectively. Steel is better in the cathodic onset while titanium features a better anodic stability. Therefore, cells with different current collectors for the positive and negative electrodes could feature an even wider electrochemical stability window. In the case of titanium, the anodic window could be further enlarged thanks to the formation of a passivating and semi-conductive layer of titania, that, however, reduces and insulates the electrodes and might increase electrode impedance.

**Acknowledgements** The authors acknowledge the support that has been given from Freschi & Vangelisti S.r.l. The Italy-South Africa joint Research Programme 2018–2020 (Italian Ministers of Foreign Affairs and of the Environments) is also acknowledged.

**Funding** This research was funded by the PRIN (“Progetti di Ricerca di Rilevante Interesse Nazionale”), by the project “Novel Multilayered and Micro-Machined Electrode Nano-Architectures for Electrocatalytic Applications (Fuel Cells and Electrolyzers)”, grant number 2017YH9MRK and by the Italy-South Africa joint Research Programme 2018–2020. Open access funding provided by Alma Mater Studiorum - Università di Bologna within the CRUI-CARE Agreement.

**Open Access** This article is licensed under a Creative Commons Attribution 4.0 International License, which permits use, sharing, adaptation, distribution and reproduction in any medium or format, as long as you give appropriate credit to the original author(s) and the source, provide a link to the Creative Commons licence, and indicate if changes were made. The images or other third party material in this article are included in the article's Creative Commons licence, unless indicated otherwise in a credit line to the material. If material is not included in the article's Creative Commons licence and your intended use is not permitted by statutory regulation or exceeds the permitted use, you will need to obtain permission directly from the copyright holder. To view a copy of this licence, visit <http://creativecommons.org/licenses/by/4.0/>.

## References

- Dunn B, Kamath H, Tarascon J-M (2011) Electrical energy storage for the grid: a battery of choices. *Science* 334:928–935
- Scrosati B, Garche J (2010) Lithium batteries: status, prospects and future. *J Power Sources* 195(9):2419–2430
- Tarascon J-M, Armand M (2001) Issues and challenges facing rechargeable lithium batteries. *Nature* 414(6861):359–367
- Goodenough JB, Kim Y (2010) Challenges for rechargeable Li batteries. *Chem Mater* 22(3):587–603
- Lux SF, Terborg L, Hachmüller O, Placke T, Meyer HW, Passerini S, Winter M, Nowak S (2013) LiTFSI stability in water and its possible use in aqueous lithium-ion batteries: pH dependency, electrochemical window and temperature stability. *J Electrochem Soc* 160(10):A1694–A1700
- Kim H, Hong J, Park K et al (2014) Aqueous rechargeable Li and Na ion batteries. *Chem Rev* 114(23):11788–11827
- Wessells C, Huggins RA, Cui Y (2011) Recent results on aqueous electrolyte cells. *J Power Sources* 196(5):2884–2888
- Qu Q, Fu L, Zhan X, Samuelis D, Maier J, Li L, Tian S, Li Z, Wu Y (2011) Porous LiMn<sub>2</sub>O<sub>4</sub> as cathode material with high power and excellent cycling for aqueous rechargeable lithium batteries. *Energy Environ Sci* 4(10):3985
- Wang X, Hou Y, Zhu Y, Wu Y, Holze R (2013) An aqueous rechargeable lithium battery using coated Li metal as anode. *Sci Rep* 3(1):1401
- Suo L, Borodin O, Gao T et al (2015) “Water-in-salt” electrolyte enables high-voltage aqueous lithium-ion chemistries. *Science* 350:938–943
- Bu X, Su L, Dou Q, Lei S, Yan X (2019) A low-cost “water-in-salt” electrolyte for a 2.3 V high-rate carbon-based supercapacitor. *J Mater Chem A* 7(13):7541–7547
- Suo L, Borodin O, Wang Y, Rong X, Sun W, Fan X, Xu S, Schroeder MA, Cresce AV, Wang F, Yang C, Hu YS, Xu K, Wang C (2017) “Water-in-Salt” electrolyte makes aqueous sodium-ion battery safe, green, and long-lasting. *Adv Energy Mater* 7(21):1701189
- Dong Q, Yao X, Zhao Y, Qi M, Zhang X, Sun H, He Y, Wang D (2018) Cathodically stable Li-O<sub>2</sub> battery operations using water-in-salt electrolyte. *Chem* 4(6):1345–1358
- Larnelougue P, Bouchal R, Moudé E, Bodin C, Olarte M, le Vos S, Favier F, Fontaine O (2018) “Water-in-Salt” for supercapacitors: a compromise between voltage, power density, energy density and stability. *J Electrochem Soc* 165(3):A657–A663
- Suo L, Han F, Fan X, Liu H, Xu K, Wang C (2016) “Water-in-Salt” electrolytes enable green and safe Li-ion batteries for large scale electric energy storage applications. *J Mater Chem A* 4(17):6639–6644
- Kühnel R-S, Lübke M, Winter M, Passerini S, Balducci A (2012) Suppression of aluminum current collector corrosion in ionic liquid containing electrolytes. *J Power Sources* 214:178–184
- Kühnel R-S, Reber D, Remhof A, Figi R, Bleiner D, Battaglia C (2016) “Water-in-salt” electrolytes enable the use of cost-effective aluminum current collectors for aqueous high-voltage batteries. *Chem Commun* 52(68):10435–10438
- Ma T, Xu G-L, Li Y, Wang L, He X, Zheng J, Liu J, Engelhard MH, Zapol P, Curtiss LA, Jorne J, Armine K, Chen Z (2017) Revisiting the corrosion of the aluminum current collector in lithium-ion batteries. *J Phys Chem Lett* 8(5):1072–1077
- Theivaprakasam S, Girard G, Howlett P et al (2018) Passivation behaviour of aluminium current collector in ionic liquid alkyl carbonate (hybrid) electrolytes. *npj Mater Degrad* 2:13
- Parsons R (1967) Atlas of electrochemical equilibria in aqueous solutions. *J Electroanal Chem Interfacial Electrochem* 13:471
- Zhang X, Devine TM (2006) Passivation of aluminum in lithium-ion battery electrolytes with LiBOB. *J Electrochem Soc* 153(9):B365
- Shirley DA (1972) High-resolution X-ray photoemission spectrum of the valence bands of gold. *Phys Rev B* 5(12):4709–4714

23. Susi T, Pichler T, Ayala P (2015) X-ray photoelectron spectroscopy of graphitic carbon nanomaterials doped with heteroatoms. *Beilstein J Nanotechnol* 6:177–192
24. Karambakhsh A, Afshar A, Ghahramani S, Malekinejad P (2011) Pure commercial titanium color anodizing and corrosion resistance. *J Mater Eng Perform* 20(9):1690–1696
25. Alivov Y, Fan ZY, Johnstone D (2009) Titanium nanotubes grown by titanium anodization. *J Appl Phys* 106(3):034314

**Publisher's note** Springer Nature remains neutral with regard to jurisdictional claims in published maps and institutional affiliations.

### 2.3.2 A novel Water in Salt electrolyte based on ammonium acetate

The chemical-physical characterization of ammonium acetate (AmAc) aqueous solution with salt concentration ranging from 1 to 30 mol kg<sup>-1</sup>, carried out by Mr. El Alimi, demonstrated that these low-cost solutions feature circumneutral pH (pH = 7–8) and ionic conductivity comparable to or higher than typical organic electrolytes. Moreover, the structure of the solutions has been investigated by IR and molecular dynamic study (MD). MD simulation, carried out by the group of Prof. Calvaresi, suggested that mixture goes from an “ion in water” (conventional solutions) to an “ionic-liquid-like” (concentrated solutions) behavior. Indeed, increasing salt concentration resulting in a change in the structure of concentrated solutions that have been related to the strong interactions between ions and/or water molecules through the formation of hydrogen bonding that cause an increase in pH values and a decrease in ions mobility. In turn, the presence of cooperative motions is suggested by the conductivity temperature dependence that follows a non-Arrhenius behaviour like ionic-liquid electrolytes.

The WiSE based on 26.4 m AmAc exhibits an ESW of 2.22 V at Al foil, 2.9 V at GC, and an outstanding value of 3.4 V when titanium grid was used. Therefore, this WiSE has been selected as the electrolyte for EDLCs based on Argan shell activated carbon (ARG-AC, provided by Mr. El Halimi), a bioderived activated carbon. The ESW evaluated using ARG-AC electrodes was only 1.3 V wide, likely due to the high carbon surface area which promoted electrochemical decomposition of the electrolyte. Indeed, the ARG-AC electrodes obtained by pyrolysis and activation of argan shells exhibited an exceptional specific capacitance of 300 F g<sup>-1</sup> in the super concentrated electrolyte. While this finding strongly suggests that ESW is dependent on the kind of electrodes used for the test, it also prevented the development of symmetric supercapacitors with the high cell voltage expected by the study carried out with GC and metal grids.

In this study, my main role has been the evaluation of the performance of an asymmetric EDLC based on AmAc. The EDLCs featured an asymmetric mass loading to fully exploit the AmAc ESW. ARG-AC electrodes have been used. The electrochemical performance of the obtained EDLCs has been measured by means of CVs and GCPL and stability tests have been run at temperatures ranging from -10 to 80 °C, leveraging the high thermal stability of the studied electrolyte. The asymmetric supercapacitor assembled with ARG-AC electrodes and 26.4 m AmAc WiSE was able to operate at 1.2 V, from -10 °C to 80 °C with outstanding specific capacitance and low resistance. The symmetric cell delivered noticeable specific energy at



extreme temperatures and ranged from 5.9 Wh kg<sup>-1</sup> at -10 °C to 15.6 Wh kg<sup>-1</sup> at 80 °C, values that are competitive with those of commercial supercapacitors featuring organic electrolytes. A promising option to explore is the increase of energy performance through AmAc WiSE in a hybrid supercapacitor involving redox or pseudocapacitive electrodes that features faradaic processes within the WiSE ESW. Overall, this study suggests that AmAc WiSE deserves consideration as a cheap, circumneutral and environmentally friendly alternative electrolytes for designing green energy storage systems.

The experimental methods and the results of this study are reported in [5], which is here attached as a complete publication.



## Circumneutral concentrated ammonium acetate solution as water-in-salt electrolyte

Mohammad Said El Halimi<sup>a,c</sup>, Federico Poli<sup>a</sup>, Nicola Mancuso<sup>a</sup>, Alessandro Olivieri<sup>a</sup>, Edoardo Jun Mattioli<sup>b</sup>, Matteo Calvaresi<sup>b</sup>, Tarik Chafik<sup>c</sup>, Alberto Zanelli<sup>d</sup>, Francesca Soavi<sup>a,d,\*</sup>

<sup>a</sup>Laboratory of Electrochemistry of Materials for Energetics, Department of Chemistry "Giacomo Ciamician", Alma Mater Studiorum Università di Bologna, Bologna 40126, Italy

<sup>b</sup>NanoBio Interface Laboratory, Department of Chemistry "Giacomo Ciamician", Alma Mater Studiorum Università di Bologna, Bologna 40126, Italy

<sup>c</sup>Laboratory of Chemical Engineering and Resources Valorization, Faculty of Sciences and Techniques of Tangier, Abdelmalek Essaadi University, Tangier 90000, Morocco

<sup>d</sup>Istituto per la Sintesi Organica e la Fotoreattività (ISOF), Consiglio Nazionale delle Ricerche (CNR), Bologna 40129, Italy



### ARTICLE INFO

#### Article history:

Received 5 February 2021

Revised 14 May 2021

Accepted 15 May 2021

Available online 24 May 2021

#### Keywords:

Water in salt electrolyte  
Superconcentrated solution  
Ammonium acetate  
Biomass-derived carbon  
Supercapacitor

### ABSTRACT

The exponentially growing market of electrochemical energy storage devices requires substitution of flammable, volatile, and toxic electrolytes. The use of Water in salt solutions (WiSE) regarded as green electrolyte might be of interest thanks to an association of key features such as high safety, low cost, wide electrochemical stability, and high ionic conductivity. Here, we report comprehensive chemical-physical study of circumneutral WiSE based on ammonium acetate so as to investigate application in electrochemical energy storage systems, with focus on the effect of pH, density, viscosity, conductivity, and the ESW with salt concentration ranging from 1 to 30 mol kg<sup>-1</sup>. Data are reported and discussed with respect to the structure of the solutions investigated by complementary IR and molecular dynamic study. The study is addressed through the showcase of an asymmetric supercapacitor based on Argan shell-derived carbon electrodes tested at temperatures ranging from -10 to 80 °C.

© 2021 Elsevier Ltd. All rights reserved.

### 1. Introduction

Today, the increasing demand for electrochemical energy storage devices (ESDs) pushes towards improving their performance and safety at lower cost and environmental impact. The electrolyte is a key component of ESDs and should address the following requirements: (i) high ionic conductivity, (ii) wide electrochemical stability window (ESW), (iii) high thermal stability, (iv) low cost, and (v) environmental compatibility.

Commercial lithium-ion batteries and electrical double layer capacitors (EDLCs) typically feature electrolytes based on lithium hexafluorophosphate in ethylene carbonate and dimethyl carbonate (LP30) and tetraethylammonium tetrafluoroborate in acetonitrile (TEABF<sub>4</sub>/ACN), respectively. Table 1 summarizes these electrolyte characteristics. The ionic conductivity ( $\kappa$ ) and ESW are 10.8 mS

cm<sup>-1</sup> and 5.7 V for LP30, 56 mS cm<sup>-1</sup>, and 6.1 V for TEABF<sub>4</sub>/ACN. Their cost is mainly affected by the salt.

Novel alternative electrolytes have been proposed and the main achievements have been excellently reviewed in the literature [1–3]. Ionic liquids are an interesting class of organic electrolytes, indeed besides their good ionic conductivity and electrochemical stability, they present important advantages associated with low vapor pressure and flammability, that are key requisites to design safe ESDs. However, they cannot be considered as totally green and their toxicity has been reported as an issue for the disposal of end-of-life devices [4]. In addition, their high cost still represents a limit to larger exploitation in batteries or supercapacitors. As an example, EMITFSI shows a conductivity of 9 mS cm<sup>-1</sup> and an ESW of 4.5 V, while for PYR<sub>14</sub>TFSI the conductivity is 2.8 mS cm<sup>-1</sup> and the ESW is 6.6 V. Their cost is more than 5 times higher than that of TEABF<sub>4</sub>/ACN and LP30 (Table 1). Hence, the use of aqueous electrolytes offers a promising opportunity to design cheap and safer devices as compared to organic electrolytes because of their non-flammability, low cost, and environmental friendliness. However, due to water splitting conventional aqueous electrolytes

\* Corresponding author at: Laboratory of Electrochemistry of Materials for Energetics, Department of Chemistry "Giacomo Ciamician", Alma Mater Studiorum Università di Bologna, Bologna 40126, Italy.

E-mail address: [francesca.soavi@unibo.it](mailto:francesca.soavi@unibo.it) (F. Soavi).

**Table 1**  
Ionic conductivity ( $\kappa$ ), electrochemical stability window (ESW) at room temperature and commercial cost of different electrolyte solutions and components used in ESDs.

Electrolyte solution components and composition	Salt Concentration	$\kappa$	ESW	Costs	Ref.
<b>Conventional Organic electrolytes</b>					
Tetraethylammonium tetrafluoroborate in Acetonitrile (ACN/TEABF <sub>4</sub> )	1 mol/L	56 mS/cm	6.1 V	3.69\$/g <sup>a</sup> 130\$/L <sup>a</sup>	[5,6]
Lithium hexafluorophosphate in ethylene carbonate and dimethyl carbonate (LP30) (1.0 M LiPF <sub>6</sub> in EC/DMC=50/50 v/v)	1 mol/L	10.8 mS/cm	5.7 V	982 \$/L <sup>c</sup>	[1,7,8]
<b>Ionic liquids</b>					
1-Ethyl-3-methylimidazolium bis-(trifluoromethylsulfonyl)-imide (EMITFSI)	3.9 mol/L	9 mS/cm	4.5 V	198 \$/g <sup>b</sup>	[9]
1-Butyl-1-methylpyrrolidinium bis(trifluoromethanesulfonyl)imide (PYR <sub>14</sub> TFSI)	6 mol/L	2.8 mS/cm	6.6V	22 \$/g <sup>b</sup>	[5]
<b>Salts used in WiSE</b>					
Lithium Bis(trifluoromethane)sulfonimide (LiTFSI)	21 mol/kg	10 mS/cm	3 V	7 \$/g <sup>b</sup>	[10]
Potassium acetate (KOAc)	30 mol/kg	25 mS/cm	3.2 V	0.35 \$/g	[11]
Lithium acetate (LiOAc) + KOAc	32 mol/kg KOAc	5.3	2.7	0.9 \$/g +	[12]
	8 mol/kg LiOAc	mS/cm	V	0.35 \$/g	
Sodium perchlorate	17 mol/kg	64 mS/cm	2.8V	0.33 \$/g	[13]
Ammonium acetate (AmAc)	26.4 mol/kg	49 mS/cm	2.9 V - 3.3V	1.2 \$/g	This work <sup>a</sup>

<sup>a</sup> solvent cost.

<sup>b</sup> salt cost.

<sup>c</sup> solution costs from Sigma Aldrich.

<sup>a</sup> using different electrodes.

place an intrinsic limitation on the ESD, and mainly EDLC, practical cell voltage.

A major breakthrough in electrolytic materials was achieved only a few years ago by increasing the salt concentration in appropriate salt-solvent combinations [14]. The so-called "water in salt electrolytes" (WiSE) are obtained with aqueous solutions containing salt to water volume or mass ratio higher than 1 [10]. Thanks to their molecular structure and water-to-ion interactions, WiSE have been demonstrated to reach unexpectedly wide ESW, beyond the thermodynamic stability limit of water. Therefore, WiSE are receiving considerable attention as safe electrolytes for batteries and supercapacitors [10,13,15]. The main WiSE investigated for batteries are based on fluorinated imide-based salts, usually lithium bis (trifluoromethane)-sulfonimide (LiTFSI). Suo et al., were the first to report about a WiSE based on a 21 mol kg<sup>-1</sup> LiTFSI water system capable of reaching an ESW of 3 V and a conductivity of 10 mS cm<sup>-1</sup> (Table 1) [10]. Since then, the interest in WiSE for lithium-ion batteries and supercapacitors has been growing [13,15–18]. Although significant improvements were achieved with imide-based WiSE systems, several economic and environmental challenges are still ahead as pointed out by Lukatskaya et al. for LiTFSI [12]. Furthermore, the limited geographical distribution of lithium deposits in the earth's crust, relative to sodium (Na) and potassium (K) deposits, raises another concern associated with the amount of lithium salt needed for WiSE electrolytes [12]. In attempt to lower the amount of lithium salts, binary salts, like eutectic mixtures of lithium and potassium acetates, have been suggested. Mixed WiSE solutions containing 32 mol kg<sup>-1</sup> potassium acetate + 8 mol kg<sup>-1</sup> lithium acetate for aqueous batteries featured ESW of 2.7 V and  $\kappa$  of 5.3 mS cm<sup>-1</sup> [12]. Moreover, EDLCs offer the possibility to us lithium-free WiSE such as potassium acetate-based WiSE, as already reported for an activated carbon-based symmetric supercapacitor that featured excellent cyclic performance under an operating voltage of 2 V [19].

Even though, superconcentrated solutions of acetates are inherently alkaline, due to the hydrolysis reaction of the acetate anion. So far, cheaper sodium perchlorate based WiSE featuring 64.2 mS cm<sup>-1</sup> and ESW of 2.8 V, has been proposed as a mild neutral electrolyte for 2.3 V EDLCs [13]. Unfortunately, this WiSE cannot be considered as totally green mainly because the perchlorate anion is known as a strong oxidizer [20].

The present work is devoted to the study of safer and less corrosive circumneutral WiSE obtained with a highly concentrated

aqueous solution of ammonium acetate (AmAc). This salt features high solubility in water of 1.48 kg L<sup>-1</sup> and is composed of ions that derive from a weak base and a weak acid with similar pKa and pKb values. Such a particular characteristic makes AmAc solutions circumneutral. Here, a comprehensive chemical-physical study of AmAc solutions with concentrations ranging from 1 to 30 mol kg<sup>-1</sup> is reported and discussed. Specifically, the trends of pH, density, viscosity, conductivity, and ESW with AmAc concentration will be discussed in terms of solution structure by complementary IR spectroscopy and molecular dynamics (MD) studies. The feasibility of the use of AmAc WiSE in electrochemical energy storage devices will be demonstrated through a showcase of supercapacitors using Argan-shell derived carbon electrodes and AmAc 26.4 mol kg<sup>-1</sup> electrolyte.

## 2. Materials and methods

### 2.1. Ammonium acetate WiSE characteristics

Ammonium acetate (98% purity) was purchased from EMSURE. The pH of the aqueous solutions was measured by a pHM210 Standard pHmeter MeterLab. The density of the solutions was obtained by weighting exact volumes of solution (100 $\mu$ L) measured with a P200 micropipette. The viscosity of the solutions was obtained by a Viscoclock SI Analytics bubble viscometer. ATR (Attenuated Total Reflection) spectra of liquid aqueous solutions were carried out with an FTIR Bruker Alpha spectrometer equipped with an ATR head. The limited length of the optical path in the sample eliminated the problem of the strong attenuation of the infrared signal by highly absorbent media such as the aqueous solutions. The ionic conductivity was measured with a CDM210 conductivity meter electrode MeterLab. The solutions were thermostated in a cryostat bath at different temperatures.

### 2.2. Molecular dynamics (MD) simulations

Setting molecular dynamics (MD) simulations. To investigate the behavior of AmAc solutions at the atomistic level, MD simulations were carried out. Boxes with different AmAc/H<sub>2</sub>O ratios (corresponding with the experimental WiSE concentrations investigated in this work) were built. The FF14SB force field was used to model acetate anions and ammonium cations [21] while water molecules were simulated by using the TIP5P water model

[22]. Minimization and equilibration. About 5000 steps of steepest descent minimization, followed by additional 5000 steps of conjugate gradient minimization were performed with PMEMD [23]. The minimized structure was considered for a three step equilibration protocol. Particle Mesh Ewald summation was used throughout and H-atoms were considered by the SHAKE algorithm [23]. A time step of 2 fs was applied in all MD runs. Individual equilibration steps included (i) 50 ps of heating to 298 K within an NVT ensemble and temperature coupling according to Berendsen, (ii) 50 ps of equilibration MD at 298 K to switch from NVT to NPT and adjust the simulation box. Isotropic position scaling was used at default conditions, (iii) 400 ps of continued equilibration MD at 298 K for an NPT ensemble switching to temperature coupling according to Andersen.

MD simulation was carried out for the equilibrated system using PMEMD [23]. Simulation conditions were identical to the final equilibrium step (iii). Overall sampling time was 100 ns.

Snapshot structures were saved into individual trajectory files every 1000 time steps, i.e. every 2 ps of molecular dynamics.

Trajectories obtained from MD simulations were post-processed using CPPTRAJ [23,24]. For each simulated box, the density of the solution, the diffusion constants of water and ions, and the radial distribution function  $g(r)$  of acetate and ammonium ions were calculated.

### 2.3. Supercapacitor electrode preparation

Agriculture waste-derived carbon was used as electrode material. The detail of the experimental preparation of this carbon was reported in previous work [25]. Briefly, Argan shells collected from the southern region of Morocco were carbonized under  $N_2$  flow at 700 °C for 1 h, in order to decompose the organic materials. The obtained material was activated with potassium hydroxide (KOH) using physical mixing process. Practically KOH beads were mixed with carbon using an activating agent-to-carbonized carbon mass ratio of 4:1. The mixture was heat-treated in a muffle furnace for 1 h at 850 °C and under  $N_2$  atmosphere; the furnace cooled to room temperature. Finally, the sample was washed with HCl (5 M) solution, rinsed with distilled water until reaching neutral pH then dried at 110 °C overnight. The obtained sample named ARG-AC yields to BET specific surface area of 1937  $m^2 g^{-1}$ . The full chemical-physical characterization of this sample (labeled as ARG-K-PM) is reported in [25]. The supercapacitor electrode was obtained using ARG-AC and polytetrafluoroethylene (PTFE) as binder (60% suspension in water), as well as multi-walled carbon nanotubes MW-CNT in an 80/10/10 weight ratio, respectively, and dried at 120 °C overnight. Finally, an amount of 6.5 mg of this mixture was pressed onto a titanium grid disk of 8 mm diameter to prepare electrodes that were subsequently dried.

### 2.4. Electrochemical measurements

All the electrochemical measurements were performed by a Bio-Logic VSP300 potentiostat/galvanostat. The ESW was evaluated by voltammetric measurements (LSV, Linear Sweep Voltammetry). The working electrode was a glassy carbon electrode (0.07  $cm^2$ ), a titanium grid (1  $cm^2$ ), or an aluminum foil (1  $cm^2$ ). Metal electrodes were used as received. The reference electrode was a saturated calomel electrode (SCE). The counter electrode was a Pt wire.

The supercapacitor was assembled by coupling two identical electrodes impregnated with a 26.4 mol  $kg^{-1}$  AmAc electrolyte for 48 h before the electrochemical measurements using a glass fiber filter (Whatman) as a separator. The electrochemical performance of the supercapacitor was evaluated by a two-electrode setup. Cyclic voltammetry (CV), galvanostatic charge-discharge (GCD), and

Electrochemical Impedance Spectroscopy (EIS) of the cell were performed at room temperature, -10 °C and 80 °C.

The supercapacitor specific capacitance ( $C_{sp}$ ) was calculated from GCD curves using the following equation [26,27].

$$C_{sp} = \frac{I \cdot dt}{m \cdot dV} \quad (1)$$

Where  $I$  is the discharge current (A),  $dV/dt$  is the slope of the discharge curve, and  $m$  is the total mass of the two electrodes (in g).

The maximum specific energy ( $E_{max}$ ) and power ( $P_{max}$ ) were determined by applying Eqs. (2) and (3), respectively [28,29].

$$E_{max}(Wh kg^{-1}) = \frac{C_{sp} (F g^{-1}) \cdot V_{max}^2 (V)}{2 \cdot 3.6} \quad (2)$$

$$P_{max}(W kg^{-1}) = \frac{1}{4} \cdot \frac{V_{max}^2 (V)}{ESR (\Omega) \cdot m (kg)} \quad (3)$$

Where  $V_{max}$  is the maximum cell voltage and ESR is the cell equivalent series evaluated by the ohmic drop ( $\Delta V$ ) measured at the beginning of discharge (Eq. (4)). Given that the same current was used for the charge and discharge,

$$ESR = \frac{1}{2} \cdot \frac{\Delta V}{I} \quad (4)$$

Practical specific energy ( $E$ ) and power ( $P$ ) delivered at different current densities were evaluated by the analyses of the discharge profiles by Eqs. (5) and (6)

$$E (Wh kg^{-1}) = I \cdot \int V \frac{dt}{3.6 m} \quad (5)$$

$$P (W kg^{-1}) = 3.6 \frac{E}{\Delta t} \quad (6)$$

where  $\Delta t$  is the discharge time in seconds.

## 3. Results and discussion

### 3.1. Physicochemical studies of ammonium acetate WiSE

Table 2 reports the acronym of the ammonium acetate solutions that were investigated with the corresponding values of molality, salt to solvent molar ratio, molarity, and density. We investigated solutions containing ammonium acetate (AmAc), with a molality of 1, 5, 10, 15, 20, 26.4 and 30 mol  $kg^{-1}$ . It is worth nothing that at the highest concentration only two moles of water are sheared every ion of ammonia  $NH_4^+$ . Table 2 also reports the values of the density ( $d$ ) that have been calculated under the hypothesis that the molar volumes of AmAc and water are additives Eqs. (1) and (2) in supplementary information). The experimental results differ only by less than 0.1% from the calculated values.

To highlight this small difference, we evaluated the excess molar volume  $EV$  (Table 2) i.e., the difference between the experimental molar volume of the solution and the value obtained by considering that salt and solvent molar volumes are additives (Eq. (3) in supplementary information). For concentrations lower than 10 m,  $EV$  is slightly negative, therefore indicating that a weak volume contraction takes place during the dissolution of AmAc in water. On the contrary, when the concentration rises above 10 m,  $EV$  increases up to 0.23 mL at 26.4 m. This relatively positive volume change can be explained by strong ionic and molecular interactions of AmAc ions and water molecules. Specifically, volume expansion could be related to the directional character of hydrogen bonding [30].

Given that our aim was to propose a neutral WiSE, we checked the pH of the different solutions within the concentration range from 1 m to 30 m (Fig 1a) AmAc is composed of weak acidic and base ions that feature the same base and acid constants. Therefore,

Table 2.

Acronym of the AmAc solutions investigated with the corresponding values of molality, salt to solvent molar ratio, molarity, density calculated by Eq. (1), experimental and from MD simulations, and excess molar volume (EV) obtained as described in the supplementary information).

Code	Molality (mol/kg)	AmAc:H <sub>2</sub> O Molar ratio	Molarity (mol/L)	Density (kg/L)			EV (mL/mol)
				Calculated	Exp	MD	
1m	1	1.8:100	0.95	1.010	1.02	1.02	-0.25
5m	5	9:100	3.79	1.042	1.05	1.09	-0.18
10m	10	1.8:10	6.06	1.067	1.07	1.13	-0.07
15m	15	2.7:10	7.5	1.084	1.08	1.15	0.01
20m	20	3.6:10	8.58	1.096	1.09	1.16	0.16
26.4m	26.4	4.8:10	9.57	1.107	1.10	1.17	0.23
30m	30	5.4:10	10.10	1.112	1.11	1.18	0.24

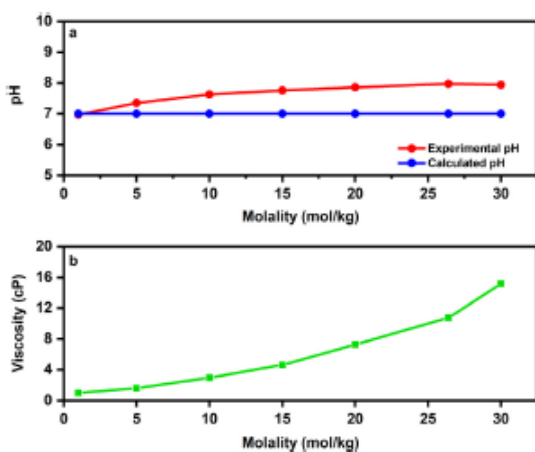


Fig. 1. (a) pH and (b) viscosity of AmAc solutions with different molality at room temperature.

as demonstrated in Section 3 of the Supplementary Information, the pH of ammonium acetate solutions should not change with the salt concentration and be equal to 7. Different from what is expected, Fig. 1a shows that the pH values change from almost neutral (1 m solution) to slightly basic along with the increase of the concentration. This is apparently attributed to the decrease of the proton activity.

The viscosity of the solution increases almost exponentially with the solution molality, as shown in Fig. 1b. This trend deviates from the linear curve expected for the diluted solution (Einstein equation) due to involved ions interactions [31]. The absence of minimum in the curve excludes the so-called "water structure breaking" associated with the solution ionic field. At the opposite, it indicates that ammonium and acetate ions are strongly hydrated and contribute to a sort of molecular order in solution [32,33].

It is known that Stokes-Einstein relation relates conductivity to viscosity [31]. In turn, ionic conductivity and temperature are usually described by an Arrhenius relation. The latter applies for solutions involving no-cooperative mechanism for ion conduction. Under this condition, the logarithm of the specific conductivity ( $\kappa$ ) linearly decreases with the reciprocal of the temperature (see Section 4 in the Supplementary Information) [34]. Fig. 2a present the Arrhenius conductivity plots of the different solutions. A higher conductivity is achieved at increased temperature, which is due to a decreased viscosity and increased ion mobility. The highest conductivity is obtained with the 5 m solutions, while the 30 m shows the lowest value in the whole temperature range. This finding agrees with the viscosity trends with ammonium acetate con-

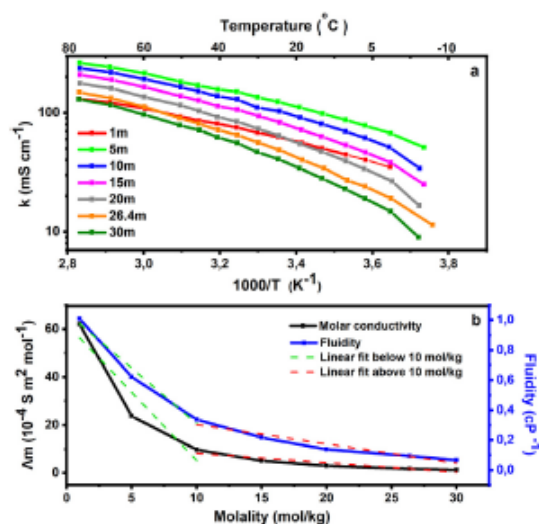


Fig. 2. Arrhenius plots build on the basis of the conductivity ( $\kappa$ ) at different temperatures of the different solutions, (b) Trend of the molar conductivity ( $\Lambda_m$ ) and fluidity versus molality at room temperature.

centration discussed above. Note that the conductivity of the most diluted solution (1 m) is in the same order of magnitude as those featured by the most concentrated ones (from 20 m to 30 m). Only the 1 m solution features a clear Arrhenius-like linear plot. When the concentration increases above 1 m, the plots deviate from linearity. This non-Arrhenius behavior has already been reported for ionic liquid electrolytes, and described by the Vogel-Tamman-Fulcher (VTF) Eq. (7) [35]

$$\kappa = A_0 \exp\left(\frac{-B}{T - T_0}\right) \quad (7)$$

where  $T$  is the absolute temperature, and  $A_0$ ,  $B$ , and  $T_0$  are adjustable parameters. According to the VTF model, ion diffusivity and conductivity are affected by several processes like molecular dissociation and cooperative motions. Particularly, the diffusivity is directly related to fluidity (the reciprocal of viscosity) and decreases with the increase of cooperativity. At the contrary, the molar conductivity is positively affected by cooperative processes [36].

Fig. 2b plots the variation of the molar conductivity ( $\Lambda_m$ ) and fluidity versus molality of the AmAc solutions. In the concentration range from 1 m to 10 m, the molar conductivity follows the decrease of fluidity, with almost the same trend. Instead, for concentrations higher than 10 m, this decrease becomes less marked. This suggests that molecular dissociation and cooperative process affects ion conductivity of WiSE.

**Table 3.** Diffusion constants (D) for H<sub>2</sub>O, acetate (AcO<sup>-</sup>) and ammonium (NH<sub>4</sub><sup>+</sup>) from MD simulations of the AmAc solutions.

Solution Code	AmAc:H <sub>2</sub> O Molar ratio	D (10 <sup>5</sup> , cm <sup>2</sup> s <sup>-1</sup> )		
		H <sub>2</sub> O	AcO <sup>-</sup>	NH <sub>4</sub> <sup>+</sup>
1 m	1.8:100	1.98	1.08	1.07
5 m	9:100	1.17	0.27	0.38
10 m	1.8:10	0.60	0.13	0.17
15 m	2.7:10	0.37	0.08	0.08
20 m	3.6:10	0.23	0.02	0.04
26.4 m	4.8:10	0.17	0.02	0.02
30 m	5.4:10	0.11	0.01	0.02

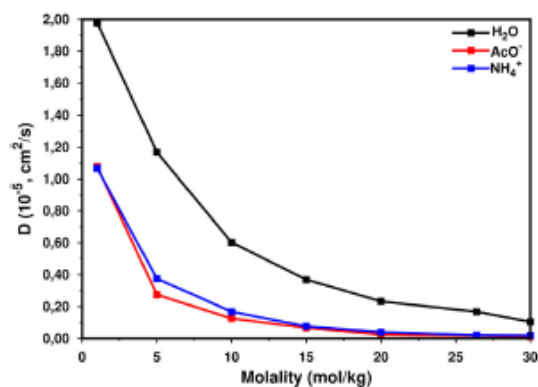


**Fig. 3.** Trend of the diffusion constants of H<sub>2</sub>O, AcO<sup>-</sup> and NH<sub>4</sub><sup>+</sup> vs. molality.

### 3.2. Molecular dynamics (MD) simulations and fourier transform infrared FTIR

The structure of the solutions was investigated using MD simulations. MD trajectories were used to calculate the solution densities as a function of the solution molality (Table 2). The computed and experimental densities present the same trend with a higher increase in density values at lower concentrations.

The diffusion constant D of water, acetate anion, and ammonium cation were calculated using the Einstein relation, on the calculated MD trajectories (as implemented in Amber [23])

$$2nD = \frac{MSD}{t} \quad (8)$$

where n is the number of dimensions, MSD is the mean square displacement. Salt concentration influences the diffusion constant of water. Increasing the salt concentration, the water molecules move slower due to their interactions with ions (Table 3 and Fig. 3). This is the consequence of increased interaction between water and AmAc, which is also reflected by the contraction of the system volume or higher density. Note also, the decreased ion mobility when molality increases, in agreement with the molar conductivity data reported in Fig. 2b. To have an atomistic insight into the structure of the mixtures, atomic radial distribution functions (g(r)) were calculated. In Fig. 4g(r) functions for the 1 m and 30 m solutions are reported. The Figure shows the cation-water, cation-cation and cation-anion and the anion-water, anion-cation and anion-anion radial distribution functions. Ammonium and acetate ions induce long-range electrostatic interactions in the mixture that goes from a "ion in water" behavior (1 m) to a "ionic liquid-like" behavior (30 m). Furthermore, for the 30 m solution, the ammonium and the acetate are strongly hydrated as supposed by the absence of minimum in the curve of Fig 1b that excludes a

"structure breaking" effect of ions in the solution. Hence, MD simulations clearly support the "structure effect" of ions suggested by the viscosity experimental data.

The FTIR characterization of the solutions was carried out to evaluate specific interactions between ions and water molecules. Fig 5 shows the superimposed IR spectra of the solutions and shows a clear trend in the evolution of the signals. Typical vibrations associated with water are the stretching of the OH bond in the area between 3000 and 3200 cm<sup>-1</sup>. This region is shared with the stretching of the undissociated acetic acid present in solution. The bending of the HOH angle is around 1640 cm<sup>-1</sup>. These peaks strongly characterize the typical 1 m aqueous solution and cover the signals referable to the pure salt [37]. On the contrary, the spectrum of the 30 m solution does not reveal interference attributed to the presence of water, looking similar to what is expected for the pure salt. It is important to emphasize that, changing solution from 1 m to 30 m, the intensity of the peak associated with HOH bending decreases and becomes insufficiently resolved, thus remaining indistinguishable from the signal relative to the carboxylate ion (symmetrical stretching around 1540 cm<sup>-1</sup>, asymmetric stretching around at 1400 cm<sup>-1</sup> for the 30 m solution). The marked change in the shape of the spectrum with the gradual emergence of peaks related to well-defined salt can be interpreted as an important index of the increase in salt activity in solution, combined with a marked decrease in water activity. The peak attributable to O-H stretching alone tends to shift towards lower wavenumbers and change shape from a single very large peak to a system of two peaks located around 3190 and 3012 cm<sup>-1</sup>. This phenomenon is probably associated with high salt concentration and possible peaks overlapping associated with the stretching of the N-H bond, occurring approximately in the same region as of O-H bonding. Simultaneously also the C=O asymmetrical stretching around 1635 cm<sup>-1</sup>, and C-O stretching around 1014 cm<sup>-1</sup>, can be appreciated.

Overall, a careful analysis of the evolution of the spectra indicates that for all the signals a certain degree of red peak shift to lower wavenumbers occurs as the salt concentration increases. Indeed, the O-H stretching shifted from 3670–2805 cm<sup>-1</sup> to 3615–2455 cm<sup>-1</sup>, N-H bending from 1545 cm<sup>-1</sup> to 1540 cm<sup>-1</sup>, and C=O symmetrical stretching from 1411 cm<sup>-1</sup> to 1395 cm<sup>-1</sup>. This is apparently associated with the increased hydrogen bond strength involving ions and water molecules yielding to an evolution in the structure of the solution, which, is consistent with the aforementioned pH, density, and viscosity trends.

### 3.3. Electrochemical measurement

The electrochemical stability of AmAc solutions was evaluated by linear sweep voltammetry (LSV) carried out at 20 mV s<sup>-1</sup> in 1 m and 26.4 m solutions at glassy carbon electrode (GC) (Fig 6a). As shown, the cathodic limit for the superconcentrated solution is -1.5 V vs SCE. It is much lower than the limit expected for hydrogen evolution via H<sup>+</sup> reduction in acidic solution (ca. 0.242 V vs SCE). The low cathodic limit of the 26.4 m solution is in line with the low H<sup>+</sup> concentration (pH≈8) and with the low availability of H<sup>+</sup> ions apparently involved in hydrogen bonds with the other ionic species in solution. Considering the anodic limit, it is at around +1.5 V vs SCE. It slightly decreases with the increase of concentration probably due to higher concentration of acetate ions whose oxidation limits anodic stability.

The most interesting aspect is that using WiSEs based on ammonium acetate it is possible to obtain ESW of 2.9 V at GC, higher than 0.4 V compared to typical aqueous solutions, and close to the performance of electrolytes based on organic solvents. In order to evaluate the feasibility of the use of WiSEs in practical devices, ESW was also evaluated at current collectors that are typically

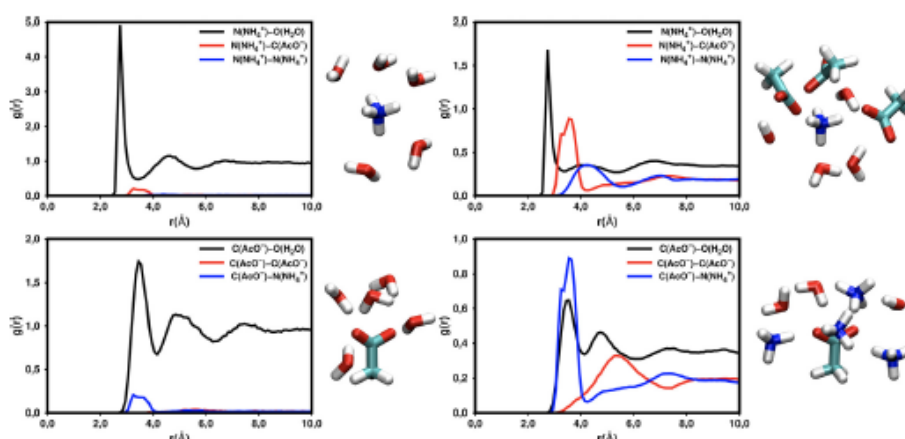


Fig. 4. Radial distribution function for a 1 m mixture (left) and 30 m mixture (right) centered on ammonium cation (top) and acetate anion (bottom). A representative cluster structure is reported.

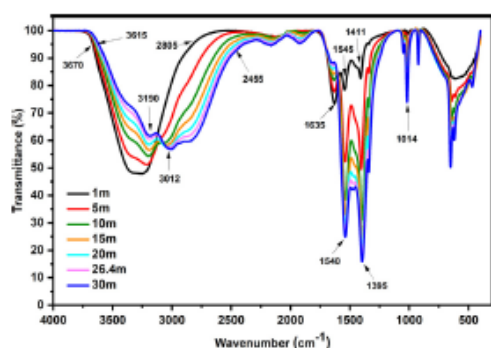


Fig. 5. IR spectra superimposed of all the studied solutions.

used in supercapacitors and batteries, namely titanium grid and aluminum foil. Fig. 6b, compares the LSVs carried out at  $20 \text{ mV s}^{-1}$  in 26.4 m AmAc. With titanium and aluminum, the cathodic limit becomes more positive because these metals promote fast kinetics hydrogen evolution compared to GC. The cathodic limits are  $-1.07 \text{ V}$  and  $-0.80 \text{ V}$  vs. SCE with aluminum and titanium, respectively. Unlike GC, aluminum features an anodic limit of  $+1.40 \text{ V}$  vs. SCE. On the contrary, for titanium it increases to  $+2.60 \text{ V}$  vs. SCE. Such a wide anodic range of titanium has been already observed in LiTFSI-based WISE and attributed to the formation of a surface Ti-oxide film that partially passivates the grids and hinders electrolyte decomposition [38,39]. Accordingly, using titanium and 26.4 m AmAc an outstanding ESW of 3.4 V should be feasible.

GCE was coated by Argan shells derived carbon (ARG-AC) and tested by CV using 1 m and 26.4 m AmAc at  $20 \text{ mV s}^{-1}$  (Fig. 6c). Unexpectedly, when ARG-AC electrodes are used, the ESW width does not change with the increase of AmAc concentration. Furthermore, the ESW is significantly narrower than what was observed with the titanium and GC electrodes. Indeed, with ARG-AC, the ESW is about 1.3 V, with cathodic and anodic limits that can be set at ca.  $0.8 \text{ V}$  vs. SCE and  $0.5 \text{ V}$  vs. SCE, respectively. In fact, the high surface area of the ARG-AC carbon ( $1937 \text{ m}^2 \text{ g}^{-1}$ ) enhances the faradic currents related to electrolyte decomposition and nar-

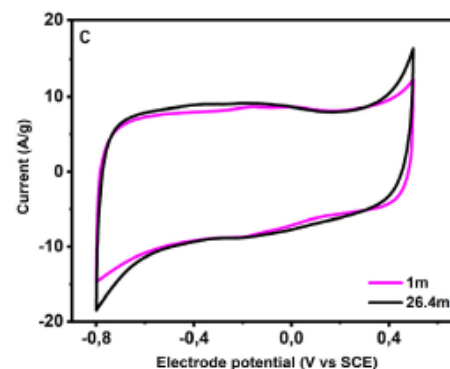
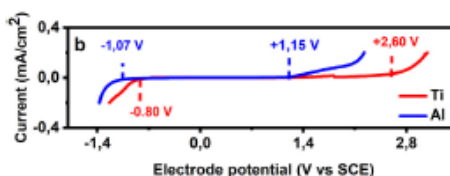
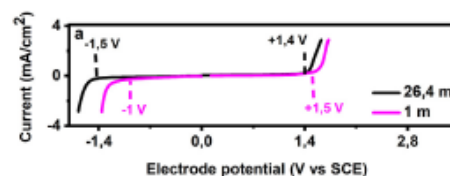
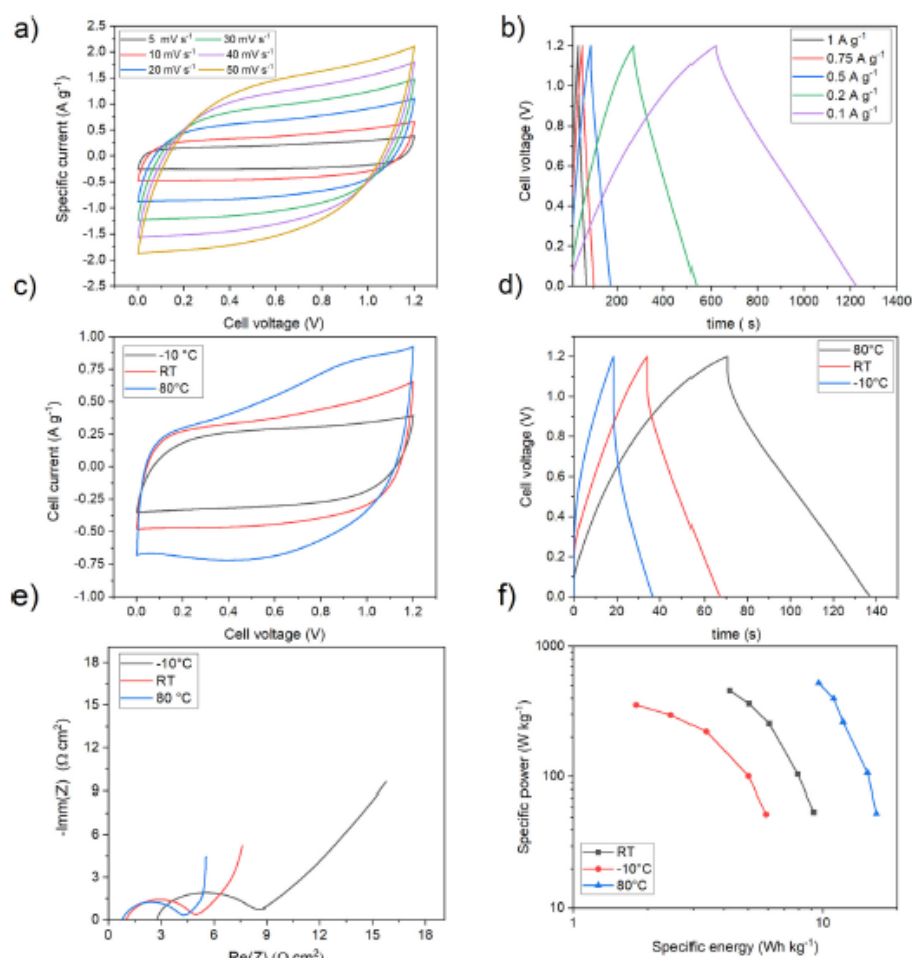


Fig. 6. Linear sweep voltammetry at  $20 \text{ mV s}^{-1}$  carried out with (a) glassy carbon electrode (GC) in 1 m and 26.4 m solutions, (b) GC, titanium grid and aluminum paper in 26.4 m solution, and (c) GC coated by 0.025 mg Argan shells derived carbon (80% ARG-AC, 10% acetylene black, 10% Nafion binder) in 1 m and 26.4 m AmAc.



**Fig. 7.** Electrochemical test of the asymmetric supercapacitor assembled with ARG-AC electrodes and 26.4 m AmAc WiSE: (a) CV of the assembled device at scan rate from 5 to 50 mVs<sup>-1</sup> and (b) GCD at current densities from 0.1 to 1 Ag<sup>-1</sup> (calculated on the basis of positive and negative electrode mass) at room temperature; (c) CV at scan rate 10 mVs<sup>-1</sup>, (d), (d) GCD at current densities from 0.1 Ag<sup>-1</sup>, (e) Nyquist plot within a frequency range from 100 KHz to 10 mHz, and (f) Ragone plots of the supercapacitor at different temperatures.

rows the potential ranges available for the supercapacitor electrode charge. This highlights the importance of the evaluation of electrolyte ESW by adopting the same electrodes that will be exploited in energy storage devices.

On the other hand, Fig. 6c even demonstrates that ARG-AC electrodes feature an excellent capacitive response, both in 1 m and 26.4 m AmAc, that is of ca. 300 F g<sup>-1</sup>. This value has been extracted from the slope of the plot of the voltammetric specific charge vs. electrode potential.

The electrochemical preliminary tests of supercapacitors were carried out by a cell with ARG-AC electrodes featuring titanium grids and 26.4 m AmAc WiSE. Fig. 6c shows that with ARG-AC electrodes the cathodic stability range is 2 fold wider than the anodic one. Therefore, to fully exploit the WiSE electrochemical stability window, we adopted an asymmetric configuration of supercapacitor with positive to negative electrode mass loading ratio equal to

ca 2 [40]. Taking into account the good conductivity response at low and high temperatures of 26.4 m AmAc, we evaluated the supercapacitor performance at room temperature (RT), -10 °C, and 80 °C. Fig. 7 reports the CV, GCD, EIS, and Ragone plots of the asymmetric supercapacitor. The highest charge cut-off voltage of the symmetric supercapacitor that enabled high coulombic efficiency (> 99%) was 1.2 V and higher than that feasible with the symmetric device (0.8 V). For comparison, the full electrochemical characterization of a symmetric supercapacitor with two identical ARG-AC electrodes and 26.4 m AmAc WiSE, that featured a maximum cell voltage of 0.8 V, is given as supplementary material (Figure S1 and Section 5 of the Supplementary Information).

Fig. 7a shows the CVs at RT carried out with increasing the scan rate from 5 to 50 mV s<sup>-1</sup> the curves exhibit a quasi-rectangular shape profile demonstrating good capacitive behaviors of the electrodes even at the highest scan rate. The GCD was performed at



current density ranging from  $0.1 \text{ A g}^{-1}$  to  $1 \text{ A g}^{-1}$ . The GCD profiles at room temperature are reported in Fig. 7b. They exhibit triangular shape indicating good reversibility and capacitive behavior of the device. Also, all GCD curves show a small ohmic drop, therefore suggesting a low ESR. Fig. 7(c–e) compare the CVs (at  $10 \text{ mVs}^{-1}$ ), the GCD profiles (at  $0.1 \text{ A g}^{-1}$ ) and the Nyquist plots ( $100 \text{ kHz} - 10 \text{ mHz}$  frequency range) collected at  $-10^\circ\text{C}$ , RT and  $80^\circ\text{C}$ . As expected, the CV currents in Fig. 7c increase with temperature, due to the higher mobility of AmAc ions. A broad peak appears above  $0.9 \text{ V}$  at  $80^\circ\text{C}$ . The specific supercapacitor capacitances from the CV curves in Fig. 7c were  $31 \text{ F g}^{-1}$ ,  $46 \text{ F g}^{-1}$  and  $71 \text{ F g}^{-1}$  at  $-10^\circ\text{C}$ , RT and  $80^\circ\text{C}$ . These values correspond to electrode specific capacitance values of  $116 \text{ F g}^{-1}$ ,  $173 \text{ F g}^{-1}$ , and  $266 \text{ F g}^{-1}$  of ARG-AC. The highest specific supercapacitor capacitances were obtained at  $0.2 \text{ A g}^{-1}$  (Fig. 7d) and resulted  $35 \text{ F g}^{-1}$ ,  $50 \text{ F g}^{-1}$  and  $98 \text{ F g}^{-1}$  at  $-10^\circ\text{C}$ , RT and  $80^\circ\text{C}$ . Correspondingly, the maximum energy densities  $E_{\text{max}}$  were  $7 \text{ Wh kg}^{-1}$  ( $-10^\circ\text{C}$ ),  $10 \text{ Wh kg}^{-1}$  (RT) and  $20 \text{ Wh kg}^{-1}$  ( $80^\circ\text{C}$ ). The ESR values evaluated by the ohmic drop at the beginning of discharge resulted in ca.  $8 \Omega \text{ cm}^2$  at  $10^\circ\text{C}$ ,  $4.5 \Omega \text{ cm}^2$  at RT, and  $2.9 \Omega \text{ cm}^2$  at  $80^\circ\text{C}$ . These values well compares with the medium low frequency resistance of the cells shown by the Nyquist plots reported in Fig. 7. It is worth noting the low ESR exhibited by the cells even at the lowest temperature. The plots indicate that the decrease of temperature mainly impacts ion diffusion in the porous electrode architecture (low frequency tail of the Nyquist plots). On the other hand, MD simulation and experimental data reported in the previous sections already indicated that cooperative mechanisms are responsible for AmAc WiSE ion conductivity. In turn, this affects the kinetics of the electrical double layer formation at the electrode/electrolyte interface, especially at the lowest temperatures. From ESR, maximum power densities  $P_{\text{max}}$  of  $3.7 \text{ kW kg}^{-1}$  ( $-10^\circ\text{C}$ ),  $6.7 \text{ kW kg}^{-1}$  (RT), and  $10.4 \text{ kW kg}^{-1}$  ( $80^\circ\text{C}$ ) were measured.

The practical specific energy and power delivered by the supercapacitor at different currents and temperatures are compared in the Ragone plot reported in Fig. 7f. The maximum specific energy is delivered at the lowest current, while the maximum power is featured at the highest current. At  $0.1 \text{ A g}^{-1}$ , the specific energy is  $5.9 \text{ Wh kg}^{-1}$  ( $-10^\circ\text{C}$ ),  $9.2 \text{ Wh kg}^{-1}$  (RT), and  $15.6 \text{ Wh kg}^{-1}$  ( $80^\circ\text{C}$ ). At  $1 \text{ A g}^{-1}$ , the specific power is  $350 \text{ W kg}^{-1}$  ( $-10^\circ\text{C}$ ),  $450 \text{ W kg}^{-1}$  (RT) and  $507 \text{ W kg}^{-1}$  ( $80^\circ\text{C}$ ).

Finally, Fig. 8a reports the results of a cycle stability test carried out at different current densities,  $0.1 \text{ A g}^{-1}$  and  $1 \text{ A g}^{-1}$  at RT and  $-10^\circ\text{C}$ . For a comparison, Fig. 8b reports the trend of the capacitance vs. cycle number of an analogous device that was assembled with the diluted electrolyte  $1 \text{ m AmAc}$ . The two cells featured very good capacitance retention with coulombic efficiencies approaching 100%. Only by the use of the superconcentrated electrolyte, it was possible to operate the cell at  $-10^\circ\text{C}$  over a period of four days. The test was also performed at  $80^\circ\text{C}$  with a lower  $V_{\text{max}}$  of  $1 \text{ V}$  and the results are reported in figure S2. Even at this high temperature, the coulombic efficiency was higher than 98%. However, in this extreme condition, the capacitance faded by 15% in 1000 cycles, because the cell was not hermetically sealed and vapor leakage occurred.

#### 4. Conclusion

The low-cost super-concentrated aqueous solutions based on ammonium acetate feature circumneutral pH ( $\text{pH} = 7\text{--}8$ ) and ionic conductivity comparable to or higher than typical organic electrolytes. MD simulations confirmed all the experimental results and provided an atomistic picture of the system. The change in the structure of concentrated solutions is due to strong interactions between ions and/or water molecules through the formation of hy-

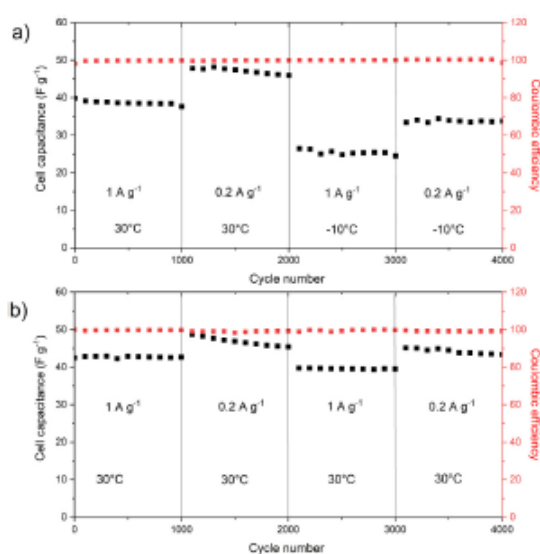


Fig. 8. Trend of the capacitance under galvanostatic cycling at  $0.1 \text{ A g}^{-1}$  and  $1 \text{ A g}^{-1}$  of (a) the asymmetric supercapacitor with  $26.4 \text{ m AmAc}$  at RT and  $-10^\circ\text{C}$  and (b) of the asymmetric capacitor with  $1 \text{ m AmAc}$  at RT.

drogen bonding that cause an increase in pH values and a decrease in ions mobility.

Ammonium and acetate are strongly hydrated as suggested by the absence of minimum in the curve excluding a "structure breaking" effect of ions in the solution, meaning that there is no destruction in the structure of water by the ionic field, in agreement with the viscosity results. In turn, the presence of cooperative motions is suggested by the conductivity temperature dependence, that follows a non-Arrhenius behavior like ionic-liquid electrolytes. Moreover, the MD simulation suggested, that mixture goes from an "ion in water" (conventional solutions) to an "ionic-liquid-like" (concentrated solutions) behavior. One of the most interesting aspects is that the WiSE based on  $26.4 \text{ m}$  exhibits an ESW of  $2.22 \text{ V}$  at Al foil,  $2.9 \text{ V}$  at GC, and an outstanding value of  $3.4 \text{ V}$  when Ti grid was used. Despite such interesting results, the ESW evaluated using ARG-AC electrodes was only  $1.3 \text{ V}$  wide and affected by the high carbon surface area which promoted electrochemical decomposition of the electrolyte. While this finding strongly suggests that ESW is dependent on the kind of electrodes used for the test, it also prevented the development of symmetric supercapacitors with the high cell voltage expected by the study carried out with GC and metal grids.

On the other hand, the ARG-AC electrodes obtained by pyrolysis and activation of argan shells exhibited an exceptional specific capacitance of  $300 \text{ F g}^{-1}$  in the super-concentrated electrolyte. The asymmetric supercapacitor assembled with ARG-AC electrodes and  $26.4 \text{ m AmAc}$  WiSE was able to operate at  $1.2 \text{ V}$ , from  $-10^\circ\text{C}$  to  $80^\circ\text{C}$  with outstanding specific capacitance and low resistance. The symmetric cell delivered noticeable specific energy at extreme temperatures and ranged from  $5.9 \text{ Wh kg}^{-1}$  at  $-10^\circ\text{C}$  to  $15.6 \text{ Wh kg}^{-1}$  at  $80^\circ\text{C}$ , values that are competitive with those of commercial supercapacitors featuring organic electrolyte. A promising option to explore is the increase of energy performance through AmAc WiSE in hybrid supercapacitor involving redox or pseudocapacitive electrodes that features faradaic process within the WiSE ESW.

Overall, our study suggests that AmAc WiSe deserves consideration as cheap, circumneutral and environmentally friendly alternative electrolytes for designing green energy storage systems.

#### Declaration of Competing Interest

The authors declare that they have no known competing financial interests or personal relationships that could have appeared to influence the work reported in this paper.

#### Credit authorship contribution statement

**Mohammad Said El Halimi:** Investigation, Formal analysis, Writing – original draft, Writing – review & editing. **Federico Poli:** Investigation, Formal analysis, Writing – review & editing. **Nicola Mancuso:** Investigation, Formal analysis. **Alessandro Olivieri:** Investigation, Formal analysis. **Edoardo Jun Mattioli:** Investigation, Formal analysis, Writing – original draft. **Matteo Calvaresi:** Investigation, Formal analysis, Writing – original draft, Writing – review & editing, Supervision. **Tarik Chafik:** Funding acquisition, Project administration, Writing – review & editing, Supervision. **Alberto Zanelli:** Writing – review & editing, Funding acquisition, Project administration. **Francesca Soavi:** Conceptualization, Writing – original draft, Writing – review & editing, Supervision, Funding acquisition, Project administration.

#### Acknowledgements

This research was funded by the Italy-South Africa joint Research Progra 2018–2020 (Italian Ministers of Foreign Affairs and of the Environments). The bilateral project CNR Italy CNRST Morocco “Green Supercapacitors” (SACAD002.014, n. 7974, C.U.P. B54I20000790005) and PPR2 16/17 project CNRST Morocco are also acknowledged. This project has received funding from the European Union’s Horizon 2020 research and innovation program under grant agreement No 963550.

#### Supplementary materials

Supplementary material associated with this article can be found, in the online version, at doi:10.1016/j.electacta.2021.138653.

#### References

- [1] A. Balducci, Electrolytes for high voltage electrochemical double layer capacitors: a perspective article, *J. Power Sources* 326 (2016) 534–540.
- [2] L. Xia, L. Yu, D. Hu, G.Z. Chen, Electrolytes for electrochemical energy storage, *Mater. Chem. Front.* 1 (2017) 584–618.
- [3] J. Zhang, X. Yao, R.K. Misra, Q. Cai, Y. Zhao, Progress in electrolytes for beyond-lithium-ion batteries, *J. Mater. Sci. Technol.* 44 (2020) 237–257.
- [4] T.P.T. Pham, C.W. Cho, Y.S. Yun, Environmental fate and toxicity of ionic liquids: a review, *Water Res.* 44 (2010) 352–372.
- [5] V. Ruiz, T. Huynh, S.R. Sivakumar, A. Pandolfo, Ionic liquid–solvent mixtures as supercapacitor electrolytes for extreme temperature operation, *RSC Adv.* 2 (2012) 5591–5598.
- [6] M. Ue, K. Ida, S. Mori, Electrochemical properties of organic liquid electrolytes based on quaternary onium salts for electrical double-layer capacitors, *J. Electrochem. Soc.* 141 (1994) 2989.
- [7] R. Younesi, G.M. Veith, P. Johansson, K. Edström, T. Vegge, Lithium salts for advanced lithium batteries: Li–metal, Li–O<sub>2</sub>, and Li–S, *Energy Environ. Sci.* 8 (2015) 1905–1922.
- [8] V. Sharova, A. Moretti, T. Diemant, A. Varzi, R.J. Behm, S. Passerini, Comparative study of imide-based Li salts as electrolyte additives for Li-ion batteries, *J. Power Sources* 375 (2018) 43–52.
- [9] L. Dagoussat, G.T. Nguyen, F. Vidal, C. Galindo, P.H. Aubert, Ionic liquids and  $\gamma$ -butyrolactone mixtures as electrolytes for supercapacitors operating over extended temperature ranges, *RSC Adv.* 5 (2015) 13095–13101.
- [10] L. Suo, O. Borodin, T. Gao, M. Olguin, J. Ho, X. Fan, C. Luo, C. Wang, K. Xu, Water-in-salt<sup>†</sup> electrolyte enables high-voltage aqueous lithium-ion chemistries, *Science* 350 (2015) 938–943.
- [11] D.P. Leonard, Z. Wei, G. Chen, F. Du, X. Ji, Water-in-salt electrolyte for potassium-ion batteries, *ACS Energy Lett.* 3 (2018) 373–374.
- [12] M.R. Lukatskaya, J.I. Feldblyum, D.G. Mackanic, F. Lissel, D.L. Michels, Y. Cui, Z. Bao, Concentrated mixed cation acetate “water-in-salt” solutions as green and low-cost high voltage electrolytes for aqueous batteries, *Energy Environ. Sci.* 11 (2018) 2876–2883.
- [13] X. Bu, L. Su, Q. Dou, S. Lei, X. Yan, A low-cost “water-in-salt” electrolyte for a 2.3 V high-rate carbon-based supercapacitor, *J. Mater. Chem. A* 7 (2019) 7541–7547.
- [14] Y. Yamada, J. Wang, S. Ko, E. Watanabe, A. Yamada, Advances and issues in developing salt-concentrated battery electrolytes, *Nat. Energy* 4 (2019) 269–280.
- [15] P. Lännelongue, R. Bouchal, E. Mourad, C. Bodin, M. Olariu, S.Le Voir, F. Favier, O. Fontaine, Water-in-salt<sup>†</sup> for supercapacitors: a compromise between voltage, power density, energy density and stability, *J. Electrochem. Soc.* 165 (2018) A657.
- [16] L. Suo, F. Han, X. Fan, H. Liu, K. Xu, C. Wang, Water-in-salt<sup>†</sup> electrolytes enable green and safe Li-ion batteries for large scale electric energy storage applications, *J. Mater. Chem. A* 4 (2016) 6639–6644.
- [17] W. Sun, L. Suo, F. Wang, N. Eidson, C. Yang, F. Han, Z. Ma, T. Gao, M. Zhu, C. Wang, Water-in-salt<sup>†</sup> electrolyte enabled LiMn<sub>2</sub>O<sub>4</sub>/TiS<sub>2</sub> Lithium-ion batteries, *Electrochem. Commun.* 82 (2017) 71–74.
- [18] Q. Dou, S. Lei, D.-W. Wang, Q. Zhang, D. Xiao, H. Guo, A. Wang, H. Yang, Y. Li, S. Shi, Safe and high-rate supercapacitors based on an “acetonitrile/water in salt” hybrid electrolyte, *Energy Environ. Sci.* 11 (2018) 3212–3219.
- [19] Z. Tian, W. Deng, X. Wang, C. Liu, C. Li, J. Chen, M. Xue, R. Li, F. Pan, Superconcentrated aqueous electrolyte to enhance energy density for advanced supercapacitors, *Funct. Mater. Lett.* 10 (2017) 1750081.
- [20] R.M. Maier, T.J. Gentry, Microorganisms and organic pollutants, *Environ. Microbiol.* (2015) 377–413 Elsevier.
- [21] J.A. Maier, C. Martinez, K. Kasavajhala, L. Wickstrom, K.E. Hauser, C. Simmerling, #145B: improving the accuracy of protein side chain and backbone parameters from #99SB, *J. Chem. Theory Comput.* 11 (2015) 3696–3713.
- [22] M.W. Mahoney, W.L. Jorgensen, A three-site model for liquid water and the reproduction of the density anomaly by rigid, non polarizable potential functions, *J. Chem. Phys.* 112 (2000) 8910–8922.
- [23] T. Lee, S. LeGrand, P. Li, C. Lin, T. Luchko, R. Luo, B. Madej, D. Mermelstein, P. Kollman, AMBER, 16, University of California, San Francisco, 2016.
- [24] D.R. Roe, T.E. Cheatham III, P.L.R.A.J. and, CPPTRAJ: software for processing and analysis of molecular dynamics trajectory data, *J. Chem. Theory Comput.* 9 (2013) 3084–3095.
- [25] O. Boujibar, A. Souikry, F. Ghamouss, O. Achak, M. Dahbi, T. Chafik, CO<sub>2</sub> capture using N-containing nanoporous activated carbon obtained from argan fruit shells, *J. Environ. Chem. Eng.* 6 (2018) 1995–2002.
- [26] D. Hulicová-Jurcakova, M. Serebych, G.Q. Lu, N. Kodiweera, P.E. Stallworth, S. Greenbaum, T.J. Bandosz, Effect of surface phosphorus functionalities of activated carbons containing oxygen and nitrogen on electrochemical capacitance, *Carbon N Y* 47 (2009) 1576–1584.
- [27] L.L. Zhang, X. Zhao, Carbon-based materials as supercapacitor electrodes, *Chem. Soc. Rev.* 38 (2009) 2520–2531.
- [28] Y. Korenblit, M. Rose, E. Kockrick, L. Borchardt, A. Kvit, S. Kaskel, G. Yushin, High-rate electrochemical capacitors based on ordered mesoporous silicon carbide-derived carbon, *ACS Nano* 4 (2010) 1337–1344.
- [29] A. Bello, F. Barzegar, M. Madito, D.Y. Momodu, A.A. Khaleed, T. Masikhwa, J.K. Dangbegnon, N. Manyala, Stability studies of polypyrrole-derived carbon based symmetric supercapacitor via potentiostatic floating test, *Electrochim. Acta* 213 (2016) 107–114.
- [30] T.G. Pedersen, A. Hvidt, Volumetric effects due to ion–solvent interaction in aqueous electrolyte solutions, *Carlsberg Res. Commun.* 50 (1985) 193.
- [31] D.E. Goldsack, R. Franchetto, The viscosity of concentrated electrolyte solutions. I. Concentration dependence at fixed temperature, *Can. J. Chem.* 55 (1977) 1062–1072.
- [32] H. Peng, A.V. Nguyen, A link between viscosity and cation-anion contact pairs: adventure on the concept of structure-making/breaking for concentrated salt solutions, *J. Mol. Liq.* 263 (2018) 109–117.
- [33] M. Kaminsky, Ion–solvent interaction and the viscosity of strong-electrolyte solutions, *Discuss. Faraday Soc.* 24 (1957) 171–179.
- [34] M. Petrowsky, R. Frech, Salt concentration dependence of the compensated Arrhenius equation for alcohol-based electrolytes, *Electrochim. Acta* 55 (2010) 1285–1288.
- [35] S. Fang, L. Yang, J. Wang, M. Li, K. Tachibana, K. Kamijima, Ionic liquids based on functionalized guanidinium cations and TFSI anion as potential electrolytes, *Electrochim. Acta* 54 (2009) 4269–4273.
- [36] M. Aniya, M. Ikeda, A Model for non-arrhenius ionic conductivity, *Nanomaterials* 9 (2019) 911.
- [37] N. NIST, Standard Reference Database 69, NIST Chemistry WebBook, National Institute of Standards and Technology, 2010.
- [38] D. Ellerbrock, D.D. Macdonald, Passivity of titanium, part 1: film growth model diagnostics, *J. Solid State Electrochem.* 18 (2014) 1485–1493.
- [39] W. Giurlani, L. Sergi, E. Crestini, N. Calisi, F. Poli, F. Soavi, M. Innocenti, Electrochemical stability of steel, Ti, and Cu current collectors in water-in-salt electrolyte for green batteries and supercapacitors, *J. Solid State Electrochem.* (2020) 1–11.
- [40] R.M. Lazzari, F. Soavi, M. Mastragostino, High voltage, asymmetric EDLCs based on xerogel carbon and hydrophobic IL electrolytes, *J. Power Sources* 178 (2008) 490–496.

## 2.4 Conclusion

In this chapter the main findings regarding the design of green supercapacitors are reported, in particular, the focus of the study has been at first on the exploitation of pullulan, a bioderived aqueous processable polymer to realize high voltage ionic liquid based EDLCs, our study highlight that the combination of aqueous processable binder and hydrophobic ionic liquid allows the realization of EDLCs featuring good energy density, bringing about a smart combination of material that enable an easy to dispose of strategy. The pullulan-based supercapacitor delivers a maximum specific power of up to  $5 \text{ kW kg}^{-1}$ , and maximum specific energy of  $27.8 \text{ Wh kg}^{-1}$  specific energy at 3.2 V, these values well compare with conventional electrical double-layer capacitor performance with the added value of being eco-friendly and cheap with cell capacitance of  $20 \text{ F g}^{-1}$ . The Pullulan-based EDLCs showed good cycling stability up to 5000 cycles. The nitrogen doping of mesoporous carbon has been explored too but the specific capacitance of the obtained materials was smaller than those of the bioderived activated carbon.

Therefore, to conclude, the exploitation of ionic liquid in combination with bioderived aqueous processable biopolymer, seems a valuable strategy to improve the sustainability of EDLCs with good energy densities. To further push the concept of sustainability a valuable strategy is the adoption of doped carbon as well as the exploitation of aqueous electrolyte.

The adoption of WiSE electrolyte indeed seems a promising route since these electrolytes allow to overcome the intrinsic limitation of aqueous electrolyte, namely the low cell voltage. On the other hand, several issues need to be addressed like the choice of the current collector and the electrolyte cost, which is much affected by the salt cost. Ammonium acetate-based WiSE is a promising option. Indeed, asymmetric EDLC delivered noticeable specific energy at extreme temperatures and ranged from  $5.9 \text{ Wh kg}^{-1}$  at  $-10 \text{ }^\circ\text{C}$  to  $15.6 \text{ Wh kg}^{-1}$  at  $80 \text{ }^\circ\text{C}$ , values that are competitive with those of commercial supercapacitors featuring organic electrolytes. The AmAc based EDLCs featured good capacitance retention with coulombic efficiencies approaching 100% for 4000 cycles, noticeably only using the superconcentrated electrolyte, it was possible to operate the cell at  $-10 \text{ }^\circ\text{C}$  over 4000 cycles (a period of four days).

Overall, the studies reported in this section demonstrate the viability of the development of a new generation of EDLCs, by sustainable materials and processes. Different approaches, that include electrode and separator processing and new electrolyte formulations, have been investigated. An additional take home message is that, depending on the selected approach, different additional advantages can be obtained, depending on the selected strategy. As an

example, the combination of IL and water processable polymers brings about a direct separation of the EDLC at the end of life. In turn, AmAc-Wises are circumneutral, which can be of interest when low-corrosive environments are needed.

The main objective of this chapter was to report the best sustainable approaches to achieve high voltage, hence, high specific energy, EDLCs. However, EDLCs are often proposed as energy storage units to be integrated with energy harvesters, like MFC that typically operate at low voltage. In the supercapacitive MFC systems, one of the main challenges is to address system sustainability and efficiency. Voltage operation is limited by the MFC, that is typically well below 1 V.

The next chapter focuses on the strategies that have been followed to design green supercapacitive MFC systems. The main focus is on sustainability of materials and system integration.

## **Chapter 2 references:**

- [1] Spina, G. E., et al., "Natural Polymers for Green Supercapacitors." *Energies*,13.12,(2020), 3115.
- [2] Poli, F., et al., "Pullulan-ionic liquid-based supercapacitor: A novel, smart combination of components for an easy-to-dispose device.", *Electrochimica Acta*, 338, (2020), 135872.
- [3] Brandiele, R., et al., "Nitrogen-Doped Mesoporous Carbon Electrodes Prepared from Templating Propylamine-Functionalized Silica.", *ChemElectroChem*, 7.8, (2020), 1914-1921.
- [4] Giurlani, W., et al., "Electrochemical stability of steel, Ti, and Cu current collectors in water-in-salt electrolyte for green batteries and supercapacitors.", *Journal of Solid State Electrochemistry*,(2020), 1-11.
- [5] El Halimi, M. S., et al., "Circumneutral concentrated ammonium acetate solution as water-in-salt electrolyte.", *Electrochimica Acta*, (2021), 138653.

# Chapter 3: Supercapacitive system

This chapter is devoted to the description of the strategies that have been explored during my Ph.D. to improve the power performance of single-chamber, air-breathing MFCs. These studies were conducted under the collaborative ISARP project with the University of Pretoria (SA). Figure 3.1 summarizes the different approaches that have been followed

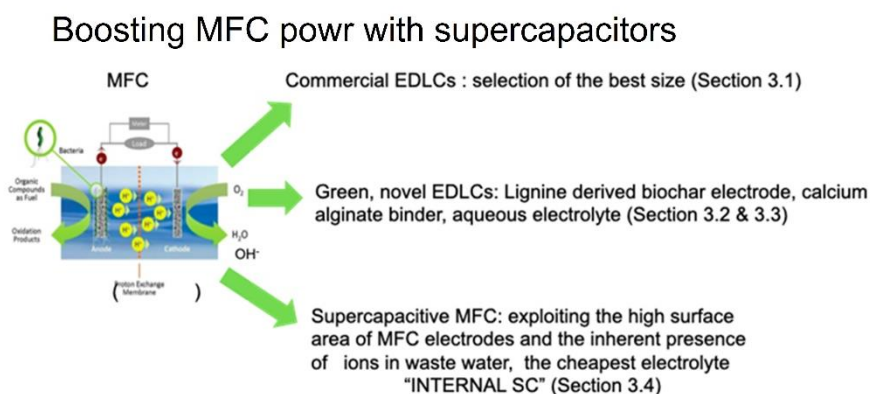


**Figure 3.1.** Strategies followed to boost MFC power by supercapacitive systems integration.

At first, the external integration of commercial supercapacitors with a microbial fuel cell has been studied (Figure 3.2). The experimental details of this study and the main results that have been achieved are summarized in section 3.1 and have been published in the attached paper [1]. The work has been selected for the front cover of the Journal.

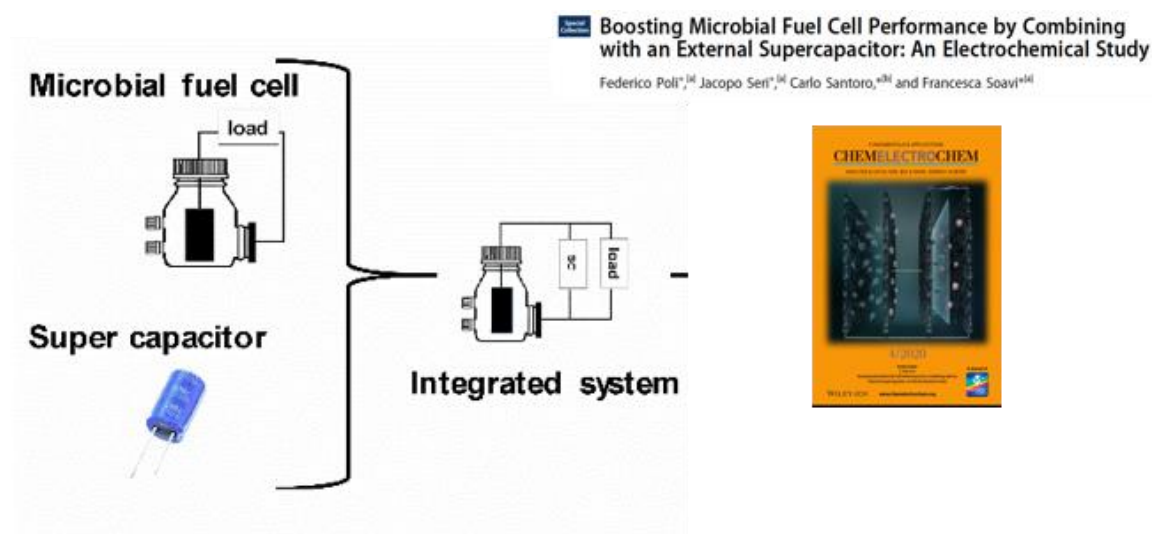


**Figure 3.2.** *External integration of MFC and commercial supercapacitors.*

Subsequently, the activity focused on the improvement of the sustainability of the supercapacitive MFC systems. With the aim of valorizing wastes for energy storage/conversion systems, lignin, i.e. the main component of the effluent of the agricultural biodigester from which the MFC inoculum was taken, has been exploited to prepare activated carbon (LAC). This carbon was investigated for use both as MFC airbreathing cathode and EDLCs electrodes. The experimental details and main results of this study and are summarized in section 3.2 and have been published in the attached paper [2]. The lignin-derived carbon was, then, exploited to design an all-aqueous supercapacitor (ASC). Here, the idea was to substitute the commercial SC externally connected to the MFC in Section 3.1, with a greener one. In addition, the all-aqueous supercapacitor featured a water processable binder like calcium alginate and an aqueous electrolyte-based  $\text{Ca}(\text{NO}_3)_2$ . The results of this study are reported in Section 3.3. Finally, Section 3.4 reports the three different strategies that have been pursued to improve the power performances of MFCs by sustainable components. The different approaches are schematized in Figure 3.3. Specifically,

- The commercial carbon of the MFC air-breathing cathode was substituted with the lignin-derived LAC2. No external SC was used (MFC system, Section 3.4.2).
- The AaSC supercapacitor described in Section 3.3 has been externally connected to an MFC that featured a commercial carbon (MFC//SC system, Section 3.4.3)
- The commercial carbon of the MFC air-breathing cathode was substituted with the lignin-derived LAC2 and an additional carbon brush has been introduced in the MFC and short-circuited to the MFC cathode. No external SC was used (ACCMFC system, Section 3.4.4).
- Finally, the lignin-derived carbon was exploited both for the MFC air-breathing cathode and to decorate the additional carbon brush. This approach brought the monolithic integration of supercapacitive components in the MFC. Even in this case, no external SC was used (MSC-MFC System, Section 3.4.5).

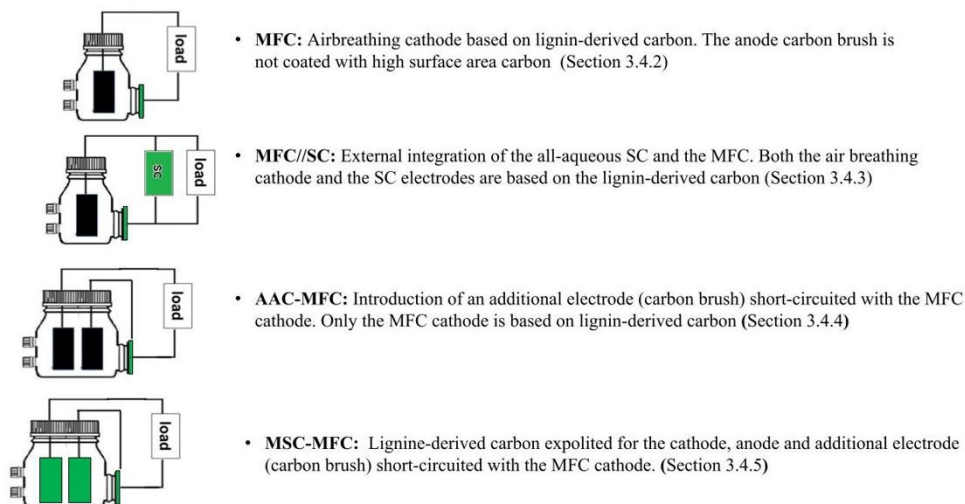


**Figure 3.3** Strategies followed to design a green capacitive MFC system.

### 3.1 Integration of MFCs with commercial supercapacitors to boost power performances

A valuable strategy to improve power performances of MFCs is the combination with an external electrochemical energy storage system, capable of releasing the stored energy at higher power than those achievable by the MFCs alone. Therefore, I conducted a detailed electrochemical study to investigate at the system level the improvement of the performance of the integration of MFCs with external commercial supercapacitors of different sizes (1,3, and 6 F). The adopted procedure consisted in investigating the performances of each MFC and SC unit and the integrated MFC-SC systems under pulsed galvanostatic charge-discharge conditions. From the pulsed test, a short circuit current of 4 mA with a maximum power of 0.55 mW at a current of c.a. 2 mA was measured for the MFC.

From the pulsed discharge test, the MFC equivalent series resistance has been measured and it resulted in 61  $\Omega$ . Moreover, the pulsed discharge at different currents highlighted that the MFC response is a mixed one in which both faradaic and electrostatic contributions were present. The three kinds of commercial supercapacitors have been studied by polarizing them at a maximum cell voltage of 500 mV which is close to the typical OCV of an MFC cell. The three commercial supercapacitors featured an extremely small equivalent series resistance with respect to the MFC cell. Values of 0.2, 0.08, and 0.035 for the 1, 3, and 6 F were measured, respectively. Given the small values of equivalent series resistance, it was possible to test the

commercial SCs up to 100 mA, which is almost 20 times the short circuit current of the MFC. The MFC has been, then, connected in parallel with each supercapacitor separately and the system has been fully discharged at increasing current pulses, from 2 mA to 100 mA. These measurements demonstrated a synergic interaction between MFC and SC with improved power (at high current regimes) and pulse energy (at low currents) performance with respect to those of the separate units. Specifically:

- At high currents pulses effect: The use of SCs enabled output power not feasible with single MFCs. Basic electrochemical characterization of MFC and SC, singularly and combined is necessary for the right sizing and application.
- At low current pulses effect: the MFC contributed to the overall system capacitance, probably owing to its faradaic component. The MFC faradic response contributed to an apparent increase of the system capacitance, a feature that we defined as “apparent capacitance”

Overall, this study highlighted that basic electrochemical characterization of MFC and SC, singularly and combined is necessary for the right system sizing and application. The experimental methods and the results of this study are reported in the following attached paper[1]



Special  
Collection

# Boosting Microbial Fuel Cell Performance by Combining with an External Supercapacitor: An Electrochemical Study

Federico Poli<sup>+, [a]</sup> Jacopo Seri<sup>+, [a]</sup> Carlo Santoro<sup>\*, [b]</sup> and Francesca Soavi<sup>\*, [a]</sup>

Microbial fuel cells (MFCs), despite representing a promising technology, suffer from low power generation that hinders, in most of the cases, their application as power sources. In fact, MFCs are usually coupled with supercapacitors or batteries and these storage units accumulate the energy harvested by MFCs and deliver it on demand. In this work, the electrodes of a MFC are used as electrodes of an internal supercapacitor and discharges and self-recharges are performed and investigated. Discharges between 1.5 mA and 4 mA were presented producing a maximum power of 1.59 mW. Discharges between 1 mA and 100 mA and recharges are systematically studied for three commercial supercapacitors (SCs) with different capacitances of 1 F, 3 F, and 6 F. The MFC was also connected in parallel with

external SCs and discharged galvanostatically. The SC was self-recharged by the MFC without any additional external power sources. At lower current pulses, the MFC contributed to the overall capacitance, probably owing to its faradaic component. At higher current pulses, the use of SCs enables the energy to be harvested by MFCs at power levels that could not be achieved with the MFC alone. This study demonstrates that, through the proper connection and operation mode of the MFC and SC, it is possible to improve and maximize the performance of every single unit. Understanding the MFC–SC combination is important for identifying the right practical application for which the combination is suitable.

## 1. Introduction

Bioelectrochemical systems (BESs) are interesting biotechnologies for treating wastewater, generating electricity and value-added products (VAPs).<sup>[1–4]</sup> Among BESs family, microbial fuel cell (MFC) is the most studied due to the possibility of simultaneous electricity production and pollutant removal.<sup>[5]</sup> In the MFC, on the anode electrode, electroactive bacteria through their metabolism are capable of consuming a variety of organic molecules<sup>[6–7]</sup> and release electrons on the electrode catalyzing the oxidation reaction. The electron transfer occurs through four main pathways: 1) directly through the outer membrane cytochrome *c*; 2) through conductive nanowires; 3) through redox mediators; 4) through direct oxidation of excreted catabolites.<sup>[8–11]</sup> Electrons move through the external circuit generating valuable electricity to the cathode where the reduction reaction takes place. Various oxidants were evaluated<sup>[12]</sup> but oxygen is the most preferred due to its specific

characteristics of low cost, high potential, and natural availability.<sup>[13–15]</sup>

Several advancements have been achieved particularly in the past two decades after the discovery that bacteria can transfer directly electrons to the electrode.<sup>[16–17]</sup> Advancement in material science for improving anode and cathode electrode has certainly been of extreme importance. Particularly, it is important to highlight the enhancement in anode materials with the final goal of increasing the material conductivity and the biotic/abiotic interface.<sup>[18–21]</sup> Carbonaceous materials, as well as metallic materials, fit with the requirement of technology.<sup>[21–22]</sup> Oxygen reduction reaction (ORR) electrocatalysis has also had an impressive boost up due to the enhancement in the catalytic activity of specific catalysts. Despite enzymes such as laccase or bilirubin oxidases are the most active catalysts for ORR in neutral media,<sup>[23–25]</sup> their elevated cost and low durability obstruct their utilization in large scale.<sup>[26]</sup> Platinum is a very active catalyst, but it is extremely expensive and sensible to poisoning in the presence of anions.<sup>[27–30]</sup> Carbonaceous-based materials<sup>[31–33]</sup> and transition metal-containing catalysts<sup>[34–37]</sup> have replaced platinum successfully. The addition of transition metals and especially Fe–N–C active sites has improved significantly the performance almost doubling the MFCs output.<sup>[38–39]</sup>

The main problem that still persists with MFCs is the low power produced that makes it difficult to use directly for practical applications. Therefore, MFCs are usually coupled with an energy storage system (e.g. supercapacitors and batteries) that accumulate the energy produced and delivers it when needed. A successful example of a combination of MFCs with batteries and supercapacitors comes from the robotic field with *Gastrobot*<sup>[40]</sup> and *EcoBots* family.<sup>[41–44]</sup> Other practical applications through a combination of supercapacitors and MFCs have

[a] F. Poli,<sup>+</sup> J. Seri,<sup>+</sup> Dr. F. Soavi  
Department of Chemistry "Giacomo Ciamician"  
Alma Mater Studiorum, Università di Bologna  
Via Selmi, 2, 40126, Bologna, Italy  
E-mail: francesca.soavi@unibo.it

[b] Dr. C. Santoro  
Bristol BioEnergy Centre  
Bristol Robotics Laboratory  
T-Block, University West of England  
Coldharbour Lane, Bristol, BS16 1QY, UK  
E-mail: carlo.santoro830@gmail.com

[\*] These authors contributed equally to this work

Supporting information for this article is available on the WWW under <https://doi.org/10.1002/celec.201901876>

An invited contribution to a Special Collection dedicated to *Giornate dell'Elettrochimica Italiana 2019 (GEI2019)*

also been reported.<sup>[45–53]</sup> The different possible combinations of MFC and power management systems are described in detail in a recent review.<sup>[54]</sup> Recently, also the capacitive features of MFCs anode<sup>[55–58]</sup> and cathode<sup>[59–66]</sup> electrodes have been explored considering the MFCs electrodes as the electrodes of an internal supercapacitor. Therefore, MFCs were discharged like a supercapacitor and the electrodes were self-recharged thanks to different anaerobic and aerobic environments occurring on the MFC anode and cathode.<sup>[60]</sup> Supercapacitive MFCs have shown the possibility of enhancing significantly the power delivered in the form of pulses.<sup>[67,68]</sup>

In this work, an applied electrochemical study is presented in which MFC firstly is considered in its supercapacitive mode and discharged galvanostatically. Then, commercial supercapacitors having a different capacitance of 1 F, 3 F, and 6 F are systematically tested, and discharges are exploited. At last, MFC was connected in parallel with each commercial supercapacitor and discharges/self-recharges were studied. Parameters of interests such as equivalent series resistance (ESR), capacitance, time for complete discharge and recharge are studied and presented. The effect of the synergic combination of MFC and

SC, that enables to improve the performance of every single unit, is discussed.

## 2. Results and Discussion

### 2.1. Microbial Fuel Cell Performance

The polarization curve was performed after the MFC stabilized its voltage output after the inoculation phase. The MFC polarization curve showed an OCV of  $\approx 570$  mV and a short circuit current of slightly over 4 mA (Figure 1). The polarization curve trend is linear indicating ohmic resistance as the main component affecting the output. The maximum power obtained by the power curve was 0.56 mW ( $93.3 \mu\text{W cm}^{-2}$ ), which agrees with previously reported results.<sup>[64]</sup>

### 2.2. Supercapacitive Microbial Fuel Cells

Supercapacitive MFC was discharged at different  $i_{\text{pulse}}$  (1.5 mA to 4 mA) and voltage profiles for discharge (Figure 2.a) and self-recharge (Figure 2.b) are presented. In Figure 2a, it is possible to appreciate the different cell voltage profiles at the tested current density. It is evident that: i) increasing the current density there is a drastic reduction of the discharging time; ii) the slope as well as the shape of the cell voltage profile in time changes. In Figure 2b, it is reported the cell voltage profile under rest condition, during self-recharging.

The parameters of interest for the discharge and the recharge are shown in Table S1. Particularly, the time of complete discharge varied between 51 sec ( $i_{\text{pulse}}$  4 mA) to 1289 s ( $i_{\text{pulse}}$  1.5 mA). Apparent capacitance has been calculated following eq. 3, as the ratio between the current pulse and the variation in voltage in the range where a linear voltage variation holds until 0 mV. Interestingly, the higher capacitance was measured for lower  $i_{\text{pulse}}$  delivered and varied between 0.59 F ( $i_{\text{pulse}}$  4 mA) to 5.25 F ( $i_{\text{pulse}}$  1.5 mA). This variation might be

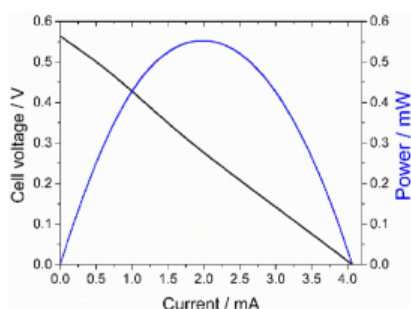


Figure 1. Polarization curve (black) and power curve (blue) of the MFC after reaching steady-state conditions.

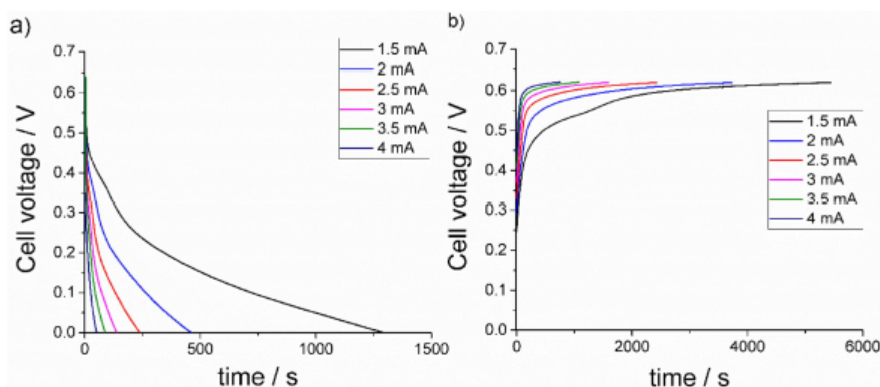


Figure 2. MFC galvanostatic trend for discharge (a) and self-recharge (b).

because, at lower imposed currents, the capacitive behavior is not only due to the electrostatic contribution, but it is also due partially to the faradaic contribution provided by the red-ox reactions occurring at the electrodes. The presence of mixed responses in a microbial fuel cell is already known and has been previously reported.<sup>164,671</sup>

ESR has been measured and had a value of  $61.7 \pm 1.7 \Omega$ . Also, the energy delivered increased with a decrease in  $i_{\text{pulse}}$ . Additionally, energy and power have been calculated too according to the eq. 4 and eq. 5. It has been found, as expected, that the energy decreased increasing the current from a maximum value of 0.078 mWh for the discharge at 1.5 mA to a minimum of 0.007 mWh for the discharge at 4 mA. For what concerns the power, this shows the opposite trend of the energy, increasing from a minimum of 0.79 mW, at a current value of 1.5 mA to a maximum of 1.59 mW at 4 mA.

The presence of the mixed electrostatic/faradaic response can be also the reason for the different self-recharge times after different discharge currents. In fact, higher self-recharge time is needed for lower current delivered.

### 2.3. Power Curves for MFCs Operated in Supercapacitive Mode

The curves related to the power pulse ( $P_{\text{pulse}}$ ) of the MFC discharged galvanostatically are presented in Figure 3. For  $P_{\text{pulse}}$  curves,  $t_{\text{pulse}}$  of 1 s, 5 s, 10 s, 20 s, 40 s, and 60 s were considered.

The maximum power recorded was 1.41 mW and 1.11 mW at  $i_{\text{pulse}}$  of 4 mA after 1 s and 5 s, respectively. At the time of a pulse of 20 seconds,  $P_{\text{pulse}}$  had a value of 0.82 mW ( $i_{\text{pulse}}$  2.5 mA). Increasing the time of discharge,  $t_{\text{pulse}}$  40 seconds, the peak of  $P_{\text{pulse}}$  was 0.67 mW for 1.5 mA current pulse. By the shape of this power curve is possible to state that this cell could be able to stand also lower and higher current.

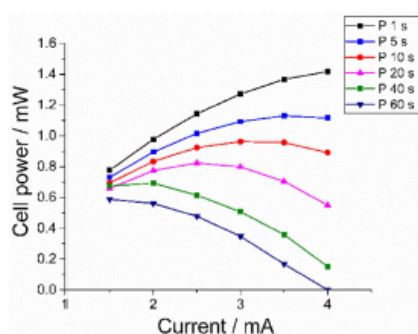


Figure 3. MFC power curves measured for  $t_{\text{pulse}}$  of 1 s, 5 s, 10 s, 20 s, 40 s, and 60 s.

### 2.4. Commercial Supercapacitor Characterization

Commercial supercapacitors featuring capacitance of 1 F, 3 F and 6 F (Table 1) were tested. SCs were charged/discharged with the technique described in Section 3.7.2. Their voltage was limited in charge at the value of 500 mV. This cell voltage has been chosen because it is comparable with the open-circuit voltage (OCV) featured by the tested MFC. Full discharge curves at  $i_{\text{pulse}}$  varying between 2 mA and 100 mA are reported in Figure 4. The data related to the ESR,  $C$ ,  $P_{\text{pulse}}$ ,  $E_{\text{pulse}}$ ,  $t_{\text{pulse}}$ , and  $t_{\text{recharge}}$  are summarized in Table S2. From Figure 4, it is possible to appreciate that the voltage decreases linearly in time, indicating that the discharge is driven only by an electrical double layer process and that these devices behave like an ideal capacitors in series with a resistance (ESR).

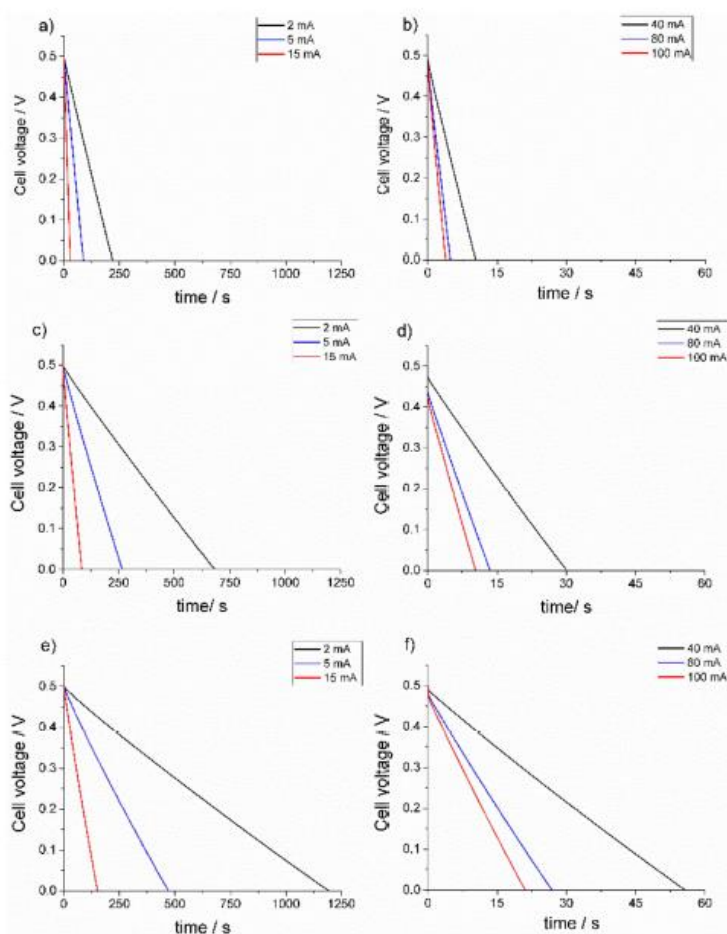
The capacitance measured for the commercial SC declaring 1 F at 2.7 V was  $0.85 \pm 0.03$  F. Lower capacitance was also measured for the commercial SC possessing a capacitance of 3 F and 6 F with values of  $2.62 \pm 0.12$  F and  $4.65 \pm 0.15$  F respectively. The lower capacitance measured compared to the one declared by the manufacturer can be attributed to the fact that the SC charging voltages were limited to 500 mV (as in an MFC) and not to the rated voltage of 2.7 V, as mentioned in the specific characteristics of commercial SCs.

The integral power ( $P_{\text{pulse}}$ ), calculated as reported in eq. 5, increased with higher  $i_{\text{pulse}}$  varying between 0.47 mW (2 mA) and 23.20 mW (100 mA) using 1 F SC, between 0.48 mW (2 mA) and 20.62 mW (100 mA) using 3 F SC and between 0.48 mW (2 mA) and 23.08 mW (100 mA) using 6 F SC (Table S2). The energy ( $E_{\text{pulse}}$ ), as expected, decreased increasing the applied current and depended on the size of the capacitor (Table S2). Indeed, the maximum energy of an ideal capacitor is directly related to its capacitance ( $E_{\text{max}} = \frac{C V^2}{2}$ ). For what concerns the discharge time, considering 1 F SC, the time of complete discharge varied between  $\approx 3$  s (100 mA) and 219 s (2 mA). SC with 3 F capacitance had a time of discharge between 10 s (100 mA) and 682 s (2 mA) and the SC with 6 F capacitance had the longest time measuring between 21 s (100 mA) and 1192 s (2 mA) (Table S2). As expected, the discharge time depends on the capacitance of the device, therefore the higher the capacitance, the higher the discharge time. At the same time, it is possible to appreciate that the capacitance slightly decreases with the increase of the discharge current.

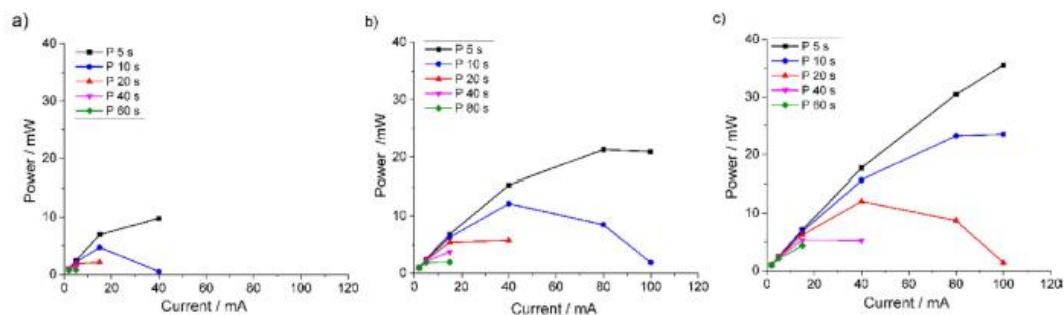
Using the discharge curves reported in Figure 4, it has been possible to draw power profiles for different times, these are reported in Figure 5. Here is possible to appreciate that the increased capacitance of the tested device, led to higher power

Table 1. Commercial supercapacitors characteristics.

Supercapacitor	Operating voltage [V]	Capacitance [F]	ESR [ $\Omega$ ]
EATON-HV0810-2R7105-R	2.7	1	0.2
EATON-TV1020-3R0605-R	2.7	3	0.08
EATON-HV0820-2R7305-R	3	6	0.035



**Figure 4.** Selected galvanostatic discharge curves (Cell Voltage against time) of the tested supercapacitors: a) low and b) high current for the 1 F SC, c) low and d) high current curves for the 3 F SC, and e) low and f) high current curves for the 6 F SC.



**Figure 5.** Power pulse curves measured for  $t_{\text{discharge}}$  of 5 s, 10 s, 20 s, 40 s, and 60 s for the commercial supercapacitors: a) 1 F SC, b) 3 F SC and, c) 6 F SC.

pulses generation since the ESR was low and similar among the tested SCs.

## 2.5. Integration of MFC with Commercial Supercapacitor

The MFC was connected in parallel with each supercapacitor separately. Full discharges with  $i_{\text{pulse}}$  varying between 2 mA and 100 mA have been carried out. After each discharge, the MFC + SC system was left in rest condition and self-recharges were recorded. The cell voltage profiles monitored during these tests are shown in Figure 6. Parameters of interest for discharges/recharges are summarized in Table S3.

As expected, the time of complete discharge was higher as higher was the nominal capacitance of the supercapacitor. Longer discharge times were achieved at  $i_{\text{pulse}}$  of 2 mA where the time for complete discharge was 476 s, 1142 s and 1760 s considering the combination of the MFC with the SC featuring a capacitance of 1 F, 3 F, and 6 F, respectively. At higher  $i_{\text{pulse}}$  of 5 mA, the time for discharge was 126 s (MFC + SC 1F), 353 s (MFC + SC 3F) and 575 s (MFC + SC 6F). At both current pulses, the integration of the MFC with the SC brought to an advantage in terms of the time of complete discharge that increased significantly. For  $i_{\text{pulse}}$  of 2 mA, the discharge time increased by 2.17, 1.67 and 1.47-fold compared to the same discharge time done utilizing only the SC with a capacitance of 1 F, 3 F and 6 F respectively. With respect to the MFC alone,

combination increased the discharge time by 1.04, 2.49, 3.83-fold, respectively. The advantage due to the combination of MFC and SC became even more noticeable for currents higher than 5 mA. Indeed, MFCs with this volume and electrode size cannot deliver any useful power at these currents rates,<sup>1601</sup> while the MFC + SC system is capable to operate up to 100 mA and above.

The recharge time increased with the size of the SC being lower for 1F SC and higher for 6F SC. Furthermore, for each system, the recharge time increased with lower current discharge. At higher  $i_{\text{pulse}}$  due to the high ESR, MFC does not contribute to the overall capacitance. In fact, from  $i_{\text{pulse}}$  of 15 mA up to higher values, the capacitance of the commercial SCs overlap the apparent capacitance of MFC + SC. The shortest recharge time was measured for MFC + SC 1F with 665 s at  $i_{\text{pulse}}$  100 mA. The longest recharge time was instead measured with MFC + SC 6F at  $i_{\text{pulse}}$  of 2 mA (18602 s).

Apparent capacitance has been calculated with equation 9 and, to better understand the trend, it has been plotted against the current pulse (Figure 7). It can be noticed that the integration of the MFC with the commercial supercapacitors enhanced the apparent capacitance especially for  $i_{\text{pulse}}$  lower than 5 mA. The capacitance actually increased with the decrease in  $i_{\text{pulse}}$  with the highest apparent capacitance of 10.02 F (MFC + SC 6F), 8.25 F (MFC + SC 3F) and 4.86 F (MFC + SC 6F) measured at the lowest  $i_{\text{pulse}}$  of 1 mA (Figure 7). The capacitance measured from the MFC discharges is due to two

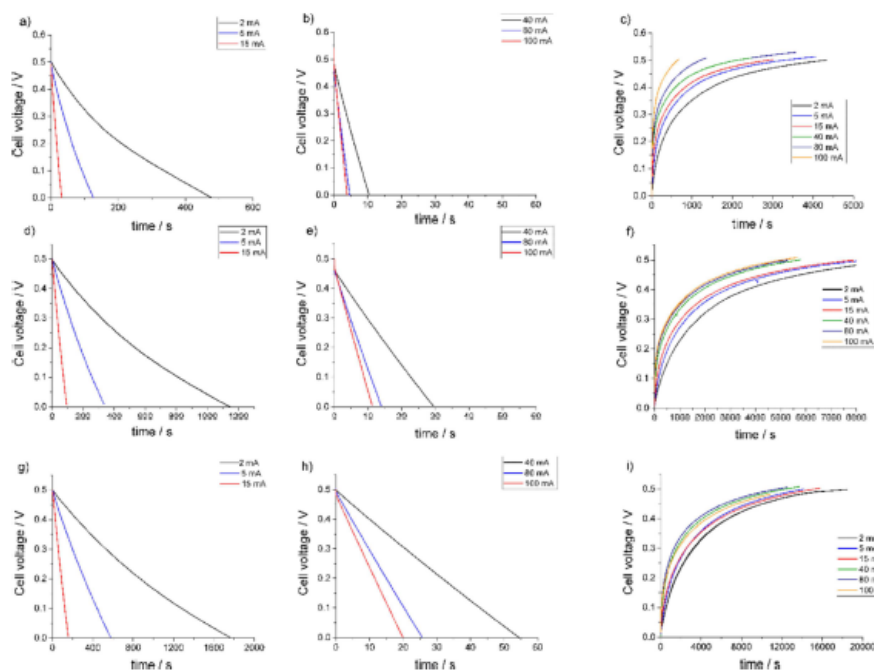
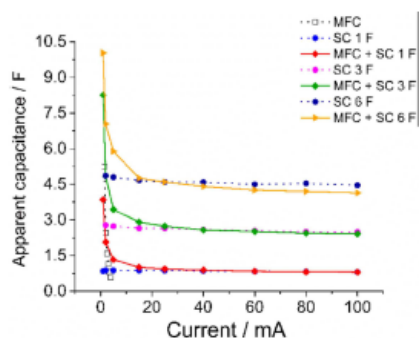


Figure 6. Complete discharges at different pulse current and self-recharges for the MFC + SC 1 F (a–c), MFC + SC 3 F (d–f) and MFC + SC 6 F (g–i) parallel connected systems.



**Figure 7.** Apparent capacitance trend for supercapacitive MFC (black), commercial supercapacitors (dotted lines) and MFC connected in parallel with the commercial supercapacitors (continue lines).

principal contributions: 1) electrostatic due to the electrochemical double layer formed on each electrode and 2) faradaic due to the red-ox reaction occurring on both electrodes. As lower is the  $i_{\text{pulse}}$ , as greater is the contribution of the faradaic component. At the contrary, at higher  $i_{\text{pulse}}$ , the major contributor is the electrostatic component.

#### 2.5.1. Power Curves of SC and MFC Connected in Parallel

Power pulse curves for  $t_{\text{pulse}}$  of 5 s, 10 s, 20 s, 40 s and 60 s obtained by the combination between MFC and SC 1F (Figure 8.a), MFC and SC 3F (Figure 8.b) and MFC and SC 6F (Figure 8.c) were measured. These data are of extreme importance because they show the power produced during a certain amount of time and therefore simulate a potential utilization for a specific application that requires that power. The power increased with: i) lower  $t_{\text{pulse}}$  and ii) higher SC capacitance (Figure 8). Compared to the  $P_{\text{pulse}}$  of the sole SCs, the  $P_{\text{pulse}}$  recorded with the integration of the SC with MFC are comparable. This is expected because the contribution of the MFC takes place only at low current pulses.

#### 2.6. Outlook

Microbial fuel cells (MFCs) have shown a promising outlook for treating or pre-treating wastewater but the production of power remains still quite low for practical applications.<sup>15,67</sup> The MFCs operation mode in intermittent and supercapacitive mode introduced recently in 2016 explores the galvanostatic discharges of the MFC electrodes considered like an internal supercapacitor.<sup>60</sup> Simple carbonaceous-based materials used in this work as electrodes for MFCs were shown previously to display supercapacitive features and enhance power output.<sup>163–66</sup> In this study, the peak in power curves showed during the polarization curve was 0.56 mW while the peak in power determined during galvanostatic discharge was 1.4 mW

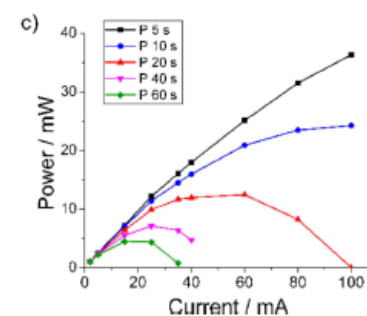
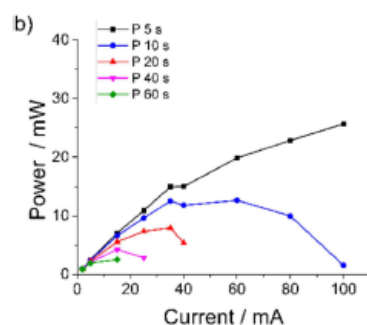
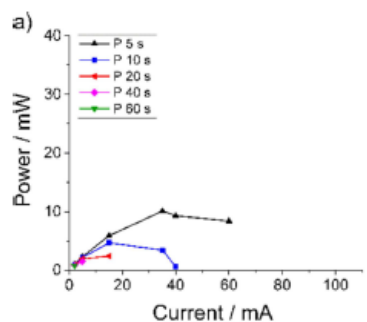


**Figure 8.** Power pulse curves of MFC + SC 1 F (a), MFC + SC 3 F (b) and MFC + SC 6 F (c) measured for  $t_{\text{pulse}}$  of 5 s, 10 s, 20 s, 40 s and 60 s.

(at  $i_{\text{pulse}}$  of 4 mA over 1 s) which was 2.5 times higher despite operated intermittently. The supercapacitive operation, therefore, present benefits compared to the continuous operation.

MFCs were then self-recharged due to the two different/opposite environments (aerobic/anaerobic) as well as to the diverse oxidant and reductant species at the MFC electrodes.

Commercial supercapacitors (SCs) with a nominal capacitance of 1F, 3F and 6F were also tested using galvanostatic discharge limiting the voltage at 500 mV (like the one of MFCs). SCs have high capacitance per volume of reactor but they must

be recharged by the utilization of an external power source. Complete electrochemical characterization considering parameters of interest of these three commercial supercapacitors has been carried out in this study. This characterization allowed understanding the time of complete discharge under a constant current pulse. Due to the low ESR and high capacitance, SCs were able to be discharged for much longer time and produce a much higher power output compared to MFCs.

Then, MFC and SCs possessing different nominal capacitance were combined and connected externally in parallel. At lower current pulses, the effect of the combination had a positive effect on the electrochemical performance. Power generation was increased as well as the capacitance was 2 times higher compared to the value measured separately (MFC or SC alone). The time of complete discharges was also increased by 1.3-fold.

The capacitance value of SC+MFC increased at lower current pulses mainly due to the reactions occurring on the two electrodes (faradaic components), which were added to the electrostatic contribution (SC contribution). The combination of MFC and SC gave another important and positive outlook. The SC was self-recharged by the MFC itself that operated as external power sources. No additional power sources were needed for recharging the supercapacitor. Therefore, despite the MFC did not contribute much to the electrochemical output for higher current pulses due to its high ESR, MFC did contribute to generating a valuable potential difference that served for recharging the SC.

The take-home message of this manuscript is that MFCs can be used as external power sources for charging SCs that can deliver high current pulses during the discharge. This was not novel since it was shown in different previous works in which MFCs were combined with external SCs.<sup>[41-53]</sup> The novelty of this work stays into measuring the parameters of interests such as ESR and capacitance of the single component and the combined systems. These measurements allow understanding that a proper parallel connection enables a synergic interaction between MFC and SC with improved current and pulse energy performance with respect to those of the separate units.

MFC and SC can be independently sized according to any tailored application. High SC size favors long term storage and high current pulses together with MFC fluctuation buffering. Small-size SCs enable short time recharging. At lower current pulses, MFC contributed to enhancing the overall capacitance and therefore enlarging the overall discharging time.

In order to effectively enhance the overall capacitance for larger intervals of  $i_{\text{pulse}}$  and the overall electrochemical performance, the MFC should have much lower overall ESR that might be achieved by i) increasing the electrode conductivity; ii) increasing the electrode sizes or iii) connecting several identical MFCs in parallel.

SCs and MFCs need to be designed in function of the specific practical application that has to be powered. A preliminary study on separate components, in this case, power system and energy storage, should be done in order to optimize the design. In function of the application desired, a capacitor possessing low capacitance should be used for

shorter and more frequent current pulses while a higher capacitance should be used for longer and less frequent current pulses. If a contribution of the MFC is needed during discharge, MFCs should have similar ESR and apparent capacitance similar to the commercial SCs.

### 3. Conclusions

In this work, an MFC was discharged through galvanostatic technique considering the MFC electrodes as the electrodes of an internal supercapacitor. ESR was quantified in  $61.7 \pm 1.7 \Omega$ , the apparent capacitance varied between 0.59 F and 5.25 F and the maximum power achieved was 0.56 mW. Commercial supercapacitors (SCs) with a different capacitance of 1 F, 3 F and 6 F respectively were also studied systematically. Diverse current pulses between 2 mA and 100 mA were performed and ESR and time of complete discharge were determined. MFC and SCs were integrated by a parallel connection and investigated through galvanostatic discharges.

These measurements demonstrated a synergic interaction between MFC and SC with improved power (at high current regimes) and pulse energy (at low currents) performance with respect to those of the separate units.

At low current pulses, the addition of the MFC enhanced the overall capacitance and therefore the time of complete discharge. At high currents, the use of SCs enabled output power not feasible with single MFCs. Basic electrochemical characterization of MFC and SC, singularly and combined is necessary for the right sizing and application.

## Experimental Section

### Single-Chamber MFC

Single chamber membrane-less microbial fuel cell (MFC) was the design adopted for this investigation. MFC consists of a glass bottle DURAN (10 cm long and 5.6 cm in diameter) with high temperature PBT screw cap on the top and a second lateral hole designed specifically for accommodating the air-breathing cathode. A small hole was made on the cap to allow the passage of a syringe, in order to be able to feed the cell at the occurrence.

### Commercial Supercapacitors

Three different commercial supercapacitors were investigated in this work and studied separately and connected in parallel with an MFC. The characteristics of the supercapacitors are shown in Table 1. The main difference consists in the capacitance that was 1 F, 3 F and 6 F respectively.

### Electrodes

Air-breathing cathode electrodes were fabricated separately before the MFC assembly. The cathode was composed of a mixture of activated carbon (AC, Norit, SX Ultra, Honeywell, USA) polytetrafluoroethylene (PTFE, 60% emulsion of water, Du Pont), carbon black (CB, PureBLACK, Superior Graphite) pressed on a steel mesh used as current collector. The weight percentage of AC, PTFE and

CB were 75%, 20% and 5% respectively. The slurry was prepared using ethanol from Fluka (purity 99,8%) and mixed with a Heating Magnetic Stirrer Falc. The average electrode thickness was approximately 0.5 mm. Round electrodes were cut by a manual puncher (geometric area = 6 cm<sup>2</sup>) while squares collectors have been cut (A = 16 cm<sup>2</sup>). The fabricated electrodes were first dried in an oven at 70 °C for 8 hours in order to remove water and ethanol. Carbon fiber Brushes wrapped around a titanium wire core were employed as anode electrodes. These non-corrosive electrodes, thanks to the small diameter of the graphite fibers, are able to achieve high specific surface areas and their characteristics are ideal to be employed as anode for the high biotic/abiotic interface for accommodating bacteria on the electrode surface.

#### Inoculation and Medium

Bacterial inoculum was collected from an anaerobic microbial culture in a hydrolysis stage of a two-phase anaerobic digestion process (hydrolysis + methanization) from agriculture waste. The sludge was taken from agroenergy biogas plant (Biotec Sys srl, Bologna, Italy). The sludge was mixed 50:50 in volumes with a 0.1 M potassium phosphate buffer solution (K-PB, K<sub>2</sub>HPO<sub>4</sub> + KH<sub>2</sub>PO<sub>4</sub>, Sigma Aldrich) and 0.1 M potassium chloride (KCl, Sigma Aldrich). 3 mL of a solution 100 g L<sup>-1</sup> of potassium acetate (CH<sub>3</sub>COOK, Fluka) has been added during the inoculation phase.

#### Experimental Settings

The cathode electrode was screwed with a metal clamp on the lateral hole, with the active face directly in contact with the electrolyte. The chamber was filled with a solution consisted of 50% in volume of the anaerobic digestion process sludge containing bacteria and 50% in volume of the 0.1 M PBS and 0.1 M KCl. The MFC was left in open circuit voltage (OCV) for a couple of hours and then connected to an external resistance of 1000 Ω. During the inoculation phase (initial 3 weeks), the external resistance was decreased roughly every week firstly to 470 Ω and then to 100 Ω in sequence. Inoculation with decrease in external resistance has been used successfully before for allowing the anode colonization. MFCs were refilled one time per month, with 2 mL of potassium acetate as organic compound and 10 mL of distilled water to replace the solution evaporated.

#### Operations

Firstly, an operating MFC was galvanostatically discharged and the discharge-self-recharge cycles were investigated. Secondly, commercial supercapacitors of different size (Table 1) were also galvanostatically charged/discharged and the parameters of interest were studied. Thirdly, the commercial supercapacitors were connected one by one to the MFC in parallel and discharged galvanostatically.

#### Electrochemical Tests

All electrochemical measurements were carried out with a VSP multichannel potentiostats/galvanostats (Bio-Logic Science Instruments) at room temperature. All data were analyzed using Bio-Logic program EC-Lab 10.23.

#### Linear Sweep Voltammetry (LSV)

Linear Sweep Voltammetry (LSV) was performed to evaluate the performance of the MFCs. Two-electrode configuration has been

chosen. In this setup the cathode was used as working electrode, and the anode was short-circuited with the counter electrode and the reference electrode channel of the potentiostat/galvanostat. The current response was plotted as a function of the applied potential, and therefore the delivered power can be calculated by multiplying voltage and current ( $P = V \times I$ ). LSV was run at low scan rate of 0.2 mV s<sup>-1</sup> from OCV to 0 mV.

#### Galvanostatic Cycling with Potential Limitation (GCPL)

Galvanostatic charging/discharging at different currents is a common technique used for testing batteries. In Galvanostatic Cycling with Potential Limitation (GCPL), the current is imposed, and the potential is limited for each step of charge and discharge. In this work, this technique has been used within the following two main sequences: 1) a discharge period in which the MFC was discharged through galvanostatic pulses at different current between the featured open circuit voltage and 0 mV, and 2) a rest (or self-recharge) period to allow the electrodes to be back in their polarized states e.g. the electrical double layer is re-established.

Supercapacitors have been characterized with GCPL charge-discharge cycles at different currents within 0 mV and 500 mV. The latter threshold voltage was selected because it corresponds to the typical cell voltage of the MFC.

#### Determination of the Parameters of Interest

The experimentation allows extracting important data such as ohmic drop ( $\Delta V_{ohmic}$ ), capacitance, specific energy and power of the MFC.

MFCs are initially left in open circuit and the corresponding open circuit cell voltage (OCV) is measured, this is defined as rest condition. The highest voltage featured by the cell in rest is named  $V_{max,OC}$ . Then galvanostatic discharge (GCPL) at a defined current ( $i_{pulse}$ ) is performed. Initially the voltage is subjected to a vertical drop due to the ohmic resistance of the systems (related to electronic and ionic resistances of electrodes and electrolyte). Knowing the ohmic drop, it is possible to calculate the equivalent series resistance (ESR) according to Equation (1).

$$ESR = \frac{\Delta V_{ohmic}}{i_{pulse}} \quad (1)$$

After the ohmic drop, the MFC reaches a new value, called  $V_{max}$  that is the maximum voltage that is featured by the MFC during the discharge process.  $V_{max}$  is calculated according to Equation (2).

$$V_{max} = V_{max,OC} - \Delta V_{ohmic} \quad (2)$$

After  $V_{max}$ , the voltage keeps decreasing with different slopes according to the applied current density. The slope ( $s$ ) is defined as the variation of voltage over time (dV/dt). The capacitance of the cell ( $C_{cell}$ ) can be calculated according to Equation (3).

$$C_{cell} = i_{pulse} \times \frac{dt}{dV} = \frac{i_{pulse}}{s} \quad (3)$$

Due to the presence of electrochemical double layer and faradaic contributions simultaneously in MFCs, it is more appropriate to identify the capacitance as apparent capacitance. This concept will be explored later in the next section.



Energy and power are also important parameters to be measured. The energy of the pulse ( $E_{\text{pulse}}$ ) is calculated from the GCPL discharge curves according to Equation (4).

$$E_{\text{pulse}} = i_{\text{pulse}} \times \int_0^t \frac{V}{3600} dt \quad (4)$$

The power delivered during the pulse ( $P_{\text{pulse}}$ ) is instead calculated as the ratio between  $E_{\text{pulse}}$  and the time of the pulse ( $t_{\text{pulse}}$ ); Equation (5).

$$P_{\text{pulse}} = \frac{E_{\text{pulse}}}{t_{\text{pulse}}} \times 3600 \quad (5)$$

### Supercapacitive Behavior of MFC and MFC-SC

Regarding both MFCs and MFCs connected in parallel with external EDLCs, the evaluation of the capacitive response must consider the parallel processes taking place during the discharge, in this case of faradaic type. It must be noted that, unlike hybrid, asymmetric or pseudocapacitors that work with reversible faradaic processes, a supercapacitive MFC exploits the combination of reversible electrostatic (capacitive) and irreversible electrochemical (faradaic) processes that convert chemical energy of wastewater into electric energy.

The different anaerobic and aerobic environments at the bioanode and at the oxygen cathode are responsible for the electrical double-layer formation at the electrodes/wastewater interface. Therefore, in equilibrium conditions, the two electrodes work like the negative (anode) and positive (cathode) electrodes of an electrochemical capacitor that store charge and energy, by electrostatic charge separation at the two electrodes. When the circuit of the MFC is closed, at high current regimes and at the shortest times, charges accumulated on the interface of both electrodes are released to the electrolyte, like in a SC discharge.<sup>[67]</sup>

Scheme 1 reports the equivalent circuits that describe the parallel connections of the MFC and SC. The MFC is represented with the impedance abbreviated as  $Z_{\text{MFC}}$ . The SC impedance  $Z_{\text{SC}}$  is modelled with an SC equivalent series resistance ( $R_{\text{SC}}$ ) in series with a capacitance ( $C_{\text{SC}}$ ). When an external SC is parallel connected to the MFC, the current generated by the MFC ( $I_{\text{MFC}}$ ) charges the external SC up to a voltage  $V_{\text{SC}}$  that corresponds to the highest voltage of the MFC exhibited in open circuit ( $V_{\text{max,OC}}$ ) (Scheme 1a), i.e.  $V_{\text{SC}} = V_{\text{max,OC}}$ . This occurs only in absence of leakage currents.

The time required to charge the SC is related to  $I_{\text{MFC}}$  and to the SC time constant,  $\tau_{\text{SC}} = R_{\text{SC}}C_{\text{SC}}$ . The SC can then deliver the stored charge while being disconnected to the MFC (Scheme 1b) or reconnected (Scheme 1c) at a current  $I_{\text{SC}}$ . As it concerns the SC branch,  $I_{\text{SC}}$  flows in the opposite direction than the charging  $I_{\text{MFC}}$  current (c.f. Scheme 1a, 1b and 1c).

When the SC is disconnected from the MFC (Scheme 1b), during the galvanostatic discharge at current  $I_{\text{SC}}$ , the discharge profile will linearly decrease over time following the characteristic behavior of a conventional SC. In this case, the delivered charge ( $Q$ ) is according to Equation (6):

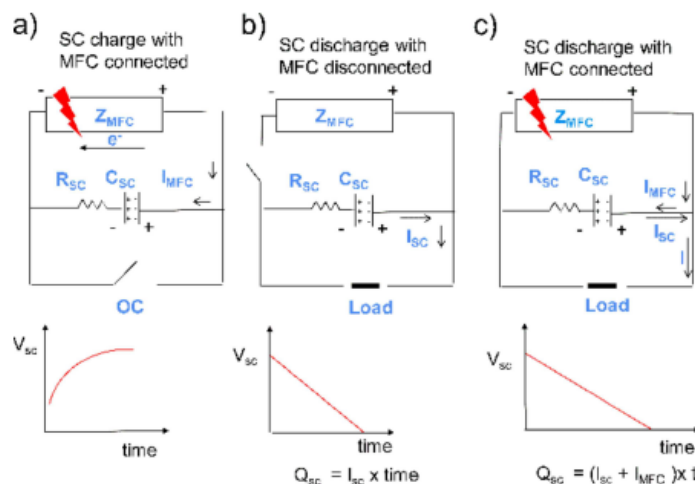
$$Q = I_{\text{SC}} \times dt \quad (6)$$

The capacitance is therefore calculated according to Equation (7):

$$C_{\text{SC}} = \frac{Q}{V_{\text{SC}}} = \frac{I_{\text{SC}} \times t}{V_{\text{MFC}}} \quad (7)$$

When the SC is discharged while being connected with the MFC, the discharge behavior will be different. This is because the SC will deliver energy at the designated current  $I_{\text{SC}}$  while being simultaneously recharged by the MFC (at  $I_{\text{MFC}}$ ). The total charge delivered by the MFC-SC when being connected is calculated in Equation (8):

$$Q = I \times dt = (I_{\text{MFC}} + I_{\text{SC}}) \times dt \quad (8)$$



**Scheme 1.** Equivalent circuits describing the parallel connections of the MFC and SC.

In this case, the integrated system features an apparent capacitance  $C'$  which is higher than the exhibited by the SC alone, as shown in Equation (9):

$$C' = \frac{dQ}{dV} = (I_{MFC} + I_{SC}) \times \frac{dt}{dV} \quad (9)$$

Faradaic and electrostatic are the two processes considered till now and involved during the MFC-SC discharge. Those two processes possess diverse rates and kinetics. Typically, the electrostatic process is much faster compared to the faradaic one. Therefore, it can be predicted that the MFC and MFC-SC apparent capacitance will be dependent on the current pulse delivered and the time of the pulse. In fact, at low  $i_{pulse}$  and long  $t_{pulse}$ , faradaic processes might be the main contributors of the response. In parallel, at high  $i_{pulse}$  and short  $t_{pulse}$ , the electrostatic contribution might be prevalent.

## Acknowledgements

F.S. acknowledges the Italian Minister of Foreign Affairs and the Ministry of the Environment, Land and Sea of the Republic of Italy under the Italy South Africa Research Project (ISARP) 2018–2020 – Progetto di Grande Rilevanza. We would like to thank also Dr. Mattia Bonoli and Biotec Sys srl for providing the inoculum for the microbial fuel cell.

**Keywords:** Microbial fuel cell · Supercapacitor · System Integration · Capacitance · Galvanostatic discharges

- [1] B. E. Logan, B. Hamelers, R. Rozendal, U. Schröder, J. Keller, S. Freguia, P. Aelterman, W. Verstraete, K. Rabaey, *Environ. Sci. Technol.* **2006**, *40*, 5181–5192.
- [2] S. Bajracharya, M. Sharma, G. Mohanakrishna, X. D. Benneton, D. P. Strik, P. M. Sarma, D. Pant, *Renewable Energy* **2016**, *98*, 153–170.
- [3] H. Wang, Z. J. Ren, *Biotechnol. Adv.* **2013**, *31*, 1796–1807.
- [4] W. W. Li, H. Q. Yu, Z. He, *Energy Environ. Sci.* **2014**, *7*, 911–924.
- [5] C. Santoro, C. Arbizzi, B. Erable, I. Ieropoulos, *J. Power Sources* **2017**, *356*, 225–244.
- [6] D. Pant, G. Van Bogaert, L. Diels, K. Vanbroekhoven, *Bioresour. Technol.* **2010**, *101*, 1533–1543.
- [7] P. Pandey, V. N. Shinde, R. L. Deopurkar, S. P. Kale, S. A. Patil, D. Pant, *Appl. Energy* **2016**, *168*, 706–723.
- [8] A. Kumar, L. H.-H. Hsu, P. Kavanagh, F. Barrière, P. N. L. Lens, L. Lapinonnière, J. H. Lienhard, V. U. Schröder, X. Jiang, D. Leech, *Nat. Rev. Chem.* **2017**, *1*, 0024.
- [9] B. E. Logan, R. Rossi, A. Ragab, P. E. Saikaly, *Nat. Rev. Microbiol.* **2019**, *17*, 307–319.
- [10] B. E. Logan, *Nat. Rev. Microbiol.* **2009**, *7*, 375.
- [11] O. Schaeztle, F. Barrière, U. Schröder, *Energy Environ. Sci.* **2009**, *2*, 96–99.
- [12] D. Ucar, Y. Zhang, I. Angelidaki, *Front. Microbiol.* **2017**, *8*, 643.
- [13] Z. Wang, C. Cao, Y. Zheng, S. Chen, F. Zhao, *ChemElectroChem* **2014**, *1*, 1813–1821.
- [14] E. Antolini, *Biosens. Bioelectron.* **2015**, *69*, 54–70.
- [15] H. Yuan, Y. Hou, I. M. Abu-Reesh, J. Chen, Z. He, *Mater. Horiz.* **2016**, *3*, 382–401.
- [16] B.-H. Kim, T. Ikeda, H. S. Park, H. J. Kim, M. S. Hyun, K. Kano, K. Takagi, H. Tatsumi, *Biotechnol. Tech.* **1999**, *13*, 475–478.
- [17] H.-J. Kim, M.-S. Hyun, I. S. Chang, B.-H. Kim, *J. Microbiol. Biotechnol.* **1999**, *9*, 365–367.
- [18] A. Rinaldi, B. Mecheri, V. Garavaglia, S. Licocchia, P. Di Nardo, E. Traversa, *Energy Environ. Sci.* **2008**, *1*, 417.
- [19] Mustakeem, *Mater. Renew. Sustain. Energy* **2015**, *4*, 22.
- [20] M. Sharma, Y. Alvarez-Gallego, W. Achouak, D. Pant, P. Sarma, X. Dominguez-Benetton, *J. Mater. Chem. A* **2019**, *7*, 24420–24436.
- [21] J. Wei, P. Liang, X. Huang, *Bioresour. Technol.* **2011**, *102*, 9335–9344.
- [22] A. Baudler, I. Schmidt, M. Langner, A. Greiner, U. Schröder, *Energy Environ. Sci.* **2015**, *8*, 2048–2055.
- [23] S. R. Higgins, C. Lau, P. Atanassov, S. D. Minteer, M. J. Cooney, *ACS Catal.* **2011**, *1*, 994–997.
- [24] N. S. Parimi, Y. Umasankar, P. Atanassov, R. P. Ramasamy, *ACS Catal.* **2011**, *2*, 38–44.
- [25] S. Shleev, A. El Kasmi, T. Ruzgas, L. Gorton, *Electrochem. Commun.* **2004**, *6*, 934–939.
- [26] C. Santoro, S. Babanova, B. Erable, A. Schuler, P. Atanassov, *Bioelectrochemistry* **2016**, *108*, 1–7.
- [27] W. Yang, J. Li, L. Lan, Q. Fu, L. Zhang, X. Zhu, Q. Liao, *Int. J. Hydrogen Energy* **2018**, *43*, 8474–8479.
- [28] U. Tylus, Q. Jia, H. Hafiz, R. J. Allen, B. Barbiellini, A. Bansil, S. Mukerjee, *Appl. Catal. B* **2016**, *198*, 318–324.
- [29] C. Santoro, M. R. Talarposhti, M. Kodali, R. Gokhale, A. Serov, I. Merino-Jimenez, I. Ieropoulos, P. Atanassov, *ChemElectroChem* **2017**, *4*, 3322–3330.
- [30] D. Sebastián, A. Serov, K. Artyushkova, P. Atanassov, A. S. Aricó, V. Baglio, *J. Power Sources* **2016**, *319*, 235–246.
- [31] X. A. Walter, J. Greenman, I. Ieropoulos, *Bioelectrochemistry* **2018**, *123*, 119–124.
- [32] S. B. Pasupuleti, S. Srikanth, S. V. Mohan, D. Pant, *Bioresour. Technol.* **2015**, *195*, 131–138.
- [33] Z. Wang, G. D. Mahadevan, Y. Wu, F. Zhao, *J. Power Sources* **2017**, *356*, 245–255.
- [34] M. Kodali, R. Gokhale, C. Santoro, A. Serov, K. Artyushkova, P. Atanassov, *J. Electrochem. Soc.* **2017**, *164*, H3041–H3046.
- [35] M. Kodali, S. Herrera, S. Kabir, A. Serov, C. Santoro, I. Ieropoulos, P. Atanassov, *Electrochim. Acta* **2018**, *265*, 56–64.
- [36] M. A. C. de Oliveira, B. Mecheri, A. D'Epifanio, E. Placidi, F. Arciprete, F. Valentini, A. Perandini, V. Valentini, S. Licocchia, *J. Power Sources* **2017**, *356*, 381–388.
- [37] M. Kodali, C. Santoro, S. Herrera, A. Serov, P. Atanassov, *J. Power Sources* **2017**, *366*, 18–26.
- [38] C. Santoro, R. Gokhale, B. Mecheri, A. D'Epifanio, S. Licocchia, A. Serov, K. Artyushkova, P. Atanassov, *ChemSusChem* **2017**, *10*, 3243–3251.
- [39] X. Zhang, D. Pant, F. Zhang, J. Liu, W. He, B. E. Logan, *ChemElectroChem* **2014**, *1*, 1859–1866.
- [40] S. Wilkinson, *Autonomous Robots* **2000**, *9*, 99–111.
- [41] I. Ieropoulos, C. Melhuish, J. Greenman, I. Horsfield, *Int. J. Adv. Robot Syst.* **2005**, *2*, 295–300.
- [42] I. Ieropoulos, J. Greenman, C. Melhuish, I. Horsfield, *12<sup>th</sup> Int. Conf. Synth. Simul. Living Syst.* **2010**, 733–740.
- [43] I. Ieropoulos, C. Melhuish, J. Greenman, *Advances in Artificial Life, Proceedings* **2003**, 2801, 792–799.
- [44] I. Ieropoulos, C. Melhuish, J. Greenman, *8<sup>th</sup> Intell. Auton. Syst. Conf.* **2004**, 128–135.
- [45] Y. M. Arias-Thode, L. Hsu, G. Anderson, J. Babauta, R. Fransham, A. Obratsova, G. Tukeman, D. B. Chadwick, *J. Power Sources* **2017**, *356*, 419–429.
- [46] L. M. Tender, S. A. Gray, E. Groveman, D. A. Lowy, P. Kauffman, J. Melhado, R. C. Tyce, D. Flynn, R. Petrecca, J. Dobarro, *J. Power Sources* **2008**, *179*, 571–575.
- [47] T. Ewing, P. T. Ha, H. Beyenal, *Appl. Energy* **2017**, *192*, 490–497.
- [48] I. A. Ieropoulos, P. Ledezma, A. Stinchcombe, G. Papaharalabos, C. Melhuish, J. Greenman, *Phys. Chem. Chem. Phys.* **2013**, *15*, 15312–15316.
- [49] X. A. Walter, I. Merino-Jiménez, J. Greenman, I. Ieropoulos, *J. Power Sources* **2018**, *392*, 150–158.
- [50] X. A. Walter, A. Stinchcombe, J. Greenman, I. Ieropoulos, *Appl. Energy* **2017**, *192*, 575–581.
- [51] C. Donovan, A. Dewan, D. Heo, H. Beyenal, *Environ. Sci. Technol.* **2008**, *42*, 8591–8596.
- [52] C. Donovan, A. Dewan, D. Heo, Z. Lewandowski, H. Beyenal, *J. Power Sources* **2013**, *233*, 79–85.
- [53] L. Hsu, A. Mohamed, P. T. Ha, J. Bloom, T. Ewing, M. Arias-Thode, B. Chadwick, H. Beyenal, *J. Electrochem. Soc.* **2017**, *164*, H3109–H3114.
- [54] H. Wang, J. D. Park, Z. J. Ren, *Environ. Sci. Technol.* **2015**, *49*, 3267–3277.
- [55] C. Borsje, T. Sleutels, M. Saakes, C. J. N. Buisman, A. Ter Heijne, *J. Chem. Technol. Biotechnol.* **2019**, *94*, 2738–2748.
- [56] A. Ter Heijne, D. Liu, M. Sulonen, T. Sleutels, F. Fabregat-Santiago, *J. Power Sources* **2018**, *400*, 533–538.

- [57] C. Borsje, D. Liu, T. H. J. A. Sleutels, C. J. N. Buisman, A. Ter Heijne, *J. Power Sources* **2016**, 325, 690–696.
- [58] A. Deeke, T. H. J. A. Sleutels, A. Ter Heijne, H. V. M. Hamelers, C. J. N. Buisman, *J. Power Sources* **2013**, 243, 611–616.
- [59] J. Houghton, C. Santoro, F. Soavi, A. Serov, I. Ieropoulos, C. Arbizzani, P. Atanassov, *Bioresour. Technol.* **2016**, 218, 552–560.
- [60] C. Santoro, F. Soavi, A. Serov, C. Arbizzani, P. Atanassov, *Biosens. Bioelectron.* **2016**, 78, 229–235.
- [61] C. Santoro, M. Kodali, N. Shamoan, A. Serov, F. Soavi, I. Merino-Jimenez, I. Gajda, J. Greenman, I. Ieropoulos, P. Atanassov, *J. Power Sources* **2019**, 412, 416–424.
- [62] C. Santoro, C. Flores-Cadengo, F. Soavi, M. Kodali, I. Merino-Jimenez, I. Gajda, J. Greenman, I. Ieropoulos, P. Atanassov, *Sci. Rep.* **2018**, 8, 3281.
- [63] C. Santoro, F. Soavi, C. Arbizzani, A. Serov, S. Kabir, K. Carpenter, O. Bretschger, P. Atanassov, *Electrochim. Acta* **2016**, 220, 672–682.
- [64] C. Santoro, M. Kodali, S. Kabir, F. Soavi, A. Serov, P. Atanassov, *J. Power Sources* **2017**, 356, 371–380.
- [65] C. Santoro, X. A. Walter, F. Soavi, J. Greenman, I. Ieropoulos, *Electrochim. Acta* **2019**, 307, 241–252.
- [66] C. Santoro, J. Winfield, P. Theodosiou, I. Ieropoulos, *Bioresour. Technol.* **2019**, 7, 100297.
- [67] L. Caizán-Juanarena, C. Borsje, T. Sleutels, D. Yntema, C. Santoro, I. Ieropoulos, F. Soavi, A. ter Heijne, *Biotechnol. Adv.* <https://doi.org/10.1016/j.biotechadv.2019.107456>.
- [68] T. Cai, Y. Huang, M. Huang, Y. Xi, D. Pang, W. Zhang, *Chem. Eng. J.* **2019**, 371, 544–553.
- [69] Z. Ge, J. Li, L. Xiao, Y. Tong, Z. He, *Environ. Sci. Technol. Lett.* **2013**, 1, 137–141.

Manuscript received: November 7, 2019  
 Revised manuscript received: December 17, 2019  
 Accepted manuscript online: December 22, 2019

### 3.2 Valorization of lignin waste from biodigester plant in MFC and SC

In this section, the valorization of wastes from anaerobic biodigester plants, as functional materials to be implemented in technologies that address the Water-Energy-Waste Nexus challenges are reported. Lignin, the main solid residue of the biodigester plant, has been valorized into activated biochar with a mild activation agent,  $\text{KHCO}_3$ . The lignin-derived carbons have been tested in view of their use as electrodes of supercapacitor and as an MFC cathode. In addition, the same sludge, that is the liquid effluent of the biodigester plant has been exploited as inoculum and electrolyte for the MFC.

In particular, three carbons have been provided by the University of Pretoria group by using lignin/ $\text{KHCO}_3$  mass ratios of 1:0.5 (LAC-0.5) and 1:2 (LAC-2). Nitrogen adsorption, Raman spectroscopy, X-ray diffraction, and TEM imaging have been used to characterize the two-carbon. By nitrogen adsorption isotherm measurement, the activated carbon shows both mesopores and micropores displaying BETs of  $1558 \text{ m}^2\text{g}^{-1}$  and  $1879 \text{ m}^2\text{g}^{-1}$ , respectively. The interconnected porous network and the high surface area made the lignin-derived porous carbons suitable electrode materials for dual applications. The Raman data showed that LAC-2 had a higher amount of disordered carbon with respect to the LAC-0.5. The carbons have been tested as the main components of electrodes of supercapacitors in 2.5 M  $\text{KNO}_3$  electrolyte. Both carbons displayed good reversible charge storage capability in both the negative (-0.8 V to 0 V vs. Ref) and the positive (0 V to + 0.8 V vs. Ref) potential windows in 2.5 M  $\text{KNO}_3$  electrolyte. In particular, from the single electrode tests, LAC-2 carbon exhibited a superior specific capacitance of  $114 \text{ F g}^{-1}$  in 2.5 M  $\text{KNO}_3$  with respect to LAC-0.5 ( $9 \text{ F g}^{-1}$ ). Therefore, LAC2 activated carbon has been selected to prepare a symmetric EDLC displaying a good specific capacitance of  $28.5 \text{ F g}^{-1}$ , corresponding to an electrode specific capacitance of  $114 \text{ F g}^{-1}$ , with specific energy-specific and power up to  $10 \text{ Wh kg}^{-1}$  and  $6.9 \text{ kW kg}^{-1}$ , respectively. Durability tests showed that the device was able to maintain capacitance retention of 84.5% after 15000 charge-discharge cycles.

The lignin-derived carbons were also studied as electrocatalysts for ORR in a neutral medium, to investigate the feasibility of the use of LAC as the main component of microbial fuel cell air-breathing cathode. The LAC-2 showed higher ORR electrocatalytic activity than LAC-0.5. Indeed, LAC-2 showed higher current density values and superior ORR activity as compared to LAC-0.5. The number of electrons transferred during ORR was higher for LAC-2. Once

integrated with an air-breathing cathode, the material exploited high electrochemical ORR activity especially at high current densities.

Overall, this study demonstrated that biochar derived from lignin waste of anaerobic bioreactor plants, activated with a mild activation agent, like  $\text{KHCO}_3$ , features capacitive and ORR electrocatalytic properties that are comparable or even superior with those of commercially available carbons. It demonstrates that waste can be effectively valorized as functional materials to be implemented in technologies that enable efficient energy management and water treatment, therefore simultaneously addressing the Water-Energy-Waste Nexus challenges. Indeed, the good supercapacitor performance and ORR electrocatalytic behavior of the lignin-derived carbons indicated a potential use as cathode catalysts and electrode materials for microbial fuel cells and supercapacitors.

The experimental methods and the results of this study are reported in [2], which is here attached as a complete publication. The good capacitive and ORR performance of the lignin-derived carbon was, then, exploited to design green supercapacitive MFC systems, as described in the next Sections 3.3 and 3.4.



## Valorization of biodigester plant waste in electrodes for supercapacitors and microbial fuel cells



Bridget K. Mutuma<sup>a</sup>, Ndeye F. Sylla<sup>a</sup>, Amanda Babu<sup>a</sup>, Ndeye M. Ndiaye<sup>a</sup>, Carlo Santoro<sup>b</sup>,  
Alessandro Brilloni<sup>c</sup>, Federico Poli<sup>c</sup>, Ncholu Manyala<sup>a,\*</sup>, Francesca Soavi<sup>c,\*</sup>

<sup>a</sup> Department of Physics, University of Pretoria, Pretoria, South Africa

<sup>b</sup> Department of Materials Science, University of Milano-Bicocca, Via Cozzi 55, Milano 20125, Italy

<sup>c</sup> Department of Chemistry "Giacomo Ciamician", Alma Mater Studiorum - Università di Bologna, Via Selmi 2, Bologna 40126, Italy

### ARTICLE INFO

#### Article history:

Received 4 March 2021

Accepted 20 July 2021

Available online 28 July 2021

#### Keywords:

Lignin

KHCO<sub>3</sub> activation

Supercapacitors

Oxygen reduction reaction

Microbial fuel cells

Waste water energy nexus

### ABSTRACT

This study aims at demonstrating that wastes from anaerobic biodigester plants can be effectively valorized as functional materials to be implemented in technologies that enable efficient energy management and water treatment, therefore simultaneously addressing the Water-Energy-Waste Nexus challenges. Lignin, the main solid residue of the biodigester plant, has been valorized into activated biochar with a mild activation agent, like KHCO<sub>3</sub>, to produce electrode of supercapacitors and microbial fuel cells. In addition, the same sludge that is the liquid effluent of the biodigester plant has been exploited as inoculum and electrolyte for the MFC. The lignin-derived carbons obtained at lignin/KHCO<sub>3</sub> mass ratios of 1:0.5 (LAC-0.5) and 1:2 (LAC-2) comprised of mesopores and micropores displaying BETs of 1558 m<sup>2</sup>g<sup>-1</sup> and 1879 m<sup>2</sup>g<sup>-1</sup>, respectively. LAC-2 carbon exhibited a superior specific capacitance of 114 F g<sup>-1</sup> in 2.5 M KNO<sub>3</sub> with respect to LAC-0.5. A supercapacitor with LAC-2 electrodes was built displaying specific energy specific power up to 10 Wh kg<sup>-1</sup> and 6.9 kW kg<sup>-1</sup>, respectively. Durability tests showed that the device was able to maintain a capacitance retention of 84.5% after 15,000 charge-discharge cycles. The lignin-derived carbons were also studied as electrocatalysts for ORR in a neutral medium. The LAC-2 showed higher ORR electrocatalytic activity than LAC-0.5. The interconnected porous network and the high surface area made the lignin-derived porous carbons suitable electrode materials for dual applications. The feasibility of the use of LAC 2 carbon incorporated in an air breathing cathode for MFC applications is also reported.

© 2021 Elsevier Ltd. All rights reserved.

### 1. Introduction

Affordable and clean energy, clean water and sanitation, and responsible consumption are three of strategic goals of the 2030 Sustainable Agenda [1]. These goals are extremely interconnected within the so-called Energy-Water-Waste Nexus [2]. Indeed, energy is needed to provide clean water from wastewater and water is required in power plants. In turn, both energy and water are needed to treat wastes. Therefore, transforming wastes into energy-related valuable products closes the loop and is expected to be a powerful strategy to address sustainability agenda goals. The transformation and valorization of organic wastes into smart materials is envisioned to be implemented in technologies that enable an efficient management of renewable energy sources and an efficient treat-

ment of waters, like electrical supercapacitors (even called electrical double layer capacitors, EDLCs) and microbial fuel cells (MFCs).

EDLCs store electric energy by an electrostatic process that gives rise to the so-called double layer capacitance at the interface between high surface area carbonaceous electrodes and the electrolyte. Their fast charge/discharge processes enable superior specific power and cycle life, but lower energy density, compared to batteries. For their fast response time, supercapacitors represent emerging technology for high peak power demanding applications, like electrical energy storage in renewable energy plants [3].

MFCs use electroactive microorganisms as biocatalysts to convert chemical energy stored in wastewater's organic matter into electricity. Bioanodes are coupled to air breathing cathodes, where electrocatalytic reduction of oxygen takes place. MFCs are alternative wastewater treatment devices. It was shown that MFCs are capable of degrading a plethora of simple organics and complex civil and industrial wastewaters [4]. However, MFCs deliver low power and are difficult to be directly used for practical applications. A solution is to couple MFCs with an energy storage system, like an

\* Corresponding authors.

E-mail addresses: [ncholu.manyala@up.ac.za](mailto:ncholu.manyala@up.ac.za) (N. Manyala), [francesca.soavi@unibo.it](mailto:francesca.soavi@unibo.it) (F. Soavi).

EDLC, that accumulates the energy produced by the MFC and delivers it when needed at high power rate [5–8].

EDLCs and MFCs share high surface area carbon-based electrodes. Indeed, high surface area carbons are used in EDLCs to provide high specific capacitance ( $100\text{--}200\text{ F g}^{-1}$ ) [3]. In turn, both MFC anode and cathode exploit carbonaceous materials in order to accommodate the electroactive biofilm and performing the oxygen reduction reaction (ORR), respectively [9].

Biomass is arising as a strategic and omnipresent carbon source. In recent years, the biochar obtained by pyrolysis and activation of biomasses has been widely explored for EDLC and MFC electrodes [10]. For EDLCs, the biochar porous architecture strongly affects electrode and device energy and power performance. High surface area has to be achieved by simultaneous tailoring pores size distribution for easy access of electrolyte ions, that is needed to set up the double layer capacitance [3]. A porous carbon matrix is created depending on the type and amount of activating agent, reaction time as well as the temperature [11–13]. For instance, high activation temperatures ( $> 600\text{ }^\circ\text{C}$ ), longer reaction time ( $> 30\text{ min}$ ) and the use of alkali hydroxides as activating agents is known to promote the creation of more pores on the carbon matrix [13–16].  $\text{KHCO}_3$  is a weak base that has been reported to result in porous carbons owing to its decomposition to  $\text{K}_2\text{CO}_3$  at higher temperatures and it is capable of creating pores resulting from the evolution of CO and  $\text{CO}_2$  gases [15]. Compared to other activating agents,  $\text{KHCO}_3$  is exceptional because, compared to KOH, it is less corrosive and more environmentally friendly. Moreover, the decomposition of  $\text{KHCO}_3$  produces more gas and creates a good expansion effect compared to KOH, which is beneficial to pore formation and production of hierarchically porous carbons [14–20].

One of the most challenging issues to be addressed for MFC application is the high cost of the electrodes material and the sluggish oxygen reduction reaction (ORR) occurring at the cathode [21]. Therefore, the development of low cost air breathing cathodes with low cost biochar material with high electrocatalytic activity is imperative. Typically, MFCs operate in a (circum)neutral medium and at room temperature to support the activity of the bacteria and their survival. At a neutral pH of 7, the low concentration of  $\text{H}^+$  and  $\text{OH}^-$  ( $10^{-7}\text{ M}$ ) influences ORR kinetics and MFC power output [22,23]. Activated carbons provide large surface areas and hierarchical porous structure that allow for faster ORR kinetics and high-power output in microbial fuel cells [24].

Activated biochar has been obtained from a wide range of biomasses and lignin stands out because it is the third most abundant natural polymer. In addition, lignin is one of the major wastes of anaerobic digestion processes and pulp and paper making industries [25–27]. Its pyrolysis processes have been deeply investigated and lignin-derived biochar has already been proposed as an EDLC electrode component [10, 28–32]. Highly porous carbons have been derived from lignin using various chemical activating agents, including  $\text{KHCO}_3$  [17]. However, the effect of lower mass ratios of lignin biomass/ $\text{KHCO}_3$  on their physicochemical, electrochemical and electrocatalytic properties is rarely reported. Besides, the ability to use a lower and an appropriate mass ratio of lignin biomass/ $\text{KHCO}_3$  is a plausible solution for environmental sustainability and the method is suitable for large scale production of activated carbons. In our previous studies, we exploited  $\text{KHCO}_3$  to activated peanut shells derived biochar. We observed that the specific surface doubled by increasing the biomass to  $\text{KHCO}_3$  mass ratio from 1:1 to 1:2. A further increase of the ratio only provided less than 10% gain in specific surface area [15].

This study emphasizes on the reusability of wastes from biorefinery industries and the use of smaller amounts of a less corrosive activating agent, like  $\text{KHCO}_3$ , as a suitable approach for sustainable cheap and easily processable porous carbons from lignin. The effect of  $\text{KHCO}_3$  activating agent on the structural and textural prop-

erties of lignin-derived activated carbons is reported. The biochar obtained is then tested in EDLCs featuring a neutral aqueous solution of  $\text{KNO}_3$  that offers the advantage of being greener with respect to organic electrolytes [3,15, 18]. In addition, the biochar is investigated as ORR electrocatalysts to be used in MFC cathodes. The same sludge that is the liquid effluent of the biodigester plant has been exploited as inoculum and electrolyte for the MFC.

## 2. Materials and methods

### 2.1. Starting materials

Potassium hydrogen carbonate,  $\text{KHCO}_3$  (99.99%), potassium nitrate,  $\text{KNO}_3$  (99.99%), hydrochloric acid, HCl (37 %), carbon acetylene black (99.95%), polyvinylidene difluoride, PVDF (99 %) and N-methyl-2-pyrrolidone, NMP (99%), were purchased from Merck chemicals. Argon, Ar (99.99%) was used as received from Afrox. Polycrystalline nickel foam (surface area of  $420\text{ m}^2\text{g}^{-1}$  and 1.6 mm thickness, Alantum (Munich, Germany) and microfiber filter paper (0.18 mm thickness, ACE chemicals) were used for the electrode preparation.

### 2.2. Preparation of lignin-derived activated carbons

The dried lignin was washed with water/ethanol mixture and dried at  $80\text{ }^\circ\text{C}$  for 12 h in an electric oven. Approximately 3 g of lignin were soaked for 24 h in a  $\text{KHCO}_3$  solution comprising of 1.5 g of  $\text{KHCO}_3$  in 40 mL of deionized water. The mixture was then dried at  $80\text{ }^\circ\text{C}$  for 12 h in an electric oven. The dried mold was transferred into a horizontal tubular furnace and gradually heated to  $850\text{ }^\circ\text{C}$  at a ramp rate of  $5\text{ }^\circ\text{C min}^{-1}$  for 1 h under  $250\text{ cm}^3\text{ min}^{-1}$  flow of Ar gas. The obtained product was soaked in 3 M HCl for 8 h, washed with deionized water until a neutral pH was achieved and thereafter dried overnight at  $80\text{ }^\circ\text{C}$ . The dried product was labelled as LAC-0.5. A similar procedure was repeated for mass ratio of 1:2 (3 g lignin, 6 g of  $\text{KHCO}_3$  and 40 mL of water) and product labelled as LAC-2. The morphology of the carbons was evaluated using scanning electron microscopy (SEM) and transmission electron microscopy (TEM). The structural and textural properties of the samples were investigated using Raman spectroscopy, powder X-ray diffraction (XRD) and nitrogen physisorption analysis (Brunner, Emmet and Teller; BET).

### 2.3. Electrode preparation for supercapacitors

The electrode materials were prepared by mixing the active material, carbon acetylene black and polyvinylidene fluoride at a ratio of 8:1:1 followed by the addition of N-methyl-2-pyrrolidone (NMP) solution to form a slurry. The slurry was coated onto a nickel foam ( $1\text{ cm} \times 1\text{ cm}$ ) and dried at  $80\text{ }^\circ\text{C}$  for 12 h. Three electrode measurements were carried out using a Bio-Logic VMP300 potentiostat (Knoxville TN 37, 930, USA) controlled by the EC-lab V 11.40 software. A glassy carbon counter electrode, Ag/AgCl reference electrode and the LACs as working electrodes were used to perform the electrochemical measurements in a 2.5 M  $\text{KNO}_3$  electrolyte solution.

A symmetric device was fabricated in a coin-cell type configuration using a fiberglass filter separator (Whatmann GF/F, thickness  $360\text{ }\mu\text{m}$ ) and an active material mass loading of approximately  $6\text{ mg cm}^{-2}$  in 2.5 M  $\text{KNO}_3$ . The cyclic voltammetry (CV) and galvanostatic charge-discharge (GCD) measurements were investigated at different scan rates and specific current values, respectively. The electrochemical impedance spectroscopy (EIS) measurements were carried out in a frequency range of 10 mHz to 100 kHz at an open circuit potential. The specific capacitances for a half-cell and single

electrode of the symmetric device were calculated from the reciprocal of the slope ( $\Delta V/\Delta t$ ) of the discharge curve of the GCD plots collected by a 3- and 2-electrode setup, respectively, using Eqs. (1) and (2) [32, 33]:

$$C_S = \frac{I \Delta t}{\Delta V m_S} \quad (1)$$

$$C_d = \frac{4I \Delta t}{\Delta V m_{tot}} \quad (2)$$

where  $I$  is the current applied,  $\Delta t$  is the discharge time and  $\Delta V$  is the potential window. In Eq. (3),  $m_S$  is the mass of the electrode in a three-electrode configuration (half-cell) and the  $C_S$  is the specific capacitance for a half-cell. In Eq. (2),  $m_{tot}$  is the total mass of the positive and negative electrode in a two-electrode configuration (full cell/device) and the  $C_d$  is the specific capacitance of a single electrode in a full-cell.

The specific energy ( $E_d$ ) is expressed in  $J g^{-1}$  as evaluated using Eq. (3). To convert the unit  $J g^{-1}$  to  $Wh kg^{-1}$  the expression in Eq. (3) was divided by a factor of 3600 and further multiplied by 1000 as illustrated in Eq. (4):

$$E_d = 0.5C_S(\Delta V) \quad (J g^{-1}) \quad (3)$$

$$E_d = 0.5C_S(\Delta V) = \frac{1000 \times C_d(\Delta V)^2}{2 \times 4 \times 3600} \quad (Wh kg^{-1}) \quad (4)$$

Thus, the specific energy and corresponding specific power of the device were calculated according to Eqs. (5) and (6), where  $IR_{drop}$  is the internal voltage drop:

$$E_S = \frac{C_d(\Delta(V - IR_{drop}))^2}{28.8} \quad (5)$$

$$P_S = \frac{3600E_S}{\Delta t} \quad (6)$$

The value expression in Eq. (4) was multiplied by 3600 to convert the discharge time from h to seconds. In Eq. (4), the value of  $C_d$  that was measured at each current density was used.

#### 2.4. Oxygen reduction reaction kinetics

Rotating disk electrode (RDE) technique was used to investigate the ORR kinetics at the carbon surfaces. The LAC-0.5 and LAC-2 inks were prepared by suspending 8 mg of each catalyst separately into 1 mL of Ethanol-Water-5% Nafion solution (67:30:3 volume ratio) and sonicated for 1 min for ensuring a good dispersion. The catalyst loading investigated during this study was  $0.56 \text{ mg cm}^{-2}$ . A neutral electrolyte solution comprising of 0.1 M potassium phosphate buffer and 0.1 M KCl was purged with pure oxygen for 30 min prior to measurements. Ag/AgCl and Pt were used as reference and counter electrodes, respectively. Electrode potential values are given vs. Normal Hydrogen Electrode (NHE,  $-0.198 \text{ V vs. Ag/AgCl}$ ). Linear sweep voltammetry (LSV) measurements were used to compare the activity of the different catalysts for the oxygen reduction reaction. LSV was run from 0.6 V to  $-0.7 \text{ V vs. NHE}$  at a scan rate of  $5 \text{ mV s}^{-1}$  with a rotation speed varying from 400 rpm to 2500 rpm.

Koutecky-Levich equation is often used for calculating the number of electrons transferred during the ORR by the catalyst of interest ( $n$ ) and it is described in Eq. (7):

$$\frac{1}{j} = \frac{1}{j_k} + \frac{1}{j_d} = \frac{1}{0.62 n F C_{O_2} D_{O_2}^{2/3} \nu^{-1/6} \omega^{-1/2}} = \frac{1}{j_k} + \frac{1}{B \omega^{1/2}} \quad (7)$$

where  $j$  is the measured current density,  $j_k$  is the electrode potential dependent kinetic current density of the ORR,  $j_d$  is the

diffusion-limited current density,  $n$  is the average number of electrons transferred per catalytic activity,  $F$  is the Faraday's constant ( $96,485 \text{ C mol}^{-1}$ ),  $C_{O_2}$  is the concentration of  $O_2$  in the electrolyte ( $1.117 \cdot 10^{-6} \text{ mol mL}^{-1}$ ),  $D_{O_2}$  is the  $O_2$  diffusion coefficient in aqueous media ( $1.9 \cdot 10^{-5} \text{ cm}^2 \text{ s}^{-1}$ ),  $A$  is the electrode geometric area,  $\nu$  is the kinematic viscosity ( $0.01073 \text{ cm}^2 \text{ s}^{-1}$ ) and  $\omega$  is the electrode rotation speed. The values used in this work were retrieved by [22, 34]

#### 2.5. Air breathing MFC cathode fabrication and testing

The feasibility of the use of lignin-derived biochar as MFC cathode was evaluated in real environment. Specifically, a cubical-shape single chamber membraneless MFC ( $3 \text{ cm}^3$ ) was assembled with symmetrical electrodes. The electrodes featured lignin biochar, conductive carbon pure black additive and PTFE based binder, in 8:1:1 mass ratio. The electrodes were prepared with the procedure described in our previous work and pressed over a Ti current collector grid with a pressure of  $1 \text{ ton cm}^{-2}$  [8]. The cathode had a mass loading of 60 mg and an area of  $1.13 \text{ cm}^2$  ( $53 \text{ mg cm}^{-2}$ ). A solution composed of 50% phosphate buffer saline solution (1x) and 50 % sludge in volume with  $160 \text{ mg L}^{-1}$  of sodium acetate was used as inoculum and MFC fuel. The sludge was the main liquid effluent of the biodigester plant (Biotech sys. S.r.l.), from which lignin waste was recovered.

The ORR performance of the lignin derived carbon was evaluated by linear sweep voltammetry (LSV). The cathode was used as the working electrode, the anode was used as the counter electrode, the reference electrode was an Ag/AgCl electrode. Electrode potential values are given vs. NHE.

### 3. Results

#### 3.1. Morphological analyze

The morphology of the LAC samples was confirmed using scanning electron microscopy (SEM) and transmission electron microscopy (TEM). Fig. 1a,b shows that the LAC samples are porous at low and high magnifications. It can be seen that in LAC-2, the higher amount of  $KHCO_3$  generates more pores that are better interconnected than in LAC-0.5. The generation of a porous network can be ascribed to the decomposition of  $KHCO_3$  at higher temperatures releasing  $K_2CO_3$ ,  $CO_2$  and  $H_2O$  [16]. The  $K_2CO_3$  can further react with the carbon atoms releasing  $CO_2$  gas and potassium compounds which create additional pores on the carbon matrix [12]. Besides, the  $K_2CO_3$  can decompose at higher temperatures ( $> 700 \text{ }^\circ\text{C}$ ) to yield  $K_2O$  and  $CO_2$  gas and form more pores on the surface. These potassium compounds can intercalate into the carbon matrix in the form of  $K_2O$  which can be readily removed by washing with concentrated HCl. The porous network of the lignin-derived activated carbons was confirmed by the TEM images (Fig. 1c,d).

#### 3.2. Structural and textural properties

Raman spectroscopy was used for evaluating the degree of graphitization of activated carbons. Raman analysis for the LAC samples showed the presence of D peaks at  $1331\text{--}1340 \text{ cm}^{-1}$  and G peaks at  $1590\text{--}1594 \text{ cm}^{-1}$ , respectively (Fig. 2a). The broad D and G peaks indicated that the carbons were amorphous which is a typical characteristic of activated carbons. The D peak is ascribed to the breathing mode of  $sp^2$  carbon due to the presence of  $sp^3$  amorphous domains and defects within the carbon lattice, while the G peak is due to the bond stretching of  $sp^2$  hybridized carbons [1]. The full-width half-maximum (FWHM) of the G peak was used



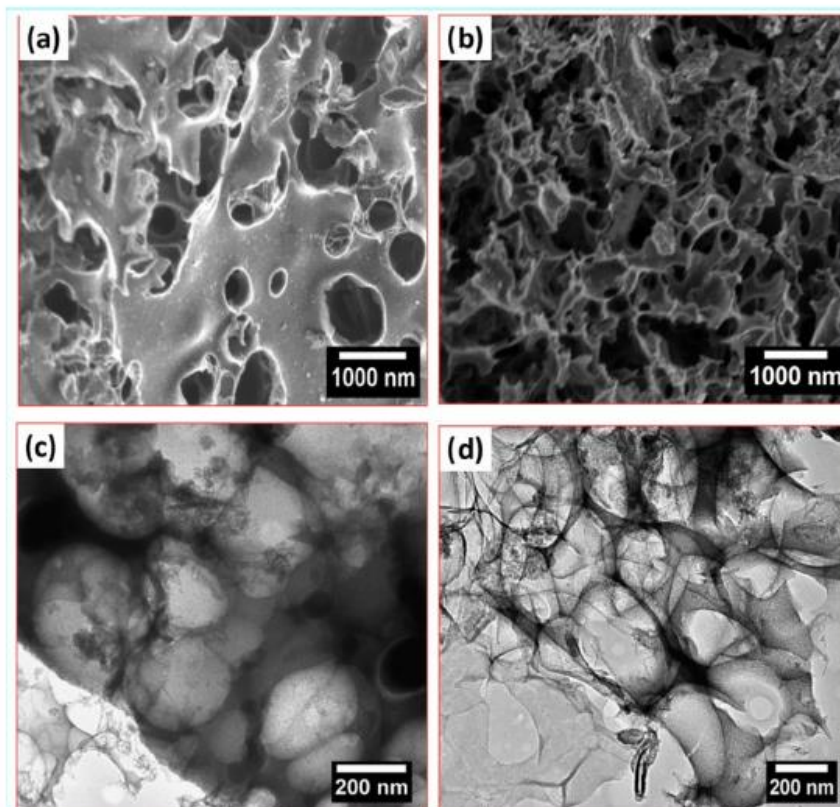


Fig. 1. (a,b) Low magnification SEM images for (a) LAC-0.5 and (b) LAC-2; and (c,d) TEM images for (c) LAC-0.5 and (d) LAC-2, respectively.

**Table 1**  
Raman data and textural properties for the lignin-derived activated carbons.

Material	D peak position (cm <sup>-1</sup> )	D peak FWHM (cm <sup>-1</sup> )	G peak position (cm <sup>-1</sup> )	G peak FWHM (cm <sup>-1</sup> )	I <sub>D</sub> /I <sub>G</sub> ratio (± 0.02)	Specific surface area (m <sup>2</sup> g <sup>-1</sup> )	Total pore volume (cm <sup>3</sup> g <sup>-1</sup> )
LAC-0.5	1340.0	167	1594.0	95	0.94	1558	0.46
LAC-2	1335.9	185	1594.0	99	0.98	1879	0.75

to show amorphous carbon defects as a measure of bond distortion associated with the structural disorder while the FWHM of D peak was used to evaluate the basal plane defects on the materials as a measure of structural defects [35–40]. The FWHM of the D peak increased with increase in the amount of KHCO<sub>3</sub> indicating the creation of structural defects at higher KHCO<sub>3</sub> content. On the other hand, the FWHM of G peak varied for the two LAC samples indicating a slight difference in the amorphous carbon defects owing to bond angle and bond length distortions.

Interestingly, a D\* peak was observed for the LAC-2 sample demonstrating the presence of sp<sup>2</sup>-sp<sup>3</sup> carbon domains in the form of dangling bonds [40]. The I<sub>D</sub>/I<sub>G</sub> of the activated carbons was calculated from the intensities of the D to G peaks and was found to be 0.94 ± 0.02, and 0.98 ± 0.02 for the LAC-0.5 and LAC-2, respectively (Table 1). This showed that all the carbons had a moderate degree of graphitization. Fig. 2b shows the diffraction patterns of the LAC samples with broad peaks observed at 2θ = 23° and 44°

corresponding to reflections of (002) and (100) planes of graphitic structures. The broad peaks suggest low crystallinity. Besides, it can be seen that with an increase in the amount of activating agent, the peaks broaden indicating the creation of a more disordered carbon matrix that is in agreement with the Raman data.

The nitrogen adsorption-desorption isotherms for all the samples are displayed in Fig. 2c. All the samples exhibited type-IV isotherms with H3 hysteresis loops at 0.45 < P/P0 < 1.0, indicating the co-existence of micropores and mesopores. The specific surface areas were 1558 m<sup>2</sup> g<sup>-1</sup> and 1879 m<sup>2</sup> g<sup>-1</sup> for the LAC-0.5 and LAC-2 samples, respectively. The surface areas increased with increase in the amount of KHCO<sub>3</sub> revealing the formation of a more porous network at higher mass ratios. Fig. 2d displays the pore size distribution of all the samples.

At lignin:KHCO<sub>3</sub> mass ratio of 1:2, a large number of micropores and mesopores were generated compared to the ratio of 1:0.5 (inset) presumably because the intercalation of KHCO<sub>3</sub> in the car-

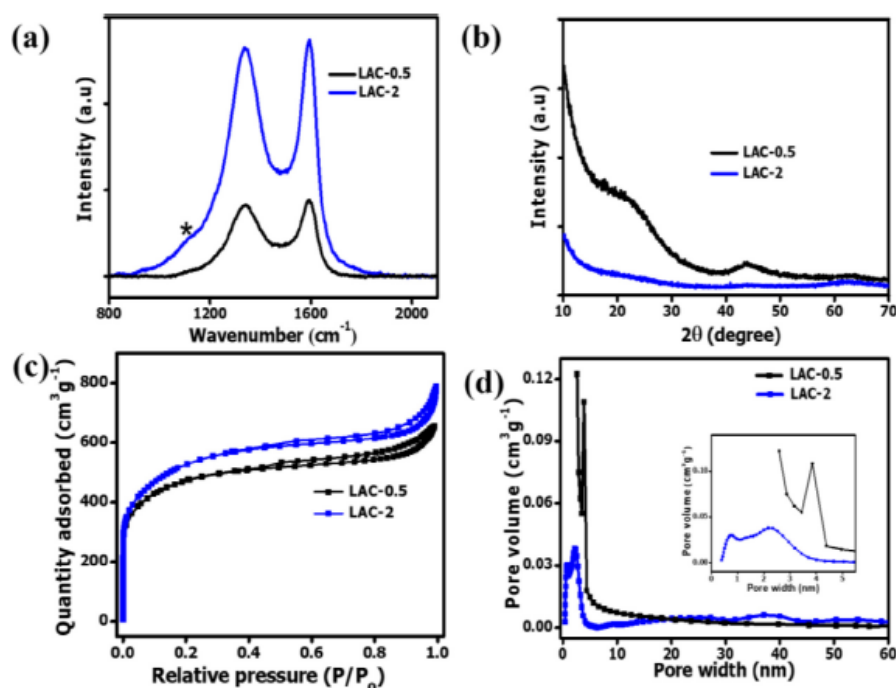


Fig. 2. (a) Raman spectra, (b) XRD patterns, (c)  $N_2$  adsorption-desorption isotherms and (d) pore size distribution plots for the activated lignin derived carbons.

bon matrix took place to a larger extent. This is in agreement with the increase in total pore volume with the increasing amount of activating agent (Table 1).

### 3.3. Supercapacitors performance

Three electrode measurements were carried out for all the materials using a carbon counter electrode, Ag/AgCl reference electrode and 2.5 M  $KNO_3$  electrolyte solution. The cyclic voltammograms of the LAC-0.5 and LAC-2 electrodes taken at varying scan rates featured a rectangular shape which is typical of an ideal EDLC behavior, both in the negative (-0.8 V to 0 V vs. Ref.) and positive (0 V to +0.8 V vs. Ref.) potential window (Figs. 3a,b and 4a,b). Figs. 3c,d and 4c,d show the galvanostatic charge-discharge plots in the negative and positive potential ranges for LAC-0.5 and LAC-2 electrode materials. The GCD plots at varying specific currents (1, 2, 3, 4, 5 and 10  $A g^{-1}$ ) displayed triangular shape, therefore confirming the capacitive behavior. LAC-2 exhibited a longer discharge time compared to LAC-0.5. This revealed better charge storage capability for the LAC-2 electrode material. The specific capacitance of the electrodes ( $C_s$ ) was calculated from the GCD plots using Eq. (1).

Fig. 5a and b display the  $C_s$  values plotted as a function of specific current taken both in the negative and the positive potential range. All the electrodes exhibited good rate capabilities for the specific current values of 1  $A g^{-1}$  to 10  $A g^{-1}$ . The specific capacitance values for the LAC-0.5 and LAC-2 at 1  $A g^{-1}$  were found to be 64 and 69  $F g^{-1}$ , respectively, in the positive potential range (Fig. 5a). In the negative potential window, the values were 89 and 100  $F g^{-1}$  for the LAC-0.5 and LAC-2, respectively (Fig. 5b). For the

various specific currents, LAC-2 electrode material exhibited higher specific capacitance values than the LAC-0.5. This can be ascribed to the higher specific surface area and pore volume as reported by the textural properties and the porous carbon network morphology of the LAC-2 material. In addition, the disordered carbon and structural defects could enhance the surface wettability of the LAC-2 electrode leading to higher specific capacitance values.

The capacitive behavior of the electrode materials was further investigated using electrochemical impedance spectroscopy (EIS). Fig. 5c displays the Nyquist plots for the LAC sample electrodes with a quasi-vertical line parallel to the imaginary  $Z''$ -axis in the low frequency region indicating a capacitive nature of the samples. LAC-2 displayed a shorter diffusion length suggesting a faster ion diffusion at the electrode-electrolyte interface compared to LAC-0.5 (Fig. 5c inset). Ideally, electrolyte ion transport highly depends on the electrolyte concentration, carbon electrode surface porosity and the pore diameter [3]. Thus, the higher surface area and pore volume of LAC-2 could provide an efficient ion-accessible surface area for faster ion diffusion. The real-axis intercept of the Nyquist plot at the highest frequency, was measured to be 1.25 and 1.07  $\Omega$  for the LAC-0.5 and LAC-2, respectively. Given that EIS was collected by a 3-electrode setup, these values are affected by the cell geometry, namely by the distance of the working electrode from the reference. Moreover, it is affected by the ionic resistance of the bulk electrolyte and electronic resistance of the carbon electrode. The latter includes the carbon/current collector and interparticle contact resistances. Generally, a lower resistance at the highest frequencies depicts a better electronic conductivity of the electrodes. Hence, the lower resistance value exhibited by LAC-2 suggested a better electronic conductivity than LAC-0.5. Besides, from

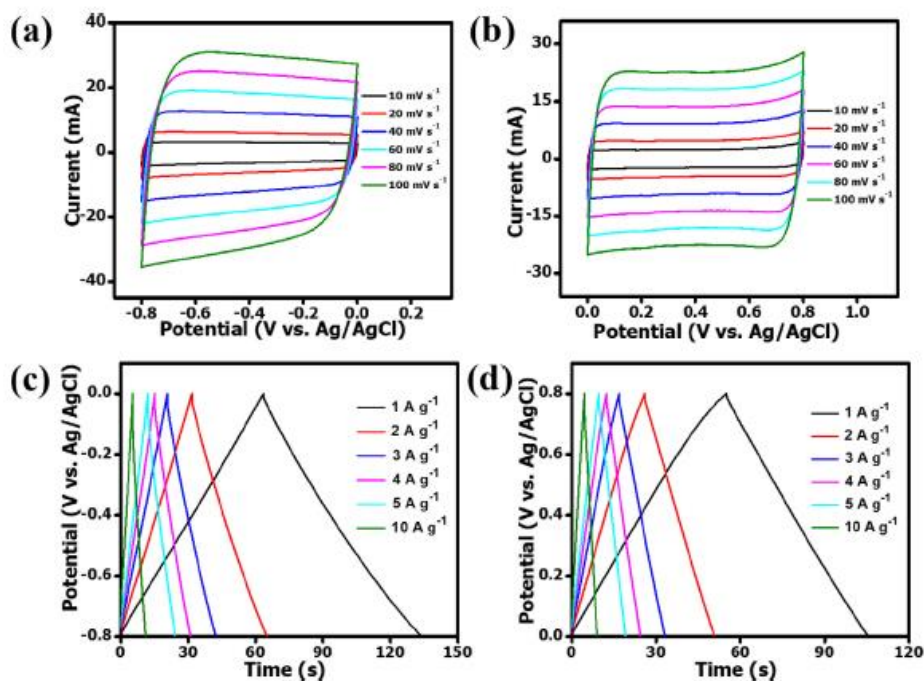


Fig. 3. (a,b) CV curves in the potential ranges (a)  $-0.8$  V to  $0$  V vs. Ag/AgCl and (b)  $0$  V to  $+0.8$  V vs. Ag/AgCl at different scan rates, and (c and d) galvanostatic charge-discharge plots in both the negative and positive potential range at different specific currents of the LAC-0.5 electrode material in  $2.5$  M  $\text{KNO}_3$  electrolyte.

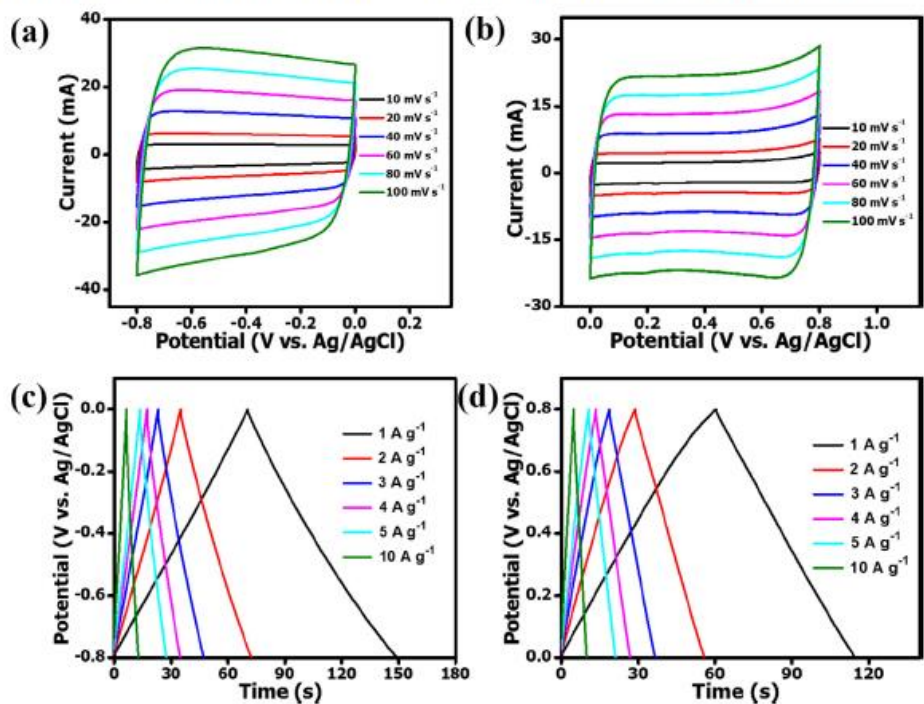


Fig. 4. (a) CV curves in the potential ranges (a)  $-0.8$  V to  $0$  V vs. Ag/AgCl and (b)  $0$  V to  $+0.8$  V vs. Ag/AgCl at different scan rates, and (c and d) galvanostatic charge-discharge plots in both the negative and positive potential range at different specific currents of the LAC-2 electrode material in  $2.5$  M  $\text{KNO}_3$  electrolyte.

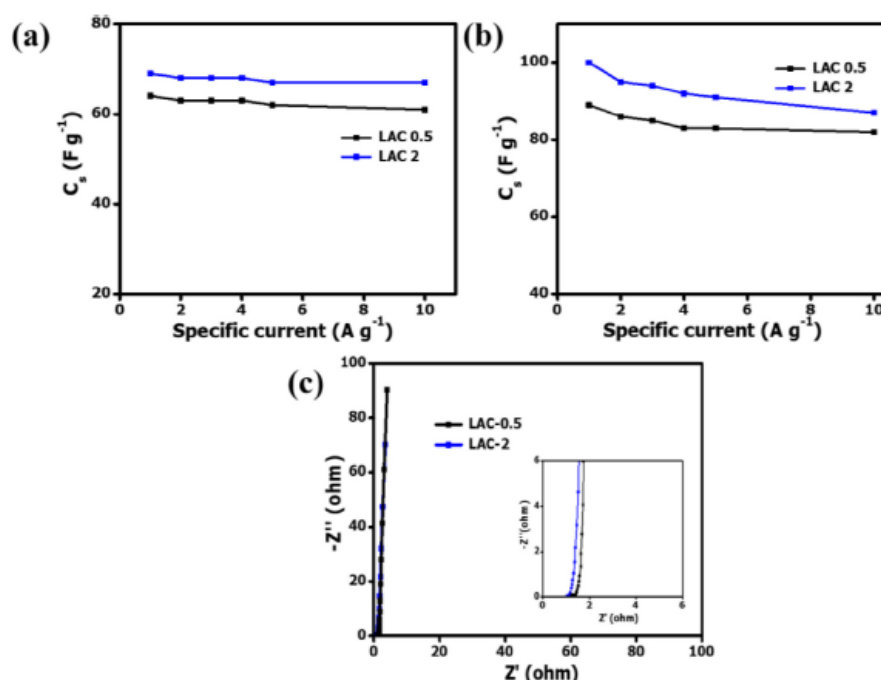


Fig. 5. (a,b) Specific capacitance plotted as a function of specific current taken at an electrode potential range of (a) 0 V to +0.8 V vs. Ref, (b) -0.8 V to 0 V vs. Ref and (c) Nyquist plots of the LAC-0.5 and LAC-2 electrodes in 2.5 M KNO<sub>3</sub> electrolyte (3-electrode setup).

the Raman data LAC-2 portrayed a moderate degree of graphitization with the presence of D\* peak that is ascribed to the presence of defects in the form of dangling bonds. An electrode material comprising a high amount of disordered carbons results in better aqueous electrolyte ion affinity and good surface hydrophilicity.

Based on the higher electrochemical performance of LAC-2, a symmetric device consisting of LAC-2 electrodes was fabricated with a 2.5 M KNO<sub>3</sub> electrolyte solution. Fig. 6a and b present the CV plots of the EDLC collected by a 2-electrode setup, at different scan rates ranging from 10 mV s<sup>-1</sup> to 100 mV s<sup>-1</sup> within a cell voltage of 1.6 V. The device exhibited a rectangular CV shape even at higher scan rates (Fig. 6b) demonstrating a good rate capability of the electrode material. The GCD plots at varying specific currents displayed a small  $\Delta V_{ohm}$  drop showing a low ESR (Fig. 6c). The specific capacitance of a single electrode ( $C_{el}$ ) in the device was calculated from the GCD plots using Eq. (2) and plotted as a function of specific current as shown in Fig. 6d. A maximum  $C_{el}$  of 114 F g<sup>-1</sup> was obtained at 0.5 A g<sup>-1</sup> and a value of 89 F g<sup>-1</sup> was maintained at a specific current of 10 A g<sup>-1</sup> showing a good rate capability of the device (Fig. 6d). This value is comparable to values in the literature on lignin-derived activated carbon electrodes [28–32]. For instance, Saha et al. [30] reported a specific capacitance of 91.7 F g<sup>-1</sup> at 2 mV s<sup>-1</sup> in 6 M KOH electrolyte for porous carbons produced by KOH activation of lignin. Similarly, Navarro and co-workers investigated the electrochemical performance of nanoporous carbon derived from KOH activated lignin and obtained a specific capacitance of 87 F g<sup>-1</sup> at 0.1 A g<sup>-1</sup> in organic electrolyte [31]. The slightly higher values reported in this study can be linked to the creation of mesopores and micropores by the activation of lignin with KHC0<sub>3</sub> yielding high pore volume and surface area of the LAC-2 sample.

Fig. 7a presents a Ragone plot showing the specific power as a function of the specific energy of the device. The maximum specific energy was calculated using Eq. (3) and found to be 10 Wh kg<sup>-1</sup> with a corresponding specific power of 397 W kg<sup>-1</sup> at a specific current of 0.5 A g<sup>-1</sup>. Besides, the specific power of 6.9 kW kg<sup>-1</sup> was achieved at a specific current of 10 A g<sup>-1</sup>. To further evaluate the stability of the device, a cycling test was carried out on the device for up to 15,000 charge-discharge cycles. The device exhibited a coulombic efficiency of 99.84 % with capacitance retention of 84.5 % at a specific current of 5 A g<sup>-1</sup> (Fig. 7b). This capacitance retention value was higher than the 80 % value reported by Shah et al. [30] on lignin derived carbon after 10,000 cycles in 1 M H<sub>2</sub>SO<sub>4</sub>. The Nyquist plots of the device before and after cycling test were almost similar with the curve close to parallel with the imaginary  $Z''$ -axis indicating a capacitive behavior (Fig. 7c). The ESR was evaluated from the real-axis intercept at the highest frequencies and, after 15,000 cycle, it was slightly higher (1.73  $\Omega$ ) than the one obtained before the cycling test (1.61  $\Omega$ ) suggesting a possible increase in the carbon/current collector contact resistance after the cycling process. On the other hand, the high frequency semicircle diameters, that represent the interparticle electronic and ionic resistances, were almost similar: 0.11  $\Omega$  before cycling and 0.12  $\Omega$  after cycling. These results show that the device was quite stable even after 15,000 charge-discharge cycles.

#### 3.4. Oxygen reduction reactions kinetics

The electrocatalytic activity towards ORR in neutral media of the two LAC materials obtained from pyrolyzed lignin was also tested. The polarization curves for the LAC catalysts obtained by RDE, at varying rotation speeds (400, 900, 1600 and 2500 rpm)

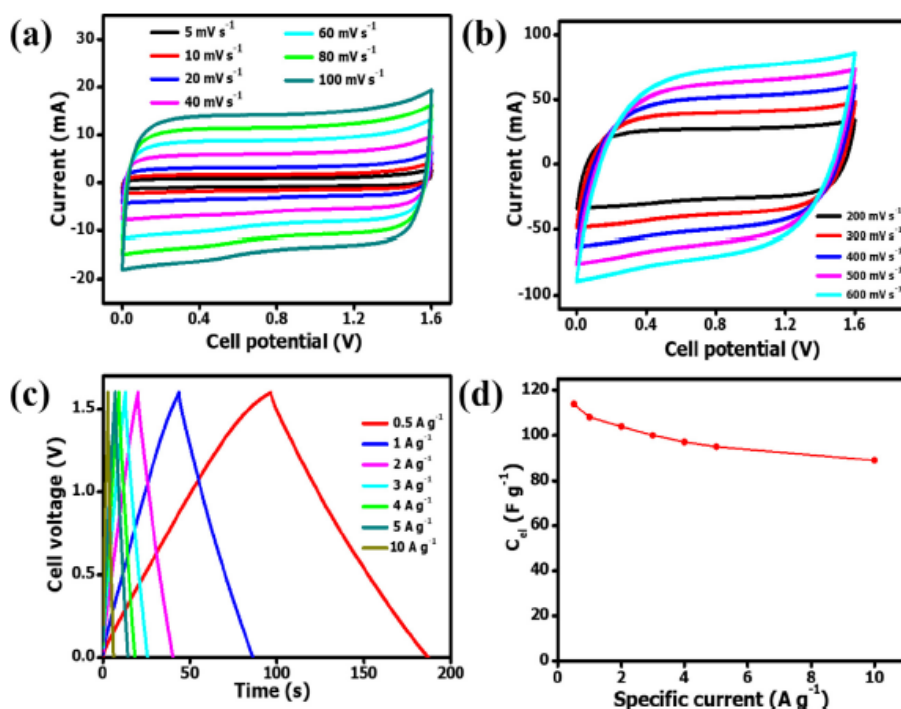


Fig. 6. LAC-2//LAC-2 symmetric device: (a,b) CV plots at low scan rates and high scan rates, (c) charge-discharge curves and (d) specific capacitance as a function of specific current taken at a cell voltage from 0 V to 1.6 V (2-electrode setup).

are presented in Fig. 8a,b. The onset potential ( $E_{on}$ ) for LAC-0.5 was 0.089 V (vs NHE) and for LAC-2 was slightly higher and corresponded to 0.122 V (vs NHE). For both LAC-0.5 and LAC-2 catalysts, no plateau corresponding to the mass transport limited current density was observed. This suggested that the ORR activity resulted from a mixed kinetic-diffusion controlled mechanism. An increase in the limiting current density with rotating speed was observed for all the catalysts indicating a higher oxygen flux from the bulk solution to the electrode surface at higher rotating speeds [41].

The current density values for the LAC-0.5 and LAC-2 were 6.23 and 8.53 mA cm<sup>-2</sup>, respectively at -0.7 V vs NHE for a rotating speed of 2500 rpm. Along the entire potential window investigated from  $E_{on}$  to -0.7 V vs NHE, LAC-2 outperformed LAC-0.5 having higher current densities at the same potentials. The differences in the ORR activity between the two catalysts can be linked to their morphologies, porosities and textural properties. For instance, LAC-2 material exhibited a well-interconnected porous network, a higher pore volume and a high surface area that can allow for exposure of the active sites to the reactants. On the other hand, the LAC-0.5 catalyst had lower pore volumes and less interconnectivity.

In order to calculate the number of electrons transferred during the ORR process, the Koutecky-Levich (K-L) graphs were plotted (Fig. 9a and b). All the curves taken between 0 V and -0.2 V (vs. NHE) exhibited a linear and almost parallel trend suggesting that the activated carbons catalysts follow first-order kinetics [41]. From the intercepts of the linear curves in Fig. 9a and b, the kinetic-limited current density ( $j_k$ ) was extracted as well as the coefficient  $B$  Eq. (7). Knowing these two values, it was possible to calculate the number of electrons involved within ORR. Fig. 9c reports the

number of electrons transferred during ORR at different potentials, estimated by Koutecky-Levich (K-L) analyze.

It is well known that carbon-based catalysts are capable of reducing oxygen following a 2e- or a 2 × 2e- transfer mechanism [41]. In this specific case, LAC-0.5 seems to follow a straight 2e- transfer mechanism while LAC-2 instead seems to follow a mixed 2e- and 2 × 2e- transfer mechanism. In fact, the number of electrons transferred were much closer to 4 with values of 3.7, 3.76 and 3.92 for the potential of 0 V, -0.1 V and -0.2 V (vs NHE), respectively. This different pathway might be correlated to the porosity and the different pore size distribution of the two samples investigated. It is possible that larger cumulative porosity might be useful for providing more active sites for the ORR to occur. It must be underlined that the catalysts loading used for this study is quite high. In fact, it was shown that an increase in the catalyst loading led to higher performance and the peroxide intermediate is disproportionated within the thick catalyst layer itself [42,43]. It was shown that simple unmodified carbon black was able to perform a 2e- reduction of oxygen. On the contrary, the activated carbon had a higher electron transfer mechanism and superior performance [44]. In Watson et al. the authors screened nine different commercially available activated carbons finding values of  $n$  between 2 and 3.5 [45]. Particularly, it was shown that overall porosity and the pore size distribution was related to the number of electrons transferred and the overall electrocatalytic activity. In another recent study, Pepè Sciarria et al. used activated biochar as a cathode catalyst for ORR finding the number of electrons transferred in the range between 2.9 and 3.9 [46].

Tafel curves were calculated in the range 0 V to -0.2 V (vs NHE) and plotted in Fig. 9d. The cathodic transfer coefficient  $\beta_n$  was cal-

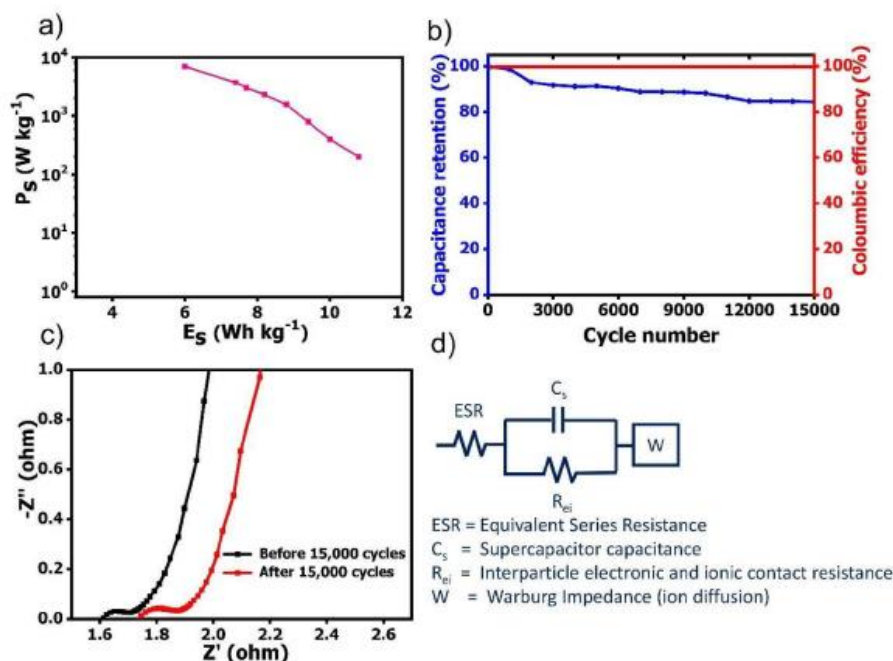


Fig. 7. (a) Ragone plot, (b) cycling test showing capacitance retention and coulombic efficiency and (c) Nyquist plots before and after 15,000 charge-discharge cycles of the LAC-2 symmetric device (2-electrode setup) with the equivalent circuit that models the SC impedance.

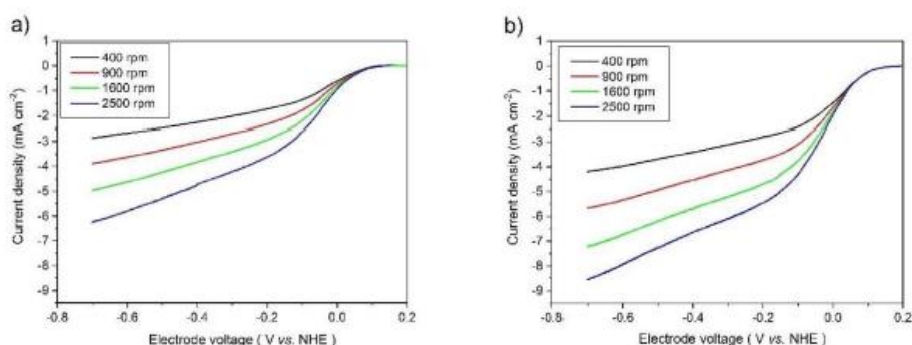


Fig. 8. Rotating disk electrode plots for (a) LAC-0.5 and (b) LAC-2 with the catalyst loading of 0.56 mg cm<sup>-2</sup> at 5 mV s<sup>-1</sup> scan rate.

culated from the Tafel slope using the following equation [47] below:

$$\ln(j_k) + \frac{\beta n F}{RT}(E - E^0) \quad (8)$$

where  $j_0$  is the exchange current density,  $R$  is the gas constant 8.314 J mol<sup>-1</sup> K<sup>-1</sup>, and  $T$  is the standard room temperature. The cathodic transfer coefficient ( $\beta n$ ) for LAC-0.5 and LAC-2 electrocatalysts was found to be 0.27 and 0.23 ( $\pm 20\%$ ), as evaluated within 0 V and -0.2 V vs. NHE. At the lowest overpotentials, i.e. between 0 and -0.1 V vs. NHE, the transfer coefficients resulted in 0.31 and 0.36 for LAC-0.5 and LAC-2, respectively. For both catalysts, at

a loading of 0.56 mg cm<sup>-2</sup>, the cathodic transfer coefficient was similar to values reported on glassy carbon electrodes in the neutral medium [48]. For the LAC-0.5 catalyst, slightly higher cathodic transfer coefficients were recorded as compared to the LAC-2. The differences in the cathodic transfer coefficient for the LAC catalysts can be ascribed to the variations in the pore diameter, pore length and electronic conductivity of the samples. It can be concluded that increasing the amount of KHCO<sub>3</sub> resulted in porous carbons with a larger number of structural defects, more pores and consequently higher surface area and pore volumes which led to an increase in the active sites and regions where the ORR can occur

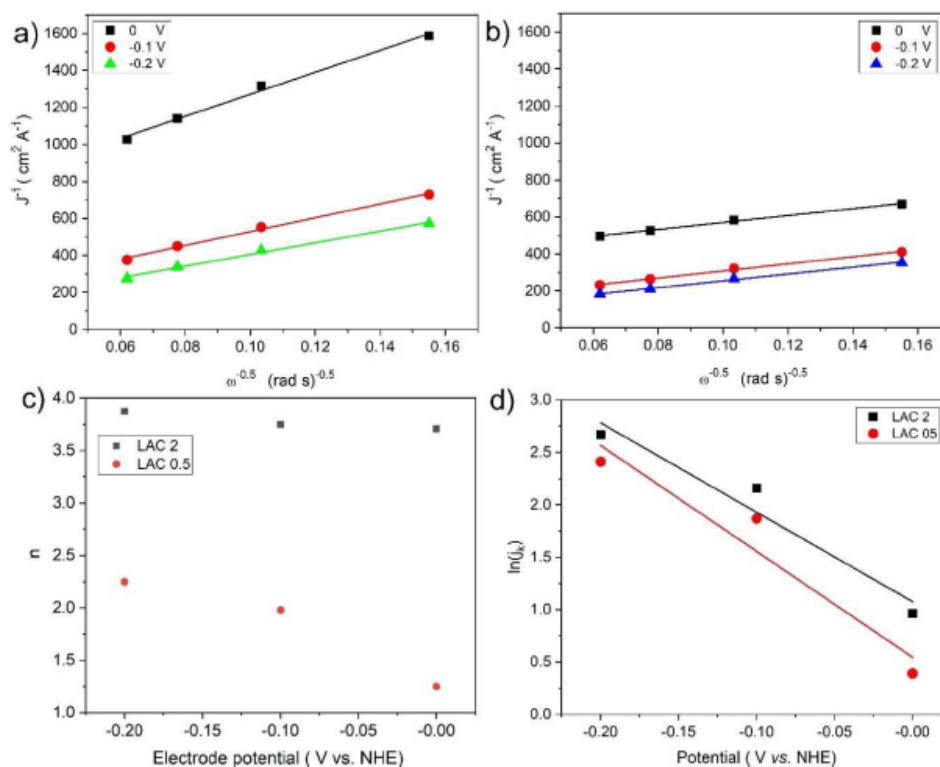


**Fig. 9.** (a,b) K-L plots taken at different potential values of 0 V, -0.1 V and -0.2 V for LAC-0.5 (a) and LAC-2 (b), (c) number of electrons transferred estimated by K-L analysis and (d) Tafel plots.

with a positive impact on their electrochemical performance. Overall, LAC-2 sample exhibited superior electrocatalytic properties as well as electrochemical performance owing to its unique porous network, a high pore volume, high specific surface area as well as unique structural properties.

### 3.5. MFC air breathing cathode operating in neutral media

The ORR electrocatalytic activity of the LAC 2 carbon was further validated in real environment, i.e. in an air breathing MFC. The air breathing cathode was fabricated utilizing LAC 2 as an electrocatalyst. The fuel as well as inoculum were mainly based on the effluent of the anaerobic biogas plant. Fig. 10 reports the polarization curve obtained by linear sweep voltammogram of the LAC 2 MFC cathode performed at 0.2 mV s<sup>-1</sup>. The Open circuit potential (OCP) is consistent with the values observed in Fig. 8. The Figure compares the LSV of LAC-2 and other air-breathing cathodes composed by commercially available activated carbons (AC) previously presented [49–51]. These air breathing cathodes had catalyst loading of roughly 40 mg cm<sup>-2</sup>, comparable with the one used in this study (53 mg cm<sup>-2</sup>). Notably, the commercial ACs showed higher OCP and electrocatalytic activity at low current density compared to LAC-2. This might be due to the iron impurities previously identified in the commercial AC samples [51]. At higher current densities, LAC-2 demonstrated superior electrocatalytic activity compared to the commercial ACs. This is probably due to the much higher available surface area of LAC 2. These results indicate the

feasibility of the use of lignin derived biochar for fabricating air breathing cathodes for MFC applications.

## 4. Conclusions

Porous carbons derived from lignin were obtained by activating with KHCO<sub>3</sub> at varying mass ratios of 1:0.5 and 1:2. A lignin biomass: KHCO<sub>3</sub> mass ratio of 1:2 was found to be the optimal ratio for high specific surface area (1879 m<sup>2</sup>g<sup>-1</sup>) and high pore volume (0.75 cm<sup>3</sup>g<sup>-1</sup>). The Raman data showed that LAC-2 had a higher amount of disordered carbon than the other LAC samples. The obtained materials were tested as electrodes for EDLC and as electrocatalysts for ORR in neutral media and integrated in air breathing cathode architecture for MFC applications. All the electrode materials displayed good reversible charge storage capability in both the negative (-0.8 V to 0 V vs. Ref) and the positive (0 V to + 0.8 V vs. Ref) potential windows in 2.5 M KNO<sub>3</sub> electrolyte. A symmetric EDLC fabricated using LAC-2 electrode material exhibited a good specific capacitance of 28.5 F g<sup>-1</sup>, corresponding to an electrode specific capacitance of 114 F g<sup>-1</sup>, with a specific energy of 10 Wh kg<sup>-1</sup> and a corresponding specific power of 397 W kg<sup>-1</sup> at a specific current of 0.5 Ag<sup>-1</sup> in a cell voltage of 1.6 V. Moreover, the device demonstrated good capacitance retention of 84.5 % after 15,000 cycles. As an electrocatalyst, LAC-2 showed higher current density values and superior ORR activity as compared to LAC-0.5. The number of electrons transferred during ORR was higher for LAC-2. Once integrated in an air-breathing cathode,

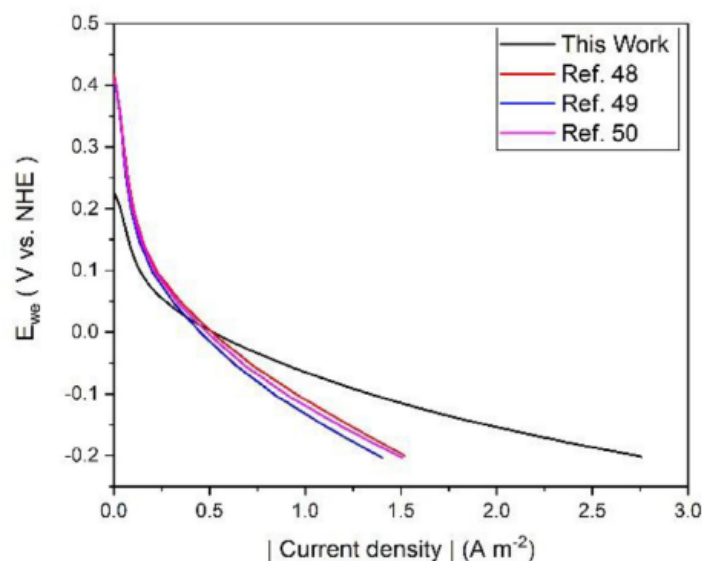


**Fig. 10.** Polarization curve obtained by linear sweep voltammogram at  $0.2 \text{ mV s}^{-1}$  of the LAC-2 MFC air breathing cathode (black curve) and commercial activated carbons: red line curve is imported from [51], Elsevier under license CC BY 4.0 (<https://creativecommons.org/licenses/by/4.0/>), the curve in blue line was imported from [50], Royal Society of Chemistry, under license CC BY 3.0 (<https://creativecommons.org/licenses/by/4.0/>), the green line is imported from [49] Elsevier under license CC BY 4.0 (<https://creativecommons.org/licenses/by/3.0/>) (For interpretation of the references to color in this figure legend, the reader is referred to the web version of this article.)

the material exploited high electrochemical ORR activity especially at high current densities.

Overall, this study demonstrates that biochar derived from lignin waste of anaerobic biogas plants, activated with a mild activation agent, like  $\text{KHCO}_3$ , features capacitive and ORR electrocatalytic properties that are comparable or even superior with those of commercially available carbons.

Therefore, our main result is the demonstration that waste can be effectively valorized as functional materials to be implemented in technologies that enable efficient energy management and water treatment, therefore simultaneously addressing the Water-Energy-Waste Nexus challenges. Indeed, the good supercapacitor performance and ORR electrocatalytic behavior of the lignin-derived carbons indicated a potential use as cathode catalysts and electrode materials for microbial fuel cells and supercapacitors.

#### Declaration of Competing Interest

The authors declare that they have no known competing financial interests that could have appeared to influence the work reported in this paper.

#### Credit authorship contribution statement

**Bridget K. Mutuma:** Investigation, Conceptualization, Formal analysis, Writing – review & editing. **Ndeye F. Sylla:** Conceptualization, Formal analysis, Writing – review & editing. **Amanda Bubu:** Investigation, Conceptualization, Formal analysis, Writing – review & editing. **Ndeye M. Ndiaye:** Investigation, Conceptualization, Formal analysis, Writing – review & editing. **Carlo Santoro:** Writing – original draft, Supervision, Writing – review & editing. **Alessandro Brilloni:** Writing – review & editing. **Federico Poli:** Investigation, Writing – review & editing. **Ncholu Manyala:** Writing – original draft, Supervision, Funding acquisition, Project administration, Writing – review & editing. **Francesca Soavi:** Writing – original draft, Supervision, Funding acquisition, Project administration, Writing – review & editing.

istration, Writing – review & editing. **Francesca Soavi:** Writing – original draft, Supervision, Funding acquisition, Project administration, Writing – review & editing.

#### Acknowledgment

This research was carried out under the Italy-South Africa joint Research Program (ISARP) 2018–2020 (Italian Ministers of Foreign Affairs and of the Environment, Grant No. PGR00764). The South African Research Chairs Initiative of the Department of Science and Technology and the National Research Foundation of South Africa (Grants No. 61056 and No. 113132) is also acknowledged. C. S. would like to thank the support from the Italian Ministry of Education, Universities and Research (Ministero dell'Istruzione, dell'Università e della Ricerca – MIUR) through the “Rita Levi Montalcini 2018” fellowship (Grant number PGR18MAZLI). F.S., F.P. and A.B. acknowledge funding from the European Union's Horizon 2020 research and innovation program under grant agreement No. 963550 (HyFlow Project).

#### References

- [1] <https://sdgs.un.org/2030agenda>
- [2] <https://www.unwater.org/water-facts/water-food-and-energy/>
- [3] F. Béguin, V. Presser, A. Balducci, E. Frackowiak, Carbons and electrolytes for advanced supercapacitors, *Adv. Mater.* 26 (2014) 2219.
- [4] P. Pandey, V.N. Shinde, R.L. Deopurkar, S.P. Kale, S.A. Patil, D. Pant, Recent advances in the use of different substrates in microbial fuel cells toward wastewater treatment and simultaneous energy recovery, *Appl. Energy* 168 (2016) 706.
- [5] C. Santoro, F. Soavi, A. Serov, C. Arbizzani, P. Atanassov, Self-powered supercapacitive microbial fuel cell: the ultimate way of boosting and harvesting power, *Biosens. Bioelectron.* 78 (2016) 229.
- [6] C. Santoro, X.A. Walter, F. Soavi, J. Greenman, I. Ieropoulos, Self-stratified and self-powered micro-supercapacitor integrated into a microbial fuel cell operating in human urine, *Electrochim. Acta* 307 (2019) 241–252.
- [7] F. Soavi, C. Santoro, Supercapacitive operational mode in microbial fuel cell, *Curr. Opin. Electrochem.* 22 (2020) 1.



- [8] F. Poli, J. Seri, C. Santoro, F. Soavi, Boosting microbial fuel cells performance by the combination of an external supercapacitor: an electrochemical study, *ChemElectroChem* 7 (2020) 893.
- [9] C. Santoro, C. Flores Cadengo, F. Soavi, M. Kodali, I. Merino-Jimenez, I. Gajda, J. Greenman, I. Ieropoulos, P. Atanassov, Ceramic microbial fuel cells stack: power generation in standard and supercapacitive mode, *Sci. Rep.* 8 (2018) 3281.
- [10] Z. Bi, Q. Kong, Y. Cao, G. Sun, F. Su, X. Wei, X. Li, A. Ahmad, L. Xie, C.M. Chen, Biomass-derived porous carbon materials with different dimensions for supercapacitor electrodes: a review, *J. Mater. Chem. A* 7 (2019).
- [11] D. Bergna, T. Hu, H. Prokkola, H. Romar, U. Lassi, Effect of some process parameters on the main properties of activated carbon produced from peat in a lab-scale process, *Waste Biomass. Valor.* 11 (2019) 2837.
- [12] C. Xia, S.Q. Shi, Self-activation for activated carbon from biomass: theory and parameters, *Green Chem.* 18 (2016) 2063.
- [13] W. Li, K. Yang, J. Peng, L. Zhang, S. Guo, H. Xia, Effects of carbonization temperatures on characteristics of porosity in coconut shell chars and activated carbons derived from carbonized coconut shell chars, *Ind. Crops. Prod.* 28 (2008) 190.
- [14] J. Sahira, A. Mandira, P.B. Prasad, P.R. Ram, Effects of activating agents on the activated carbons prepared from lapi seed stone, *Res. J. Chem. Sci.* 2231 (2013) 1.
- [15] N. Sylla, N. Ndiaye, B. Ngom, D. Momodu, M. Madito, B. Mutuma, N. Manyala, Effect of porosity enhancing agents on the electrochemical performance of high-energy ultracapacitor electrodes derived from peanut shell waste, *Sci. Rep.* 9 (2019) 1.
- [16] M. Sevilla, A.B. Fuertes, A green approach to high-performance supercapacitor electrodes: the chemical activation of hydrochar with potassium bicarbonate, *ChemSusChem* 9 (2016) 1880.
- [17] Y. Xi, D. Yang, X. Qiu, H. Wang, J. Huang, Q. Li, Renewable lignin-based carbon with a remarkable electrochemical performance from potassium compound activation, *Ind. Crop. Prod.* 124 (2018) 747–754.
- [18] F.O. Ochai-Ejeh, D.Y. Momodu, M.J. Madito, A.A. Khaleed, K.O. Oyedotun, S.C. Ray, N. Manyala, Nanostructured porous carbons with high rate cycling and floating performance for supercapacitor application, *AIP Adv.* 8 (2018) 055208.
- [19] D. Momodu, N.F. Sylla, B. Mutuma, A. Bello, T. Masikhwa, S. Lindberg, A. Matic, N. Manyala, Stable ionic-liquid-based symmetric supercapacitors from Capsicum seed-porous carbons, *J. Electroanal. Chem.* 838 (2019) 119–128.
- [20] F. Poli, D. Momodu, G.E. Spina, A. Terrella, B.K. Mutuma, M.L. Focarete, N. Manyala, F. Soavi, Pullulan-ionic liquid-based supercapacitor: a novel, smart combination of components for an easy-to-dispose device, *Electrochim. Acta* 338 (2020) 135872.
- [21] H. Rismani-Yazdi, S.M. Carver, A.D. Christy, O.H. Tuovinen, Cathodic limitations in microbial fuel cells: an overview, *J. Power Sour.* 180 (2008) 683.
- [22] S. Rojas-Carbonell, K. Artyushkova, A. Serov, C. Santoro, I. Matanovic, P. Atanassov, Effect of pH on the activity of platinum group metal-free catalysts in oxygen reduction reaction, *ACS Catal.* 8 (2018) 3041.
- [23] D. Malko, A. Kucernak, T. Lopes, In situ electrochemical quantification of active sites in Fe-N/C non-precious metal catalysts, *Nat. Comm.* 7 (2016) 1.
- [24] H. Yuan, Y. Hou, I.M. Abu-Reesh, J. Chen, Z. He, Oxygen reduction reaction catalysts used in microbial fuel cells for energy-efficient wastewater treatment: a review, *Mater. Horiz.* 3 (2016) 382.
- [25] J.H. Lora, W.G. Glasser, Recent industrial applications of lignin: a sustainable alternative to nonrenewable materials, *J. Polym. Environ.* 10 (2002) 39.
- [26] P. Carrott, M.R. Carrott, Lignin—from natural adsorbent to activated carbon: a review, *Bioresour. Technol.* 98 (2007) 2301.
- [27] H. Wang, Y. Pu, A. Ragauskas, B. Yang, From lignin to valuable products—strategies, challenges, and prospects, *Bioresour. Technol.* 271 (2019) 449.
- [28] J.I. Hayashi, A. Kazehaya, K. Muroyama, A.P. Watkinson, Preparation of activated carbon from lignin by chemical activation, *Carbon* 38 (2000) 1873.
- [29] J.W. Jeon, L. Zhang, J.L. Lutkenhaus, D.D. Laskar, J.P. Lemmon, D. Choi, M.I. Nandasi, A. Hashmi, J. Xu, R.K. Motkuri, Controlling porosity in lignin-derived nanoporous carbon for supercapacitor applications, *ChemSusChem* 8 (2015) 428.
- [30] D. Saha, Y. Li, Z. Bi, J. Chen, J.K. Keum, D.K. Hensley, H.A. Grappe, H.M. Meyer III, S. Dai, M.P. Paranthaman, Studies on supercapacitor electrode material from activated lignin-derived mesoporous carbon, *Langmuir* 30 (2014) 900.
- [31] A.M. Navarro-Suárez, J. Carretero-González, V. Roddatis, E. Goikolea, J. Ségolini, E. Redondo, T. Rojo, R. Mysyk, Nanoporous carbons from natural lignin: study of structural–textural properties and application to organic-based supercapacitors, *RSC Adv.* 4 (2014) 48336.
- [32] B. Moyo, D. Momodu, O. Fasakin, A. Bello, J. Dangbegnon, N. Manyala, Electrochemical analyze of nanoporous carbons derived from activation of polypyrrole for stable supercapacitors, *J. Mater. Sci.* 53 (2018) 5229.
- [33] G.E. Spina, F. Poli, A. Brilloni, D. Marchese, F. Soavi, Natural polymers for green supercapacitors, *Energies* 13 (2020) 3115.
- [34] V.Ča. Ficca, C. Santoro, A. D'Epifanio, S. Licocchia, A. Serov, P. Atanassov, Effect of active site poisoning on iron-nitrogen-carbon platinum-group-metal-free oxygen reduction reaction catalysts operating in neutral media: a rotating disk electrode study, *ChemElectroChem* 7 (2021) 3044–3055.
- [35] A.C. Ferrari, Raman spectroscopy of graphene and graphite: disorder, electron–phonon coupling, doping and nonadiabatic effects, *Solid State Commun.* 143 (2007) 47.
- [36] M. Pimenta, G. Dresselhaus, M.S. Dresselhaus, L. Cancado, A. Jorio, R. Saito, Studying disorder in graphite-based systems by Raman spectroscopy, *Phys. Chem. Chem. Phys.* 9 (2007) 1276.
- [37] A. Ferrari, J. Robertson, Resonant raman spectroscopy of disordered, amorphous, and diamondlike carbon, *Phys. Rev. B* 64 (2001) 075414.
- [38] A. Ferrari, S. Rodil, J. Robertson, Interpretation of infrared and Raman spectra of amorphous carbon nitrides, *Phys. Rev. B* 67 (2003) 155306.
- [39] C. Casiraghi, A. Ferrari, J. Robertson, Raman spectroscopy of hydrogenated amorphous carbons, *Phys. Rev. B* 72 (2005) 085401.
- [40] A. Sadezky, H. Muckenhuber, H. Grothe, R. Niessner, U. Pöschl, Raman microspectroscopy of soot and related carbonaceous materials: spectral analysis and structural information, *Carbon* 43 (2005) 1731.
- [41] K. Kinoshita, Electrochemical Society, *Electrochemical Oxygen Technology*, Wiley, 1992.
- [42] C. Santoro, M. Kodali, S. Herrera, A. Serov, I. Ieropoulos, P. Atanassov, Power generation in microbial fuel cells using platinum group metal-free cathode catalyst: effect of the catalyst loading on performance and costs, *J. Power Sour.* 378 (2018) 169.
- [43] A. Bonakdarpour, M. Lefevre, R. Yang, F. Jaouen, T. Dahn, J.P. Dodelet, J.R. Dahn, Impact of loading in RRDE Experiments on Fe-N-C catalysts: two- or four electron oxygen reduction? *Electrochem. Solid State Lett.* 11 (2008) B105.
- [44] I. Merino-Jimenez, C. Santoro, S. Rojas-Carbonell, J. Greenman, I. Ieropoulos, P. Atanassov, Carbon-based air-breathing cathodes for microbial fuel cells, *Catalysts* 6 (2016).
- [45] V. Watson, C.N. Delgado, B.E. Logan, Influence of chemical and physical properties of activated carbon powders on oxygen reduction and microbial fuel cell performance, *Environ. Sci. Technol.* 47 (2013) 6704.
- [46] T.P. Sciarria, M. Costa de Oliveira, B. Mecheri, A. D'Epifanio, J.L. Goldfarb, F. Adani, Metal-free activated biochar as an oxygen reduction reaction catalyst in single chamber microbial fuel cells, *J. Power Sour.* 462 (2010) 228183.
- [47] R. Taylor, A. Humffray, Electrochemical studies on glassy carbon electrodes: I. electron transfer kinetics, *J. Electroanal. Chem. Interf. Electrochem.* 42 (1973) 347.
- [48] C. Santoro, M. Kodali, S. Kabir, F. Soavi, A. Serov, P. Atanassov, Three-dimensional graphene nanosheets as cathode catalysts in standard and supercapacitive microbial fuel cell, *J. Power Sour.* 356 (2017) 371–380.
- [49] C. Santoro, A. Serov, R. Gokhale, S. Rojas-Carbonell, L. Stariha, J. Gordon, K. Artyushkova, P. Atanassov, A family of Fe-NC oxygen reduction electrocatalysts for microbial fuel cell (MFC) application: relationships between surface chemistry and performances, *Appl. Catal. B Environ.* 205 (2017) 24–33.
- [50] C. Santoro, A. Serov, L. Stariha, M. Kodali, J. Gordon, S. Babanova, O. Bretschger, K. Artyushkova, P. Atanassov, Iron based catalysts from novel low-cost organic precursors for enhanced oxygen reduction reaction in neutral media microbial fuel cells, *Energy Environ. Sci.* 9 (2016) 2346–2353.
- [51] M. Kodali, C. Santoro, S. Herrera, A. Serov, P. Atanassov, Bimetallic platinum group metal-free catalysts for high power generating microbial fuel cells, *J. Power Sour.* 366 (2017) 18–26.

### 3.3 Supercapacitor based on Lignin-derived carbon and calcium alginate binder

In this section, the design of green supercapacitors that exploit sodium alginate as a bio-derived aqueous processable binder and the aqueous electrolyte is reported. Sodium alginate is a biopolymer extracted from the brown seaweeds, it contains 1,4-linked beta-D mannuronate and alpha L guluronate which can be arranged to form copolymer or homopolymer. An important property of this material is that it contains a carboxylic group on each monomeric unit that enables a great number of hydrogen bonds between the binder and the electrode [1]. To further reduce the environmental footprint of EDLCs, the aqueous electrolyte has been exploited, to do so it has been necessary to find a strategy to avoid the dissolution of the aqueous processable electrode. To transform the water-processed electrode into a water-insoluble one, I took inspiration from the field of cooking in which the jellification reaction of sodium alginate with calcium lactate is widely exploited to prepare edible gels [2].

This process is based on the ion exchange between sodium and calcium. It has been demonstrated in the previous scientific literature that  $\text{CaCl}_2$  is an extremely good candidate to achieve fast and efficient ion exchange. This ion-exchange reaction passes through the capability of the alginate to chelate the calcium ion [3]. To avoid the backward ion exchange, between the EDLC electrode and electrolyte, a calcium-based electrolyte has been selected, in particular, a 2 M  $\text{Ca}(\text{NO}_3)_2$  solution has been used. In turn, it has been previously reported that 2 M  $\text{Ca}(\text{NO}_3)_2$  solution enables the design of EDLCs designed with Nickel foam current collectors and CMK-3 carbon, with good capacitance ( $210 \text{ F g}^{-1}$ ) [4].

To further push the concept of sustainability, activated carbon obtained from the pyrolysis of biomass, with the mild activation agent  $\text{KHCO}_3$  has been exploited as the main electrode component. Lignin has been selected as the main biomass source, and the pyrolysis procedure, as well as the chemical-physical characterization of the carbon, has been widely described in section 3.2 [5].

The main novelty of this study is the design of a totally green supercapacitor, that exploits biochar from waste lignin featuring natural aqueous processable polymer as a binder and an aqueous electrolyte. This combination inertly avoids the main criticality of modern commercial supercapacitors, like the usage of fluorinated polymers as binders and organic solvents both as electrolytes and for electrode processing [6]. The aim was the design of a green EDLC to be

directly integrated with an MFC, given that MFCs typically operate at a cell voltage of c.a. 0.6 V, the EDLC was designed targeting this value as maximum cell voltage.

In the next subsection, the main components of the EDLC are briefly reported together with the electrode processing.

### ***3.3.1 Electrode preparation and EDLC assembly***

#### *Activated carbon*

Bioderived activated carbon has been exploited as the main electrode component in this work. Activated carbon (LAC2) has been obtained from the carbonization/Chemical activation of Lignin, the main solid waste of the biodigester plant from which the microbial fuel cell inoculum was taken. The preparation of the lignin-derived activated carbon (LAC) has been widely explained in section 3.2, and the complete procedure, as well as chemical-physical characterization of this material, has been widely described in our recent work [5]. Briefly, the chemical activating agent was  $\text{KHCO}_3$ , dried and washed Lignin was mixed overnight with  $\text{KHCO}_3$  in a 5% solution, containing the double of the activating agent with respect to the dried Lignin. The resulting suspension has been dried in an oven at  $80^\circ\text{C}$  overnight and the obtained solid paste has been put in a tubular oven for the carbonization/activation. The pyrolysis has been carried out under an Ar atmosphere with an heating rate of  $5^\circ\text{Cmin}^{-1}$  up to a temperature of  $850^\circ\text{C}$  with an isothermal treatment at that temperature of 2 h. The oven was therefore subsequently naturally cooled down by the Ar flux. The resulting carbon has been washed several times with HCl and then with deionized water and exploited to prepare the SC electrode and MFC's air-breathing cathodes.

#### *Supercapacitor's electrodes preparation*

Supercapacitor electrodes have been prepared by drop-casting of an aqueous suspension of activated carbon (LAC2), conductive carbon additive (Carbon black C65), and Sodium Alginate (SIGMA Aldrich) as an aqueous processable binder on Nickel foam current collectors. The composite composition was 80% activated carbon, 10% conductive carbon additive, and 10% binder. The casted electrodes have been dried and soaked into a  $50 \text{ mg ml}^{-1}$  solution of  $\text{CaCl}_2$  (SIGMA Aldrich) to perform the sodium-calcium ion exchange. The resulting electrodes have been rinsed several times in distilled water to remove the excess of  $\text{CaCl}_2$  and dried in a thermostatic oven at  $60^\circ\text{C}$  overnight before being tested. For single electrode measurement, a Nickel foam strip was coated by drop-casting and tested as a working electrode of a three necks

electrochemical cell, with a Pt counter and an SCE reference electrode. For EDLC two-electrode measurements, Swagelok-like cells featuring 9 mm diameter disc-shaped electrodes have been exploited. The device featured a Whatmann GF/F separator, and an aqueous solution of 2 M Ca(NO<sub>3</sub>)<sub>2</sub> as the electrolyte

### 3.3.2 LAC2-alginate electrode performance

To design the all-aqueous supercapacitor, at first, three-electrode measurements have been performed with a three-electrode setup. The electrochemical cell featured a Nickel foam current collector coated with 1 mg cm<sup>-2</sup> (0.5 cm<sup>2</sup>) of Calcium alginate-based composite working electrode, a platinum wire as counter, and SCE as a reference electrode in a 2 M Ca(NO<sub>3</sub>)<sub>2</sub> solution.

The electrochemical stability window of the electrodes in 2 M Ca(NO<sub>3</sub>)<sub>2</sub> solution has been investigated by three-electrode cyclic voltammetry (CV) at 5 mVs<sup>-1</sup>. This scan rate has been chosen to amplify any electrochemical side reaction that could occur in the investigated potential window at the working electrode. Different asymmetric electrode potential windows have been investigated changing the positive and the negative charge cut-off potentials while maintaining a difference between the positive and the negative potentials of 600 mV. Indeed, as mentioned above, the cell maximum voltage of an EDLC connected to an MFC is not higher than 0.6 V (Section 3.1) The electrochemical stability window was selected based on a coulombic efficiency of the capacitive charge/discharge voltammograms higher than 95%. Coulombic efficiency has been calculated according to the following equation

$$C_{eff}(\%) = \frac{\int i_{rid} dt}{\int i_{ox} dt} \cdot 100 \quad (3.3.1)$$

Where  $C_{eff}(\%)$  is the coulombic efficiency percentage, and  $\int i_{rid} dt$  (mAs) is the charge calculated as the integral of the experimental current over the discharge cycle (negative current branch),  $\int i_{ox} dt$  (mAs) is the charge calculated as the integral of the charge current (positive current branch) over the charge time. The selected voltage window, in which an acceptable (>95%) coulombic efficiency was achieved was -0.4 V to 0.2 V vs. SCE. Figure 3.3.1a reports the cyclic voltammograms carried out in the selected electrode potential window at different scan rates, namely 5, 10, 20, 50, 100, 150, 200 mVs<sup>-1</sup>. Figure 3.3.1b reports the electrode voltage profile of the selected galvanostatic charge/discharge cycle in the selected voltage window.

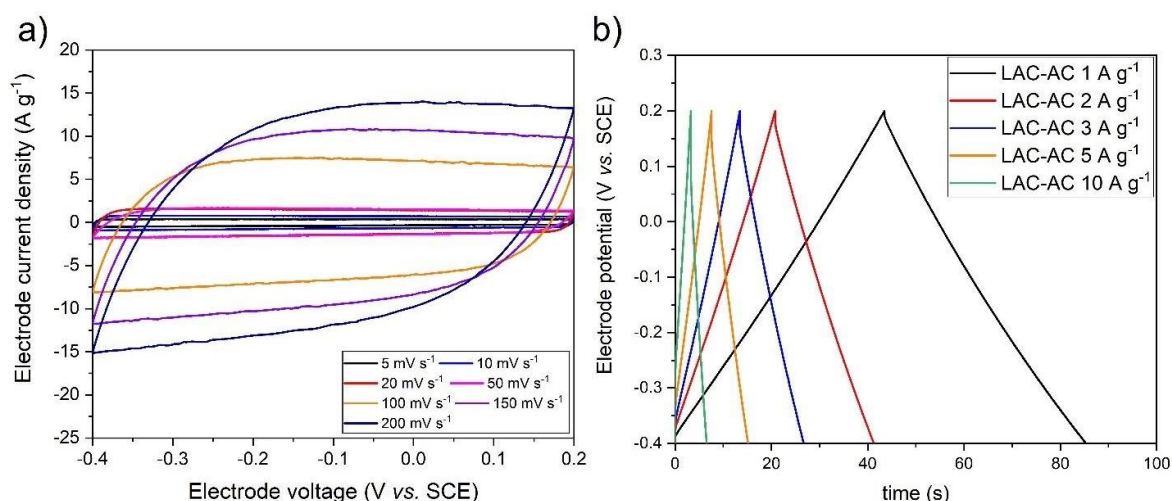


**Figure 3.3.1** a) Single electrode cyclic voltammograms at different scan rate of the LAC2-alginate electrode in 2 M  $\text{Ca}(\text{NO}_3)_2$ , and b) galvanostatic charge/discharge profile of the tested electrode in the investigated potential range at different current densities.

The CVs in Figure 3.3.1 feature an asymmetrical box-shaped voltammogram at each scan rate, as expected for a capacitive charge/discharge process. The specific current monotonically increases with the scan rate. Specific capacitances have been calculated by the slope of the discharge charge (C) vs. the electrode voltage, normalized by the electrode mass. Voltammetric capacitance has been calculated at each scan rate, and the results are reported in Table 1 along with the coulombic efficiency values.

**Table 3.3.1** Voltammetric electrode specific capacitance (normalized to the composite electrode mass) and coulombic efficiency at tested scan rate of LAC2-alginate tested electrode in 2 M  $\text{Ca}(\text{NO}_3)_2$

Scan rate ( $\text{mV s}^{-1}$ )	Electrode specific capacitance ( $\text{F g}^{-1}$ )	Coulombic efficiency (%)
5	75	96.5
10	74	98.6
20	73.3	99.2
50	72.7	99.4
100	71.4	99.7
150	69.6	99.8
200	67.8	99.8

As expected, increasing the scan rate, brings about a reduction of the electrode voltammetric capacitance, with a simultaneous increase of the coulombic efficiency. Indeed, the electrode features a maximum capacitance at  $5 \text{ mVs}^{-1}$ , which slightly decreases with a minimum at the

maximum tested scan rate of 200 mVs<sup>-1</sup>. 75 Fg<sup>-1</sup> with coulombic efficiencies of 97%, and 68 Fg<sup>-1</sup> with a coulombic efficiency of c.a. 100 %, have been measured at a scan rate of 5 mV s<sup>-1</sup> and 200 mV s<sup>-1</sup>, respectively. Noticeably, the capacitance retention is extremely high 10% of specific capacitance fading between the minimum scan rate and the maximum one. This could be attributed to a positive combination of good textural properties of the electrode and high ionic conductivity of the electrolyte [7]. The voltage profiles under galvanostatic charge/discharge are triangular shaped and symmetrical as expected for a process dominated by the formation of a double layer. Remarkably, the electrode is capable of standing very high specific current up to 10 A g<sup>-1</sup>, due to the low equivalent series resistance, as it is possible to see from the small ohmic drop of the galvanostatic profiles reported in figure 3.3.3b). Specific galvanostatic capacitance has been calculated from the slope of the galvanostatic discharge voltage profile. The electrode specific capacitances have been calculated from the slope of the linear interpolation of the voltage profile according to the following equation

$$C = \frac{dV}{dt} \cdot i \sim \frac{\Delta V_{cell}}{\Delta t} \cdot \frac{1}{i} \quad (3.3.2)$$

Where C (mF) is the capacitance of the cell, and  $\Delta V/t$  (V s<sup>-1</sup>) is the slope of the linear interpolation of the cell voltage profile, while i (mA) is the applied current. Specific capacitance values calculated at each current density, by considering the composite mass, are reported in Table 3.3.2.

**Table 3.3.2** Electrode specific capacitance and coulombic efficiency evaluated from the electrode voltage profile during galvanostatic discharge at the tested specific currents

Electrode specific current (A g <sup>-1</sup> )	Electrode specific capacitance (F g <sup>-1</sup> )	Coulombic efficiency (%)
1	73	96.5
2	72.45	98.6
3	71.8	99.29
5	70.5	99.45
10	70	99.7

The electrode galvanostatic specific capacitance reported in Table 3.3.2 are in good agreement with the values that have been evaluated from the cyclic voltammetries. As expected, increasing the electrode-specific current brings a reduction of the electrode capacitance, with an increase of the coulombic efficiency that approaches 100% at the highest specific current, indicating that at that specific current value the response is dominated by the formation of an

electrical double layer. The electrode featured a maximum specific capacitance at the minimum current density,  $73 \text{ Fg}^{-1}$ , at  $1 \text{ Ag}^{-1}$  that slightly decreased to a minimum of  $70 \text{ Fg}^{-1}$  at  $10 \text{ Ag}^{-1}$ .

The results of the single electrode study have been exploited to realize an all-aqueous supercapacitor that has been used to boost the power performance of MFC (Sections 3.4 and 3.5). The electrochemical performance of this device is exposed and discussed in the following section.

### 3.3.3 All aqueous supercapacitor (AaSC)

To fully exploit the asymmetrical electrochemical electrode potential windows reported in Figure 3.3.1 a), electrodes featuring an asymmetric mass balance are required, as highlighted by the application of the charge balance at the electrodes in absolute value

$$q^+ = q^- \quad (3.3.3)$$

where  $q^+$  and  $q^-$  are the positive and negative charges stored in the EDLC of the positive and negative electrodes, respectively. Since the electrodes, behave as EDLCs, in general, it is possible to write the following equation that related to the electrode voltage excursion to the stored charge in the EDL

$$\Delta V^+ C^+ = \Delta V^- C^- \rightarrow \Delta V^+ m^+ C_e^+ = \Delta V^- m^- C_e^- \quad (3.3.4)$$

Where  $\Delta V^+$ ,  $\Delta V^-$  are the positive and the negative electrode voltage excursion during the polarization,  $C_e^+$ ,  $C_e^-$  are the positive and negative material-specific capacitance, and  $m^+$  and  $m^-$  are the positive and the negative electrode mass. In our case, and as highlighted by the voltammeteries in Figure 3.3.3a), the capacitance of the positive side of the polarization is the same as the capacitance of the negative side of the polarization, and therefore it is possible to simplify the previous equation into

$$\frac{\Delta V^+}{\Delta V^-} = \frac{m^-}{m^+} = \frac{0.2}{0.4} \rightarrow m^+ = 2m^- \quad (3.3.5)$$

Therefore, for this particular electrode, the result of this procedure is that the mass of the positive electrode must be twice the mass of the negative one. This equation reflects the intuitive idea that the greatest electrode will be the one that undergoes the smallest voltage variation ( the positive one), while the negative will exploit the largest potential excursion. By controlling the drop cast volume it was possible to reach a positive mass of  $1.5 \text{ mg}$  ( $2.5 \text{ mg cm}^{-2}$ )

<sup>2</sup>) with a negative one of 0.7 (1.16 mg cm<sup>-2</sup>) closely approaching the desired mass ratio ( $\frac{m^+}{m^-} = 2.14 \sim 2$ ).

Therefore, AaSC cells with this electrode mass loading ratio have been prepared, and electrochemically characterized by two electrodes measurements. A Swagelok-like cell has been assembled with the positive and negative electrode, featuring a Whatman GF-F separator soaked in the 2 M Ca(NO<sub>3</sub>)<sub>2</sub> electrolyte. The assembled SC has been electrochemically characterized by two electrodes cyclic voltammetry and galvanostatic charge and discharge tests at selected specific currents. The maximum cell voltage set for both CV and GLV tests was 600 mV since this is the typical microbial fuel cell open circuit potential. In particular, cyclic voltammeteries at different scan rates, namely 5, 10, 20, 50, 100, 150, and 200 mVs<sup>-1</sup> have been run, and the resulting voltammograms are reported in Figure 3.3.2a). For each scan rate the capacitance as well the coulombic efficiency has been calculated and plotted (Figure 3.3.2b). Two electrodes galvanostatic charge/discharge tests have been run and the selected voltage profiles are reported in Figure Figure 3.3.2c). From the galvanostatic charge/discharge test, capacitance, coulombic efficiency as well as specific energy and power have been calculated and plotted. The cell impedance has been measured as well and the resulting Nyquist diagram is reported in Figure 3.3.2f).



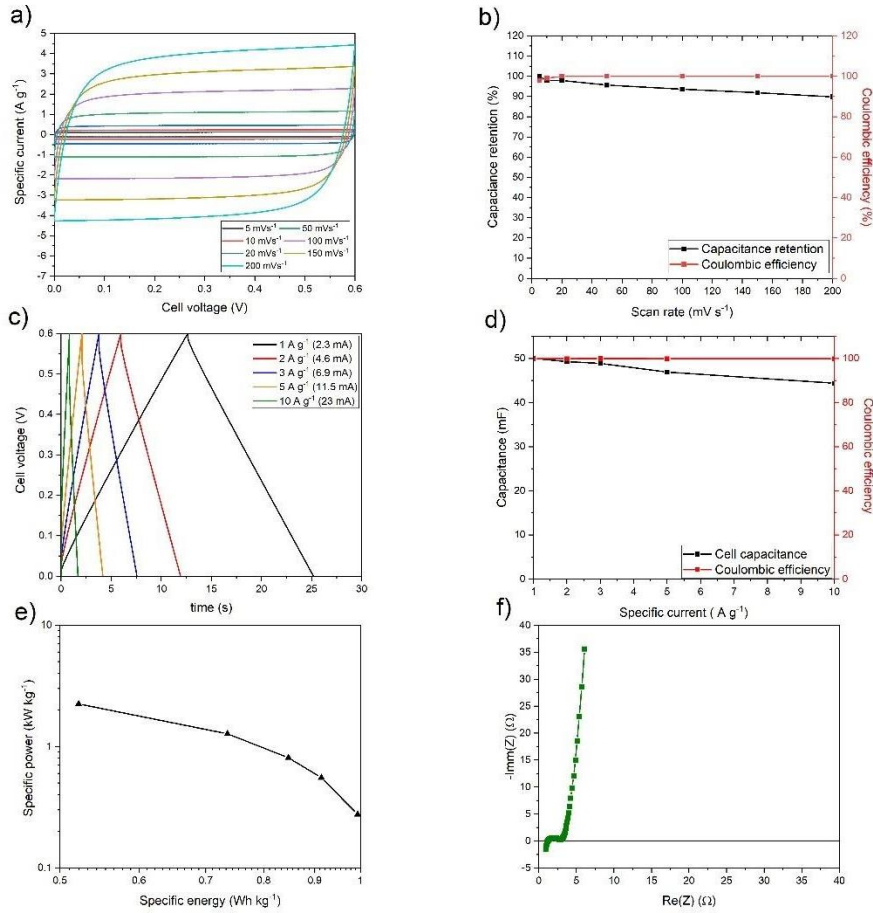


**Figure 3.3.2 a)** AaSC (two electrodes) cyclic voltammograms at different scan rate in the selected voltage window, **b)** Voltametric capacitance retention and coulombic efficiency; **c)** Selected cell's voltage profile under galvanostatic charge/discharge at different specific current; **d)** galvanostatic charge/discharge capacitance and coulombic efficiency at the tested specific current, **e)** Ragone plot of the device, and **f)** Nyquist plot.

Figure 3.3.2a) shows that between 0 and 600 mV, the CV is square-shaped and symmetric at each scan rate, which indicates a process driven by the formation of an electrical double layer without secondary Faradaic reactions. Moreover, Figure 3.3.2a shows that the device can stand a very high specific current without losing its capacitance. EDLC capacitances have been also converted into electrode capacitance according to the procedure described by Conway [8] adapted for the mass loading of this supercapacitor and briefly discussed by the following equations. In general, in an EDLC, the positive electrode and the negative one are in series and therefore the total EDLC capacitance can be written as

$$\frac{1}{C_T} = \frac{1}{C^+} + \frac{1}{C^-} \rightarrow C_T = \frac{(m^+ \cdot m^-)}{m^+ + m^-} \cdot C_e \quad (3.3.6)$$

Where  $C_T$  is the total capacitance of the device. The total capacitance of the EDLC is related to the specific capacitance of the EDLC by the following equation

$$C_S = \frac{C_T}{(m^+ + m^-)} \quad (3.3.7)$$

Therefore, by substitution it is possible to relate the specific capacitance of the device to the specific capacitance of the electrode material

$$C_S = \frac{(m^+ \cdot m^-)}{m^+ + m^-} \cdot \frac{1}{m^+ + m^-} \cdot C_e \quad (3.3.8)$$

since as previously discussed  $m^+ = 2 m^-$  equation (3.3.8) simplifies into

$$C_S = \frac{2}{9} C_e \quad (3.3.9)$$

Therefore, exploiting the asymmetric design allows to fully exploit the capacitive potential window offered by the electrolyte, with the major drawback of reduced exploitation of the capacitance of the electrode material. Full EDLC capacitance ( $C_T$ ), EDLCs specific capacitance ( $C_S$ ) obtained from the voltammeteries reported in Figure 3.3.2a, and the calculated electrode capacitance ( $C_e$ ) according to the equation (3.3.9) are reported together with the EDLC coulombic efficiency ( $C_{eff}$ ) at each scan rate are in Table 3.3.3

**Table 3.3.3** Total EDLC capacitance ( $C_T$ ), specific EDLC capacitance ( $C_S$ ), calculated electrode specific capacitance ( $C_e$ ) and coulombic efficiency ( $C_{eff}$ ) evaluated by the voltammogram reported in Figure 3.3.2a

Scan rate (mVs <sup>-1</sup> )	$C_T$ (mF)	$C_S$ (Fg <sup>-1</sup> )	$C_e$ (F g <sup>-1</sup> )	$C_{eff}$ (%)
5	52.7	22.9	103.2	98
10	51.6	22.4	100.9	99
20	51.6	22.5	101.1	100
50	51.6	21.9	98.7	100
100	49.4	21.5	96.1	100
150	48.4	21.0	94.8	100
200	47.4	20.6	92.7	100

As in the case of the single electrode measurements discussed in Section 3.3.2., the capacitance of the EDLC decreases, increasing the scan rate. In particular, the cell features a maximum EDLC capacitance of 53 mF at 5 mVs<sup>-1</sup>, which slightly decreased (10%) at 47 mF at 200 mVs<sup>-1</sup>, indicating good capacitance retention, 11% of capacitance fading. These values correspond to specific electrode voltammetry capacitance of 100 Fg<sup>-1</sup> at 5 mVs<sup>-1</sup> that decreases to 90 Fg<sup>-1</sup> at 200 mVs<sup>-1</sup>. Interestingly, this calculation overestimates the electrode capacitance, with respect to those that have been measured by three-electrode setups reported in Section 3.1, which indicates that a limiting process other than the electrode capacitance depletion related to the series connection of the electrodes is present. Figure 3.3.2b) reports the capacitance retention and the coulombic efficiency at increasing the scan rate, noticeably the device maintains 90% of the capacitance that has at 5 mVs<sup>-1</sup> at 200 mVs<sup>-1</sup>. At the same time at all the tested scan rates, the device has a coulombic efficiency higher than 98% that approaches 100% for scan rate higher than 20 mV s<sup>-1</sup>. This is a further indication that the device can stand high specific current without losing capacitance, which highlights the good combination of textural properties of the carbonaceous electrode, together with the high ionic conductivity of the selected aqueous electrolyte [9].

The galvanostatic cell voltage profiles reported in Figure 3.3.3c) are triangular shaped and symmetric, confirming that the charge/discharge accumulation process is capacitive and related to the formation of an electrical double layer. Noticeably, the cell is capable to stand very high specific current (10 A g<sup>-1</sup>) confirming the good rate capability of the prepared electrodes. This is highlighted by the fact that the voltage profile shows modest instantaneous voltage drop ( $\Delta V_{ohmic}$ ) at beginning of discharge, which in turn represents a small ohmic drop also at high current. Equivalent series resistances  $R_{ESR}$  ( $\Omega$ ) at the tested current of the EDLC have been calculated according to the equation (3.3.10)

$$R_{ESR} = \frac{\Delta V_{ohmic}}{2 \cdot i} \quad (3.3.10)$$

where  $i$  is the galvanostatic discharge current. Specific energy  $E_{cell}$  (J g<sup>-1</sup>) has been calculated by the integral of the cell's galvanostatic discharge voltage profile divided by the mass of the two composite electrodes ( $m_{cell}$ ) according to the equation (3.3.11).

$$\bar{E}_{cell} = \frac{E}{m_{cell}} = i \int V_{cell} dt \cdot \frac{1}{m_{cell}} \quad (3.3.11)$$

From the specific discharge energy, the average discharge power  $P_{cell}$  (W g<sup>-1</sup>) has been calculated by the (3.3.12), that is equation (3.3.10) divided by discharge time  $t$  (s).

$$\bar{P}_{cell} = \frac{P}{m_{cell}} = \frac{\bar{E}_{cell}}{\Delta t} \quad (3.3.12)$$

The total EDLC galvanostatic capacitance, equivalent series resistance, specific energy and specific power, and the coulombic efficiency featured at different specific currents are reported in Table 3.3.4.

**Table 3.3.4** AaSC EDLC capacitance, equivalent series resistance, specific energy and specific power, and the coulombic efficiency evaluated by the galvanostatic voltage discharge profile reported in Figure 3.3.2c)

Specific current (A g <sup>-1</sup> )	C <sub>T</sub> (mF)	R <sub>ESR</sub> (Ω)	E (Whkg <sup>-1</sup> )	P (kW kg <sup>-1</sup> )	C <sub>eff</sub> (%)
1	50.0	-	1	0.3	100
2	49.3	2.07	0.9	0.5	100
3	48.9	2.0	0.8	0.8	100
5	46.9	2.0	0.7	1.3	100
10	44.4	2.0	0.5	2.2	100

Except for the lowest tested specific current, the cell features almost constant calculated equivalent series resistance. At 1 Ag<sup>-1</sup>, the ohmic drop was extremely small and therefore its evaluation was strongly affected by the acquisition system. A mean value of 2Ω has been calculated from the R<sub>ESR</sub> calculated from the other tested specific currents. From the ESR it is possible to calculate the short circuit current at 600 mV, that is 300 mA, which corresponds to a specific current of 20 Ag<sup>-1</sup>. The EDLC specific capacitance obtained from the galvanostatic charge/discharge test is in good agreement with those calculated from the voltammetric test. The cell featured a maximum galvanostatic capacitance at the lowest current, 1 Ag<sup>-1</sup> (2.3 mA) of 50 mF that slightly decreased to 44.38 mF at 10 Ag<sup>-1</sup>, a capacitance loss of 12%. From the galvanostatic charge/discharge test, specific energy converted in Wh kg<sup>-1</sup>, and the specific power has been calculated with equations (3.3.11) and (3.3.12), respectively and the results are reported in the Ragone plot in Figure 3.3.3 d). The Ragone plot has the shape expected for EDLCs, with the typical horizontal profile at high current that bends through lower specific power values at low current densities. The cell features maximum specific power of 1 kW kg<sup>-1</sup>

<sup>1</sup>, at 10 Ag<sup>-1</sup> where it has the minimum value of the specific energy (0.5 Wh kg<sup>-1</sup>). With maximum specific energy at the lowest current, 0.99 Wh kg<sup>-1</sup> at 1 Ag<sup>-1</sup>, where it has the minimum of the specific power (0.27 kW kg<sup>-1</sup>). Overall, the cell features specific power that is comparable with those of modern supercapacitors with an acceptable specific energy. The specific energy is considerably lower with respect to that of commercial EDLC and this is mainly due to the low maximum voltage 600 mV set in the tests in view of the integration with the MFC. Note that commercial EDLCs with acetonitrile-based electrolyte feature up to 2.7 V of modern supercapacitor. Since the maximum energy of an EDLC goes as  $E_{max} = 1/2CV_{max}^2$ , decreasing the maximum voltage strongly afflicts the maximum energy [7,8,9].

Figure 3.3.3 f) reports the Nyquist diagram obtained by the electrochemical impedance spectroscopy of the cell. The Nyquist diagram can be divided into two regions, a high-frequency semicircle and a low-frequency line that approaches a slope of 90°, respectively. The intercepts at the highest frequencies of the semicircles represent the ohmic resistances (electronic and ionic) of the electrodes and electrolyte-separator system (1.23 Ω). The small semicircle has been attributed to the ion transport at the electrolyte-carbon interface and the contact between the electrode and the current collector [9]. The low-frequency line represents the capacitive behaviour of the electrodes and the EDLC. For an ideal EDLCs, a vertical line is expected, while in the Nyquist diagram reported in In Figure 3.3.3 f), the lines deviate from this ideal behaviour because of ion diffusion into the carbon electrodes (transmission line). Finally, the supercapacitor has been cycled for 2500 cycles at 1 Ag<sup>-1</sup> and the capacitance retention over cycling is reported in Figure 3.3.4.

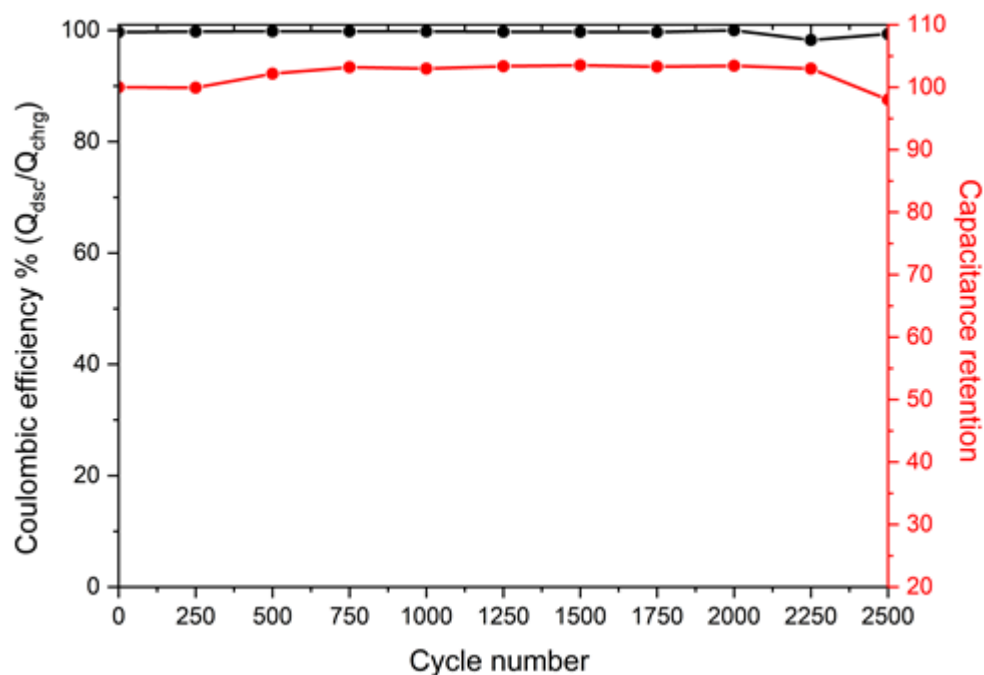


**Figure 3.3.4** Coulombic efficiency and Capacitance retention during cycling at  $1 \text{ Ag}^{-1}$  of the tested AaSC EDLC.

Overall, the EDLC featured good capacitance retention with coulombic efficiencies close to 100%. This approach follows our previous work in which aqueous processable binder has been widely exploited as a valuable route to tackle the sustainability of modern productive processes based on organic solvent slurries roll to roll, reported in Section 2.2 [11,12].

### 3.3.4 Conclusions

In this section, it has been shown at the proof-of-concept level that it is possible to realize an all-aqueous supercapacitor by a smart design that exploits only bio-derived components and sustainable processes. The extremely high conductivity of the  $\text{Ca}(\text{NO}_3)_2$ -based aqueous electrolyte brings about extremely low equivalent series resistance of the EDLC that enables high specific power also at low maximum voltage. Indeed, the exploitation of aqueous electrolytes offers a sustainable alternative to the organic solvent-based one of the modern commercial supercapacitors, with the major drawback of limiting the maximum cell voltage and hence limiting the cell's specific energy. However, the AaSC was designed in view of its direct integration with an MFC, an application that does not require high-voltage energy storage units, but that has a typical operating voltage of 0.6 V.

### **3.4 Strategies to improve MFC power output**

In this section, experimental results about three different strategies implemented to improve the power performance of microbial fuel cells are shown and the results are discussed in detail. Indeed, one of the major limitations of MFC that kept unleashing the promise of an intrinsically sustainable device, that allows water purification while producing electric energy, is the low power output [1]. Nowadays, different strategies have been proposed by modern research to tackle these issues such as i) the exploitation of external energy harvesting devices with higher specific power, capable of releasing the energy produced by the MFC releasing it at higher current pulses [13] ii) the exploitation of catalysts to improve the sluggish cathodic kinetics, and iii) the monolithic integration of supercapacitive features in MFCs.

In this section three different strategies to improve the MFC power performance are reported:

- The exploitation of the green AaSC supercapacitor described in Section 3.3, as high specific power element, capable to store the energy produced by the MFC releasing it at high current densities
- The exploitation of an additional capacitive cathode, an additional electrode based on lignin derived LAC2 activated carbon.
- The exploitation of an activated carbon anode, in combination with the additional capacitive cathode, to realize a monolith supercapacitive MFC. Here all the electrodes are manufactured by using the lignin derived LAC2 carbon.

In the first part of this section, the materials and methods exploited are reported. At first, an MFCs assembled with a biomass-derived activated carbon-based air-breathing cathode have been characterized electrochemically as a benchmark by means of three-electrode pulsed galvanostatic discharges.

#### ***3.4.1 MFC assembly and MFC-EDLC integration***

##### ***Single chamber microbial fuel cell***

Single chamber microbial fuel cells with a single chamber bottle of 125 mL, featuring airbreathing cathode and carbon brush-based anode have been used in this work. The sludge exploited for the colonization of this work was provided by an agronomical plant and was obtained as the solid part of a biodigester of agricultural wastes. The electrolyte solution was

composed of PBs 1x bought from Oxid, with a composition: 8.0 g sodium chloride, 0.2 g of potassium chloride, 1.15 g di-sodium hydrogen phosphates, and 0.2 g of potassium dihydrogen phosphate.

### *MFC Air breathing cathode preparation*

Air-breathing cathodes have been prepared with lignin-derived activated carbon (LAC2). In particular, the composite was a 75% LAC2, 5% conductive carbon additive (Carbon black C65), and 20% Teflon binder (Dupont). The electrodes were prepared by a Teflon-Et(OH) suspension procedure. In particular, at first, the composite carbonaceous powder was dissolved in Et(OH) and stirred for 2h at 30°C, subsequently, the Teflon based binder was added and the temperature was rising up to 80°C in a thermal bath to evaporate the Et(OH), until a malleable carbon paste was obtained. The composite carbon paste was, therefore, cut in disks with a diameter of 28 mm and pressed against a titanium grid with a hydraulic press. The electrodes have been dried in an oven at 100°C overnight, composites cathodes with a mass of 600 mg have been obtained.

### *Carbon brush decorated with activated carbon LAC2 based composite*

Carbon brushes have been coated with a composite layer based featuring LAC 2 as the main component. The decoration has been obtained by means of soaking the carbon brush in a suspension of the composite, with a composition of 80% of activated carbon (LAC2), 10 % of conductive carbon additive (Carbon black C65), and 10% of PvdF (Arkema) based binder, in N-methyl pyrrolidone (NMP). The coating has been obtained by repetitively soaking the carbon brush in the activated carbon-based slurry, the resulting electrode has been dried at first in an oven at 80°C overnight and subsequently in a buchi oven under vacuum at 120°C for another night.

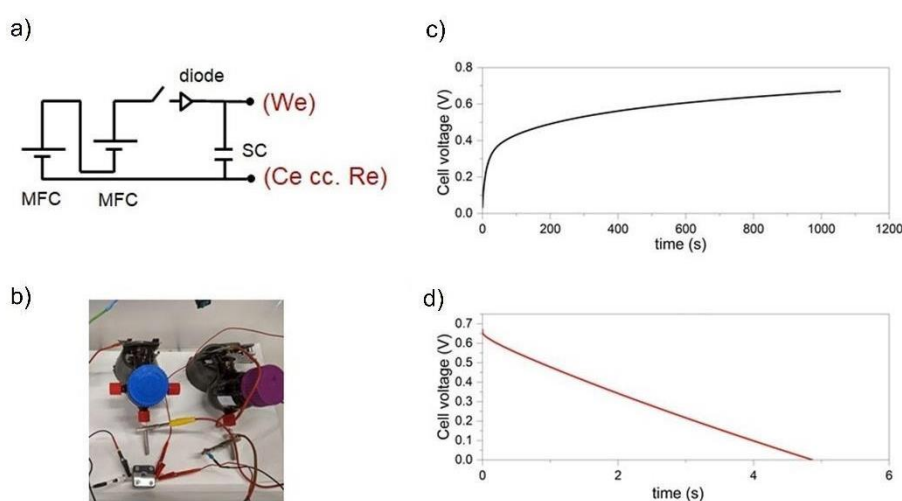
### *Green supercapacitor*

A green supercapacitor based on LAC2 carbon and calcium alginate e binder, with  $\text{Ca}(\text{NO}_3)_2$  as electrolyte has been realized and electrochemically characterized, the complete characterization is reported in Section 3.3. This section reports the electrochemical characterization at the system level of the integration of the Ca-Alginate-based EDLCs with the MFCs, referred in the latter part of the test as MFC//SC.



## *Electrochemical investigation of the integration of green supercapacitor with MFCs*

The circuit that has been realized as well as the experimental measurements run to investigate the result of the integration between the MFCs, and the green supercapacitor are briefly reported and discussed. To investigate the performances at the system level of the MFC connected with the designed AaSC, two MFCs have been connected in series through a diode in parallel to the designed SC, as reported in Figure 3.4.1.



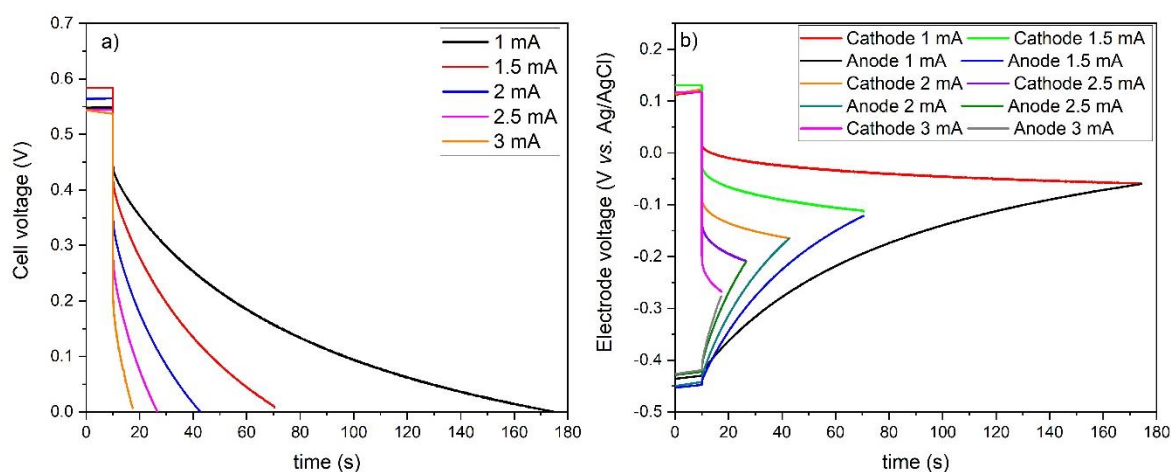
**Figure 3.4.1, a)** Sketch of the circuit adopted to assemble the system to power up the MFCs power output (MFC//SC), **b)** picture of the actual system and **c), d)** Selected voltage profile of the technique during the tests.

Figure 3.4.1 a), reports a Sketch of the circuit exploited to study the MFCs in parallel with the designed SC. A diode has been inserted between the MFCs and the SC to avoid backward current during cycling, which would have harmful effects at the system level. The exploitation of the diode induces an ohmic drop that needs to be compensated by adding two MFCs in series. To overcome the voltage, drop induced by the diode that was 0.6 V, two MFCs have been connected in series to polarize the SC at 600 mV. A picture of the actual system is reported in Figure 3.4.1b), where it is possible to see the two single chamber microbial fuel cells and the supercapacitor on the bottom of the picture. Figure 3.4.1 c), d) report the selected voltage profile of the test technique. In particular, the two MFCs were used to charge the SC that was subsequently discharged at different currents. Therefore, the terminal of the SC was let into open circuit condition, recording the cell potential (Figure 3.4.1c), until a cell potential of 600 mV was measured, subsequently, without detaching the MFC from the SC, galvanostatic

discharges at different specific currents were performed and the resulting voltage profile was recorded (Figure 3.4.1d).

### 3.4.2 LAC2-based Microbial fuel cell (MFC) performance

MFC, without any supercapacitive component, rather than the air-breathing cathode based on the LAC2-activated carbon has been electrochemically investigated as a benchmark system with a three-electrode set-up. The anode brush was not coated with additional carbon. The working electrode was the airbreathing cathode, the counter electrode the carbon brush anode, and a reference Ag/AgCl electrode in a lugging capillary with PBs 1x as supporting electrolyte was connected to the reference electrode. Three electrode-galvanostatic pulsed discharges at different currents from 1 to 3 mA, were run to electrochemically characterize the response of the prepared MFC. Between each pulsed discharge, the cells were let into an open circuit until the initial potential was restored. The working electrode was the airbreathing cathode, the counter was the carbon brush anode, and the reference was a silver/silver chloride reference in a lugging capillary with a PBs 1x solution as the supporting electrolyte. The parameters of interest are shown in Tables 1 and 2. The selected pulsed discharge cell's voltage and single electrodes voltage profile, are reported in Figure 3.4.2a) and 3.4.2b), respectively.



**Figure 3.4.2 a)** Cell voltage profile under galvanostatic discharge, and **3.4.2 b)** single electrode voltage profile under galvanostatic discharge at 1,1.5, 2,2.5, and 3 mA of the MFC.

Figure 3.4.2a), reports the cell voltage profile at different discharge currents, as expected, increasing the current led to increased instantaneous voltage drop, accompanied by a strong reduction of the discharge times. Moreover, increasing the discharge current, the cell voltage profile appears to become more linear since, at high current densities, the capacitive response of the cell becomes dominant over the faradaic one. Figure 3.4.2b), reports the single electrodes

voltage profile obtained under galvanostatic discharge obtained with the three electrodes measurements. The open-circuit potential of the electrode that composes the fuel cells is aligned with the open circuit potential reported in the literature, indeed, the anode OCP is -400 mV vs. Ag/AgCl c.a. while the cathode OCP is c.a. 100 mV vs. Ag/AgCl. From Figure 3.4.2b) it is evident that the ohmic drop of the cathode is significantly higher with respect to one of the anodes at each tested current. This is likely due to the geometry of the cell since the cathode in the single-chamber MFC is considerably far from the reference with respect to the anode and therefore this evidence can be considered as an artifact related to the cell construction. On the other hand, the trend of the single electrode voltage vs. time is independent of the geometry. Since the slope of the anode during the discharge is always greater than the slope of the cathode, it is possible to conclude that for this cell, with this inoculum and electrodes, the anode is limiting the capacitive response. Electrodes apparent capacitance  $C_{app}$  (See section 3.1) has been calculated from the slope (s) of the discharge curve in the capacitive region (m) according to the following equation (3.4.1)

$$C_{app} = \frac{i}{m} \quad (3.4.1)$$

Moreover, from the discharge curve voltage profile, the cell's equivalent series resistances ( $R_{ESR}$  in  $\Omega$ ), discharge energy, and power have been calculated according to equations (3.4.2), (3.4.3), and (3.4.4)

$$R_{ESR} = \Delta V_{ohmic} \frac{1}{2 \cdot i} \quad (3.4.2)$$

Where  $\Delta V_{ohmic}$  is the ohmic drop (V) and  $i$  is the galvanostatic discharge current. Cell energy  $E_{cell}$  (J) has been calculated by the integral of the cell's galvanostatic discharge voltage profile according to equation 3.4.3

$$E_{cell} = \int V_{cell} dt \quad (3.4.3)$$

From  $E_{cell}$  the average discharge power  $P_{cell}$  (W) has been calculated by equation (3.4.4)

$$P_{cell} = \frac{E_{cell}}{\Delta t} \quad (3.4.4)$$

The cell's apparent capacitance and the electrode apparent capacitance at the different tested pulsed current are reported in Table 3.4.1 and Table 3.4.2 respectively.

**Table 3.4.1** *Microbial fuel cell apparent capacitance, equivalent series resistance, energy, and power*

Pulsed current (mA)	$C_{app}$ (mF)	$R_{ESR}$ ( $\Omega$ )	Energy ( $\mu$ Wh)	Power (mW)
1	302.8	91.6	6.4	0.1
1.5	173.1	95.3	3.9	0.2
2	131.8	93.0	2.4	0.2
2.5	83.2	92.0	1.2	0.2
3	71.4	92.8	0.5	0.2

The cell's apparent capacitance decreases with the increase of the magnitude of the discharge pulsed current. In particular, it decreases from a maximum of 302 mF at 1 mA, to a minimum of 71.43 mF at the maximum tested current of 3 mA. With the three-electrode set-up, it has been possible to investigate the single electrode voltage profile during the pulsed discharge and the resulting voltage profiles are reported in Figure 3.4.2b). The slope of the discharge voltage profile is indicative of the electrode's apparent capacitance as highlighted by equation (1). Indeed, the slope of the anode is considerably higher than the slope of the cathode at all the values of the tested current. This makes the anode the limiting electrode in this cell set-up. The calculated values are reported in Table 2. From figure 3.4.2a), it is evident that at the cell level, the ohmic drop plays a critical role. Indeed the instantaneous voltage drop related to the ohmic resistance of the cell ( $R_{ESR}$ ) translates the cell voltage discharge profile towards 0 V. In turn, this will take down the integral of equation (3.4.3), reflecting the fact that ohmic drops are extremely important in reducing the available discharge energy. Table 3.4.1 reports the ohmic drop of the cell under consideration, these quantities take into account all the ohmic elements that are present in the cell, which due to the complex design of the cell are a great number (e.g. all the ohmic elements in the cathode such as interparticle resistance, current collector-air-breathing cathode resistance, the ionic term of the electrolyte, and similarly the ohmic resistance of the Anode). The ohmic resistance is almost constant at all the current values and the average value of  $92.94 \pm 1.42 \Omega$ .

**Table 3.4.2** Apparent capacitance of the anode and the cathode, calculated by equation (1) from the discharge curves reported in Figure 2b).

Pulsed current (mA)	$C_{app}$ Anode (mF)	$C_{app}$ Cathode (mF)
1	523.7	3238.5
1.5	315.3	1453.7
2	267.7	1247.1
2.5	214.9	808.8
3	186.7	466.7

Both anode and cathode capacitance decreased with the increase of the current. The apparent capacitance of the anode is considerably smaller than the apparent capacitance of the cathode, namely at their maximum value of 523 mF vs. 3238 mF, for the anode vs. the cathode respectively. Nevertheless, at high current pulses, the anode loses 65% of its initial capacitance while the cathode loses 85%. The calculated average power and average energy, reported in Table 3.4.1 have been plotted in Figures 3.4.3 a) and 3.4.3 b) and interpolated, respectively by a polynomial equation and by an exponential function. Figure 3.4.3 a) reports the average power, averaged on the different tested cells (3 cells), together with their experimental standard deviation. Figure 3.4.3 b), reports the average energy, converted in  $\mu Wh$ . In both figures, the experimental values are reported along with the curves extrapolated from the fit of the experimental data.

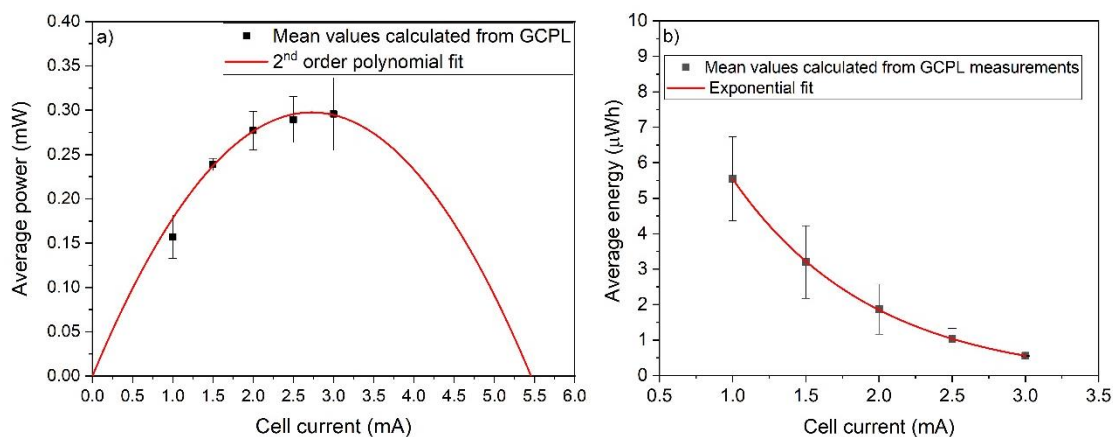


**Figure 3.4.3** a) Average power of the cells with experimental standard deviation (black squares) with the second-order polynomial fit extrapolated to the short circuit current (red line). Figure 3b) Experimental average energy (black square) first-order exponential function (red line).

From Table 3.4.1 and figure 3.4.3 a), it is evident that increasing the pulsed current up to a certain value leads the average power to rapidly decrease. Indeed, the average power of the tested cells has been fitted with a second-order polynomial function. Moreover, interpolating the experimental data with a second-order polynomial function allowed us to evaluate the short circuit current of 5.5 mA. This estimation is in line with the short circuit current that could be calculated from the equivalent series resistance. Indeed, assuming an OCV of 600 mV it is possible to calculate a 6.1 mA short circuit current. At the short circuit current, the average power is zero and therefore the cell doesn't deliver any exploitable energy. From the figure, it is evident that the cells were tested in the region closest to the maximum of the average cell power.

In Figure 3.4.3 b) the average energy constantly decreases, increasing the current, demonstrating that the exploitation of the MFCs closer to their short circuit current doesn't allow noticeable physical work. Moreover, it seems it is possible to extrapolate the energy of the cell at extremely low current, it is worth mentioning that the curve must be continuous up to zero and therefore there must be a maximum of the energy.

### **3.4.3 External integration of MFC with the green AaSC supercapacitor (MFC//SC)**

In this section, the integration of the green AeSC supercapacitor with MFCs by the circuit described in Figure 3.4.1), is reported, and discussed. Briefly, 2 MFCs were connected in series and the 2-cell stack was connected to the AaSC through a diode. The diode was needed to avoid backward current from the SC to the MFC. Two MFCs were necessary to overcome the ohmic drop induced by the diode, and to polarize the SC up to 600 mV.

The electrochemical performances have been evaluated by means of pulsed discharge and the apparent capacitance of the system, together with the system average pulsed discharge power and energy. Pulsed discharges at different current densities, namely 1 Ag<sup>-1</sup> (2.3 mA), 2 Ag<sup>-1</sup>, (4.6 mA), 3 Ag<sup>-1</sup> (6.9 mA), 5 Ag<sup>-1</sup> (11.5 mA), and 10 Ag<sup>-1</sup> (23.3 mA) have been tested and the results are reported in Figure 6. Before the pulsed test, the MFC cells were fed with 5 mL of NaAc 0.1 M.

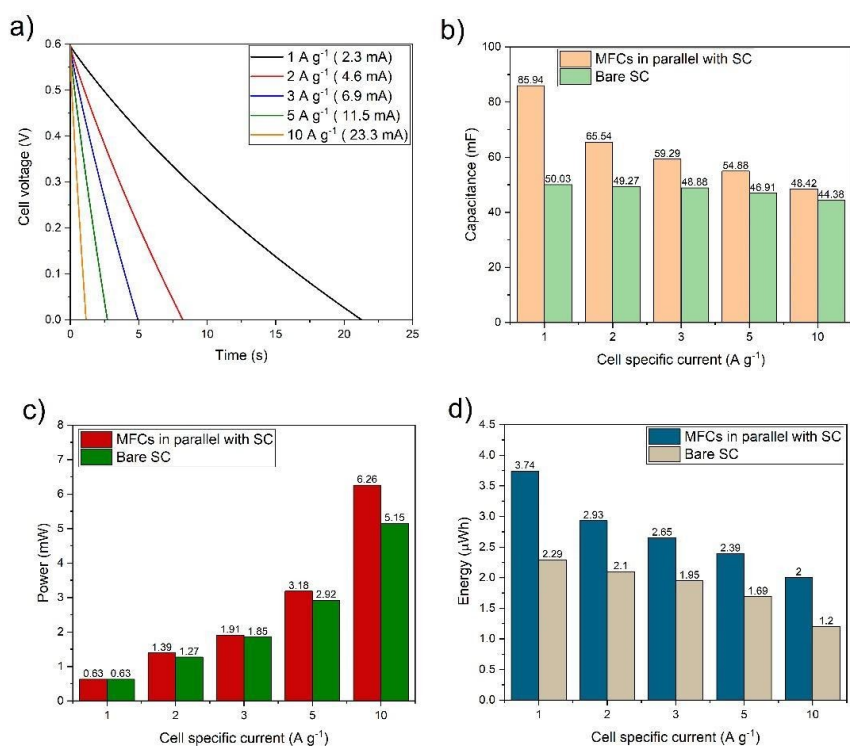


**Figure 3.4.6a)** Galvanostatic discharge profiles of the MFC//SC system, **b)** apparent capacitance of the system vs. the capacitance of the SC, **c)** average power of the system vs. the one of the SC, and **d)** the average energy of the system vs. the one of the SC as a function of the current, normalized by the SC composite mass.

Figure 3.4.6 a) reports the system voltage profile during the galvanostatic discharge. At the lowest currents, the system voltage profile deviates from the linear profile of the EDLC. Moreover, the system is capable to reach the absolute current value that the MFC alone wouldn't be capable to stand, indeed the short circuit current for MFC featuring this electrolyte, this volume, and electrodes are expected to be 5.5 mA. This is a first confirmation that coupling MFC with an external supercapacitor is a valuable strategy to improve the MFCs power output in terms of improving the output current. The system apparent capacitance has been calculated according to equation 3.4.1. Histograms of the calculated apparent capacitances at the tested pulsed current are reported in Figure 3.4.6 b). While the EDLCs show good capacitance retention, increasing the applied current, the system shows an evident positive effect that is maximum at low specific current. Indeed, the system's apparent capacitance at low current is greater than the SC apparent current. This effect decreases to a minimum value at the maximum pulsed current, where the system capacitance approaches the one of the SC, 86 mF vs 48.42 mF at 2.3 mA and 23 mA. This confirms our previous finding reported in section 3.1 in MFC-SC integrated systems there is a synergic effect at low current that is related to the Faradaic activity of the MFC at low current. increased the pulsed current, the response is dominated by the contribution of the SC since the MFC can't stand current higher than its short circuit ones.

Figure 6c reports the comparison between the system power and the SC power, for all the tested current, the power is comparable with the one of the SC highlighting that the SC dominates the response in terms of power. Interestingly, the trend, in this case, is reversed concerning the apparent capacitance one, that is, the system power becomes greater than the SC one increasing the pulsed current. Finally, Figure 3.4.6 c) reports the trend of the system-specific energy vs the SC ones. For all the tested pulsed current values, the system energy is always greater than the one of the SC, moreover, the difference decreases, increasing the current pulse magnitude. This again underlines the fact that microbial fuel cells can actively contribute only at low specific currents. Overall, this experiment shows that the system integration allows microbial fuel cells to reach pulsed current considerably higher than those featured by the MFC alone, with output power one order of magnitude higher than those of the bare MFC. In turn, these results demonstrate that MFC can effectively recharge SC, which is of paramount importance for the design of energy-autonomous (not connected to the grid) systems.

Finally, the MFC-SC system has been cycled at different current densities and the resulting maximum voltage (achieved after each SC recharge by the MFC) and apparent capacitance trends vs cycle number are reported in Figure 3.4.7.

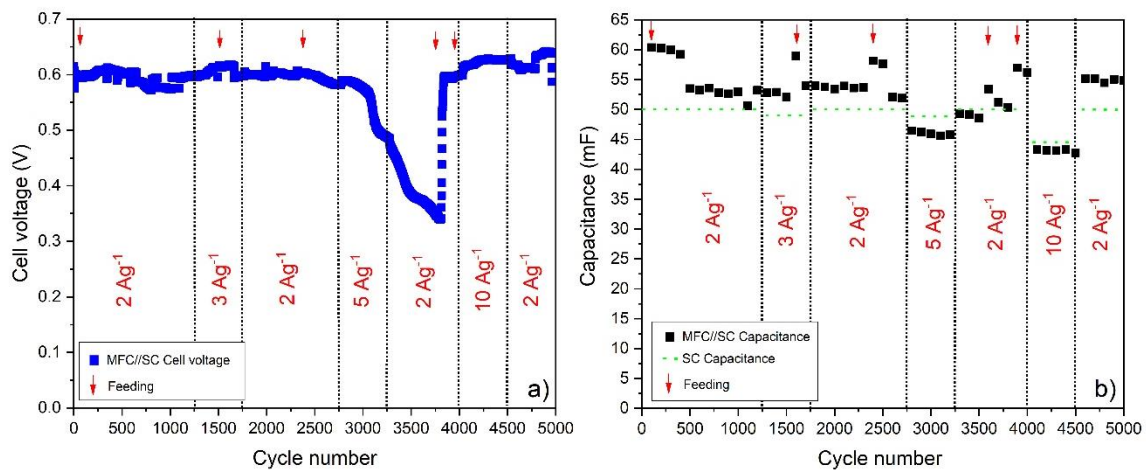


**Figure 3.4.7a)** MFC-SC system maximum voltage and **7b)** apparent capacitance at different supercapacitor specific current and cycle numbers.

Figure 3.4.7 a), reposts the trend of the maximum voltage of the MFC-SC system 1 under cycling at different current densities. Microbial fuel cells have been fed constantly with 5 ml of 0.1 M NaAc solution. Between cycle 3000 and cycle 3750, the feed has been interrupted and due to starving conditions, the cell voltage had suddenly dropped. The cells have been subsequently fed at cycle 3750, resulting in an instantaneous increase of the voltage that



approaches the initial values. The cycling test highlights the need for the cell to be constantly fed and the fact that the amount of nutrients plays a critical role in terms of cell performance. The quick response of the cell, in terms of voltage recovery, once it has been fed, shows how these systems are resilient. Figure 3.4.7 b), reports the capacitance of the system (black dots), and the capacitance of the SC dotted green line. Here is evident the effect of the cell feeds on the apparent system capacitance, highlighting the fact that the effect on the SC response of the MFC is related to the Faradaic reactions of the MFCs. Interestingly, it is possible to appreciate the feeding from Figure 3.4.7 b), which is related to the position in which the capacitance quickly reaches a local maximum value that rapidly decreases to values that are comparable to the one of the bare SC, that are reported as dotted lines in the figure.

The need of being constantly fed of the cells reflects into the capacitance of the system. Indeed, the capacitance under cycling (Figure 3.4.7) is smaller than the capacitance that has been measured by the rate capability tests (Figure 3.4.6), where the MFC was continuously fed before each test at a given rate.

#### ***3.4.4 Capacitive additional electrode, short-circuited with MFC cathode (AAC-MFC)***

MFC with an additional capacitive cathode have been realized and electrochemically characterized. Indeed, in [12], it has been demonstrated that the use of the additional electrode decreased the  $R_{ESR}$ , mainly because of the decrease of the cathode impedance, that even in the MFC under study limits power output (See 3.4.1). The additional electrode was a bare carbon brush. In this section are reported the results of the galvanostatic pulsed discharge at increasing current pulse of this system. In the latter part of the text, this MFC is referred to as “Additional Capacitive Cathode MFC (ACC-MFC)”. The ACC-MFC has been electrochemically characterized with the same three-electrode setup exploited for the first MFC. A sketch of the cell, together with the single electrode’s voltage profile obtained from the galvanostatic discharge is reported in Figure 3.4.8.

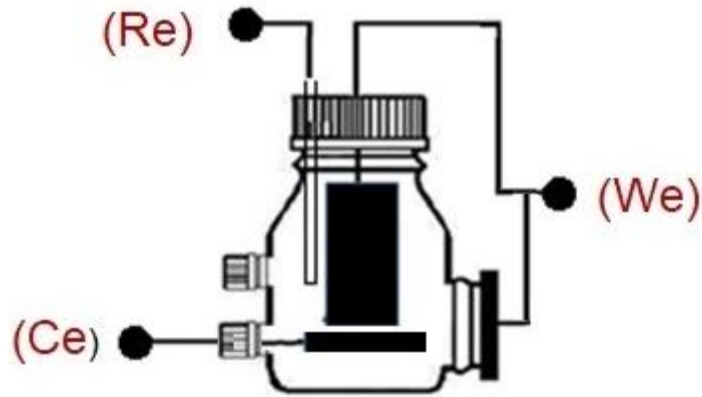


**Figure 3.4.8:** Sketch of the MFC with the additional capacitive cathode ACCMFC, with highlighted electrical connection to the galvanostat/potentiostat.

Figure 3.4.8a reports a sketch of the cell, with the additional capacitive cathode, that has been short-circuited with the airbreathing cathode and the electrical connection of the three-electrode setup that has been used to characterize the cell through pulsed discharges. The additional capacitive cathode was a carbon brush. The electrochemical performance of the ACC-MFC cell was evaluated by pulsed galvanostatic discharges. In particular, galvanostatic pulsed discharges with a current magnitude of 5, 10, 15, 20, 25, and 30 mA have been run and the electrode voltage profile, as well as the cell voltage profile, are reported in Figure 3.4.9.

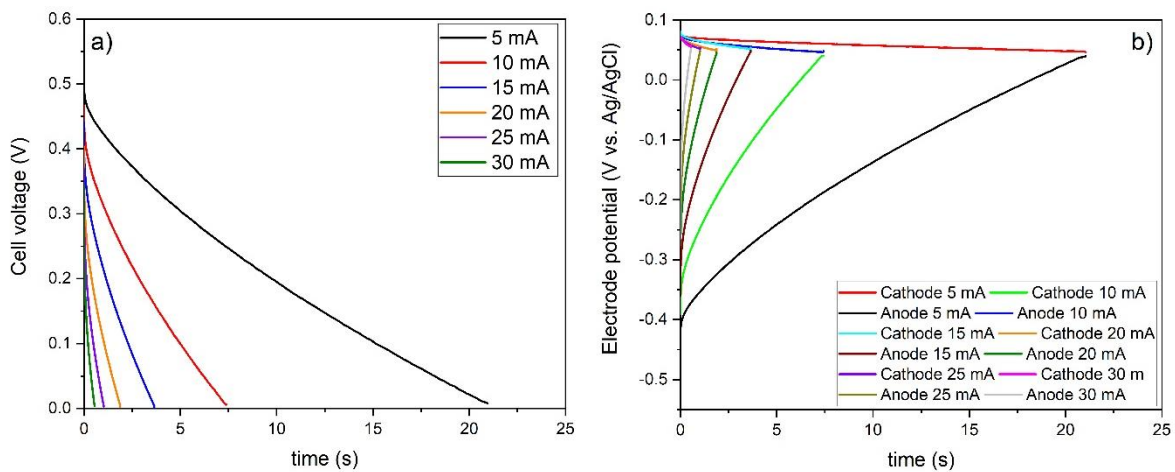


**Figure 3.4.9:** a) ACC-MFC Cell voltage profile under galvanostatic discharge, and b) single electrode voltage profiles under galvanostatic discharge at 5,10,15,20,25 and 30 mA.

The addition of the capacitive cathode has the effect of enabling pulsed discharge current one order of magnitude higher than those of the MFC (cfr. Table 1). The apparent capacitance, equivalent series resistance, energy, and power calculated with equations (3.4.1), (3.4.2), (3.4.3), and (3.4.4), respectively are reported in Table 3.4.3.

**Table 3.4.3** Apparent cell capacitance, equivalent series resistance, energy, and power of the ACC-MFC.

Pulsed current (mA)	$C_{app}$ (mF)	$R_{ESR}$ ( $\Omega$ )	Energy ( $\mu Wh$ )	Power (mW)
5	245.5	9.1	5.9	1
10	207.2	8.6	3.5	1.7
15	167.5	8.15	2.3	2.3
20	135.8	8	1.3	2.5
25	113.3	8.5	0.7	2.6
30	80	8.5	0.4	2.7

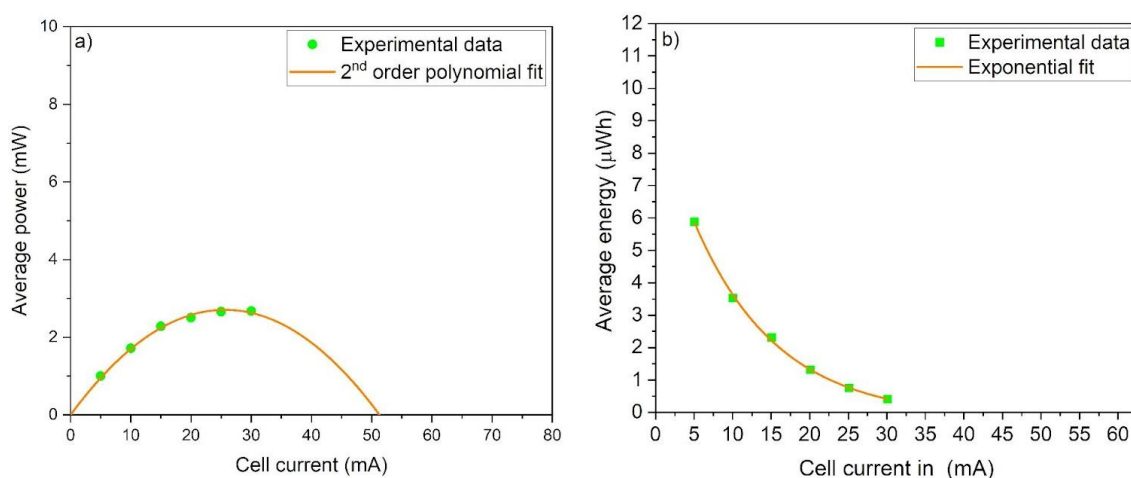
Increasing current density brings about a reduction of the apparent capacitance, that decreases from a maximum value of 245 mF to a minimum of 80 mF, from 5 mA to 30 mA. The equivalent series resistance is almost constant with a mean value of 8.47  $\pm$  0.38. Noticeably equivalent series resistance for the ACC-MFC is almost one order of magnitude smaller with respect to the one of the MFC without the additional capacitive cathode. Figure 3.4.9b reports the electrode voltage profile, at each current value measured by a 3-electrode setup, i.e. vs a reference electrode. The slope of the anode discharge curves is always greater than the one of the cathodes, which is an indication that the electrode limiting cell capacitance is the anode. From equation (3.4.1) the apparent capacitances of both anode and cathode have been calculated for each current pulse and are reported in Table 3.4.4

**Table 3.4.4** Apparent capacitance of, the anode and the cathode of the ACC-MFC.

Pulsed current (mA)	$C_{app}$ Anode (mF)	$C_{app}$ Cathode (mF)
5	267	4773
10	230	3304

15	184	2539
20	161	1966
25	134	1426
30	88	997

The apparent capacitances of both anode and cathode show a significant decreasing trend with the increase of the magnitude of the galvanostatic discharge current. The capacitance of the cathode is significantly higher with respect to the capacitance of the anode c.a. one order of magnitude. The apparent capacitance of the cathode shows a capacitance fade of 79%, while the anode features 67%. The average power and energy reported in Table 3.4.4 have been plotted in Figure 3.4.10.



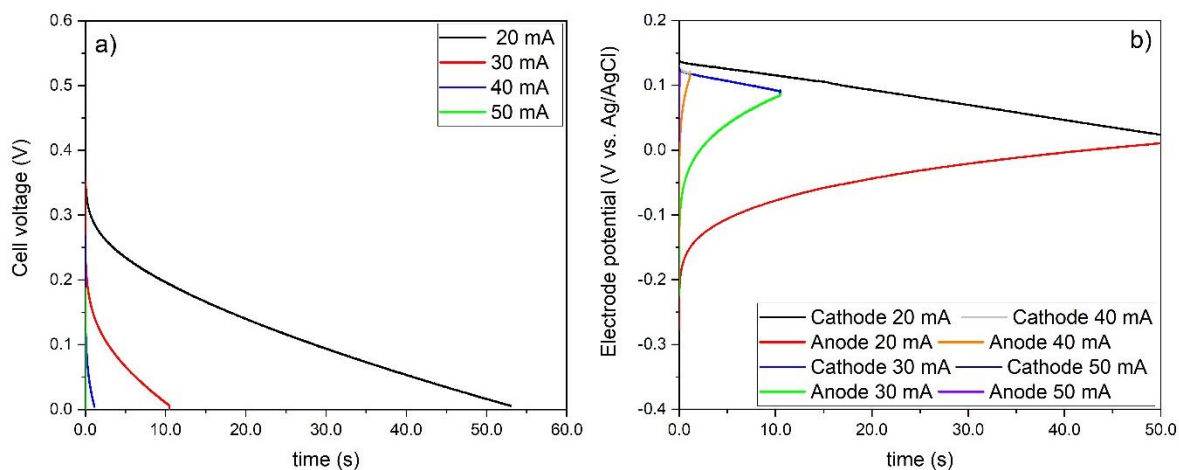
**Figure 3.4.10:** **a)** Average power of the cell (green circles) with the second-order polynomial fit extrapolated to the short circuit current (orange line), **b)** Experimental average energy of the pulsed discharge (green squares) with the interpolated first-order exponential function (orange line) of the ACC-MFC.

Figure 3.4.10 reports the trend of the average power and the average discharge energy as a function of the pulsed discharge current. Also, for the ACC-MFC, the average power is well fitted by a second-order polynomial function that predicts a maximum of the average discharge power at 25 mA with a maximum average power of 2.7 mW. The predicted short circuit current is 51 mA. The average energy, reported in Figure 3.4.10 b), decreases with the increase of the applied pulsed discharge and in this case, the experimental data are well fitted also in this case by an exponentially decaying function.

### 3.4.5 Monolithic Supercapacitive MFC (MSC-MFC)

From the measurements discussed in the previous section, it is evident that for all the tested cells, the anode was limiting cell capacitance, while the cathode mainly affected ESR. To improve the MFC capacitive performance, the anode carbon brush was decorated with the LAC2-derived activated carbon. Therefore, a microbial fuel cell featuring an additional capacitive cathode, decorated with the activated carbon LAC2, an anode decorated with the same activated carbon, has been realized and electrochemically characterized by means of pulsed galvanostatic discharges at different currents. This MFC is referred to in the latter part of the test as “Monolithic Supercapacitive MFC” (MSC-MFC). The carbon brush has been coated with an PvdF based ink, with a composition 80% (LAC2), 10 % conductive carbon additive (carbon black C65), and a 10% of PvdF in NMP. The carbon brush was coated by dipping in a suspension and drying it at first in a hoven at 80°C overnight and subsequently in a buchi oven at 120°C under vacuum, overnight. The coating procedure resulted in a mass of carbon of composite electrode of 1.2 g. After this procedure, the two electrodes featured a total mass of 226.70 mg (Cathode) and 490 mg (Anode).

The electric connections were the same as those reported in Figure 8. The additional capacitive cathode was short-circuited with the air-breathing cathode (that also featured the LAC2 carbon), and connected to the instrument at the working electrode, the anode decorated with the activated carbon was connected to the counter electrode and a reference electrode in a lugging capillary featuring a PBs 1x solution as supporting electrolyte. The cell has been therefore characterized by galvanostatic pulsed discharge at increasing current densities exploiting the same three-electrode set up and the cell voltage profile and electrode voltage profile are reported in Figure 3.4.11 a), and 11 b) respectively.



**Figure 3.4. 11:** a) cell voltage profile and b) single electrode voltage profile under galvanostatic discharge at 20,30,40 and 50 mA of the MSC-MFC.

Figure 3.4.11 a) shows that the MSC-MFC can stand extremely high current, up to 50 mA. Figure 11 b) highlights that also for this cell, the capacitance limiting electrode is the anode, as it is possible to see from the slope of the electrode discharge profile. The cathode during the discharge maintains an almost linear profile, the anode increasing the current pulses starts to bend deviating from a linear voltage profile. From the discharge voltage profiles, reported in Figure 3.4.11, apparent capacitance, equivalent series resistance, energy, and power were calculated with equations (3.4.1), (3.4.2), (3.4.3), and (3.4.4), respectively, and the results are reported in Table 3.4.5.

**Table 3.4.5** Apparent cell capacitance, equivalent series resistance, energy, and power of the MSC-MFC.

Pulsed current (mA)	$C_{app}$ (mF)	$R_{ESR}$ ( $\Omega$ )	Energy ( $\mu$ Wh)	Power (mW)
20	4264	7.9	35	1
30	2291	7.6	3.5	1.7
40	457	8.0	2.3	2.3
50	40	7.9	1.3	2.5

As observed for the previous cells, the apparent capacitance decreases with the increase of the current. The equivalent series resistance is almost constant and a mean value of 7.89  $\pm$  0.2  $\Omega$  has been measured. From the electrode voltage profile under pulsed discharge, the electrodes' apparent capacitances at the different tested currents, have been calculated and are reported in Table 3.4.6.

**Table 3.4.6** Apparent capacitance of the anode and the cathode of the MSC-MFC.

Pulsed current (mA)	$C_{app}$ Anode (mF)	$C_{app}$ Cathode (mF)
20	7692.3	8658.0
30	3275.1	8333.9
40	601.1	6655.5
50	50.3	1131.2

The capacitance of the anode constantly decreases starting from a very high value of c.a 7.6 F at 20 mA to a minimum of 50 mF at 50 mA, losing almost 99% of the initial capacitance. The cathode shows a different behavior The average discharge energy, as well as the average discharge power, have been plotted and the experimental data together with the polynomial and exponential fit are reported in Figure 3.4.12.

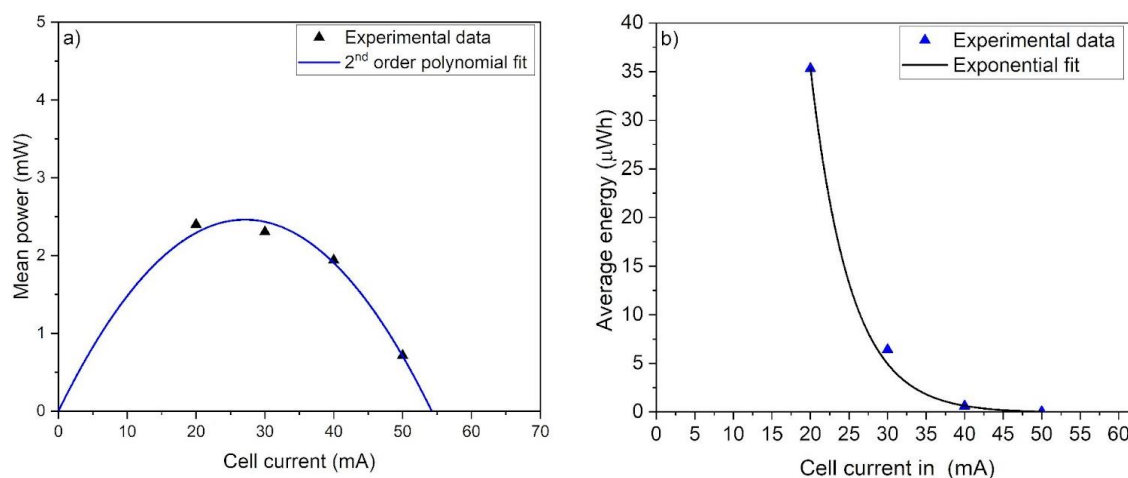


**Figure 3.4.12:** **a)** Average power of the cell (black triangles) with the second-order polynomial fit extrapolated to the short circuit current (blue line), **b)** Experimental average energy of the pulsed discharge (blue triangles) with the interpolated first-order exponential function (black line) of the MSC-MFC.

The MSC-MFC average power is well fitted by a second-order polynomial function that predicts a maximum of the average discharge power at 27 mA with a maximum average power of 2.5 mW. The predicted short circuit current is 55 mA. Interestingly, the MSC-MFC features an extremely high c energy if compared with the previous systems that are fitted by a first-order exponential decay function.

### 3.4.6 Comparison of the different strategies

In this section, a comparison of the different strategies pursued to improve the power output of microbial fuel cells is reported and discussed. At first, the power output of the different systems is compared. In Figure 3.4.13 a), the power output of the systems is reported and plotted together with the second-order polynomial interpolation.

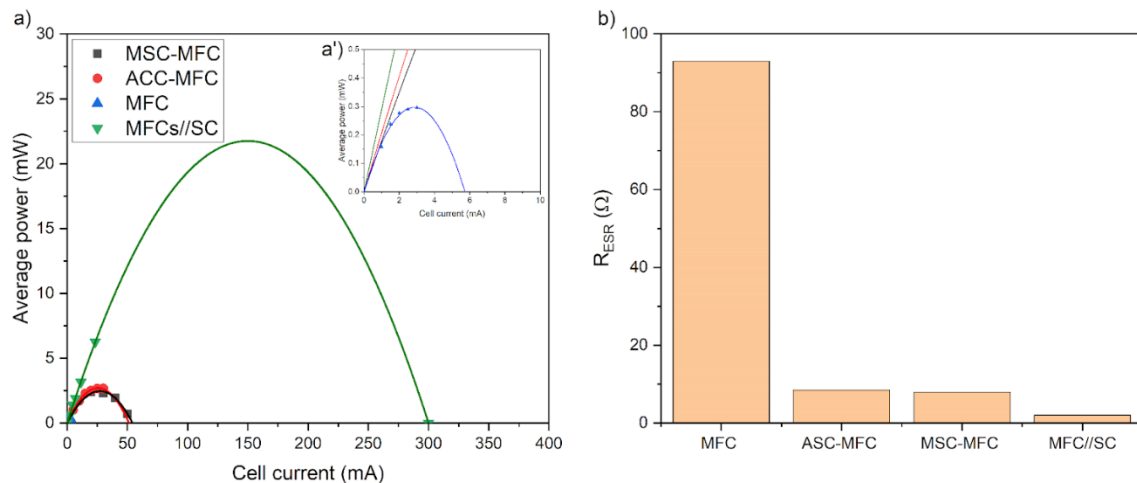


**Figure 3.4.13:** a) Comparison of the average power of the tested systems experimental values (symbols) with the second-order polynomial fit extrapolated to the short circuit current (lines), a') magnification of the average power of the MFCs, b) Equivalent series resistance measured for the tested systems.

From figure 13a), it is evident that the MFCs//SC configuration allows impressive power densities, compared with the single MFC (Figure 3.4.13 a) magnification a'). The introduction of the supercapacitive features into the MFC strongly improves the power output with respect to the MFC alone. Interestingly, the curve of the ACC-MFC and the one of the MSC-MFC almost overlap. The MFC//SC featured a predicted maximum power of 20 mW at a maximum current of 150 mA, the ASC-MFC, featured a maximum power of 2.7 mW at 2.5 mA, which is similar to that of the MSC-MFC that featured a maximum power of 2.5 mW at 27 mA, finally, the MFC featured a maximum power of 0.29 mW at a current of 3 mA. This trend is extremely similar to the one of the equivalent series resistances, reported in Figure 3.4.13 b), i.e. the system with the lowest equivalent series resistance is the one that features the maximum power among the other, namely MFC//SC, followed by the ACC-MFC and MSC-MFC that feature comparable values of internal resistance, followed by the MFC that has the highest internal resistance and the lowest average power. Moreover, the internal resistance is related to the short circuit current, and therefore the system with the lowest internal resistance is also the one capable of reaching higher current pulses. The relation between the internal resistance and the maximum power is highlighted by the comparison of Figures 3.4.13 a) and 3.4.13 b). The



highest power is achieved at the lowest  $R_{ESR}$ . Indeed, the MFC//SC system features the lowest  $R_{ESR}$  of  $2 \Omega$ , which is 1/5 than that of the other systems (MFC-AAC, MSC-MFC), with a maximum power of 20 mW that is 10 times the one of the MFC-AAC and MSC-MFC, c.a. 2 mW. Indeed in Section 3.1, it is highlighted that at high current pulses, in the MFC//SC, the power response is dominated by the EDLC, since the MFC works at currents magnitude which is considerably higher than their short circuit one. However, a deeper analysis that includes the evaluation of the energy delivered under galvanostatic discharge, brings about a different rating of the performance of the different systems.

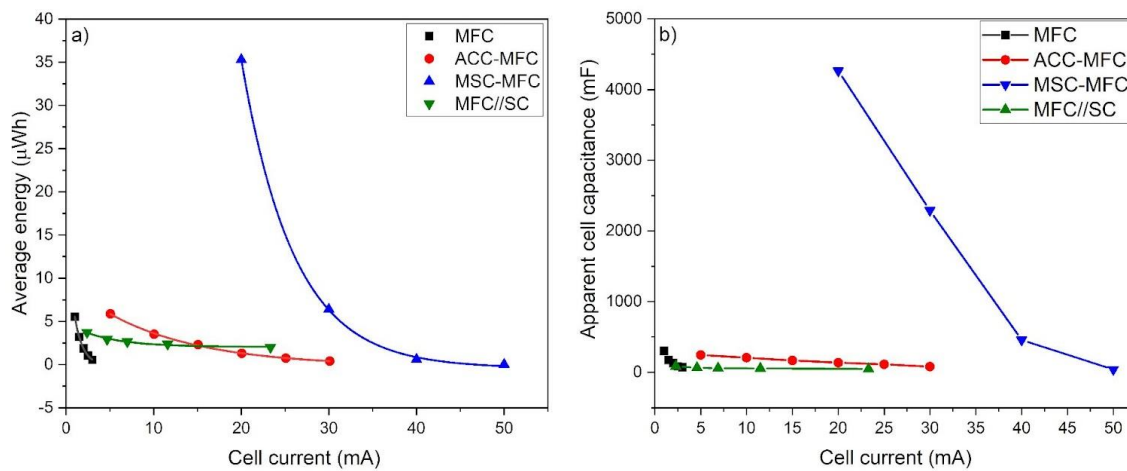


**Figure 3.4.14:** a) average discharge energy and b) apparent capacitance of the studied systems

Figure 3.4.14 a), reports the average discharge energy as a function of the pulsed current. For all the tested cells, the average energy decreases, increasing the applied current pulse and decays following a first-order exponential function. The average energy of MSC-MFC at its lower tested current, 20 mA, is considerably higher than that of the other tested cell and is 35  $\mu Wh$ , followed by the ACC-MFC with the maximum of the measured energy at 5.9  $\mu Wh$  at 5 mA, the MFC with a maximum of the average energy at 1 mA, 6.4  $\mu Wh$  and finally the MFC//SC with a maximum of the average energy of 3.8  $\mu Wh$  at 1 mA. Overall, the MSC-MFC overwhelms the other cells in terms of average energies delivering higher values at considerably higher current. The energy retention of the MFC//SC on the other hand is considerably higher than that of the other tested cells, this is likely related to the fact that the EDLC is dominating the response of the MFC//SC at higher current pulses. Figure 3.4.14 b), reports the trend of the apparent capacitance of the tested cell as a function of the applied current pulses, interestingly, this trend is similar to one of the average discharge energies. Indeed, the MSC-MFC shows a higher apparent capacitance value if compared to the other

cells, at each tested current. This, in turn, reflects the fact that the cell performances are limited by the anode, and the MSC-MFC is the only setup capable to improve the anode apparent capacitance, as highlighted by Figure 3.4.15.

### **3.4.6 Conclusion:**

In this section different methods to improve MFCs' power output have been studied, compared, and discussed. The first strategy that has been followed is the integration with an external green supercapacitor. This represents advancement with respect to the work reported in section 3.1 since a green supercapacitor instead of a commercial one has been exploited and it follows the results of the work reported in section 3.2 since the LAC2 carbon has been used as the main EDLC's electrode component. The electrochemical characterization of the AaSC reported in Section 3.3, briefly, the EDLC featured lignin-derived biochar (LAC2), calcium alginate binder, and a 1.5 M  $\text{Ca}(\text{NO}_3)_2$  solution as electrolyte. The integration with the MFCs, that is the MFC//SC system featured the higher discharge power, likely since the AaSC dominates the response of the system at high-rate capability, and it features extremely small  $R_{\text{ESR}}$ . The second strategy that has been investigated in this work is the exploitation of an additional supercapacitive cathode. Specifically, an additional carbon brush, shortcircuited to the airbreathing cathode of the MFC was used. In this strategy, the ACC-MFC featured output power considerably higher than those of the MFCs.

### **Conclusion:**

In our previous work, we demonstrated the synergic effect of the coupling of MFC with external supercapacitors. Our main finding was the observation of a synergic effect in the integration of MFC with SC at a system level. The MFC allows the recharge of the SC that in turn can deliver the energy accumulated by the MFC at higher power that the bare MFC wouldn't be able to stand. At the same time, at low current pulses, the MFC allows an increase of the apparent capacitance of the SC. In this work to further push the concept of process and component sustainability on this system integration, we design carbon-based EDLCs that exploit only aqueous processable components and aqueous electrolytes.

### Chapter 3 references:

- [1] Bigoni, F., et al., "Sodium alginate: a water-processable binder in high-voltage cathode formulations.", *Journal of the Electrochemical Society*, 164.1, (2016), A6171.
- [2] Qin, Y., Jiang, J., Zhao, L., Zhang, J., and Wang, F., Applications of alginate as a functional food ingredient., *Biopolymers for food design*, (2018),(pp. 409-429). Academic Press.
- [3] Lee, P., and Rogers, M. A., "Effect of calcium source and exposure-time on basic caviar spherification using sodium alginate.", *International Journal of Gastronomy and Food Science*, 1.2 ,(2012), 96-100.
- [4] Luo, H., et al., "Supercapacitive behavior of mesoporous carbon CMK-3 in calcium nitrate aqueous electrolyte.", *Korean Journal of Chemical Engineering*, 31.4, (2014), 712-718.
- [5] Mutuma, B. K., et al., "Valorization of biodigestor plant waste in electrodes for supercapacitors and microbial fuel cells." *Electrochimica Acta*, 391, (2021), 138960.
- [6] Dura, H., et al., "Cost analysis of supercapacitor cell production.", *2013 international conference on clean electrical power*, (2013), (ICCEP). IEEE,.
- [7] Kötz, R., and Carlen, M. J. E. A., "Principles and applications of electrochemical capacitors.", *Electrochimica acta*, 45.15-16, (2000), 2483-2498.
- [8] Conway, B., E., *Electrochemical supercapacitors: scientific fundamentals and technological applications.*, Springer Science & Business Media, 2013.
- [9] Pandolfo, A. G., and Hollenkamp A.F., "Carbon properties and their role in supercapacitors.", *Journal of power sources*, 157.1, (2006), 11-27.
- [10] Yoo, H.D.; Jang, J.H.; Ryu, J.H.; Park, Y.; Oh, S.M., Impedance analysis of porous carbon electrodes to predict rate capability of electric double-layer capacitors., *J. Power Sources*, (2014), 267, 411–420.
- [11] Spina, G. E., et al., "Natural Polymers for Green Supercapacitors." *Energies*,13.12,(2020), 3115.
- [12] Poli, F., et al., "Pullulan-ionic liquid-based supercapacitor: A novel, smart combination of components for an easy-to-dispose device.", *Electrochimica Acta*, 338, (2020), 135872.
- [13] Poli, F., et al., "Boosting microbial fuel cell performance by combining with an external supercapacitor: an electrochemical study.", *ChemElectroChem*, 7.4, (2020), 893-903.
- [14] Santoro, C., et al., "Self-powered supercapacitive microbial fuel cell: the ultimate way of boosting and harvesting power.", *Biosensors and Bioelectronics*, 78, (2016), 229-235.

# Chapter 4: Getting insight into the electrode/electrolyte interface

In section 3.4, the resistive and capacitive behavior of bioanodes were reported, discussed, and finally exploited to design green supercapacitive systems. To get further insight into the bioanode/electrolyte interface electrochemical and electronic properties, I carried out electrochemical impedance spectroscopy (EIS) study of carbon paper electrodes in a real wastewater environment. The aim was to follow the “in vivo” evolution of the electrochemical response of the bioanode during the electrode colonization. The results of this study, reported in Section 4.1, highlighted that both the capacitive and resistive responses of the biofilm change during colonization. Notably, EIS suggested a decrease in the electronic resistance of the bioanode that could be ascribed to the increase of both ionic and electron conductivity of bacteria grown on carbon paper. However, EIS does not permit clear discrimination between ionic versus electronic contributions to the overall electrode impedance. One powerful approach that enables discriminating ionic and electronic contributions is to investigate materials by an ion-gate transistor (IGT) setup. Indeed, IGTs are considered for fundamental studies on metal-insulator transitions in different classes of materials, from inorganic and organic compounds, and also to monitor the electrical response of cellular interface not only in vitro but also in vivo [1,2]. With the aim of being trained in a such fascinating approach, I spent a period at the University of Montreal, in the groups led by Prof. C. Santato and F. Cicoira, recognized worldwide for their expertise in Ion Gated Transistors (IGTs) and organic electronics. The idea was to learn the fundamentals of IGTs and to transfer the acquired knowledge to the field of electrochemical energy storage and bioelectrochemistry. Unfortunately, due to the pandemic emergency, I was not able to exploit IGT for the study of the bioanodes, and my main work on IGT focused on more conventional, but no less important materials, namely the lithium-ion insertion cathodes used in lithium-ion batteries. The results of this study are reported in Section 4.2. Hence, in this Chapter two different systems have been investigated, leveraging on two different experimental techniques. The idea behind the adopted

methodology was to exploit a more consolidated technique. like EIS, for a complex system like the MFC bioanodes, and, vice versa, a novel technique, like IGT, for a more consolidated system, like commercial cathodes of lithium-ion batteries. Indeed, EIS is a traditional technique used to investigate the phenomena that occur on different scales of time at an electrode-electrolyte interface. IGT configuration has been here exploited for the first time to investigate the electronic properties of lithium-ion batteries material during lithium intercalation/deintercalation processes.

#### **4.1 Electrochemical Investigation of the biofilm growth**

This activity aims to get insight into the electrochemical features of the biofilm formed in MFC anodes. Specifically, in this section, the experimental results of the investigation of the electrochemical interface that is developed during the bacterial colonization of carbonaceous electrodes are reported and discussed. The electrolyte exploited for this study was a 50% in volume of sludge, the effluent of a biodigester of agricultural waste aimed at carrying the bacteria for the anode colonization, and a 50% phosphate buffer saline 1x i), (Oxid). In microbial fuel cells, the biofilm developed by the bacterial colony on the anode is responsible for the electrocatalytic oxidation of the organic substances that microbial fuel cells exploit as the main component of the fuel. Biofilm growth monitoring has several applications, from prevention of biocorrosion, bacterial contamination in industrial processes, and biofouling [3,4]. Indeed, it is known that the bacterial colonies are arranged to form biofilms, a syntrophic consortium of microorganism in which the microbial cells are embedded into an extracellular matrix that feature an extremely complex chemical environment in which protein, genetic material, and redox mediator are presents [5]. Due to this plethora of chemical substances but also to the reported ability of bacteria to allow direct electron transfer [6], biofilm growth can be studied employing electrochemical methods, due to the rapidity and the fact that exploit small voltage perturbation, electrochemical impedance spectroscopy is arising as a method capable to monitor biofilm growth [7]. Variation of the double-layer capacitance of Pt disc, measured by electrochemical impedance spectroscopy, has been correlated with biofilm growth [8]. A three-electrode electrochemical cell has been exploited for this study featuring one carbon paper electrode, one Pt wire, and an SCE reference electrode. This section is articulated in three main subsections, a first one in which the electrochemical data obtained

before the colonization are discussed, a second one in which the colonization data are reported and a third one in which the data after the colonization are discussed.

#### 4.1.1 Carbon paper before the colonization

Immediately after the cell was assembled, electrochemical impedance spectroscopy of the carbon paper electrode was carried out with three electrodes set up in which the carbon paper was the working electrode, Pt wire as counter, and SCE as the reference electrode. The resulting Nyquist diagram is reported in Figure 4.1.1 together with the equivalent circuit that has been exploited to fit the resulting impedance.

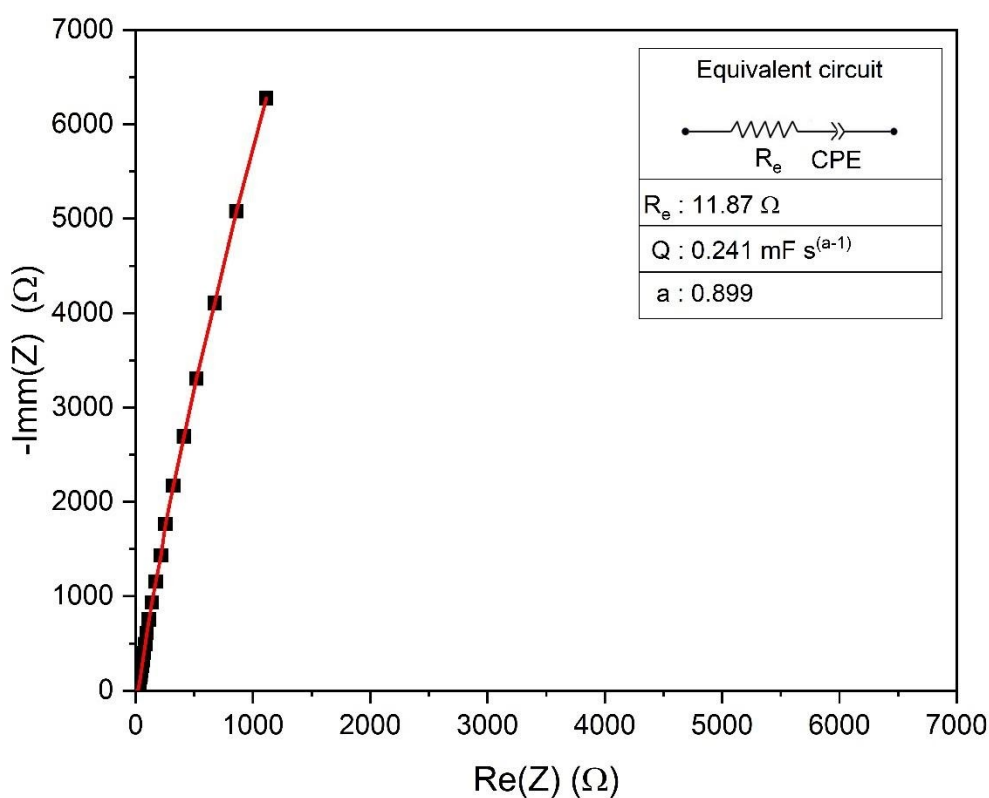


**Figure 4.1.1:** Nyquist diagram of the carbon paper electrode before the colonization, dotted is the experimental measurement, while the continuous red line represents the spline interpolation of the point calculated with the circuitual model reported in the figure upper right side.

The proposed circuitual model assumes that the response of the electrode is assimilable to a single series resistance in series with a CPE element. The resistor  $R_e$ , represents all the uncompensated resistance, and includes electrolyte ionic resistance, electrode electronic resistance, and is affected by the distance between the working and the reference electrode.  $e$  (CPE element, represents the formation of the electrical double layer and takes into account the

deviation with respect to an ideal capacitor. For an ideal capacitor, the Nyquist diagram would be a straight line, perpendicular to the real axis. For a real capacitor, the slope of the capacitive line is lower than  $90^\circ$  [9,10]. In practice, the CPE element is extremely exploited in electrochemical impedance fitting. The impedance of the CPE element is given in equation (4.1.1)

$$Z_{CPE}(\omega) = \frac{1}{(Q\omega)^\alpha} \quad (4.1.1)$$

Where  $Q \left(\frac{F}{s^{\alpha-1}}\right)$  represent the non-ideal double-layer capacitance, and  $\alpha$  represents the deviation of the CPE from a pure capacitance. This latter parameter is related to capacitance changes with the frequency, and for this reason, it was initially referred as “capacitive dispersion” or “frequency dispersion of capacitance”. Nowadays, it is widely accepted that these terms originate from current and potential distributions at the electrode due to interface inhomogeneities. Indeed, CPE has been attributed to surface disordered and roughness, and electrode porosity [9]. The model reported in Figure 1 was initially proposed by [9] to represent an electrode in which no faradaic contribution other than the formation of the electrical double layer at the interface between the electrode and the current collector.

To investigate the performance of the studied electrode, as the anode of a microbial fuel cell, before the colonization, cyclic voltammtries in three electrodes set up were performed. In particular, the carbon paper electrode was working, the platinum counter, and the reference the SCE. The resulting voltammogram is reported in Figure 4.1.2.

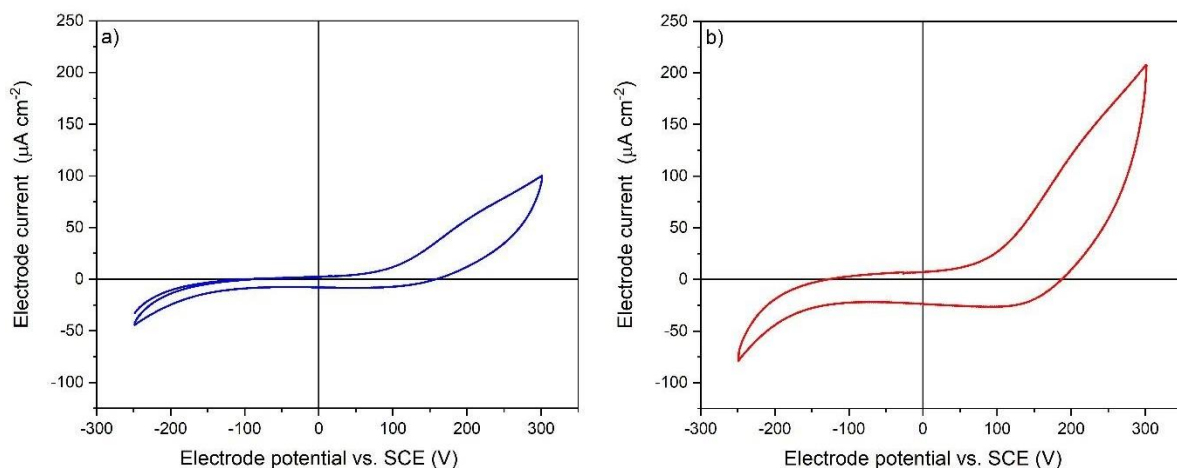


**Figure 4.1.2:** Cyclic voltammogram at **a)**  $5 \text{ mVs}^{-1}$  and **b)**  $20 \text{ mV s}^{-1}$  between 250 mV and 300 mV vs. SCE.

Figure 4.1.2 reports the cyclic voltammogram run with the three-electrode set up between a positive vertex potential of 300 mV vs. SCE and a negative one of -250 mV vs. SCE at 5 mVs<sup>-1</sup> a) and b) 20 mV s<sup>-1</sup>. This CV electrode potential range is the typical MFC anode operating potential. Both voltammograms share a similar shape, in particular, two onset potentials of irreversible oxidation and a reduction reaction are evident. At 5 mVs<sup>-1</sup> the oxidation reaction potential is at 71 mV vs. SCE and a reduction one at -130 mV vs. SCE. At 20 mVs<sup>-1</sup> the oxidation current increases and the oxidation onset potential becomes more evident around 80 mV vs. SCE, similarly the reduction one at -150 mV vs. SCE. The anodic wave has to be related to the oxidation of the organic molecules present in the sludge solution, including the acetate salt. The cathodic signal corresponds to H<sub>2</sub> evolutions by proton reduction. To investigate the effect of the growth of the biofilm on the electrochemical response of the carbon paper, electrochemical impedance spectroscopy measurements have been run at fixed intervals of time, and the results are reported and discussed in the next subsection.

#### 4.1.2 Carbon paper colonization

Electrochemical impedance spectroscopy measurements each hour have been run with a three-electrode set up to investigate the effect of the colonization. The electrochemical impedance spectroscopy measurements have been run each hour for 130 hours with a perturbation amplitude of 5 mV from a high frequency of 100 kHz to a low frequency of 100 mHz. The resulting Nyquist plot is reported in Figure 4.1.3.

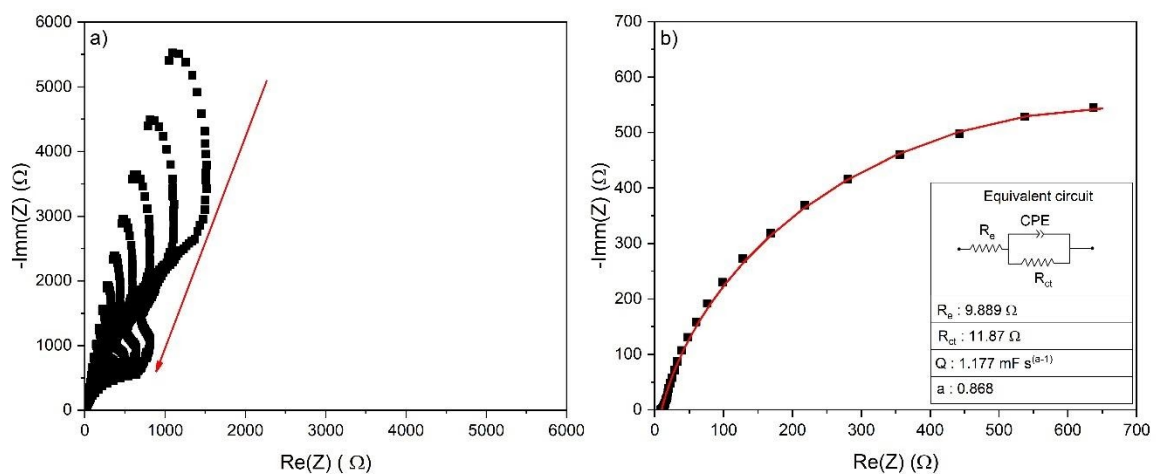




**Figure 4.1.3: a)** Complete set of data of the colonization process in the form of Nyquist plot, the red arrow indicates the evolution of the impedance **b)** final impedance together with the equivalent circuit model exploited to fit the Nyquist spectrum

Figure 4.1.3 a) reports the experimental Nyquist plots, the equivalent circuit model that has been used to fit the experimental, and the predicted Nyquist plot of the equivalent circuit. During the experiment, the Nyquist diagram of the electrode shows a significant evolution highlighted by the red arrow in Figure 4.1.3 a). Indeed, during the 130 h of the experiment, there is a strong reduction of the impedance, accompanied by a drastic change in the shape of the Nyquist diagram. For this reason, a different circuit model to fit the Nyquist plot associated with this impedance is reported in Figure 4.1.3 b), and the second branch of the equivalent circuit starts to appear. The proposed Nyquist plot features a two-branch circuit in which the first resistance  $R_e$  represents the uncompensated resistance (mainly affected by ohmic terms),  $R_{ct}$  represents the charge transfer resistance and is characteristic of a chemical reaction, and CPE represents the double layer capacitance in parallel with  $R_{ct}$ . Brug et al [10], proposed a simple model to explain the CPE behaviour based on the idea of a double layer capacity distribution along the interface caused by surface inhomogeneity. Therefore, they suggested relating the double layer capacitance  $C_0$  to the parameter of the circuit reported in Figure 4.1.3

$$C_0 = \left( Q \left( \frac{1}{R_e} + \frac{1}{R_{ct}} \right)^{\alpha-1} \right)^{1/\alpha} \quad (4.1.2)$$

The capacitance of the system without the faradaic contribution,  $t$  can be evaluated by the previous equation by taking the limit of  $R_{ct} \rightarrow \infty$  in equation (4.1.2).

$$C_0 = \left( Q \left( \frac{1}{R_e} + \frac{1}{R_{ct}} \right)^{\alpha-1} \right)^{1/\alpha} = \left( Q \left( \frac{1}{R_e} \right)^{\alpha-1} \right)^{\frac{1}{\alpha}} \quad (4.1.3)$$

This limit applied to the circuit reported in Figure 4.1.1 is equivalent to the transformation of the branch of  $R_{ct}$  in an open circuit and therefore in the equivalent circuit reported in Figure 4.1.2.

It is worth mentioning that an important idea arises from the work of Brug [10], which is that the CPE element can couple both Faradaic terms as well as electrical double layer ones [9]. Therefore, the quantity  $C_0$  doesn't take into account only the double layer capacitance but also the faradaic contribution, as highlighted by the presence of the  $R_{ct}$  terms in the equation.

To investigate the carbon paper colonization, the evolution of the faradic  $C_0$  has been followed as a variation percentage according to equation 4.

$$\Delta C_0 = \frac{C_0(t) - C_0(t_0)}{C_0(t_0)} \cdot 100 \quad (4.1.4)$$

where  $C_0(t)$  is the capacitance of the circuit reported in Figure 4.1.3, calculated at the time (t) of the experiment and  $C_0(t_0)$  is the initial one.  $C_0(t_0)$  is the capacitance of the carbon paper before colonization that, as reported in Section 4.1.1, corresponds to the capacitance of the carbon paper in absence of faradaic reactions. The evolution of the two parameters  $R_e$  and  $R_{ct}$  has been also investigated over time and the results are reported in Figure 4.1.4

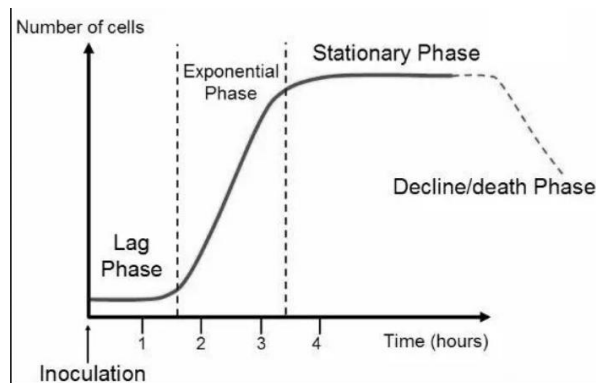
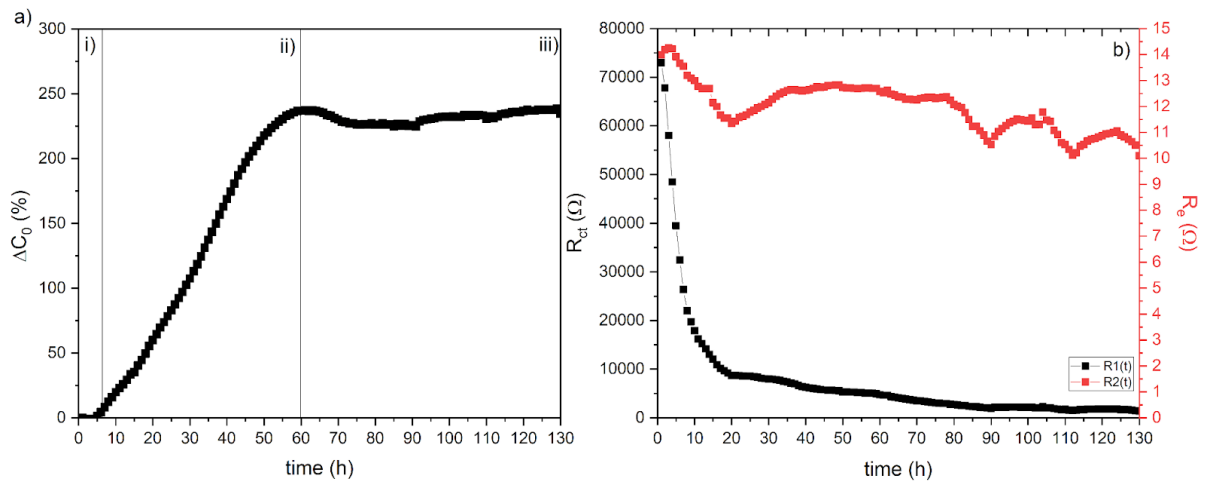


**Figure 4.1.4:** Trends of **a)** the variation percentage of  $C_0$ , **b)**  $R_e$  and  $R_{ct}$  over the colonization time, and **c)** example of a bacterial growth curve, as cell number vs. time.

Figure 4.1.4 reports the trend of  $\Delta C_0\%$  as of time. In the plot, it is possible to see three different zones: a first one that lasted 7 h, in which the capacitance doesn't change, a second one in which almost exponential growth is present that lasted from the 7<sup>th</sup> hour to the 62<sup>nd</sup> when a sudden slow of the growth of the double-layer capacitance occurs. This 3-phase plot strongly resembles the kinetics of bacterial growth (bacterial growth curve) that is reported in Figure 4.1.4 c) as an example. Indeed, the plot in Figure 4.1.4 c) is composed of three phases, i) the "lag phase", in which the colony doesn't grow because microorganisms are adapting themselves to the new environment. This phase is followed by ii) the log phase, the logarithmic phase, (sometimes called the exponential phase), which is a period characterized by cell doubling, in a large number of cells, into a logarithmic or exponential growth in time. The cell doubling cannot continue indefinitely since the medium is soon depleted of nutrients and enriched in colonial waste. Therefore, the log phase is followed by iii) the stationary phase, which is the condition in which the number of new cells is equal to the number of dead cells [9]. Interestingly it is possible to recognize these three-growth phases in the evolution of the capacitance reported in Figure 4.1.4 a). Figure 4.1.4 b), reports the trend of both the uncompensated resistance of the electrode and the charge transfer resistance. The charge transfer resistance decreases from an initial value of 73  $k\Omega$  to a final value of 1340  $\Omega$ , highlighting the fact that during the colony development the kinetics of the electrooxidation processes driven by the bacteria is enhanced.  $R_e$ , on the other hand, shows a small decrease from a maximum value of 13  $\Omega$  to a minimum one of 10  $\Omega$ . The constant decrease of the charge transfer resistance may indicate the fact that the development of the colony is accompanied by the improved ability of the electrode to catalyze reaction at the interface with the electrolyte often referred to as the ability of biofilm to run direct electron transfer with the electrolyte. The constant reduction of  $R_e$  deserves much attention. Indeed, it would have been expected that the growth of the biofilm would have partially insulated the carbon paper surface from the electrolyte solution and decreased the electrical connection between the carbon paper fibers, with a consequent increase of  $R_e$ . The unexpected decrease of  $R_e$ , therefore, suggests that the biofilm is not insulating, but that features an inherent electronic conductivity and good permeability to electrolyte ions. On the other hand, the evaluation of the electron conduction properties of the biofilm is extremely challenging. It has been reported [13,14] that biofilm can feature an inherent electronic conductivity that is required to set the electrochemical oxidation

of the nutrients. It is worth stressing that, with a traditional setup, like EIS, it is not possible to discriminate between the electronic resistance and the ionic one, in the high-frequency region of the signal. Nowadays, it is widely accepted that biofilm features a capacitive behavior that can be biofilm capacitance is evaluated in terms of CPE capacitance, and geometrical argumentation is carried out [8]. The model proposed by [9], proposes that different contributions other than the simple geometrical one, such as the improvement of charge transfer and ionic conductivity but also the capacitance dispersion, may play a role. Indeed, as highlighted by equation 4.1.2 decreasing in  $R_e$  and  $R_{ct}$  lead to an increase of  $C_0$ . The activation of the oxidative processes by the biofilm growth on the carbon paper was proven by cyclic voltammetry tests that were carried out after the colonization, The resulting voltammograms are reported in Figure 5. Figure 4.1.5 a) and 4.1.5 b) reports the CVs after the colonization at  $5\text{mVs}^{-1}$  and at  $20\text{mVs}^{-1}$ . Interestingly the oxidation onset potential has shifted to less positive values with respect to what was observed with the bare carbon paper. Indeed, they moved to c.a.  $0\text{mV}$  vs. SCE and at c.a.  $-50\text{mV}$  vs. SCE at  $5\text{mVs}^{-1}$ . The comparison of Figure 4.1.5 and Figure 4.1.2 shows that the oxidation overpotential is reduced by ca.  $250\text{mV}$ , therefore demonstrating the bio-electrocatalytic properties of the biofilm.

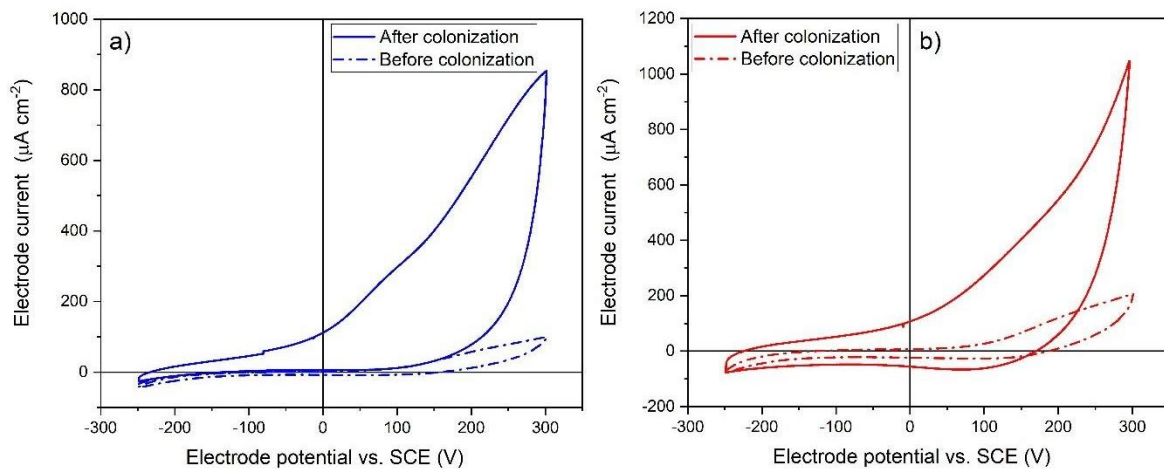


**Figure 4.1.5 a)** cyclic voltammogram at **a)**  $5\text{mVs}^{-1}$  and **b)**  $20\text{mVs}^{-1}$  between  $250\text{mV}$  and  $300\text{mV}$  vs. SCE.

### 4.1.3 Conclusion

To conclude this section, electrochemical impedance spectroscopy is a powerful technique capable of investigating the evolution of the interface properties also in presence of bacterial growth. Moreover, electrochemical impedance spectroscopy has been proved to be a powerful technique, capable to follow the evolution of the impedance of the biofilm. Highlighting that

during the colonization process, a reduction of the impedance occurs, consisting of a reduction in the high-frequency resistance together with an increase of the double-layer capacitance. To get further insight, namely, to discriminate the electronic conductivity reduction from the ionic one, a valuable experimental approach that could be exploited is the Ion Gated Transistor (IGT) set up. The application of this novel technique to a more consolidated system such as Lithium-ion batteries high voltage cathodes has been reported and discussed in the following section.

## **4.2 Investigation of the electronic properties of lithium-ion battery materials through ion-gated transistors**

The previous section highlighted the importance of monitoring the electronic properties of electrode materials under operation. One of the most interesting approaches that enable an in-operando evaluation of the electronic conductivity of materials is exploited in ion-tronics and consists of the well-known ion-gated transistor (IGT) setup. With aim of learning and exploiting this approach for electrochemical energy storage/conversion materials, I had the opportunity to be hosted in the groups led by Prof. Clara Santato and Prof. Fabio Cicoira at Ecolè Polytechnique du Montréal, who are worldwide recognized for their achievements in ion-tronics and organic electronics. The idea was that of proving at first the use of IGT on well-established commercial electrode materials, like ion-insertion cathodes of lithium-ion batteries, and then, to prove the method on novel electrodes, including bio-anodes. Unfortunately, due to the COVID-19 pandemic situation, only the first set of experiments on commercial materials was carried out and the results are reported in this section. I am planning to conclude the planned work in the near future, by a second internship at Polytechnique, possibly in the first months of 2022, even under the collaborative projects, namely (OAK RIDGE NATIONAL LABORATORY/CENTER FOR NANOPHASE MATERIALS SCIENCESPROJECT, Subvention de projets de recherche IE/Appel à projets 2020) Therefore, this section reports the results and the experimental details of the exploitation of Ion Gated Transistors (IGTs) as novel techniques to investigate the evolution of the electronic transport properties of lithium-ion high voltage cathode materials in situ, i.e., during the lithium-ion intercalation/de-intercalation. Specifically,  $\text{LiNi}_x\text{Mn}_y\text{O}_2$  (LNMO) and  $\text{LiNi}_{0.5}\text{Mn}_{0.3}\text{Co}_{0.2}\text{O}_2$  (NMC532) composite electrodes with and without carbon additives, are investigated. The present section is articulated in the first part in which the electronic properties of Lithium transition Metal Oxide-based materials ( $\text{LiMO}_x$ ) are introduced and discussed, further ion

gated transistors are introduced and finally, a detailed description of the device assembled and exploited together with experimental detail is reported.

#### 4.2.1 *Electronic properties of LiMO<sub>x</sub>*

Electronic properties of Lithium transition Metal Oxide-based materials (LiMO<sub>x</sub>) play a critical role in modern lithium-ion batteries, in real electrodes ionic and electronic processes occur at the same time affecting the cell response in a different manner [15,16]. Low ionic conductivity translates into low effects on lithium transport rate in the insertion host, and, hence, rate capability of the electrode. Low electronic conductivity can negatively affect the gravimetric capacity of the electrode. Indeed, electrodes featuring a poor electronic percolation network may lead some active material crystallites to be electronically insulated. These portions of the active material, since disconnected from the electrode during polarization, behave as dead weight, taking down the gravimetric performances of the electrode (e.g., specific capacity). This is why typically composite electrodes featuring carbon additives are used. In turn, a similar situation may arise during aging or damaging of the contact between the current collector and the electrode. In addition, both ionic and electronic resistances of the electrodes affect the internal resistance (ESR) of the cell.

Electronic transport properties of pure LiMO<sub>x</sub>, is usually measured through AC methods such as electrochemical impedance spectroscopy (EIS), under ion blocking condition, which is the exploitation of a completely anhydrous environment with the inert current collector, like gold, platinum, or stainless-steel [17,18]. Another method that has been widely exploited is four-point probe measurement [19]. For the EIS-based methods, the samples under investigation are polished and silver-painted pure LiMO<sub>x</sub> pellets, on which EIS measurements at different temperatures are run with ion blocking electrodes. The resulting Nyquist diagrams at different temperatures are therefore fitted over an equivalent circuit. As an example, *Amir R.* and co-workers investigated the variation of the electronic conductivity of NMC based pellets at different degrees of lithiation/delithiation. The authors prepared different pellets lithiated galvanostatically by GCPL at a different time in a Swagelok cell with a lithium counter. As an example, the methodology followed by the authors is reported in Figure 4.2.1.

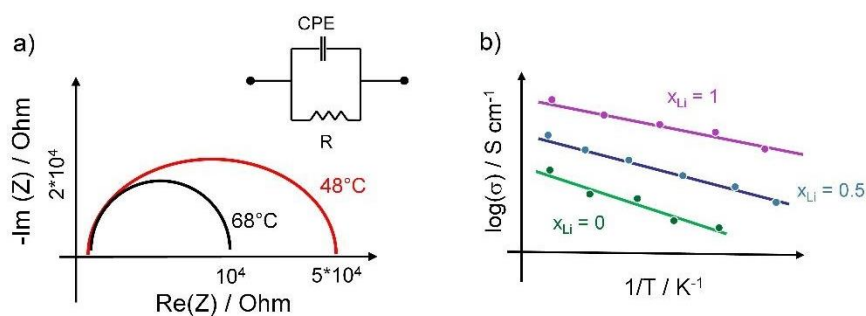


**Figure 4.2.1:** a) representation of the Nyquist diagram obtained in the work of [16] with the equivalent circuit exploited to fit it, b) Arrhenius plot of the conductivity of the different tested samples

The authors concluded that the electronic conductivity of NMC increases monotonically with the degree of de-lithiation, showing a thermally activating behavior with activation energy in the order of 0.42 eV. Moreover, the authors were able to relate the variation of the electronic conductivity to the  $\text{Ni}^{3+}/\text{Ni}^{4+}$  multivalency and the  $\text{Co}^{3+}/\text{Co}^{4+}$  [16]. Figure 4.2.1 reports a general methodology that has been also applied to investigate the electronic conductivity of LNMO cathode material, and how this is affected by crystal lattice parameters. The authors concluded in this study that the ordered disordered spinel structures featured a thermally activated behavior with different activation energy 0.45 eV for the fully ordered vs. 0.32 eV for the disordered one. Moreover, the authors concluded that the increased degree of disorder, related to the increased content of the  $\text{Mn}^{3+}$  cation increases the electronic conductivity [18]. These experiments highlight the relation between the electronic conductivity of pure  $\text{LiMOx}$  based materials to the electronic valence state of the metallic cation and to the crystal lattice parameters (which in turn will affect the electronic bandgap of the resulting material). EIS measurements on composite electrodes in the electrolytic solution, i.e. by not blocking electrodes, are not reliable in discriminating between the ionic and the electronic contribution. Indeed, the high-frequency signal part of the EIS signal contains both the electronic transport, together with the bulk ionic contribution, and the other ohmic part of the circuit that connects the instrument to the electrode. Therefore, novel techniques capable of investigating the electronic transport of lithium-ion batteries electrodes are needed.

In this context, IGTs are extremely attractive, since, in this transistor configuration, electrolytes are a fundamental component of the gate and may be exploited to investigate material used for electrochemical energy storage. In the following subsection, the ion gated transistors are introduced and briefly discussed.

#### 4.2.2 Ion Gated transistors (IGTs)

IGTs are a relatively novel technology and underpin the development of ion-tronics [18]. The main difference with respect to the traditional field-effect transistor is the electrolyte in replace of the dielectric that acts as a gate with a high mobility ionic medium. A sketch of an IGT is reported in Figure4.2.2. In Which the Gate, Drain, electrolyte, and source are highlighted.

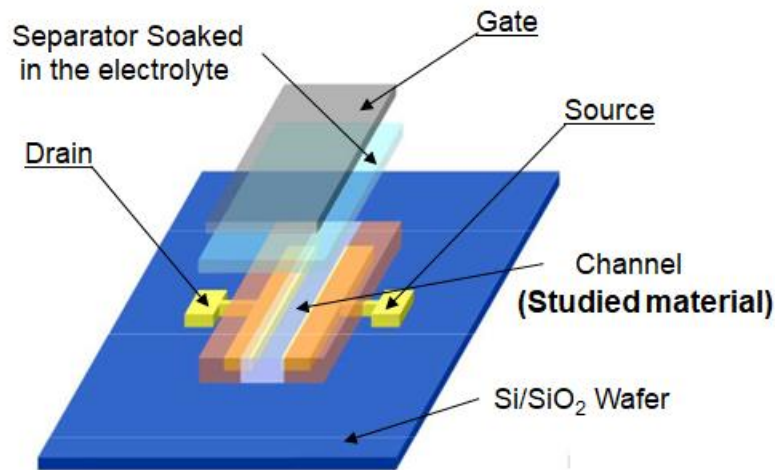


**Figure 4.2.2.** Sketch of the ion-gated transistor with highlighted components, from [18]

As highlighted in the figure, an electrolyte is placed between the gate and the channel that is composed of the material under test. The source acts as a ground and by modulating the gate-source potential ( $V_{gs}$ ), variation of the drain-source signals are expected ( $I_{ds}$ ,  $V_{ds}$ ). The channel is in short circuit with the source, therefore, modulation of the  $V_{gs}$  is equivalent to one of the gate/channel potentials. Since an electrolyte is present, the channel acts as an electrode in an electrolyte. By changing the gate-source potential, at low  $V_{gs}$ , if no faradaic reactions are present, at first there is the formation of the electrical double layer with very large specific capacitance (up to  $100 \mu\text{F cm}^{-2}$ ). This brings about high induced charge carrier densities up to  $10^{15} \text{ cm}^{-2}$  at extremely low  $V_{gs}$  voltages if compared with traditional field-effect transistors [18]. This mechanism of action defines a first-class of IGTs that is called Electric Double Layer transistors, in which the electrical double layer at the interface is exploited to modulate at low gate-source voltages, the drain-source signal. A further possibility to modulate the  $I_{ds}$  IGTs is enabled by the exploitation of faradaic reactions in the channel that may trigger variation of the gate-source signal. This latter mechanism is exploited in redox transistors.



The following subsection reports the experimental details of the preparation of the IGTs that have been exploited in this thesis. In particular, the substrate preparation, the channel coating with lithium-ion battery material-based slurry, and the encapsulation, and finally the discussion of the technique that has been exploited.

### 4.2.3 IGT set up and components

#### *Substrate preparation*

The transistor substrates were prepared in a cleanroom by the following procedure. At first, HMDS (hexamethyldisilane) treatment was performed on the SiO<sub>2</sub>/Si substrates using an HMDS priming oven (Yield Engineering Systems (YES)). Therefore, spin coating within the Resist AZ 900 MIR for a time of 30 s at 3000 r.p.m. with first baking at 90°C for 1 minute and 30 seconds was performed. The system was then exposed to UV with the Karl Suss MA6 Mask Aligner, to pattern the Silicon wafer with the desired transistor geometry. The UV exposure was followed by a second, baking at 110°C for one minute and 30 seconds. To Develop the photoresist, the silicon wafer with the desired pattern was washed with the AZ 726 developer agent. The resulting patterns were subsequently inspected with an optical microscope to verify the goodness of the process. Metallization was performed at first depositing 5 nm of Cr within a tailormade electron-beam evaporator. Secondly, with the same device, 40 nm of gold were deposited. Square-shaped substrates containing each a T-shaped pattern as reported in Figure 4.2.2 were therefore cut from the silicon wafer at the end of the previously discussed process.

#### *Channel coating*

The IGTs channels were coated with LNMO or NMC532 composite electrodes. Both LNMO (LiMn<sub>1.5</sub>Ni<sub>0.5</sub>O<sub>4</sub>, NANOMYTE. SP-10) and NMC(532) (LiNi<sub>0.5</sub>Mn<sub>0.3</sub>Co<sub>0.2</sub>O<sub>2</sub>, Shandong Gelon Lib.Co) both materials were ultra-pure. The composite layers were prepared by using a procedure that is typically adopted to produce LIB cathodes. In summary, the channel has been coated by drop-casting LNMO or NMC slurries. The slurries featured the active powders (LNMO or NMC) and polyvinylidene fluoride binder (pVdF, Arkema) in 1:8 mass ratio, dispersed in N-methyl Pyrrolidone (NMP, Sigma Aldrich). Carbon additive (Timcal C65) was eventually added with a ratio 1:8. After casting, the samples were vacuum dried at 80°C overnight. The gate electrodes were carbon papers (CP, Spectracorp 2050) coated with an ink

of activated carbon (PICACTION SUPERCAP BP10, Pica) and PVDF, KYNAR HSV900) binder in NMP (Fluka, >99.0%). The coating was followed by thermal treatment at 80°C for several hours to remove the solvent and water traces. The resulting mass loading of the carbon coating was 0.5 mg cm<sup>-2</sup>.

### *IGT configuration*

The scheme of the first type of IGT, referred to as the “well-EGT”, is reported in Figure 4.2.3 a).

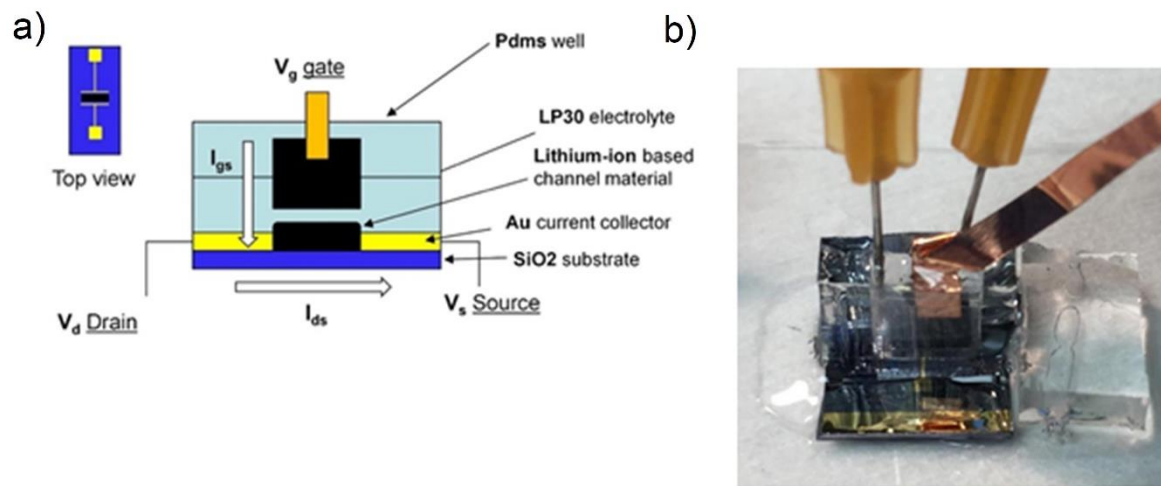


**Figure 4.2.3:** a) Sketch and b) picture of the “well-IGT”: the main components and physical quantities that have been measured are highlighted.

The top view, on the left upside of Figure 4.2.3, shows the silicon-based substrates with its two gold current collectors. The black strip between the T shaped gold current collector a black represents the channel coated with the LiMOx based electrode. Gold current collectors were prepared by means of photolithography, lift off and metallization of a Silicon wafer, and the precise experimental procedure that has been used to prepare the substrate is reported in Subsection *Substrate preparation*. The width of the channel was 4000 μm, with a length of 10 μm. The quality of the substrates was verified with optical microscopy, to investigate the integrity of the channel and the absence of gold flakes between the drain and the source. After this step, polydimethylsiloxane (PDMS) well has been placed over the top (as reported in Figure 4.2.3). The cover was sealed with PDMS exploiting its polymerization reaction. To properly eliminate the reticulating agent needed to polymerize the PDMS, the obtained system

has been left in a vacuum oven overnight at 80°C. A carbon paper electrode (0.5 cm<sup>2</sup>) coated with activated carbon (BP10T 0.5 mg cm<sup>-2</sup>) acting as gate electrode was placed inside the PDMS well, as reported in Figure 4.2.3, the carbon paper was stucked with copper tape. Two syringe needles have been used to fill the transistor with LP30 based electrolyte, the filling, as well as the test procedure, were run into an N<sub>2</sub> filled glovebox with a controlled atmosphere to avoid the oxygen electrochemical interference. After being transferred into the nitrogen-filled glovebox the device was filled with the electrolyte and tested.

#### 4.2.4 IGT characterization

The carbon-coated gate electrode acted simultaneously as a counter-electrode and as a quasi-reference counter electrode with respect to the channel material that in this setup can be considered as the working electrode. It has been previously demonstrated that when a voltage difference is imposed at the Gate-Source, the high surface area carbon electrode, for its high capacitance, will be experiencing a small potential excursion (a few mV) forcing the Channel material to experience most of the applied voltage difference. Therefore, the Gate-Source signal in this configuration is mainly affected by the channel electrochemical response [20,21] Electrochemical measurements of LIB cathodes are traditionally conducted using a lithium metal reference electrode. In our case, the reference was the carbon gate. The carbon gate potential was measured vs. lithium metal in the selected organic electrolytes and resulted in 3 V vs. Li<sup>+</sup>/Li has been found. Hereafter, the channel potentials are given vs. Li<sup>+</sup>/Li.

The characterization of the IGTs was carried out in a N<sub>2</sub> glove box (H<sub>2</sub>O, O<sub>2</sub> < 5 ppm) using a B1500A Agilent semiconductor parameter analyzer. Both transfer and output curves were collected. Table 1 reports the identification code, the active material chemical formula, and the composition of the IGT channels. Specifically, three different samples have been tested: LiMn<sub>1.5</sub>Ni<sub>0.5</sub>O<sub>4</sub> based channels without conductive carbon additive (LNMO) and with conductive carbon (LNMOc) and LiNi<sub>0.6</sub>Mn<sub>0.2</sub>Co<sub>0.2</sub>O<sub>2</sub> with carbon additive.

**Table 4.2.1** Identification code, chemical formula of the active material studied, and electrode composition of the tested materials.

Code	Active material	Electrode components mass ratio (Active material/ binder/conductive carbon additive)
LMNO	LiMn <sub>1.5</sub> Ni <sub>0.5</sub> O <sub>4</sub>	8/1/0
LMNOc	LiMn <sub>1.5</sub> Ni <sub>0.5</sub> O <sub>4</sub>	8/1/1
NMC	LiNi <sub>0.6</sub> Mn <sub>0.2</sub> Co <sub>0.2</sub> O <sub>2</sub>	8/1/1

### *LNMO and LNMOC-IGTs*

In this subsection are reported the results of the test that have been run on  $\text{LiNi}_{0.5}\text{Mn}_{1.5}\text{O}_4$  electrodes with and without the presence of conductive carbon additive C65, LNMO, and LNMOC respectively. The LMNO sample without carbon was investigated to get insight into the inherent behavior of the LNMO active powder and to set the experimental procedure. Indeed, the presence of carbon was expected to strongly impact the electronic signal of the device. Both sets of experiments were run with the well configuration reported in Figure 4.2.3, with LP30 as electrolyte.

In addition,  $V_{\text{gs}}$  was swept from 0.3 V to -1.4 V. This corresponds to channel potentials ranging from 2.7 V vs  $\text{Li}^+/\text{Li}$  to 4.4 V vs.  $\text{Li}^+/\text{Li}$ . LNMO cathodes are known to feature reversible lithiation up to 5 V vs.  $\text{Li}^+/\text{Li}$ , in our tests the upper potential was kept lower than 4.6 V vs  $\text{Li}^+/\text{Li}$  to avoid the well-known side reactions related to the electrolyte oxidative decomposition. These reactions bring about the so-called cathode electrolyte interface (CEI). The CEI is an electronically insulating, but Li-ion conductive layer, that protects the LNMO cathodes and enables their stable operation in high-voltage LIBs [22]. However, for this study, the formation of CEI would have affected the electronic response of the LNMO channel. The cyclic voltammetry (CV) of a conventional LNMO electrode, obtained in a conventional 3-electrode cell is reported in Figure 4.2.4

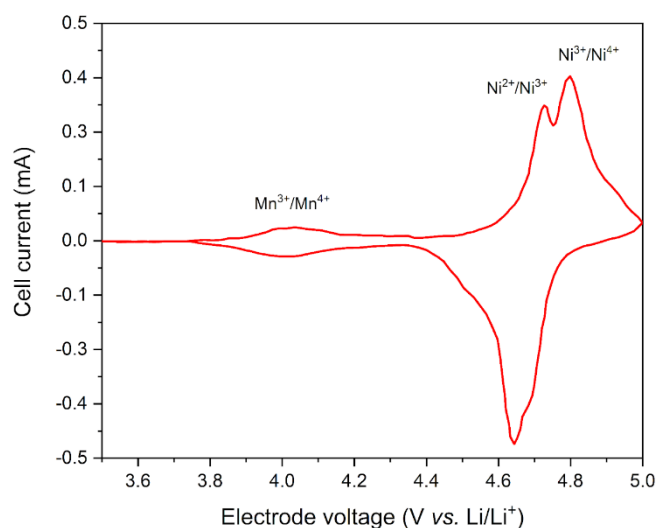


**Figure 4.2.4** voltammogram of LNMO based electrode in LP30 electrolyte in Swagelok-like cell with metallic lithium counter electrode and reference at  $50 \mu \text{Vs}^{-1}$ , with highlighted valence state variation.

The shape of the CV is as expected for LNMO, with reversible anodic peaks at ca. 4 V, 4.7 V and 4.8 V. No additional signals were detected. These listed peaks can be assigned to the  $\text{Mn}^{4+}/\text{Mn}^{3+}$ ,  $\text{Ni}^{3+}/\text{Ni}^{2+}$ , and  $\text{Ni}^{4+}/\text{Ni}^{3+}$  redox couples, respectively [23]. The CV in Figure 4.2.4 shows that within the set  $V_{gs}$ , only the first redox process, involving the redox couple  $\text{Mn}^{4+}/\text{Mn}^{3+}$  takes place.

Figure 5 reports the Transfer curves of the IGT featuring the channel coated with LNMO without carbon. The curves have been obtained at  $20 \text{ mVs}^{-1}$  (Figure 4.2.5a) and  $100 \text{ mVs}^{-1}$  (Figure 4.2.5b)  $V_{gs}$  scan rate, at constant  $V_{ds}$  of 200 mV.

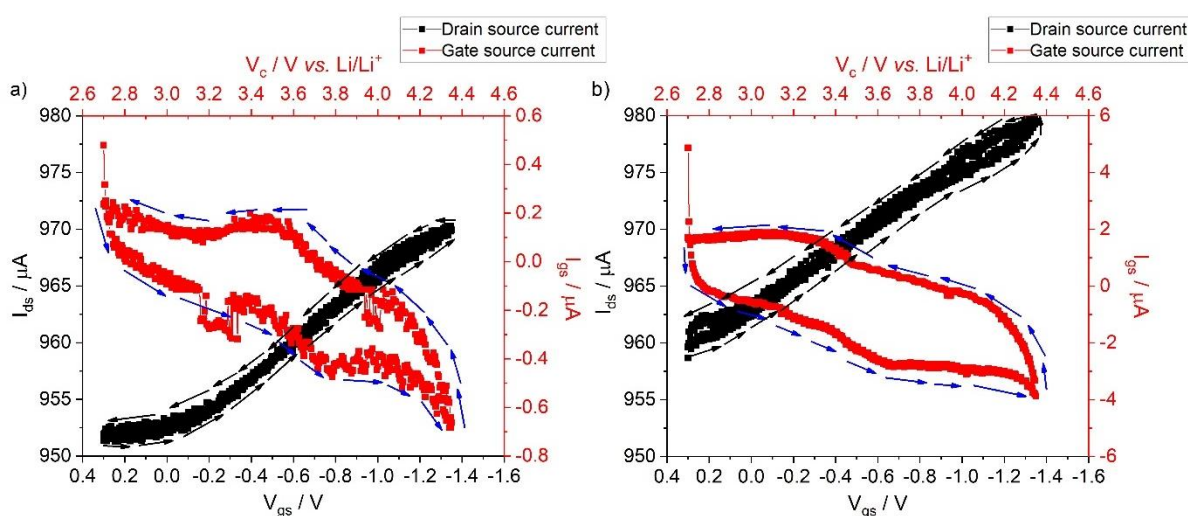


**Figure 4.2.5.** Transfer curves of the IGT featuring LNMO (without carbon) as channel coating at the  $V_{gs}$  scan rates of **a)**  $20 \text{ mV s}^{-1}$  and **b)**  $100 \text{ mV s}^{-1}$ , with  $V_{ds}$  of 200 mV.

$I_{GS}$  signals feature large peaks above 3 V vs  $\text{Li}^+/\text{Li}$  that can be attributed to  $\text{Mn}^{4+}/\text{Mn}^{3+}$  involving the lithiation/delithiation step of LNMO, The CV shape is different from the CV of bulk electrodes (Figure 4.2.5) The large peaks overlap a quasi-rectangular CV response that is almost proportional to the  $V_{gs}$  scan rate. Indeed, a tenfold increase of  $I_{GS}$  can be appreciated by increasing  $V_{gs}$  scan rate from  $20 \text{ mV s}^{-1}$  (Figure 4.2.5 a) to  $200 \text{ mV s}^{-1}$  (Figure 4.2.5 b). This is indicative of fast faradaic reactions, not limited by solid-state diffusion processes and that brings about an electrochemical response that is like that of the capacitive charging processes. Such behavior can be explained considering i) the thin layer of the LNMO channel, and ii) the evolution of the LNMO electronic properties with the lithiation. In the case of very thin layers of nanometric powders, like LNMO, the reactions change from bulk to surface redox reactions. The Li-ion diffusion length in the solid phase significantly shortens with respect to bulk electrodes. In these conditions, LNMO could exhibit the so-called “*extrinsic*”

"pseudocapacitance" [23,24]. On the other hand, *Constantin et al.* reported that the pseudocapacitive behavior can be observed when faradic reactions, like the  $\text{Li}^+$  insertion/deinsertion in LNMO, bring about an evolution of the electronic structure of the material from an insulating/semiconducting state to a conductive state. Consequently, the material approaches the status of an electronic conductor forming an electrical double-layer at contact with the electrolytic solution [25].

The  $I_{\text{DS}}$  signal can give useful indications about the change of the electronic behavior of the channel induced by electrochemical processes. Figure 4.2.5 that  $I_{\text{ds}}$  have a different trend compared to  $I_{\text{gs}}$ .  $I_{\text{ds}}$  increase almost linearly from 0.952 mA to 0.97 mA and from 0.960 mA to 0.980 mA for  $20 \text{ mV s}^{-1}$  and  $100 \text{ mV s}^{-1}$  experiments, respectively. Interestingly, the magnitude of the maximum values of  $I_{\text{DS}}$  is considerably greater than those of  $I_{\text{GS}}$ , 0.970 mA vs. -0.8 mA, and 0.980 mA vs. -4 mA for the  $20 \text{ mVs}^{-1}$  and  $100 \text{ mV s}^{-1}$ , respectively. This is an indication of the different nature of physical processes that give rise to the Gate-Source and the Drain-Source signal. Indeed, as postulated above and considering the geometry of the cell reported in Figure 4.2.2, it is possible to conclude that  $I_{\text{gs}}$  current is mostly ionic and related to the Li-ion intercalation/deintercalation in LNMO. This consideration is strengthened by the fact that  $I_{\text{gs}}$  is strongly affected by  $V_{\text{gs}}$  scan rate. Unlike  $I_{\text{gs}}$ ,  $I_{\text{DS}}$  is independent of the scan rate, and  $I_{\text{DS}}$  values are three orders of magnitude greater than those of  $I_{\text{gs}}$ .

$I_{\text{ds}}$  reversibly increase along with the delithiation (oxidation) of LNMO, therefore indicating the parallel increase of the LNMO electronically conductivity with the lithiation state. This behaviour was already reported, but it was achieved based on conventional experiments carried out by ex-situ analyses of bulk LNMO pellets or EIS experiments, where, however, a clear distinction between electronic and ionic conduction is difficult to be obtained [17]. In Figure 4.2.2a, at  $20 \text{ mV s}^{-1}$ ,  $I_{\text{ds}}$  trend is sigmoidal and becomes almost linear at  $20 \text{ mV s}^{-1}$ ,  $I_{\text{ds}}$ . At the lowest scan rate, the appearance of the  $I_{\text{ds}}$  onset at  $V_{\text{gs}} = 0 \text{ V}$  (3 V vs  $\text{Li}^+/\text{Li}$ ) unveils that LNMO changes its conduction state and that this is triggered by the change of the Mn oxidation state and LNMO delithiation. The LNMO-IGT device response is that of an IGT working in depletion mode. Therefore, overall, our preliminary study demonstrates that by an IGT setup is it possible to resolve the ionic and electronic conduction properties of LIMs.

The transfer curves were analyzed to get quantitative data for the channel carrier density ( $n$ ) by eq. (4.2.1) [19].

$$n = \frac{Q}{eA} = \frac{(\int I_g dV_g)}{r_v eA} \quad (4.2.1)$$

where  $Q$  is the accumulated charge during the forward scan in the transfer curve (obtained through the integration of the gate-source current,  $I_{gs}$ , vs time),  $A$  is the geometric area of the LNMO film exposed to the electrolyte ( $4 \cdot 10^{-4} \text{ cm}^2$ ),  $r_v$  is the  $V_{gs}$  scan rate and  $e$  is the elementary charge. The charge carrier density obtained at  $20 \text{ mV/s}$  and  $100 \text{ mV s}^{-1}$  was  $7 \cdot 10^{16} \text{ cm}^{-2}$  and c.a.  $5 \cdot 10^{17} \text{ cm}^{-2}$ , respectively. Please note that these figures refer to the LNMO-pVdF composite layer and, being affected by the presence of the binder, cannot be considered as a figure of merit of the LNMO active powder alone. Rather, they are representative of the composite material that is used in real LIB. A further step is to consider the presence of the carbon conductive additive. The charge carrier mobility wasn't not calculated since the devices did not feature a saturation region. Then, IGTs featuring an LNMOC channel with the composition LNMO/pVdF /conductive carbon additive 8:1:1 were tested. Figure 6 reports the transfer curves of this device, recorded with  $V_{gs}$  can rates of  $20 \text{ mV s}^{-1}$  (Fig 6a) and  $200 \text{ mV/s}$  (Fig. 6b) with  $V_{ds}$  of  $200 \text{ mV}$ . The green curves represent  $I_{GS}$ , while the black ones are the  $I_{DS}$ . In Figure 6, the  $I_{gs}$  and  $I_{ds}$  trends vs.  $V_{gs}$  of the LNMOC-IGT are similar, but with higher values than those recorded for the LNMO-based IGT (Figure 5). The presence of the carbon additive, as expected, promotes the lithium-ion deintercalation/intercalation in LNMO and enables a better exploitation of the active material and a higher charge storage in the channel. In turn this results in a higher modulation of the channel conductivity. Indeed,  $I_{ds}$  currents in LNMOC are 3-fold higher than in LNMO (without carbon). While the electron conduction through the channel is certainly affected by the presence of carbon, the  $I_{ds}$  reversible linear trend with  $V_{gs}$  further demonstrates that LNMO electron conductivity increases with  $i$ . Indeed, maximum  $I_{ds}$  current for LNMOC sample is  $3.45 \text{ mA}$  while  $0.980 \text{ mA}$  was measured for the LNMO sample oxidation state. Unexpectedly, even in the presence of the carbon additive, it is possible to observe that  $I_{ds}$  start to increase only behind a  $V_{gs}$  onset, which suggests a change in the conduction state of the composite layer, from insulating to conductive. For LNMOC the  $I_{ds}$  onset is at  $V_{gs} = -0.2 \text{ V}$  ( $2.8 \text{ V vs Li}^+/\text{Li}$ ), i.e. at lower channel potentials than LNMO. This indicates that the presence of carbon lowers the activation overpotential of Li-deintercalation/intercalation in LNMO and the conductivity-state transition.

The carrier density of the composite LNMOC channel was tentatively evaluated by eq. 1 and resulted in  $7 \cdot 10^{16} \text{ cm}^{-2}$  and  $4 \cdot 10^{17} \text{ cm}^{-2}$ , respectively at  $5$  and  $100 \text{ mV s}^{-1}$ .

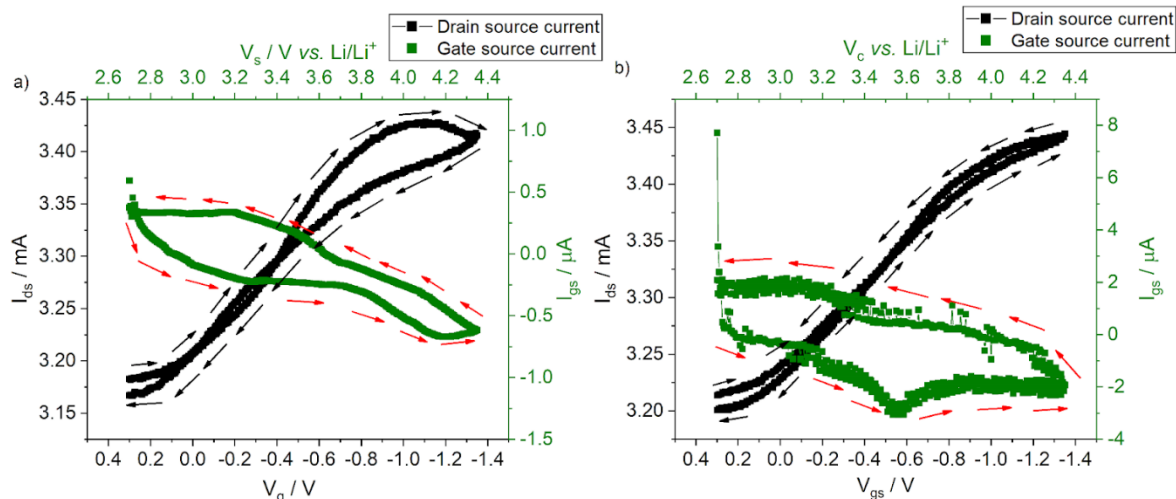


**Figure 4.2.6:** Transfer curves of the IGT featuring LNMOC (with carbon) as channel coating at the  $V_{gs}$  scan rates of **a)**  $5 \text{ mV s}^{-1}$  and **b)**  $100 \text{ mV s}^{-1}$ , with  $V_{ds}$  of 200 mV.

### NMCC-IGT

NMCC-IGTs featured a “planar” design (Figure 2) and 0.5 m LiTFSi TEGDME electrolyte as a gating medium. Indeed, as previously discussed, the planar setup requires the use of an electrolyte solution with lower vapor pressure than LP30, whose volatility strongly affects the performance of the device during tests. The channel was coated with a composite layer featuring the composition NMC/pVdF /conductive carbon additive 8:1:1.

The device was tested by evaluating its output characteristics, i.e. the  $I_{ds}$  current flowing in the channel when stepping  $V_{gs}$  at different values. Specifically, the NMC-IGTs output characteristics were characterized by recording  $I_{ds}$  while scanning  $V_{ds}$  at  $20 \text{ mV s}^{-1}$  from 0 V to -0.1 V, at different  $V_{gs}$ , from 0 and -1.6 V, corresponding to channel potentials ranging from 3 V vs  $\text{Li}^+/\text{Li}$  to 4.6 V vs  $\text{Li}^+/\text{Li}$ . In this potential range, the reversible delithiation/lithiation of NMC takes place, as shown by That reports the typical CV of a bulk NMC composite electrode carried out in a conventional 3-electrode cell.



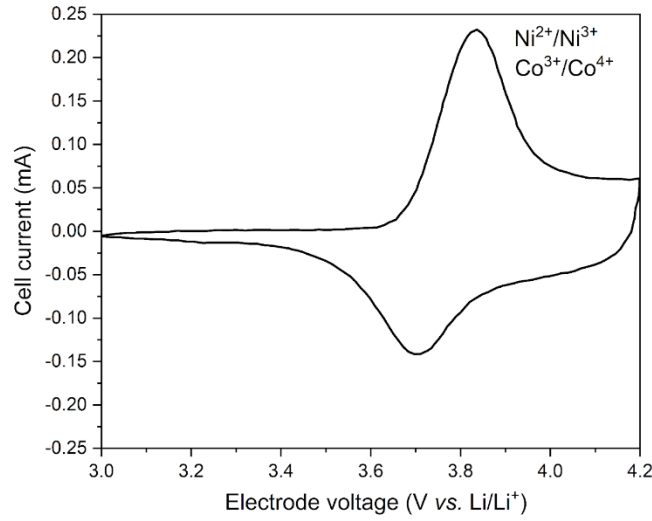


**Figure 4.2.7** voltammogram of NMC(523) based electrode in LP30 electrolyte in Swagelok-like cell with metallic lithium counter electrode and reference at  $50 \mu\text{Vs}^{-1}$ , with highlighted valence state variation.

The CV curve shows a cathodic peak at about 3.7 V, and an anodic peak at about 3.8 V vs.  $\text{Li}^+/\text{Li}$ . The redox peaks correspond to the  $\text{Ni}^{2+}/\text{Ni}^{4+}$  and  $\text{Co}^{3+}/\text{Co}^{4+}$  redox couples as highlighted in Figure 4.2.7. Figure 4.2.8 a) reports the results obtained by scanning  $V_{\text{gs}}$  from 0 to -1.6 V (from 3 V vs  $\text{Li}^+/\text{Li}$  to 4.6 V vs), i.e. at increased NMC oxidation state (delithiation) the NMC layer. Figure 4.2.8 b) shows the curve obtained by reversing the steps, i.e. from -1.6 V to 0 V (from 4.6 V vs  $\text{Li}^+/\text{Li}$  to 3 V vs  $\text{Li}^+/\text{Li}$ ), i.e. under progressive reduction (lithiation) of the oxidized NMC.

At each set  $V_{\text{gs}}$ , linearly change with  $I_{\text{ds}}$ , with a slope that increases with the NMC potential. The linear response of  $I_{\text{ds}}$  with  $V_{\text{ds}}$  can be taken as evidence of the ohmic conductor nature of the channel composite material. This is likely related to the presence of the conductive carbon additive that under this condition drives the majority of the electronic current. Under this assumption, the electronic resistivity of the channel ( $R_{\text{ds}}$ ) can be evaluated by the slope of the  $I_{\text{ds}}$  curves as a function of  $V_{\text{ds}}$ , being

$$\Delta V_{\text{ds}} = R_{\text{ds}} \cdot \Delta I_{\text{ds}} \quad (4.2.2)$$

$R_{\text{ds}}$  were evaluated by eq. (4.2.2) for different  $V_{\text{g}}$ , and the results are reported in Table 4.2.2.  $R_{\text{ds}}$  ranged from 1018 to 763  $\Omega$  (forward  $V_{\text{g}}$  step) and from 841 to 727  $\Omega$  (reverse  $V_{\text{g}}$  step).

**Table 4.2.2** Identification code, chemical formula of the active material studied, and electrode composition of the tested materials.

$V_g$ V vs. C ( $V_g$ V vs. Li/Li <sup>+</sup> )	R ( $\Omega$ ) Forward	R( $\Omega$ ) Backward
0 (3 V vs. Li/Li <sup>+</sup> )	1018	841
-0.4 (3.4 V vs. Li/Li <sup>+</sup> )	973	833
-0.8 (3.8 V vs. Li/Li <sup>+</sup> )	883	800
-1.2 (4.2 V vs. Li/Li <sup>+</sup> )	831	757
-1.6 (4.6 V vs. Li/Li <sup>+</sup> )	763	727

Interestingly,  $R_{ds}$  decrease by decreasing the degree of lithiation of the NMC channel, i.e. bringing the channel towards more positive values against Li/Li<sup>+</sup>, and this trend has a certain degree of reversibility. This finding agrees with other works reported in literature, that however have been obtained by conventional ex-situ or EIS techniques [1].

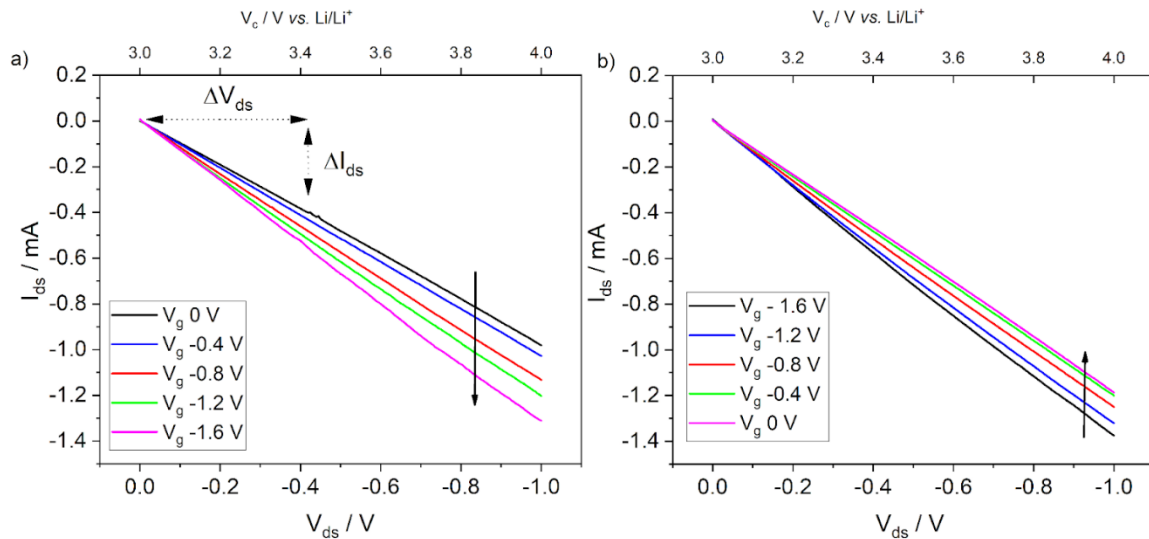


**Figure 4.2.8:** Output curves of the NMC-IGT at  $V_{ds}$  scan rate of  $20 \text{ mV s}^{-1}$  and different  $V_g$ s with 400 mV steps: **a)** from 0 to -1.6 V, corresponding to NMC potentials from 3 V to 4.6 V vs Li<sup>+</sup>/Li, and **b)** from -1.6 V to 0 V, corresponding to NMC potentials from 3 V to 4 V vs Li<sup>+</sup>/Li.

#### 4.2.4 Conclusion

To the best of my knowledge, this is the first time that LIB composite cathodes have been investigated by an IGT setup. Although preliminary, the reported results demonstrate IGTs as a simple technique to analyze and evaluate the variation of the electronic conductivity of LIB

composite electrodes as well as pristine materials in-situ, i.e. during their polarization. It enables the separate evaluation of the electronic and the ionic current in LIB composite cathodes. The characterization of LNMO and NMC-based IGT unambiguously confirmed that for these materials the electronic conductivity increases with the decrease of the lithiation.

The IGT approach can pave the way towards novel in situ and in operando diagnosis tools, that are urgently needed to carefully follow the dependence of the electronic properties of battery electrodes on their state of charge. The use of in situ tools is expected to improve the sustainability of LIBs through the identification of optimized operation conditions, bringing about optimized performance. In addition, the successful realization of LIM-IGTs could be the first building block of novel logic components based on lithium-ion batteries materials and the lithium-ion trionics.

## Chapter 4 references:

- [1] Spanu, A., Martines, L., and Bonfiglio A., "Interfacing cells with organic transistors: a review of in vitro and in vivo applications.", *Lab on a Chip*, 21.5, (2021), 795-820.
- [2] Bonné, R., et al., "Cable bacteria as long-range biological semiconductors.", *arXiv preprint arXiv*, (2019), 1912.06224.
- [2] Beech, I. B., and Sunner, J., "Biocorrosion: towards understanding interactions between biofilms and metals." *Current opinion in Biotechnology*, 15.3, (2004), 181-186.
- [3] Costerton, J., Philip W., Stewart, S., and Greenberg E.P., "Bacterial biofilms: a common cause of persistent infections.", *Science*, 284.5418, (1999), 1318-1322.
- [4] Watnick, P., and Kolter, R., "Biofilm, city of microbes.", *Journal of bacteriology*, 182.10 (2000), 2675-2679.
- [5] McLean, J. S., et al., "Quantification of electron transfer rates to a solid phase electron acceptor through the stages of biofilm formation from single cells to multicellular communities.", *Environmental science & technology*, 44.7, (2010), 2721-2727.
- [6] Felice, C. J., et al., "Impedance microbiology: quantification of bacterial content in milk by means of capacitance growth curves.", *Journal of microbiological methods*, 35.1, (1999), 37-42.
- [7] Kim, T., Kang, J., Lee, J. H., and Yoon, J. Influence of attached bacteria and biofilm on double-layer capacitance during biofilm monitoring by electrochemical impedance spectroscopy., *Water research*, 45(15), (2011), 4615-4622.
- [8] Córdoba-Torres, P., et al., "On the intrinsic coupling between constant-phase element parameters  $\alpha$  and  $Q$  in electrochemical impedance spectroscopy.", *Electrochimica Acta* 72, (2012), 172-178.

- [9] Brug, G. J., et al., "The analysis of electrode impedances complicated by the presence of a constant phase element.", *Journal of electroanalytical chemistry and interfacial electrochemistry*, 176.1-2, (1984), 275-295.
- [10] Zoltowski, P., *Journal of Electro analytical Chemistry*, 443, (1998), 149.
- [11] G.J. Brug, A.L. G. Van Den Eeden, M.Sluyters Rehbach, J.H.Sluyters, *Journal of Electroanalytical Chemistry* 176, (1984), 275
- [12] Tortora, G. J., Berdell R. Funke, and Christine L. Case. *Microbiology: an introduction*. Benjamin-Cummings Publishing Company, (2010).
- [13] Gorby, Yuri A., et al., "Electrically conductive bacterial nanowires produced by *Shewanella oneidensis* strain MR-1 and other microorganisms.", *Proceedings of the National Academy of Sciences*, 103.30, (2006), 11358-11363.
- [14] Reguera, G., et al., "Extracellular electron transfer via microbial nanowires.", *Nature*, 435.7045, (2005), 1098-1101.
- [15] Amin R, Chiang YM. *Journal of The Electrochemical Society*, 13;163(8), (2016), A1512.
- [16] Waag, W., Stefan K., and D. U. Sauer., "Experimental investigation of the lithium-ion battery impedance characteristic at various conditions and aging states and its influence on the application.", *Applied energy*, 102, (2013), 885-897.
- [17] Muharrem, K., Jafar F. Al-Sharab, and Glenn G. Amatucci *Chemistry of Materials* 18, (15), (2006), 3585-3592
- [18] Leighton, C., "Electrolyte-based ionic control of functional oxides." *Nature materials* 18.1, (2019), 13-18.
- [19] Valitova, I. et al. "Photolithographically patterned TiO<sub>2</sub> films for electrolyte-gated transistors." *ACS applied materials & interfaces* 8.23 (2016): 14855-14862.
- [20] Sayago, J., et al. "Low voltage electrolyte-gated organic transistors making use of high surface area activated carbon gate electrodes." *Journal of Materials Chemistry C* 2.28 (2014): 5690-5694.
- [21] Tang, Hao, et al. "Conducting polymer transistors making use of activated carbon gate electrodes." *ACS applied materials & interfaces* 7.1 (2015): 969-973.
- [21] Park, Kyusung, et al. "Electrochemical nature of the cathode interface for a solid-state lithium-ion battery: interface between LiCoO<sub>2</sub> and garnet-Li<sub>7</sub>La<sub>3</sub>Zr<sub>2</sub>O<sub>12</sub>." *Chemistry of Materials* 28.21 (2016): 8051-8059.
- [22] Chemelewski, Katharine R., et al. "Factors influencing the electrochemical properties of high-voltage spinel cathodes: relative impact of morphology and cation ordering." *Chemistry of Materials* 25.14 (2013): 2890-2897.
- [23] Jiang, Yuqi, and Jinping Liu. "Definitions of pseudocapacitive materials: a brief review." *Energy & Environmental Materials* 2.1 (2019): 30-37.
- [24] Liu, Y., S. P. Jiang, and Z. Shao. "Intercalation pseudocapacitance in electrochemical energy storage: recent advances in fundamental understanding and materials development." *Materials Today Advances* 7 (2020): 100072.

[25] Constantin, T. R. Porter, J. M. Savéant, *ACS Appl. Mater. Interfaces* 2017, 9, 8649–8658.

[26] Li, Xing, et al. "Improved rate capability of a  $\text{LiNi}_{1/3}\text{Co}_{1/3}\text{Mn}_{1/3}\text{O}_2/\text{CNT}/\text{graphene}$  hybrid material for Li-ion batteries." *RSC Advances* 7.39, (2017), 24359-24367.

# Chapter 5: Conclusions and perspectives:

## 5.1 Summary

The continuous growth of the population together with the rising incomes bring about the willingness to spend their incomes on energy-water-intensive goods. These two sectors (energy and water) are deeply interlinked in the so-called water-energy nexus. Common strategies are needed to address a sustainable consumption of the water capable of limiting the depletion of this precious resource, together with a reduced environmental footprint. In this context, electrochemical energy storage systems play a key role. Novel electrochemical conversion systems such as microbial fuel cells rise as a valuable technology that aims to produce clean water while providing direct electric energy. However, the low power output of these systems is limiting their practical applications. The low cell voltage is an intrinsic characteristic of MFCs and therefore strategies that aim at improving the output current are more likely to be adopted to improve power performances. For this reason, under the frame of this Ph.D. thesis, the integration of supercapacitive features in MFCs has been explored. The adopted strategies have been carried mainly in three research lines: i) the development of green supercapacitors,

ii) their external integration with MSCs and, iii) the development of supercapacitive microbial fuel cells by the monolithic integration of supercapacitive features in MFC electrodes. In addition, a new approach, based on the exploitation of the IGTs has been exploited to investigate the electrode/electrolyte interfaces. These activities have been carried out under national and international, collaborative projects that involved different research groups, and specifically groups of the Department of Chemistry “Giacomo Ciamician” (Polymer science and biomaterials Lab – Prof. ML.Focarete and Prof. C. Gualandi, and the Nanobio interface Lab-Prof. M. Calvareis), with the University of Padova (Electrocatalysis and Applied Electrochemistry Lab -Prof. C. Durante), the University of Firenze (Dept. of Chemistry Ugo Schiff, Prof. M. Innocenti), Prof. C. Santoro (University of Milano-Bicocca), the University of Pretoria (Research Group Carbon Technology and material - Prof. N. Manyala), and the Polytechnique Montreal (Organic electronics labs-Prof. C. Santato and Prof F. Cicoira). These extremely fruitful collaborations were carried out under different national and international projects, namely ISARP 2018-2020 /Italy-South Africa joint Research Programme 2018-2020 (Italian Ministers of Foreign Affairs and the Environment and NRF of South Africa, grant No. 113132), Fondazione CARISBO/Progetto ricerca n° 354, Piano Triennale di Realizzazione 2019-2021/Progetto ricerca n° 354, Subvention de projets de recherche IE/Appel à projets 2020 (Institut de l'énergie Trottier), Collaborative project “Study of ion insertion and evolution of the electric double layer in ion-gated metal oxide transistors operating under different gating mechanisms” (NSERC: Natural Sciences and Engineering Research Council of Canada,CNMS2020-B-00495) Oak Ridge National Laboratory center For Nanophase Materials Sciences - Polytechnique Montreal – University of Bologna.

At first, green supercapacitors were developed, and the main results are discussed in Chapter 2. In parallel, strategies to both integrate external supercapacitors and monolithically integrate supercapacitive features in MFCs have been carried out and are reported in Chapter 3. These two activities merge into the development of a green supercapacitive system that has been discussed in section 3.4. A third more explorative line of research followed on this thesis regards the study of electrochemical interfaces and is discussed in Chapter 4. Therefore, at first Pullulan a novel biopolymer has been exploited as the main component (binder and electrospun separator) to prepare high voltage ionic liquid based EDLCs (section 2.1). After evaluating the contribution to the cell resistance of the different combinations of electrospun separator and electrolytes, the ionic liquid EmimTFSi has been selected as the electrolyte to assemble green supercapacitors. This IL is known for its good electrochemical properties in terms of chemical

and electrochemical stability, conductivity ionic. However, here an additional advantage in the use of this IL was demonstrated. Indeed, the exploitation of pullulan, an aqueous processable biopolymer in combination with hydrophobic ionic liquid, brings about a smart combination of material that enables an easy to dispose of strategy. Indeed, by soaking in water the device at its end of life, the aqueous processable binder quickly dissolves and the immiscible ionic liquid separates enabling the direct recovery of the EDLCs main components. The pullulan-based supercapacitor delivered a maximum specific power of up to  $5 \text{ kW kg}^{-1}$ , and maximum specific energy of  $27.8 \text{ Wh kg}^{-1}$  specific energy at  $3.2 \text{ V}$ , these values well compare with conventional electrical double-layer capacitor performance with the added value of being eco-friendly and cheap with cell capacitance of  $20 \text{ F g}^{-1}$ . The Pullulan-based EDLCs showed good cycling stability up to 5000 cycles. Notably, the EDLC assembled with pepper seeds-derived carbon, outperformed the EDLC based on a commercial carbon. Two further approaches have been followed through collaborative projects with partner universities, namely the adoption of N-doped carbon, to improve the energy density of ionic based EDLCs, reported and discussed in section 2.2, and the adoption of superconcentrated electrolyte, to improve the cell voltage of EDLCs featuring aqueous electrolyte, to improve the energy densities of more sustainable EDLCs that avoid organic-based solvent electrolytes, reported, and discussed in section 2.3. As a parallel activity, the response at the system level of MFCs integrated with a commercial supercapacitor, has been carried out. The results of the system integration are reported and discussed in section 3.1. At first, the integration of MFCs with commercial supercapacitors highlighted two main effects, the first one at high current densities and another at low current pulses. At high currents pulses effect, the response is dominated by the SC that in turn enable output power not feasible with single MFCs. At low current pulsed the MFC contributed to the overall system capacitance, probably owing to its faradaic component. This first study highlighted that basic electrochemical characterization of MFC and SC, singularly and combined is necessary for the right system sizing and application. This study enabled the evaluation of MFC-EDLC performance at the system level and represented the first step, which has been followed by the substitution of the commercial supercapacitor with a green one designed in this thesis. Has been carried out. The results of the external integration of the MFC with a green supercapacitor designed in this thesis are reported in section 3.4.3. Sustainability and waste valorization have been central themes in this thesis, therefore, the main solid waste of the biodigester from which the MFCs inoculum was taken has been adopted as bio precursor to prepare activated carbon. Carbons were activated by a mild activating agent like  $\text{KHCO}_3$  using different activating agents to precursor mass ratios (1:0.5, 1:2 respectively for LAC0.5-

and LAC2). The best carbon (LAC2) has been exploited to prepare electrodes with a conventional binder and to assemble a symmetric EDLC with  $\text{KNO}_3$  aqueous electrolyte. This EDLC displayed a good specific capacitance of  $28.5 \text{ F g}^{-1}$ , corresponding to an electrode specific capacitance of  $114 \text{ F g}^{-1}$ , with specific energy-specific and power up to  $10 \text{ Wh kg}^{-1}$  and  $6.9 \text{ kW kg}^{-1}$ , respectively. Durability tests showed that the device was able to maintain capacitance retention of 84.5% after 15000 charge-discharge cycles. The lignin-derived carbons were also studied as electrocatalysts for ORR in a neutral medium, to investigate the feasibility of the use of LAC as the main component of microbial fuel cell air-breathing cathode. The LAC-2 showed higher ORR electrocatalytic activity than LAC-0.5. Indeed, LAC-2 showed higher current density values and superior ORR activity as compared to LAC-0.5. The number of electrons transferred during ORR was higher for LAC-2. Once integrated with an air-breathing cathode, the material exploited high electrochemical ORR activity especially at high current densities. To further demonstrate the sustainable manufacturing of EDLC, and to advance with respect to the work reported in section 3.1a green supercapacitor exploiting only bioderived components, like the LAC-2 carbon electrodes with calcium alginate binder, and  $\text{Ca}(\text{NO}_3)_2$  aqueous electrolyte has been developed (AaSC). This study was carried out focusing on the sustainability of the system and in view of the AaSC EDLC external integration with the MFC. Hence, the EDLC was tested at low cell voltages, compatible with the voltage output of MFC, i.e.  $0.6 \text{ V s}$ . The AaSC EDLCs featured good specific capacitance of  $22.9 \text{ F g}^{-1}$  cycling stability over 2000 cycles. The specific energy was lower than that of commercial systems mainly because of the selected low voltage. The design of the AaSC supercapacitor is reported in section 3.3.3 and the results of its external integration with the MFC (SC//MFC system) are reported in section 3.4.3. The SC//MFC system boosted the power output by 2 orders of magnitude than those of the single MFC. Moreover, the system has been cycled for 5000 cycles at  $1 \text{ Ag}^{-1}$  of specific current of the EDLC.

Finally, the LAC2 carbon has also been exploited as the main component of both MFC and SC monolithically integrated systems, where the adoption of an additional supercapacitive cathode (AAC-MFC section 3.4.4) and the decoration of the anode with LAC2 (MSC-MFC section 3.4.5) was pursued. The best performance was achieved with the MSC-MFC system, which featured an outstanding energy  $35 \mu\text{Wh}$  at current rate of  $20 \text{ mA}$ , considerably higher than that of the other tested systems and, mainly, with respect to the single MFC that delivered only  $6.4 \mu\text{Wh}$  at its lowest tested current of  $1 \text{ mA}$ .



Overall, this study highlighted that the adoption of the external supercapacitor allows the MFCs to release high current pulses at high power, but more detailed analysis shows that at the energy level the monolithic supercapacitive MFC dominates the response in terms of energy. Therefore, as a prospective study, the integration of these two systems, external green supercapacitor, and monolithic supercapacitive fuel cell, should be carried out.

To get further insight into the bioanode/electrolyte interface electrochemical and electronic properties, I carried out electrochemical impedance spectroscopy (EIS) study of carbon paper electrodes in a real wastewater environment. The aim was to follow the “in vivo” evolution of the electrochemical response of the bioanode during the electrode colonization. The results of this study reported in Section 4.1. EIS suggested a decrease of the electronic resistance of the bioanode that could be ascribed to the increase of both ionic and electron conductivity of bacteria grown on carbon paper. However, EIS does not permit clear discrimination between ionic versus electronic contributions to the overall electrode impedance. One powerful approach that enables discriminating ionic and electronic contributions is to investigate materials by an ion-gate transistor (IGT) with the aim of being trained in such fascinating approach, I spent a period at University of Montreal, in the groups led by Prof. C. Santato and F. Cicoira, recognized worldwide for their expertise in IGT and organic electronics. The idea was to learn the fundamentals of IGTs and to transfer the acquired knowledge to the field of electrochemical energy storage and bioelectrochemistry. Unfortunately, due to the pandemic emergency, I was not able to exploit IGT for the study of the bioanodes and my main work on IGT focused on more conventional, but not less important materials, namely the lithium-ion insertion cathodes used in lithium-ion batteries. The main result of this study is that IGTs allow investigating the electronic properties of LIBs material in operando, further study on the exploitation of this set-up on microbial fuel cell anode as well on chemistries other than the studied one will be carried out.

## **5.2 Conclusions and outlook**

Overall, the activities carried out during my Ph.D. project are extremely challenging and include the study of different electrochemical processes, from capacitive, to bio electrochemical and electrocatalytic, the optimization of electrodes and systems manufacturing, with a focus on sustainability, and device characterization and system integration.

The main novelty of my work has therefore been the exploitation and merging of different electrochemical systems and their components, by a green approach, to boost MFCs performance up to two orders of magnitude than conventional air-breathing MFCs. This thesis demonstrates that, by exploiting smart design, is possible to realize sustainable energy storage and conversion system, capable of improved power performances with respect to the state of the art in the case of the MFCs, and comparable with the state of the art in the case of the Ionic liquid-based pullulan EDLCs.

As highlighted in the introduction of this work, the concept of sustainability without the improvement of the performance is not enough to sustain the challenges of our times and in particular the one of the water-energy nexus. Multidisciplinary and contamination from other fields such as one of the organic electronics are a valuable approach to develop novel methods that are capable to explore the electrode/electrolyte interface, like IGTs, triggering research on novel exciting fields such as one of the lithium-ion trionics. Indeed, as an example, the IGTs reported in this thesis, enable the study of the electronic response of the material or lithium-ion batteries that can be exploited for developing novel transistors. In parallel, IGTs can also be used to investigate electronic properties of living electrodes, like MFCs anode, which is a research line that I would like to further explore in my future.

### *Acknowledgments*

I would like to thank at first my supervisor, Professor Francesca Soavi, for her patience, scientific rigor, and for being one of the most important person to me, that I've ever met so far. I would like to thank Professor Ncholu Manyla and his group for their hard work and help in the development of carbon-based EDLCs and MFCs, Carlo Santoro for his consistency and passion in the field of MFCs, Professor Clara Santato and Professor Fabio Cicoira and their groups for their support in the field of IGTs, Professor Durante and his group for their great material synthesis and characterization, the group of Professor Innocenti for their great work in the field of current collector corrosion, Professor Maria Letizia Focarete and Professor Chiara Gualndi for their exceptional work in electrospinning of natural polymer, and professor Matteo Calvaresi and his group for the modeling studies.

I would like to thank all the people that helped me so far, most of all who believe in me, who teach me, and who stay with me as a friend and colleague. For the rest, I do understand, it is cold outside and there is no time. Finally, I would like to thank whoever took the time to read this work, which, hopefully, represents just a beginning.

My personal take-home message is that I will have to keep studying for the rest of my life with discipline and method.

## Appendix A (Supercapacitors)

### Appendix A.1 Double-layer capacitance and the ideally polarizable electrode

It must be clearly stated that there is a profound difference between the response of an ideal EDL-driven process and a real activated carbon electrode one. In practice, the equation that is obtained from the ideal EDL model are widely adopted to compare the performance of lab prototypes of EDLCs, and therefore in this section, these equations are derived and the limitations that the hypothesis under which are obtained are discussed in detail.

The concept of the ideally polarizable electrode has been described in the work of Grahame:

*“An ideally polarizable electrode is one where changes of potential due to current flow to or from an electrode cause only changes of charge density on the metal and conjugately of ion density on the solution side of the electrode interface, leading to charging of the resulting double layer”*

The essential aspect of the ideally polarizable electrode is that within changes of potential, charges flow from the external circuit and within the solution, only to charge the double layer, with no charge passing across the double layer. The electrochemical response of a plain electrode, dominated by the formation of an electrical double layer with a capacitance  $C_{EDLC}$  without any Faradaic reaction is well described by the equivalent circuit reported in Figure A.1.1. Being an ohmic conductor, this electrode will have an associated series resistance  $R_{ESR}$ .

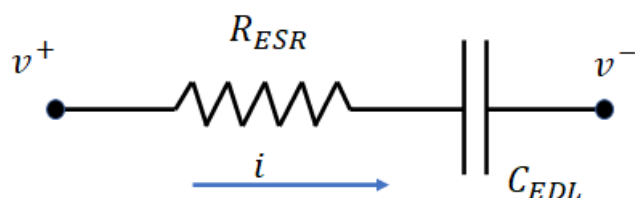


Figure A.2.1: Equivalent circuit of the ideally polarizable electrode

Figure A.1.1 is reported the equivalent circuit that models the electrical response of a plain electrode. Where  $R_{ESR}$  is the equivalent series resistance ( $\Omega$ ), while ( $C_{EDL}$ ) is the capacitance associated with the formation of the electrical double layer (F).

*A.1.1 Electrochemical response under galvanostatic charge/discharge with voltage limitation*  
 When the circuit reported in the figure is tested under constant current condition (Galvanostatic) the measured quantity is the voltage at the terminal and the imposed quantity is the current. Applying the *Kirchhoff voltage law* at the two terminals of the circuit reported in Figure A.2.1 (during the charge, in the assumption of the capacitor to be completely discharged) yields

$$v(t) = v^+(t) - v^-(t) = i \cdot R_{ESR} + \frac{q(t)}{C} \quad (A.1.1)$$

Where  $v(t)$  is the voltage at the two-terminal,  $i$  is current and  $q(t)$  is the charge stored in the electrical double layer. At constant current,  $i \cdot t = q(t)$ , and therefore is possible the substitution and the simplification of equations (A.1.1) into (A.1.2)

$$v(t) = i \cdot \left( R_{ESR} + \frac{t}{C_{EDL}} \right) \quad (A.1.2)$$

Assuming that the electrode is charged up to a terminal voltage  $V_t$ , similar argumentation can be drawn for the equation that models the discharge

$$v(t) = V_t - i \cdot \left( R_{ESR} + \frac{t'}{C_{EDL}} \right) \quad (A.1.3)$$

Where  $V_t$  is the terminal voltage at which the EDLSC is charged, if the equation is plotted, the typical triangular shape expected at constant current, galvanostatic condition is obtained and has been plot in Figure A.1.2.

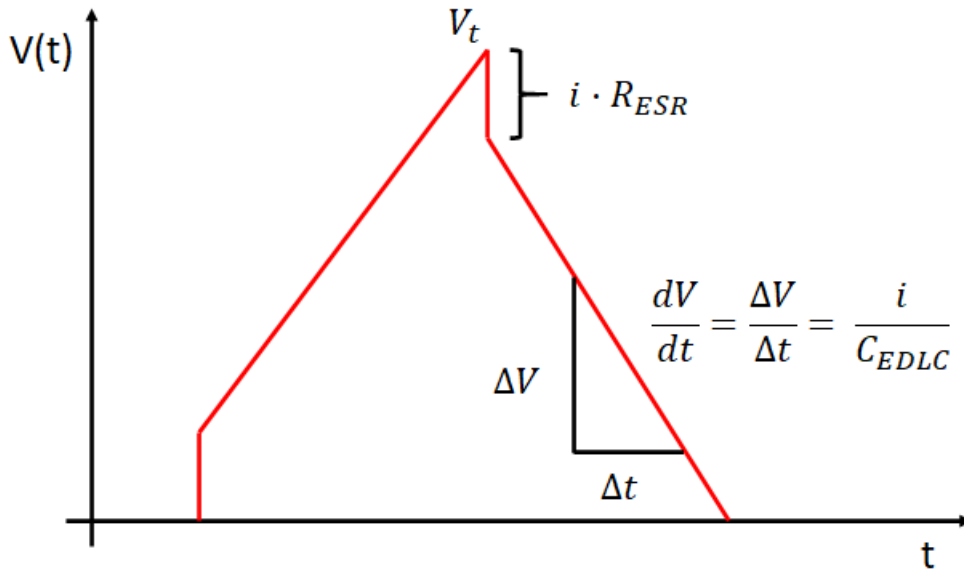


**Figure A.1.2** Expected voltage profile for ideally polarizable electrode under galvanostatic charge/discharge

The experimental procedures consist of obtaining the voltage profile of the EDLSC under galvanostatic charge/discharge, at different specific currents. condition is possible to evaluate the capacitance from the slope of the discharge curves, that is

$$\frac{dV}{dt} = \frac{i}{C_{EDLC}} \rightarrow C_{EDLC} = \frac{i}{\frac{dV}{dt}} \quad (A. 1.4)$$

In practice, both the charge and the discharge profile aren't perfectly linear, the straight consequence is that there are several deviations from the circuit reported in Figure A.1.1,. Indeed, in AC-based electrodes, the hierarchical pore's structure brings about different degrees of accessibility of the ions to the surface of the electrode as well as mass transport limitation and also specific interactions lead to voltage profiles that deviate from the linearity.

The capacitance of a supercapacitor under galvanostatic conditions is therefore evaluated by the slope of the tangent line to the discharge curve. Nevertheless, the evaluation of the capacitance from the slope of the tangent line is equivalent to the reduction of the system at a single RC as reported in Figure A.1.1, which yields great practical applications.

With this simple model, it is possible to appreciate that the produce  $iR_{ESR}$  cause an instantaneous voltage to drop that can be related to a loss of storable energy, therefore the minimization of this quantity plays a critical role in optimizing the performance of EDLSCs.

From the definition of energy associated with electrical work, it is possible to evaluate the average energy delivered during the discharge of a net charge  $Q$  to 0 in a time  $\Delta t = \tau - t_0$  that is

$$E = \int_Q^0 V \cdot dq = \int_{t_0}^{\tau} V \cdot i \cdot dt = i \cdot \int_{t_0}^{\tau} V \cdot dt \quad (A.1.5)$$

Since the experiment are done under constant current conditions, where  $E$  is the energy (Joule).

It should be highlighted that during the charge phase if no Faradaic reactions are present, the voltage will keep increasing and therefore the area of the  $V(t)$  curves during the discharge.

The average power associated with the discharge can be evaluated by the formula

$$P = \frac{E}{\Delta t} \quad (A.1.6)$$

Where  $P$  is the average power (Watt) and  $\Delta t$  is the discharge time (seconds).

Usually, to compare different electrodes and electrolyte formulation, specific quantities are reported instead of not normalized ones moreover, it is common to report the specific energy as  $Wh/kg$  and the specific power in  $kW/kg$ .

The maximum energy can be obtained assuming a purely capacitive behavior, that the device is charged between 0 and  $V_{max}$ , it is possible to obtain the equation for the maximum energy

$$\int_{t_0}^{\tau} V \cdot i \cdot dt = \int_{t_0}^{\tau} V \cdot C \frac{dV}{dt} \cdot dt = C \int_0^{V_{max}} V \cdot dV = \frac{CV_{max}^2}{2} = E_{max} \quad (A.1.7)$$

It is worth mentioning that to yield this equation, it is necessary to assume the capacitance independent from the time (charge), which underlines the fact that we are assuming an ideal process taking place at the electrode/electrolyte interface during the polarization. Moreover, this equation underlines the fact that it is worth pushing the research in the direction of high voltage EDLCs, since the energy goes as a quadratic function of the voltage, and it is linear in the capacitance. For a capacitor electrode of c.a.  $1000 \text{ m}^2 \text{ g}^{-1}$  operating at 1 V with a specific double-layer capacitance of  $30 \mu\text{F cm}^{-2}$  (e.g. carbon black), the total capacitance is c.a.  $300 \text{ F g}^{-1}$ , the maximum energy stored is given by equation xx and lead to  $E_{max} = \frac{1}{2} \cdot 300 \cdot 1^2 = 150 \text{ kJ} \cdot \text{kg}^{-1} = 42 \text{ Wh kg}^{-1}$ ; In practice, it will be substantially less owing to the inaccessibility of electrolyte solution to the fines pores of the porous electrodes, the weight of the packaging, and the weight of the electrolyte ( both acting as dead components).

Indeed, it is well known that to overcome the intrinsic limitation of EDLSCs one strategy that has been widely explored is the adoption of Ionic liquid-based electrolytes that enable higher maximum voltage, with respect to the traditional acetonitrile ones and therefore higher average energies.

The maximum power can be calculated applying the Maximum power transfer theorem, which states:

*“To obtain maximum external power from a source with a finite internal resistance, the resistance of the load must equal the resistance of the source as viewed from its output terminals”*

Applying this theorem to the circuit reported in figure A.2.1.3., it is possible to evaluate the maximum power, by imposing the load resistance equal to the internal resistance, as reported in figure A. 1.3

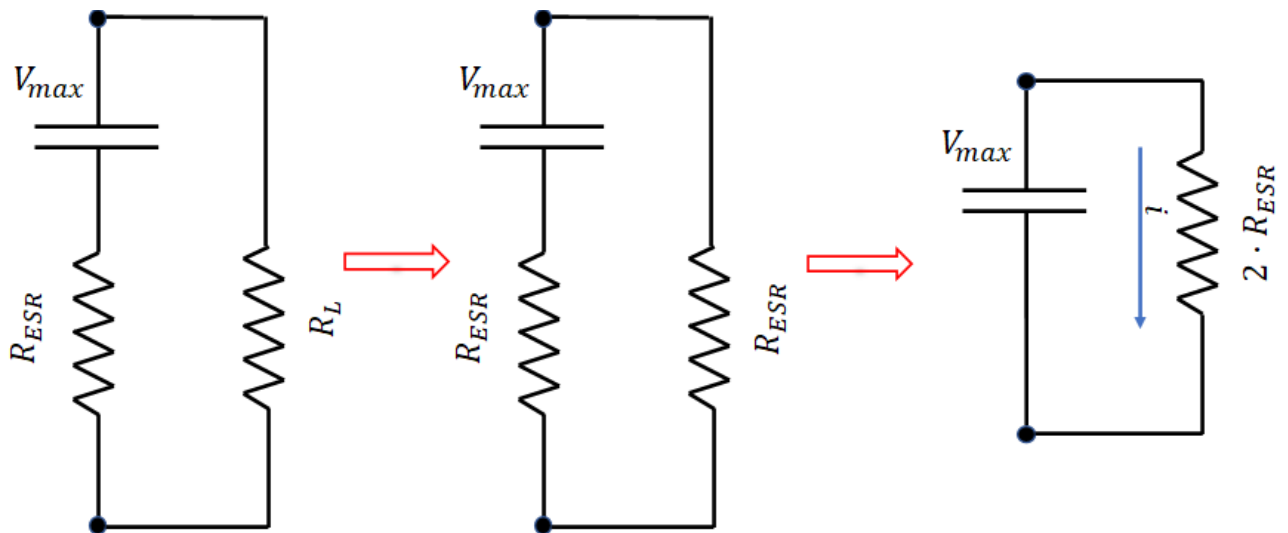


**Figure A. 1.3** Graphical application of the maximum transfer theorem.

Therefore, to maximize the power output, the current  $i$  that passes in the circuit when the  $R_L$ , that is the load resistance is equal to the internal resistance is given by the ohms law, and is

$$i = \frac{V_{max}}{2 \cdot R_{ESR}} \quad (A. 1.8)$$

The maximum power at the load is transferring to the resistance is equal to the power that resistance is consuming and therefore, given the definition of instantaneous power consumed by a resistor

$$P_{max} = R_L \cdot i^2 = R_{ESR} \cdot i^2 = V_{max}^2 \cdot \frac{R_{ESR}}{4 \cdot R_{ESR}^2} = \frac{V_{max}^2}{4 \cdot R_{ESR}} \quad (A. 1.9)$$



This equation is usually reported to quantify the maximum power output of a supercapacitor, it should be highlighted that this value represents an instantaneous power rather than a mean one and therefore it doesn't give solid information on the effective energy that can be drawn from the discharge of the device.

Given the electrostatic nature of the electrical energy storage, a high degree of reversibility is expected between the charge and the discharge, a useful quantity that can be exploited to measure this is the coulombic efficiency ( $\eta$ ) that is the ratio between the charge stored during the charge phase and the charge delivered during the discharge.

$$\eta = \frac{Q_{dsc}}{Q_{chrg}} \quad (A.1.9)$$

Where  $Q_{dsc}$  and  $Q_{chrg}$  are the discharge and charge charges, respectively. The coulombic efficiency together with capacitance retention, that is the ratio between the capacitance of the device during the initial cycle and one of the  $i^{\text{th}}$  cycles are reported vs. the cycle number to evaluate the cycle life of the device. Indeed, secondary unwanted irreversible Faradaic reactions, dissolution of the electrode, and corrosion of the current collector can be spotted under cycling by a decreasing trough cycling of these two quantities.

### *A.1.3 Cyclic voltammogram of an ideally polarizable electrode*

Similarly, by exploiting the equivalent circuit reported in the figure it is possible to predict the shape of an EDL-driven process under voltammetric conditions. Under voltammetry, the potential is imposed between an initial value ( $V_i$ ) and a terminal one ( $V_f$ ) with a sweep rate  $\nu$  and the current is measured. Under these circumstances, by applying the Kirchhoff voltage law the following equation is obtained

$$V(t) = \nu \cdot t = R_{ESR} \left( \frac{dq}{dt} \right) + \frac{q}{C_{EDL}} \quad (A.1.10)$$

That is a first-order differential equation at constant parameters, with the boundary condition  $q_0 = 0$ , the solution of this equation is

$$i(t) = \nu \cdot C_d \left( 1 - \exp \left( - \frac{t}{R_{ESR} C_{EDL}} \right) \right) \quad (A.1.11)$$

Assuming similar argumentation for the discharge, therefore a sweep rate of  $-\nu$  with a boundary condition of

$$i(t) = -v \cdot C_d \left( 1 - \exp\left(-\frac{t}{R_{ESR}C_{EDL}}\right) \right) \quad (\text{A.1.12})$$

Graphical procedures to obtain the cyclic voltammogram that is usually used for this kind of evaluation are reported in figure A.2.3.1

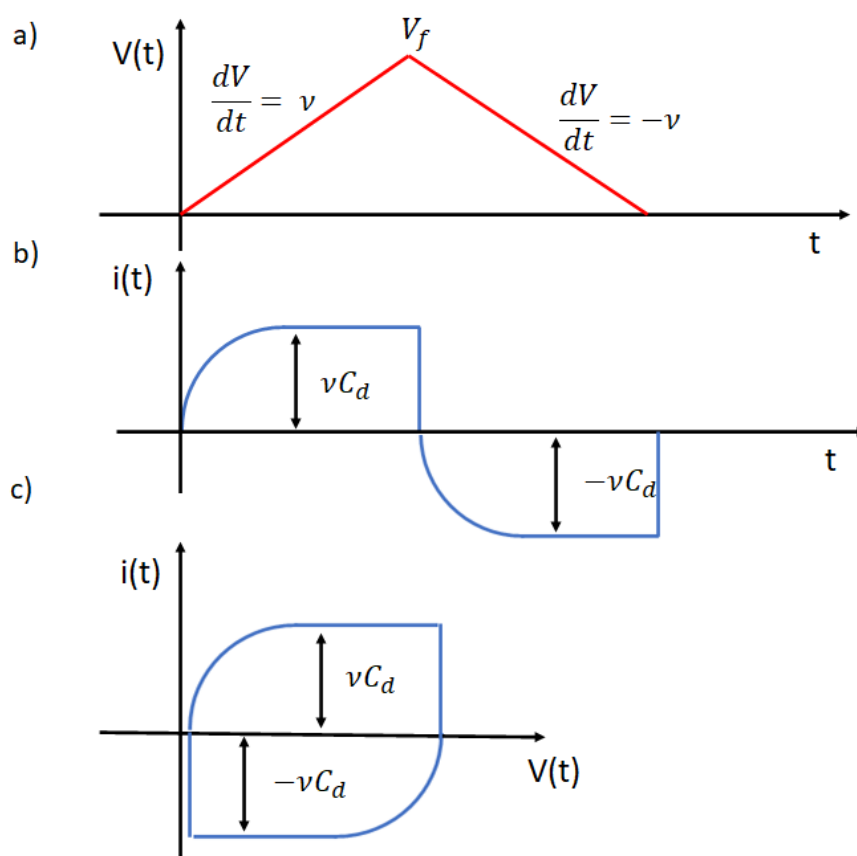


**Figure A.1.4** Graphical procedure to obtain the voltammogram of an ideally polarizable electrode. a) potential profile imposed over time with a sweep velocity of  $v$  up to a terminal potential  $V_f$ , b) current response of the electrode as a function of time under the cyclic voltammetry and, c) cyclic voltammogram of a purely capacitive electrode.

From this figure is possible to evaluate the graphical procedure that yields the voltammogram of an electrical double layer driven process. Indeed, in figure A.1.4 c) is reported the typical box-shaped symmetric voltammogram that indicates a reversible electrical double layer driven process. In a real system, several deviations may occur related to a particular pores size distribution in the case of a high specific surface area electrode, specific adsorption/desorption phenomena as well as quick faradaic reaction that may cause deviation from this shape. Nevertheless, the simple circuitual model proposed here is capable to predict the traditionally box shaped cyclic voltammetry as well as the dependency of the voltammetric current by the scan rate that is widely adopted when a single electrode's specific capacitance is evaluated under cyclic voltammetry experiments. Is worth noticing that often in the scientific practice,

the equation for the ideally polarizable electrodes is exploited to evaluate the electrochemical response of laboratory prototypes of EDLCs cells.

#### A.1.4 Evaluation of electrode capacitance from device measurements

Referring to the circuit model reported in figure xxx, it is possible to model a complete device as two capacitors in series connected by resistance, as reported in Figure A.1.5.

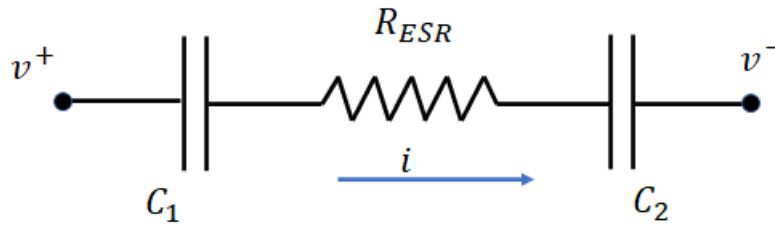


**Figure A.1.5:** Equivalent circuit of an EDLCs featuring two electrodes

Here  $C_1, C_2$  are represent the capacitance of the positive, and the negative electrode, respectively. While  $R_{ESR}$  is the equivalent series resistance that is the sum of the ohmic contribution that are present in the complete device (e.g., the ohmic resistance of the electrolyte, the ohmic resistance of the current collector, the electrodes). It is possible to show that the specific capacitance of the device is related to the specific capacitance of the single electrode and is strongly related to the mass balance of the electrodes.

#### Symmetrical mass balance in EDLCs

If the mass of the electrode material is taken as the normalizing parameter and for the device reported in Figure A.1.5 a total capacitance  $C_T$  is measured, the specific capacitance of the two-electrode system is given by the equation

$$C_S = \frac{C_T}{2 \cdot m} \quad (A. 1.13)$$

If the two electrodes have specific capacitance  $C_1$  and  $C_2$  being in parallel, the total capacitance of the device is given by

$$\frac{1}{C_T} = \frac{1}{C_1} + \frac{1}{C_2} \rightarrow C_T = \frac{C_1 C_2}{C_1 + C_2} \quad (A. 1.14)$$

If the system is symmetric,  $C_1 = C_2 = C$  and therefore the equation simplifies to

$$C_T = \frac{C}{2} \quad (A. 1.15)$$

Therefore, substituting equation

$$C_s = \frac{C}{4m} = \frac{C_1}{4m} = \frac{C_2}{4m} \quad (\text{A. 1.16})$$

According to this equation, the specific capacitance of the electrode can be evaluated as four times the specific capacitance of the device.

### Asymmetric mass balance in EDLCs

In a capacitor in which the electrodes are not symmetric due to a different mass loading but with identical electrode materials and composition the equation that relates the single electrode capacitance and the material ones becomes

$$C^+ = m^+ C \quad (\text{A. 1.17})$$

$$C^- = m^- C \quad (\text{A. 1.18})$$

Where  $m^+$ ,  $C^+$  and  $m^-$ ,  $C^-$  are the mass loading, the specific capacitance of the negative and the positive electrodes, respectively. Therefore, the specific capacitance of the device becomes

$$C_s = \frac{C_T}{m^+ + m^-} \quad (\text{A. 1.19})$$

As in the example of the two symmetric electrodes, the total capacitance of the device is given by equation A.1.14, and substituting equation A.1.17 and A.1.18 the relation A.1.14 becomes

$$C_T = \frac{m^- m^+}{m^- + m^+} \cdot C \quad (\text{A. 1.20})$$

Substituting into equation A.1.19 the general expression A.1.20 is yield

$$C_s = \left( \frac{m^- m^+}{m^- + m^+} \right) \cdot \frac{1}{m^+ + m^-} C \quad (\text{A. 1.21})$$

Is obtained, e.g. ( $m^+ = 2 \cdot m^-$ )

$$C_s = \frac{2}{9} C \quad (\text{A. 1.22})$$

That is, with respect to the case of a symmetric capacitor, the capacitance of the device is the capacitance of the single electrode reduced by a factor of 0.222 rather than a 0.25, which is a 12.5 % less. This calculation can be used as argumentation that the exploitation of asymmetric mass loading to exploit the widest electrochemical stability window can be used when the gain in energy is greater than the loss in specific capacitance of the single electrode.

## Appendix B: BET surface area measurements

BET measurements are widely adopted together with a pores size distribution, in this section the main hypothesis under which the BET theory is obtained are discussed together with the relevant equations. In general, the capacitance expressed per gram of electrode has been found to increase with the surface area of porous carbon. However, in some cases, no clear relationship between the surface area and the total surface area was observed. In general, this deviation is explained by the difference between the specific capacitance on the micropore surface and on the external surface

Specific surface area pores size distribution and pores volume are textural properties that strongly affect the performance of the carbonaceous materials, for supercapacitors applications. Pores are categorized by IUPAC according to their diameter as

- Micropore: Width < 2nm
- Mesopore  $2 < \text{Width} < 50 \text{ nm}$
- Macropores > 50 nm

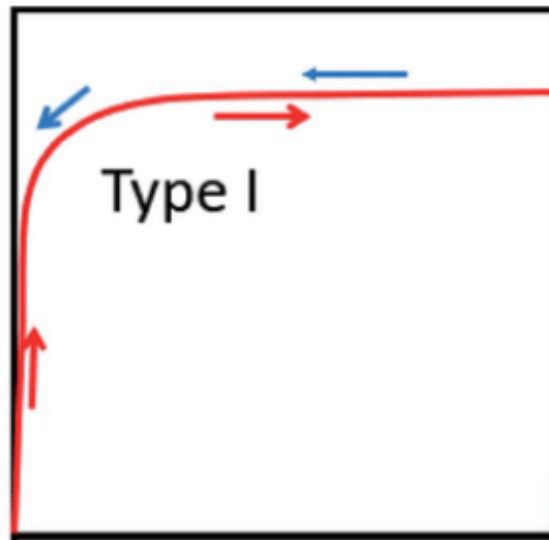
Micropores size extends down to molecular dimension and play an important role in the adsorption-based process, through restricted diffusion and molecular sieve effects. Fine micropores exhibit a greater adsorbent-adsorbate affinity. Adsorption in fine pores can occur via a pore filling mechanism rather than the surface coverage hypothesized by the Langmuir and BET theory, that lead to unrealistic high surface area estimation. Mesopores contribute to surface area and their relatively large size allow adsorbate accessibility. Macropores, on the other hand, generally make negligible contribution to the surface area of porous carbon and their main function is to act as “transport avenue” into the interior of carbon particles. Materials with the highest surface area are consistently obtained by highly microporous activated carbon, in which the micropores occupy the 90% of the total volume. Activated carbon derived from naturally occurring precursors tend to contain pores from all three classes and the selection of the precursor as well as the activation conditions, lead to significant control over the relative contribution of each size class. Isotherm nitrogen adsorption isotherm can be exploited as a technique to determine the specific surface area as well as the pores volume and the pores size distribution. Adsorption is the attaching of gas molecules to the surface of a solid including the surface inside the open pores, increasing the pressure of the gas over the solid leads to an increase in the adsorption. The desorption, on the other hand, is the removal of gas molecules

from the surface of a solid including its inner pores and decreasing the pressure of the gas over the solid leads to an increase in the desorption. When the interaction between a surface and an adsorbate takes place and it is driven by weak forces such as Van der Waals forces the adsorption mechanism is called physisorption. During physisorption, the heat of adsorption is relatively low, and the process involves a multilayer of adsorbed molecules with high isothermal reversibility. On the other hand, when electronic interaction between the atoms of the surface and the adsorbed molecules are present, the adsorption mechanism is called chemisorption. Chemisorption is characterized by large interaction which leads to high heats of adsorption, given its nature, it is a monolayer process, and being a chemical reaction, this kind of interaction has activation energy associated with it. Moreover, with respect to the physisorption it has poor isotherm reversibility. Physisorption is exploited when surface area measurements are needed while, Chemisorption is exploited when the measurements to evaluate the number of active sites on the surface of a material, this technique indeed is exploited to evaluate the activity of the catalyzer. In physical adsorption, the driving force is the unbalance of forces between the bulk of the material and its surface

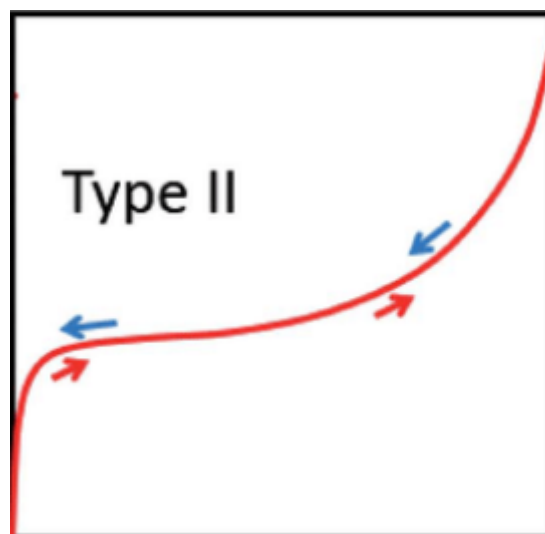
The specific surface area of activated carbon is measured through physisorption measurement. The most exploited gas for this measurement is nitrogen, it is possible to run physisorption measurements also with Ar, CO<sub>2</sub>, CO, O<sub>2</sub>, and CH<sub>4</sub>H<sub>10</sub>. As known nitrogen is an inert gas with a modest reactivity, therefore the interaction with most of the adsorbing surface is related to weak interaction such as Van der Waals and therefore is physisorption. Since adsorption is an Exothermic process, high temperatures tend to inhibit the physical adsorption; therefore, the measurements are run in a bath of liquid nitrogen that keeps the system under isotherm condition at low temperatures (77 K). Physical adsorption is fully reversible, allowing adsorbate to fully adsorb/desorb. The output of the measurement is the adsorption isotherm that is obtained by measuring the amount of gas adsorbed across a wide range of relative pressure at a constant temperature. Indeed, the fraction of the surface covered by adsorbed molecules increases with the relative pressures. Conversely, desorption measurements are achieved by measuring the gas removed as pressure is decreased. The first adsorption layer is called the Langmuir adsorption layer, on the second and further adsorption layer condensation of gas into liquid occurs. The relation between physisorption and the determination of the surface area of the material is related to the fact that once the monolayer of adsorbed molecules is formed, this will completely cover the area of the surface and therefore

$$S = A_{cs} \cdot N_m \quad (B.1)$$

Where  $S$  is the surface of the material,  $A_{cs}$  is the correctional area of the adsorbed molecule, and  $N_m$  is the number of molecules that are needed to adsorb a monolayer over the surface of the adsorbent material. Nitrogen adsorption isotherm data are reported in the form of adsorption isotherm, according to the morphology of the surface but also to the kind of process that occurs, the isotherm curves are classified into six kinds

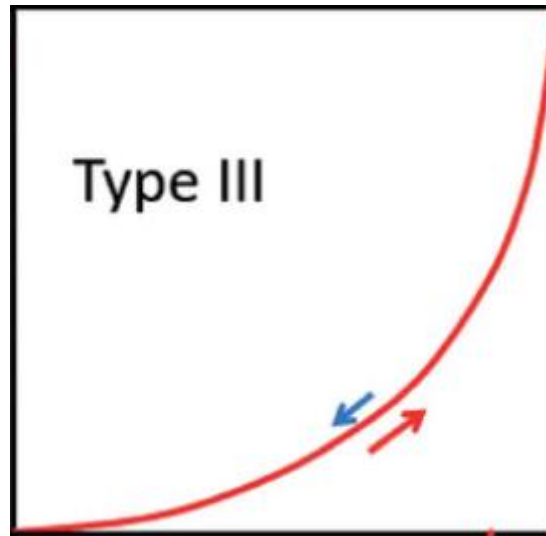


**Type I:** Adsorption in micropores, adsorption isotherm are related to microporous surface with the exposed surface residing almost exclusively inside the micropores, which once filled with adsorbate, leave little or no external surface for further adsorption. Moreover, the adsorption is limited to a few molecular layers and is characteristic of activated carbon and zeolites.

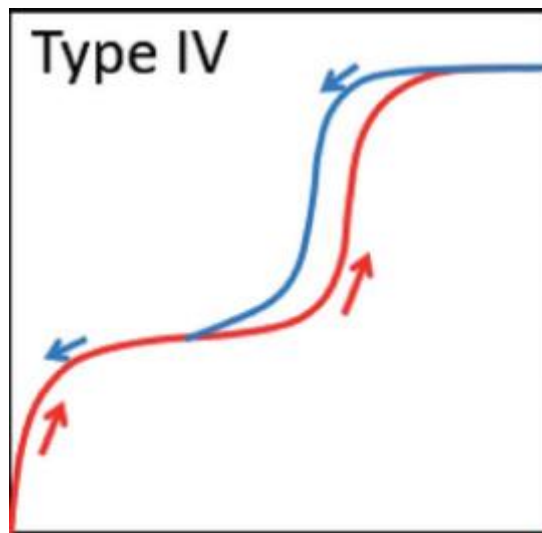


**Type II** Unrestricted monolayer-multilayer adsorption, this are related to non-porous powders or microporous powders. Is characterized by an evident inflection point occurs near

*the completion of the first adsorbed monolayer. This point represents the complete coverage of the monolayer.*

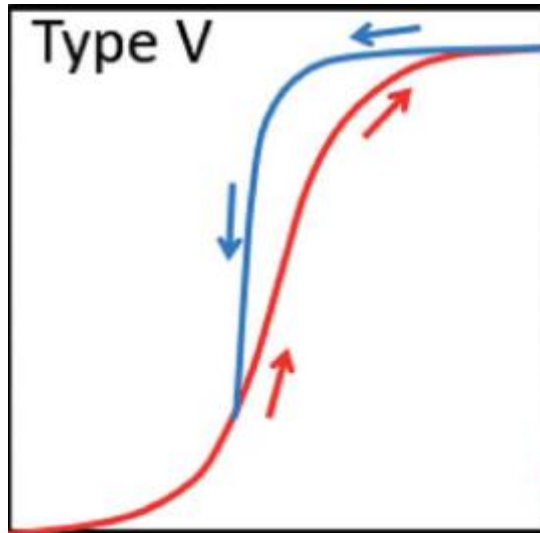


**Type III** adsorption isotherm appears when the interaction between the adsorbed molecules are greater than the interaction with the adsorbant surface. This phenomenon is characterized by heats of adsorption less than the adsorbate heat of liquification, as an example nitrogen on polyethylene.

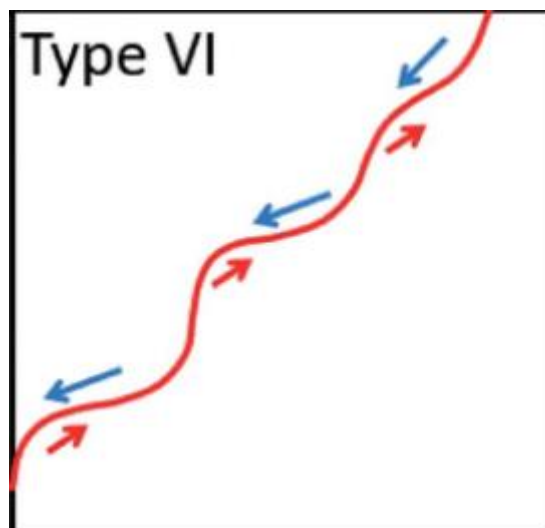


**Type IV** Monolayer-multilayer adsorption and capillary condensation, this isotherm occurs when the pores distribution is in the range 1.5-100 nm. At higher pressure, the slope shows and increase uptake of the adsorbate as pores become filled, inflection point typically occurs neat the completion of the first monolayer and is related to the complete pore filling.





**Type V** Weak interaction and capillary condensation, this isotherm are observed when small adsorbate-adsorbent interaction similar to Type III and are also associated with pores in the 1.5-100 nm range



**Type VI** Stepwise multilayer adsorption on a non-porous non-uniform surface. An example of this is the adsorption of Ar or Kr on graphitized carbon.

The mathematical description of the adsorption/desorption isotherm allows to determine the surface area and pore data, the models used for the mathematical description are empirical models that fit the experimental and therefore, the discussion of the results should take into account that surface area or pore volume determined using empirical volume is approximated.

There are two theories that give access to the monolayer capacity using the isotherm which is the Langmuir and the BET, in this Appendix BET theory and its limitation is described.

Specific area of activated carbon is often estimated through the Brunauer-Emmet-Taller (BET) specific surface area, this theory assumes that

- Gas molecules behave ideally
- There is the formation of a single monolayer
- All sites on the surface are equal
- There aren't adsorbate-adsorbate interactions
- Adsorbate molecules are immobile

Under this hypothesis, the BET theory states that the Surface is homogeneous, that there aren't lateral interactions between molecules, that the uppermost layer is in equilibrium with the vapor phase, that all surface sites have the same adsorption energy for the adsorbate. The main limitation of the BET is that the BET equation, is applicable for non-porous materials since it is difficult to separate the pores filling from the monolayer formation. The BET equation is

$$\frac{1}{W \cdot \left( \left( \frac{P_0}{P} \right) - 1 \right)} = \frac{1}{W_m \cdot C} + \frac{(C - 1)}{W_m C} \cdot \left( \frac{P}{P_0} \right) \quad (B. 2)$$

Where  $W_m$  is the weight of the gas adsorbed,  $P/P_0$  is the relative pressure,  $W_m$  is the weight of the adsorbate monolayer and  $C$  is the BET constant. The BET equation requires a linear plot of  $\frac{1}{W \cdot \left( \frac{P_0}{P} \right) - 1}$  vs  $\frac{P}{P_0}$ , indeed the BET equation can be rearranged as

$$\frac{1}{W \cdot \left( \left( \frac{P_0}{P} \right) - 1 \right)} = m \cdot \left( \frac{P}{P_0} \right) + q \quad (B. 3)$$

Where  $m$  and  $q$  are the slopes and the intercept that is determined from the experimental adsorption isotherm. The linear trend is yield in the region in which the monolayer is completed that has been empirically determined as the region between  $0.05 < \left( \frac{P}{P_0} \right) < 0.3$ . This limitation is related to the fact that high energy sites are occupied at low relative pressure, and this is related to the assumption  $0.05 < \left( \frac{P}{P_0} \right)$ , at the same time polarization forces

These two quantities that are determined by linear fit are related to

$$m = \frac{C - 1}{W_m C} \quad (B.4)$$

$$q = \frac{1}{W_m C} \quad (B.5)$$

Therefore, since  $m$  and  $q$  are experimentally determined it is possible to calculate the  $W_m$  and  $C$  as

$$W_m = \frac{1}{m + q} \quad (B.6)$$

$$C = \frac{m}{q} + 1 \quad (B.7)$$

Finally, the weight of the adsorbate monolayer can be related to the specific surface of the adsorbent  $S$  as

$$S = \frac{W_m \cdot N_A \cdot A_{cs}}{P_m \cdot w} \quad (B.8)$$

Where  $N_A$  is the Avogadro number,  $P_m$  is the molecular weight and  $w$  is the weight of the tested sample.